MEMS Turbomachinery Rotordynamics: Modeling, Design and Testing

By

CHIANG JUAY TEO

B. Eng., Mechanical Engineering, National University of Singapore, 1997
M. Eng., Mechanical Engineering, National University of Singapore, 2001

Submitted to the Department of Aeronautics and Astronautics
in Partial Fulfillment of the Requirements for the Degree of

Doctor of Philosophy
at the
Massachusetts Institute of Technology
June 2006

Author: _____
Department of Aeronautics and Astronautics
February 17, 2006

Certified by: _____
Professor Zoltan S. Spakovszky
C. S. Draper Associate Professor of Aeronautics and Astronautics
Committee Chairman

Certified by: _____
Professor Alan H. Epstein
R. C. Maclaurin Professor of Aeronautics and Astronautics

Certified by: _____
Dr. Stuart A. Jacobson
Principal Research Engineer

Accepted by: _____
Professor Jaime Peraire
Professor of Aeronautics and Astronautics
Chair, Committee on Graduate Students

MEMS Turbomachinery Rotordynamics: Modeling, Design and Testing

By

CHIANG JUAY TEO

Submitted to the Department of Aeronautics and Astronautics
on February 17, 2006 in partial fulfillment of the requirements for the degree of
Doctor of Philosophy

Abstract

One of the major challenges encountered for the successful operation of high-power-density micro-devices lies in the stable operation of the bearings supporting the high-speed rotating machinery. This thesis presents the analysis, design, microfabrication, testing and operation of high speed micro-hydrostatic gas bearings for microturbomachinery in power-MEMS applications. A novel turbine driven microbearing test device for demonstrating repeatable high-speed gas bearing operation was designed, microfabricated and tested. The new microbearing test device incorporates numerous features, including a four plena journal bearing feed system enabling both isotropic and anisotropic journal bearing operation, labyrinth seals for reducing rotordynamic coupling, a redesigned turbine for satisfying power requirements, reinforced thrust bearing structural design, a novel rotor fabrication technology for achieving low radial imbalance and a symmetric feed system to avoid rotor sideloading arising from pressure or flow non-uniformities.

A rigorous theory is presented to analyze the effects of compressibility in micro-flows (characterized by low Reynolds numbers and high Mach numbers) through hydrostatic thrust bearings for application to microturbomachines. Operating protocols for ensuring thrust bearing static stability have been established and successfully demonstrated on several micro-devices in the MIT Microengine Project. In addition, a simple and useful dynamic stability criterion has been identified: Dynamic instability occurs when the flow through both thrust bearings chokes. A-priori dynamic stability predictions were subsequently verified experimentally for the first time on a micro-turbocharger. A generalized Green's function approach has been successfully implemented for analyzing tilting effects and geometric non-uniformities in micro-hydrostatic gas thrust bearings.

The effects of a non fully-developed circumferential flow in low length-to-diameter ratio ($L/D << 1$) micro-hydrostatic journal bearings are analyzed for the first time. Effects on journal bearing whirl stability and viscous power dissipation are quantified using a simple analytical model and CFD calculations. A dimensionless parameter characterizing the ratio of the flow-through time of the axial hydrostatic flow to the viscous diffusion time was identified to govern the evolution of the circumferential flow field. Singular behavior of the stability boundary or whirl-ratio occurs when the flow through time of the axial hydrostatic flow is approximately half the characteristic viscous diffusion time. Operating conditions for high speed, stable journal bearing operation can thus be ascertained.

Experimental techniques and data reduction schemes facilitating the evaluation of key journal bearing rotordynamic information such as the stiffness, natural frequency and damping ratio, as well as the imbalance of the rotor have been successfully implemented. Imbalance-driven whirl response curves for providing an improved understanding of the rotordynamic behavior of micro-hydrostatic gas journal bearings have been obtained for the first time.

Effects of journal bearing width and anisotropy are systematically investigated on the redesigned microbearing test device. For low levels of journal differential pressures DP, high whirl ratios ranging between 20 and 40 were achieved. These whirl-ratios were one order of magnitude higher than those encountered in macro-scale journal bearings. Almost all devices tested anisotropically at high values of DP achieved speeds in excess of 1 million rpm. The improvements in bearings and seals design, the high reliability of the novel microfabrication processes, and the repeatability and successful implementation of the operating protocols were vindicated. A first-of-a-kind controlled high speed operation up to 70% of the design speed was also demonstrated. This corresponds to a rotation rate of 1.7 million rpm, a rotor tip speed of 370 m/s and a DN number of 7 million mm-rpm. The technical feasibility of high-speed gas bearings required for achieving high power densities in MEMS-based micro-turbomachinery has thus been experimentally demonstrated.

Thesis Supervisor: Zoltan S. Spakovszky
Title: Charles Stark Draper Associate Professor of Aeronautics and Astronautics

ACKNOWLEDGEMENTS

First and foremost, I wish to acknowledge my thesis advisor Professor Zoltan Spakovszky for the precious guidance, encouragement and support he has given me throughout these years. I am grateful for the many hours of discussion we had on issues related to bearings and other non-rotordynamic related stuff. His excellent mentorship and keen interest in my work and wellbeing have been a great source of inspiration.

I also wish to express my sincere appreciation to the other members of my Thesis Committee, Professor Alan Epstein and Dr. Stuart Jacobson, who are essentially like co-advisors to me. I am indebted to Professor Epstein for allowing me to work on such a challenging project, for always having an interesting and memorable story to tell in order to drive home a point, and for his remarkable ability to keep such a macro-scale project on micro-scale devices going on for so many years. I am thankful to Stu for numerous insightful discussions, for sharing his valuable experiences on experimentation, for always being supportive and for keeping the project going.

I wish to extend my appreciation to Dr. Fred Ehrich who has been very enthusiastic and supportive throughout the course of this research. I am also thankful to Dr. Ehrich for painstakingly reading through my entire thesis and pointing out many typos and errors. I also wish to express my heartfelt thanks to Professor Edward Greitzer for agreeing to serve as an examiner for my Generals and his inspiring book on Internal Flows. I wish to thank Dr. Choon Tan for sharing with me many important facts of life and reminding me about the importance of graduating. Many thanks to Dr. Jim Paduano for providing me with the initial codes for reducing the unintelligible experimental data. I am grateful to Dr. Yifang Gong for his assistance on turbine design and his invaluable advice on Fluent-related issues. The help and advice provided by Dr. Gerry Guenette on experimental matters are gratefully acknowledged. I thank Professor Kerrebrock for taking time off to read my Dissertation. I also wish to acknowledge Professor Mark Spearing for useful discussions on matters regarding structural mechanics. I would also like to thank Professor Jaime Peraire for his willingness to serve as my Minor Advisor. Shawn Berry from Lincoln Laboratory has been very helpful in assisting with some FEM calculations.

I am indeed privileged to be able to work with such a large number of extremely talented and dedicated researchers, staff and students in many diverse disciplines.

In terms of microfabrication, I wish to say a big thank you to Dr. Hanqing Li, Dr. Li Wang and Linhvu Ho. I learnt a great deal about microfabrication from all of them. Hanqing essential served as a microfabrication advisor to me. Linhvu has been a good buddy in the clean room and rendered me lots of assistance in wafer processing. I also wish to thank the staff from the Microsystems Technology Laboratories (MTL), in particular Kurt Broderick, Donal Jamieson, Dave Terry and Paul Tierney.

Back in GTL, I wish to express my gratitude to Jimmy Letendre for being such an effective laboratory manager. I apologize for always having to bother him to replenish the empty bottles of gases. Both Jimmy and Jack Costa have been instrumental for helping me with instrumentation issues and setup of the experiment. Despite his endless list of job requests, Viktor Dubrowski has been very kind in helping me machine some device packages. The late Paul Warren has been a great source of strength whenever I get bitten by the Dogs. May his soul rest in peace. The administrative support rendered by Lori Martinez, Susan Parker and Holly Anderson is kindly appreciated.

Lixian Liu has taught me much more rotordynamics than anyone else during the past five years. He has been a great friend and colleague, and I will always cherish the long hours we spent together doing experiments and chatting about everything under the sun.

I also wish to thank Shana Diez, Nick Savoulides and Lodewyk Steyn for allowing me to perform experiments on their precious devices to validate the analytical models, despite the fact that they did not have many more devices to survive on.

Vei-Man Lei has been a wonderful and supportive friend for the past four years in GTL. I also wish to thank Harn Wei Kua, Leonard Lee and Melvyn Sim, especially the former two who embarked on and persevered through this half-decade "marathon" together with me in the world's finest institute.

I dedicate this work to my parents and sister, and I thank them for their unyielding support, care and concern throughout these years.

I am thankful for the generous financial support provided by the National University of Singapore, who has kindly paid for my tuition and stipend during the first five years of my doctoral studies. This research was sponsored by DARPA and the US Army Research Laboratory under the Collaborative Technology Alliance Program. This support is gratefully acknowledged.

TABLE OF CONTENTS

LIST OF FIGURES

LIST OF TABLE

NOMENCLATURE

A	area
AR	area ratio
α	contact angle of liquid-gas interface
β_x, β_y	Euler angles
β_{FD}	ratio of axial flow-through time to characteristic viscous diffusion time
C	journal bearing width
C_f	friction coefficient
c	damping
χ	dynamic imbalance
D, d	orifice diameter; rotor diameter
D_h	hydraulic diameter
DP	hydrostatic differential pressure across journal bearing
ε	rotor radial eccentricity
ε_0	permittivity of free space
F	force
F_p	generator pull-in force
f	friction coefficient
G	Green's function
g	generator gap
γ	ratio of specific heats
h	thrust bearing gap or clearance
I	diametral moment of inertia
I_p	polar moment of inertia
k	angular stiffness
K	axial stiffness
K^{hd}	cross-coupled hydrodynamic tilting stiffness
K^{hs}	direct-coupled hydrostatic tilting stiffness
L	orifice length; journal bearing length

Λ	bearing number
$\dot{m}$	mass flow
m_R	mass of rotor
M	Mach number
μ	dynamic viscosity
ν	kinematic viscosity
$\hat{\omega}$	reduced frequency
ω_H	Helmholtz resonance frequency
P, P_t	static pressure, stagnation pressure
P_{supply}	thrust bearing supply pressure
P_{pump}	pressure at pump outlet
r	radial location of orifices; radial coordinate
R	radius of thrust bearing pad; radius of rotor
Re	Reynolds number
$\Re$	specific gas constant; journal bearing whirl ratio
ρ	fluid density
s	Laplace variable
σ	surface tension; structural stress
T, T_0	static temperature, total temperature
ζ	damping coefficient; non-dimensional hydrodynamic moment
V	fluid velocity
υ	voltage difference between stator and rotor
ψ, Φ, ϕ	functions
Ω	rotational speed
Ω_N	natural frequency
Ω_W	stability boundary (threshold speed at onset of whirl instability)
$\{\}^{hd}$	hydrodynamic
$\{\}^{p}$	hydrodynamic $\{\}$ due to the rotor pumping action
$\{\}^{v}$	hydrodynamic $\{\}$ due to the viscous drag

CHAPTER 1

INTRODUCTION

This dissertation documents the analysis, design, microfabrication, testing and operation of high speed micro-hydrostatic gas bearings for microturbomachinery in power-MEMS applications. In the first part of this chapter, the background and motivation behind the research and development of power-MEMS devices and the micro-scale bearings required to support the high-speed spinning rotors in these devices are presented. The salient challenges encountered in the analytical modeling, design, microfabrication and operation of microbearings are subsequently discussed. This is followed by a review of previous research work pertaining to bearings and rotordynamics in the context of the MIT microengine project. The remaining challenges and unresolved issues from previous research efforts are identified, thus laying down the foundation for the objectives and goals of this thesis. Next, the bearing system requirements for power-MEMS applications are presented, and the applicability of various different bearing systems technologies is assessed. The organization of this thesis is detailed in the final part of this chapter.

1.1 Background and Motivation

The advent of the computer age has heralded a new era. During the past four decades, the electronics industry has grown by leaps and bounds, thanks to the revolution in microelectronics. Today's integrated circuits consist of billions of transistors, a phenomenon which was deemed ridiculous and impossible in the 1960's. Researchers soon realized that the microfabrication techniques developed for standard Silicon IC processing could be employed for fabricating Silicon sensors and actuators, thus carving out a whole new discipline now widely and popularly known as MEMS (MicroElectroMechanical Systems). A variety of MEMS devices have been developed during the past decades and several of them have been mass-produced. Examples of successful MEMS sensors include accelerometers for the deployment control of automobile airbags and pressure transducers for automotive and bioengineering

applications. Examples of successful MEMS actuators include video display systems employing electrostatically controlled micromirrors, ink-dispensing nozzles in the heads of ink jet printers, as well as microvalves and micropumps which constitute integral facets of microfluidic systems.

One discipline which could potentially reap the benefits accruing from miniaturization is power generation. Owing to the advances in digital technology and the development of portable consumer appliances that incorporate wireless Internet services and applications, the importance of having a reliable energy source has greatly accentuated. Portable and long-life sources of power have always been the aspiration of numerous commercial and military applications. One commercial application that highlights this is the laptop computer. The portability of a laptop is severely hampered by the weight of its battery, which constitutes a significant fraction of its overall weight. Despite the significant advances achieved in reducing the size of electronic components and increasing the clock speeds of microprocessors, the size, weight and battery cycle life of laptop batteries have failed to exhibit simultaneous improvements (not to mention the continuous degradation in cycle life after numerous charging-discharging cycles). Other consumer products that strive for portable and long-life energy sources include (but are not limited to) cellular phones, personal digital assistants, iPods and other mobile entertainment equipment. In the military arena, the modern-day soldier is equipped with amenities like night vision devices, riflescopes, global positioning systems (GPS) and portable radio communications (PRC) devices to enhance his combativeness. All these equipment and other advanced firing systems like missile launchers require some form of portable power. Due to the lack of recharging facilities out in the battlefield, soldiers are compelled to carry heavy batteries and spares to power these equipment. Batteries constitute a huge portion of the load borne by an infantry personnel. Special personnel whose essential responsibility is to carry and transport batteries are occasionally deployed, thus reflecting inefficiencies in terms of human resource management. Significant logistics and supply issues arise as a consequence of portable power with limited life span.

One promising solution to the problems posed above is to use power sources employing hydrocarbon fuels, which have significantly higher energy and power densities than the best primary, non-rechargeable batteries available in today's market. It

is evident from the above discussion that high specific power and high specific energy are two important figures of merit for the next generation of portable power sources. A power source with higher specific power is tantamount to requiring fewer batteries or a reduced battery load for meeting the power specifications of a given device. A portable power source possessing higher levels of specific energy translates directly into longer life cycles and is hence synonymous with requiring fewer batteries to power a given appliance for a specified period of time. Even fuel cells, which are fast emerging as a viable candidate for replacing modern-day batteries, lag behind power sources fueled by hydrocarbons in terms of specific power.

Nearly a decade ago, Epstein et al. made a farsighted proposal to design and build shirt-button sized microengines using semiconductor microfabrication technology [1,2]. A multidisciplinary program was initiated to develop MEMS-based gas-turbine engines, turbogenerators and rocket engines. This opened a whole new chapter in the field of MEMS, and the term "Power-MEMS" was coined to describe microsystems that generated power or pumped heat. A microengine operating based on a Brayton cycle would potentially have power densities approaching those of their macro-scale counterparts. In addition to the business of power generation, power-MEMS devices could also be configured to serve the functions and satisfy the requirements of airbreathing propulsion (especially for the powerplants of micro-unmanned-aerial-vehicles (MUAV's)), space propulsion incorporating micro rockets, fluidic pumping and pressurization utilizing motor compressors and turbopumps, cooling and heat pumping employing micro-coolers. These power-MEMS devices on a chip ride on the greatest marvel of semiconductor manufacturing technology – the ability to fabricate a large number of similar devices in parallel. Figure 1-1 shows dozens of radial turbine devices fabricated on a single Silicon wafer. Batched processed miniature MEMS-based gas turbine engines and generators endowed with the desirable attributes of high specific power and energy would thus pave the road leading towards tomorrow's portable sources of power.

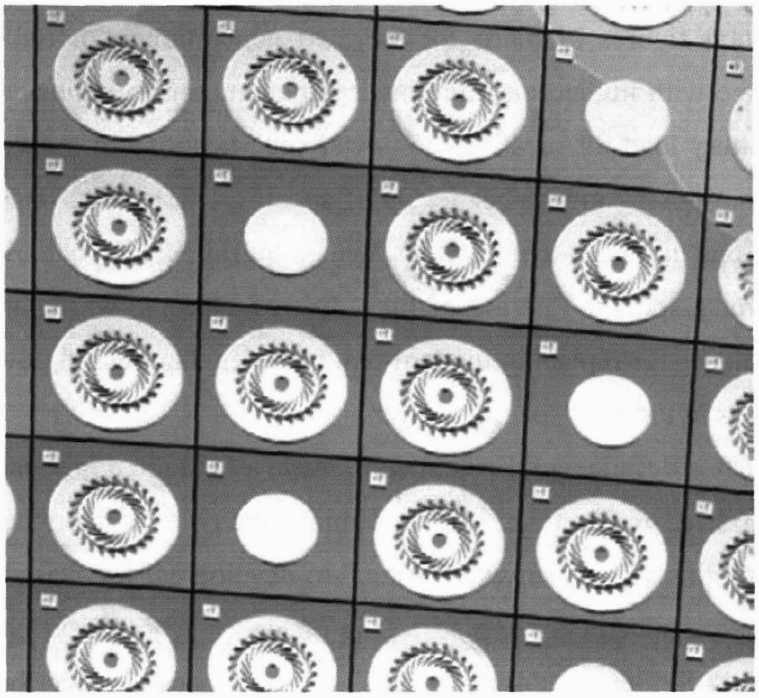

Figure 1-1: Silicon wafer with dozens of radial inflow turbine devices [2].

Similar to (and perhaps even more so than) their full-size brethrens, micro gas turbine engines are complicated devices whose technology spans across several diverse and distinct disciplines. An operational prototype hinges upon the successful and simultaneous implementation of high speed, high performance turbomachinery, high speed bearings, reliable and innovative microfabrication and wafer-bonding techniques, advanced MEMS materials capable of withstanding high stresses and temperatures, compact combustors utilizing practical, non-toxic fuels and compatible catalysts, efficient electrostatic and magnetic generators, low-loss power electronics, sound thermal management and device packaging capable of withstanding high temperatures. The following list, although not meant to be complete, provides some flavor of the formidable technological challenges facing the development of microengines:

- Thermal isolation between the compressor and turbine. In view of the high temperature difference between the turbine and compressor, the small length scales and the high thermal conductivity of Silicon, substantial heat transfer occurs between the turbine and the compressor. The non-adiabatic conditions under which the turbomachinery operates causes an efficiency penalty to be

incurred on the engine, since more power is required to compress a hotter gas.

- Pure Silicon exhibits thermal softening above 900 K. The creep rate of pure Silicon increases monotonically with temperature. In order to extend the range of achievable turbine operating temperatures to boost efficiency, hybrid structures of Silicon and Silicon Carbide have been considered a viable candidate. The bonding of Silicon Carbide to Silicon and the associated technologies which are consistent with current microfabrication process flows for the microengine pose numerous challenges which are non-trivial.
- Since the components in the microengine are almost entirely microfabricated using Deep Reactive Ion Etching (DRIE) via Surface Technology Systems (STS) plasma etching machines, only planar features with almost constant heights can be created. This severely restricts the geometry of the blade passages that can possibly be etched and leads to adverse effects in turbomachinery performance arising from flow blockage and separation. An even greater challenge pertains to the inability to control the repeatability of the microfabrication processes, the DRIE etch uniformities, the profiles of high aspect ratio (HAR) features and the bonding misalignment between wafers.
- Stable high speed micro-gas bearing operation. DRIE severely restricts the geometrical configuration of the micro-hydrostatic gas journal bearings that can be feasibly microfabricated. Analytical models and design charts that hold for conventional, macro-scale gas journal bearings do not apply to micro-scale gas journal bearings microfabricated using DRIE. New analytical models have to be developed to account for the underlying flow mechanisms characterizing these micro-scale gas bearings to accurately predict bearing performance and stability. Stable, high speed bearing operation is further inhibited by the lack of repeatability of microfabrication processes and the absence of reliable experimental techniques for elucidating and understanding rotordynamic behavior.

This dissertation addresses the final formidable challenge in the above non-exhaustive list. The following section provides further elaboration regarding the challenges facing the design, analysis, microfabrication and operation of high speed micro-hydrostatic gas bearings for microturbomachinery in power-MEMS applications.

1.2 Challenges and Nature of the Issues

Numerous daunting challenges are encountered in the analysis, design, microfabrication and operation of micro-hydrostatic gas bearings for application to power-MEMS systems. The salient challenges and issues are related to the following.

Analytical Modeling and Design

The low Reynolds numbers (Re = O(100)), high pressure ratios (PR = O(4)) and high Mach numbers (Ma = O(1)) encountered in micro-hydrostatic gas thrust bearings and annular seals give rise to increased interactions between viscous and compressible flow effects, thus necessitating new flow models to be developed to accurately predict their performance and rotordynamic stability.

Due to microfabrication and Deep Reactive Ion Etching (DRIE) limitations, the micro-gas journal bearings are situated along the outer periphery of the turbomachinery rotor disk, and are further constrained to plain, fixed cylindrical geometries. Current DRIE technology imposes an upper limit of approximately 300 to 400 μm on the length (L) of the journal bearing. Since the diameter (D) of the rotor disk is typically several millimeters, the L/D ratio of the micro-gas journal bearings is typically 0.1, which is one order of magnitude lower than that encountered in conventional gas journal bearings. This inherently modifies the flow mechanisms in the journal bearing and the rotordynamic stability of the rotor-bearing system. The low L/D ratios of the micro-hydrostatic journal bearing imply a very short flow-through time for the hydrostatic fluid through the bearing. The flow in the circumferential direction fails to become fully-developed, in view of the fact that the vorticity due to the spinning rotor has insufficient time to diffuse outwards away from the moving wall across the bearing clearance. Such non fully-developed flow effects have to be accounted for in order to accurately evaluate the rotordynamic forces and stiffness coefficients, so that journal bearing rotordynamic stability can be predicted with accuracy. Furthermore, according to [5], large L/D ratios are required for achieving high damping ratios to facilitate transcritical operation, whereas a high whirl ratio for stable bearing operation requires an L/D ratio of order $\sqrt{C/R}$, where C and R are the journal bearing clearance and rotor radius, respectively.

Hence, the very high whirl ratios required in ultra-high speed power-MEMS devices demand ultra-short (low L/D) bearings, which in turn give rise to reduced damping ratios.

Microfabrication constraints further render drastically different engine architecture for MEMS turbomachines and conventional axial-flow turbomachines, which is evident from Figure 1-2(b). It is important to note that engine architecture and rotordynamics are closely intertwined. Unlike conventional axial-flow turbomachines, such as shown in Figure 1-2(a), where engine architecture is based on long slender shafts supporting the rotating structure, the rotors of the MIT micro-devices consist of thin disks with very low L/D ratios and thrust bearings located near the center of the disk. The rotors are thus more susceptible to unwanted pitch and yaw tilting and the journal bearing system is unable to exert an appreciable torque to counteract the tilting. The responsibility for providing a tilting stiffness thus lies in the thrust bearings, and it is therefore crucial to its design to quantify its magnitude.

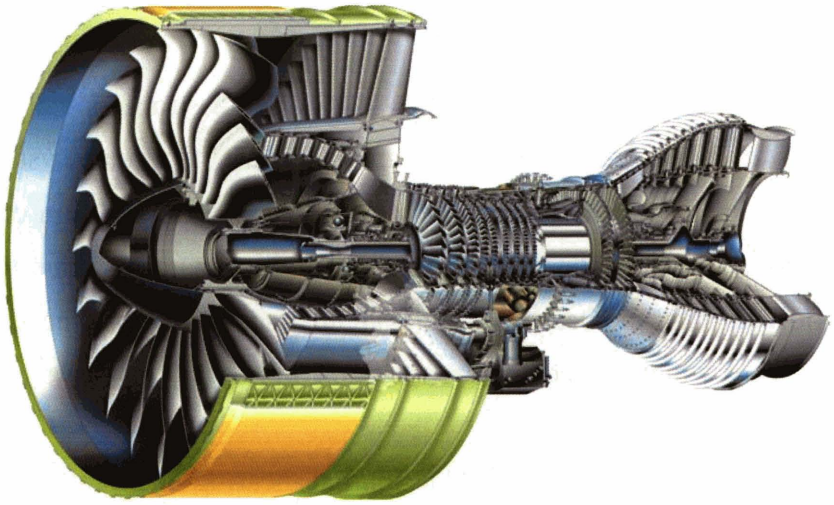

(a)

Figure 1-2: (a) An example of a macro-scale axial-flow turbomachine is the GP7200 turbofan engine, which will power Airbus' A380.

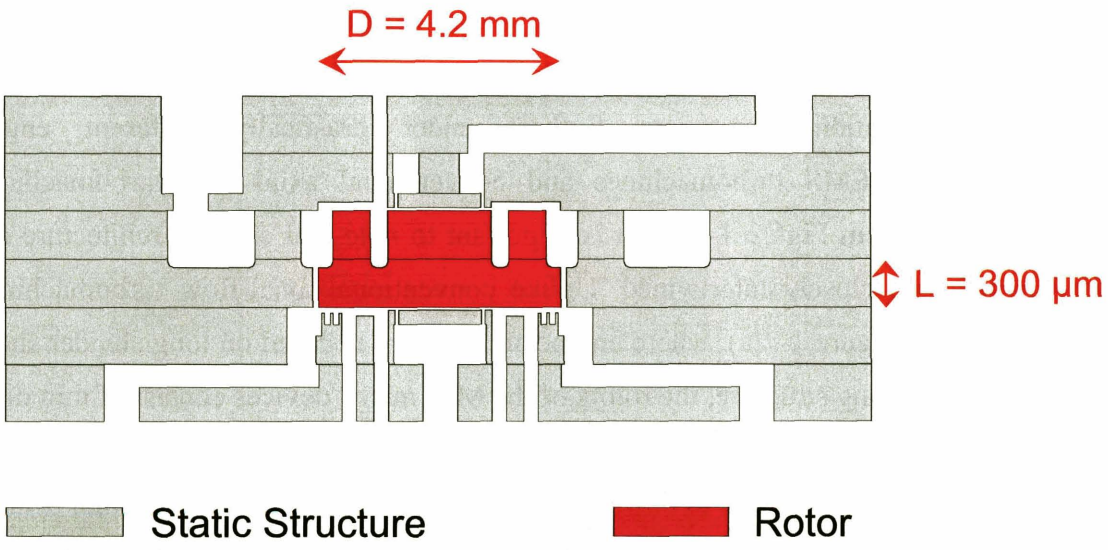

(b)

Figure 1-2: (b) An example of a micro-scale turbomachine is the redesigned microbearing test device. The engine architecture and bearings layout are drastically different for MEMS turbomachines and their conventional axial-flow counterparts.

Operation and Experimental Testing

In many of the MIT micro-devices, there exists a strong coupling between the thrust bearings and the other integral components of the microsystem. Operating protocols have to be established in order to ensure the stable operation of the bearings. Furthermore, adverse effects on journal bearing stability may arise due to the pressure drop of the flow through the bearing and the annular seals affecting the pressures acting on the disc surfaces which affects the disc position and hence the clearance and pressure drop in the seals.

In terms of operation, since the journal bearing damping ratio is directly proportional to the square of L/D [3,4,5], micro journal bearings have significantly lower levels of damping ratios, and transcritical operation may be impeded due to the large radial imbalance of the rotor occasionally encountered in the "as-fabricated" rotors.

The whirl-ratio is defined as the ratio of the maximum stable operating speed to the natural frequency of the journal bearing. In order to achieve the high operating speed requirements of the MIT micro-devices, a whirl-ratio in excess of 20 is required. This is one order of magnitude higher than that encountered in most macro-scale journal bearing systems. Two critical rotordynamic issues in terms of journal bearing operation have to be addressed. First, while many conventional journal bearing systems operate

subcritically, the MIT micro-devices have to operate supercritically in order to achieve the design speeds. This necessitates transcritical operation with rotors that are not readily balanced, where large whirling amplitudes are experienced, and physical contact between the rotor and the static structure is liable to occur. Furthermore, supercritical journal bearing operation may be challenging due to non-linear effects manifested as supercritical subharmonic pseudo critical peaks which potentially involve reduced distance-to-contact of the rotor from the journal bearing sidewalls.

In experimental test of macro-scale devices, the radial and axial location of the spinning rotor can be ascertained by means of strategically located displacement or proximity sensors. These sensors can further provide a wealth of information pertaining to the whirling orbits of the rotor for the purpose of rotordynamic investigations and imbalance measurements. Unfortunately, such a luxury does not exist for micro-devices, which offer limited access to displacement sensors. As a consequence, it is very challenging to deduce whirling orbits and perform detailed rotordynamic measurements. Novel techniques have to be developed for the measurement of critical frequencies and imbalance. The radial and axial location of the rotor has to be inferred via indirect means. Moreover, one is not at liberty to "drill" holes into the micro-device for tapping off and measuring the local static pressure. At times, there is substantial ambiguity in analyzing the reasons which have culminated in a rotor crash.

Microfabrication

In terms of microfabrication, the main snag that has to be surmounted arises from the lack of repeatability and limitations of the microfabrication processes. Numerous crucial physical dimensions of the bearings, such as seal, journal and thrust bearing clearances and thrust bearing orifice lengths and diameters, are limited by fabrication uncertainties. Deep Reactive Ion Etching (DRIE) imposes an upper limit on the maximum aspect ratio of the etched features. Controlling and predicting the journal bearing profile is by no means a straightforward task, due to the lack of repeatability of the DRIE process. In addition, the journal bearing sidewall roughness is on the order of 1 to 2 μm, and may not be negligible compared to the bearing clearance. Rotor imbalance levels are significantly affected by DRIE etch rate variations across the wafer, due to the non-uniform plasma flow distribution across the wafer and the existence of hot-spots

within the plasma-etcher. Limitations in photolithographic processes preclude the creation of perfectly aligned features, and limitations associated with wafer bonding technology culminate in inter-wafer bonding misalignments. Lengthy and complex process flows give rise to increased fabrication variability, increased time and resources required for troubleshooting, increased wafer through-put time and a potential reduction in overall yield due to an escalation in accidental damage arising from increased wafer handling.

Microfabrication uncertainties have a snowballing effect which presents many challenges on the operation of the bearings. For example, variability and non-uniformities in fabrication may result in excessively large magnitudes of rotor imbalance and may render transcritical operation impossible. Unlike macro-scale rotors, large mass imbalances on micro-rotors cannot be easily rectified by simply adding or removing masses. Journal bearings with negatively tapered profiles may yield negative radial stiffness due to diffusion of the hydrostatic axial flow [3], with concomitant difficulties in traversing the natural frequency. On the other hand, journal bearings with positively tapered profiles may be more susceptible to nonlinear effects manifesting themselves as subharmonic pseudo critical peaks which decrease the distance-to-contact of the rotor with the journal bearing sidewalls. Narrow features which fail to etch through completely, such as thrust bearing orifices and journal bearing trenches might adversely affect the performance and rotordynamics of the bearings.

1.3 Review of Previous Work

Since bearings and rotordynamics constitute such an important facet of the MIT microengine project, substantial research efforts have been devoted to this area ever since the inception of the project. It is thus timely to provide a brief review of the previous work which has been performed.

Ehrich performed the original conceptual and detailed design of the micro-bearing test device layout including the location of the journal bearing on the outer diameter of the turbine disc, the pressurization of the journal bearing and hydrostatic thrust bearings [6]. Lin built and tested a microfabricated turbine-driven air bearing test device [7]. The 4 mm diameter and 300 μm thick rotor was supported by a nominally 10 μm wide journal

bearing, and a maximum operating speed on the order of 100,000 rpm was demonstrated. Piekos performed numerical simulations of hydrodynamic journal bearings and concluded that large bearing eccentricities are required for stable operation, particularly at low operating speeds [8]. Such large eccentricities translate to a physical separation on the order of 1 μm between the rotor and the static structure. This in turn places extremely stringent microfabrication tolerances on the journal bearing profile, surface roughness and roundness. Ehrich designed a 26X scaled-up macro bearing test device to accommodate detailed instrumentation and to acquire experience in its operation [6]. Experimental investigations on the 26X scaled-up macro-bearing test device were performed by Orr, who identified and discovered an inherent hydrostatic stiffness of the journal bearing associated with the axial flow through the bearing clearance [9]. This hydrostatic stiffness was subsequently identified to be due to the "Lomakin effect" [10]. Orr operated the macro test device using two distinct modes: pure hydrodynamic and hybrid, and the highest speeds were attained when the test device was operated in the pure hydrodynamic mode. Savoulides performed low-order models for hybrid gas journal bearings and concluded that the best operating protocol should rely on hydrostatics at low speeds and hydrodynamics at high speeds [11]. However, bearing instability is liable to occur during the transition from hydrostatic to hydrodynamic operation. Jacobson, Frechette and Wong achieved a maximum rotational speed of 1.4 million rpm on a 4.2 mm diameter turbine-driven microrotor [12,13]. This corresponds to a periphery speed of 300 m/s. Wong designed, fabricated and tested micro-hydrodynamic thrust bearings [14]. Only limited high speed operation up to 450,000 rpm was demonstrated. Liu performed extensive and comprehensive analytical and modeling work on hydrostatic gas journal bearings [3]. Fluid dynamic models were developed for the hydrostatic, hydrodynamic and damping forces and the criterion for singular whirl instability was established for isotropic journal bearings. Anisotropic journal bearing operation was also investigated and found to significantly improve the whirl stability boundary and substantially relieve the previously stringent microfabrication tolerance requirements [15].

Although many achievements and new insights resulted from previous extensive research efforts, many challenges persist and numerous questions remain yet to be addressed nor answered. For example, there is a dearth of experimental techniques for quantifying the rotordynamics of the rotor-bearing system. Vital rotordynamic

information such as the amplitude of the rotor whirling motion, the bearing stiffness, natural frequency and rotor imbalance could not be experimentally determined. There is also a lack of generic hydrostatic thrust bearing models which are capable of assessing their performance and stability, and for developing operating protocols for the stable high speed operation of the MIT micro-devices. Although a maximum periphery speed of 300 m/s has previously been demonstrated, this record speed has only been successfully demonstrated on one single occasion and many devices fail to show similar levels of performance. Each previous build of microbearing test devices resulted in low yields, with many devices suffering from large radial imbalances, failing to spin or undergo transcritical operation. The reliability of the fabrication processes and the repeatability of the testing procedures and operating protocols await improvements. Although extensive analytical models have been established for hydrostatic gas journal bearings, the circumferential flow has always been assumed to be fully-developed. The non-fully-developed nature of the circumferential flow, and its effect on the rotordynamic forces and stiffness which directly impact journal bearing rotordynamic stability have hitherto been unaccounted for.

This dissertation endeavors to address the above issues and to overcome the shortcomings of the previous work as highlighted above.

1.4 Thesis Goals and Objectives

This thesis focuses on the analysis, design, microfabrication and operation of bearings for supporting low L/D ratio turbomachinery disks for power-MEMS applications. The main objectives of this research are listed as follows.

1. To develop an analytical model for predicting the steady-state characteristics, static and dynamic stability of micro-hydrostatic gas thrust bearings, and to develop operating protocols for the individual MIT micro-devices.
2. To generalize and extend the capabilities of the original analytical hydrostatic thrust bearing model to analyze non-axisymmetric thrust bearing configurations, for the purpose of quantifying thrust bearing tilting stiffness, to assess the performance of novel thrust bearing configurations and to analyze the effects of geometric non-uniformities arising from microfabrication imperfections.

3. To analyze and quantify the effects of a non-fully developed circumferential flow on the power requirements and rotordynamic or whirl instability of hydrostatic gas journal bearings with low L/D ratios.
4. To develop experimental methodologies for quantifying the rotordynamic behavior of ultra-short hydrostatic journal bearings, to experimentally determine journal bearing natural frequencies, whirl amplitudes and rotor imbalance.
5. To redesign and fabricate a new microbearing test device that improves the performance and stability of the original design based on lessons previously learnt and new insights developed. To incorporate features and salient geometric variations for the purpose of performing systematic parametric investigations on bearing operation and stability.
6. To demonstrate repeatable high speed and high whirl-ratio bearing operation.

1.5 Bearing System Requirements

One pivotal issue that has to be contended with prior to the design of the bearing system for supporting the high-speed rotors of the MIT power-MEMS devices is the choice of the type of bearing system. Before such a choice can be made, it is first useful to list down and examine the desirable attributes of a bearing system suitable for the application at hand.

1. High DN number requirements.

   A fundamental requirement that leads to the need for high DN numbers is the need for 400-500 m/s tip speed to achieve high power density in the turbomachinery. This translates to a rotational speed of 1.2 million rpm for a 6 mm diameter rotor, and a DN number (the product of the rotor diameter and the rotational speed) of approximately 10 million mm-rpm. This is one order of magnitude higher than the DN numbers typically encountered in conventional bearing systems, and is indeed one of the most daunting challenges hampering the progress of the MIT microengine project.
2. Low power consumption.

   Since one of the primary objectives of the MIT microengine project is to produce power, the power consumption due to the bearings should ideally be minimized.

The Brayton cycle adopted by the engine might fail to produce a net positive output power due to excessive power dissipated in the bearings. Stated equivalently, the overall efficiency of the engine increases if bearings consuming less power are employed.

3. High temperature compatibility.

   Since the typical turbine inter-blade row temperatures are on the order of 1000 K, the journal bearing system deployed for supporting the high-speed spinning rotor should be capable of withstanding such harsh conditions of temperature.

4. Engine system compatibility.

   The performance of the selected bearing system should not be severely impaired by other components of the microengine system over the entire range of operating conditions. Coupling effects culminating in bearing system instability or performance deterioration should be stamped out. Conversely, bearing operating requirements should not handicap the overall performance of the engine system. For instance, the mass flow rates and pressure requirements of gas bearings should be kept within practical limits which are consistent with the operating requirements of the engine. The bearing system of choice should bear the capability of being easily integrable into the rest of the microsystem.

5. Ease of fabrication and compatibility with microfabrication processes.

   This criterion is special and unique to bearing systems for power-MEMS applications. Conventional bearings can be manufactured using a whole spectrum of machining tools and novel manufacturing techniques, and bearings of all sorts of shapes and geometric dimensions for diverse applications are readily available off the shelf. However, microfabrication technology imposes narrow and rather pessimistic restrictions on the shapes, geometric dimensions and configurations of bearings that can possibly be microfabricated. Intricated three dimensional features and geometries like ball bearings, tilted pad thrust bearings and Herringbone spiral grooves on the journal bearing walls are not amenable to microfabrication using DRIE technology. The prospective bearing configuration should also be compatible with the high aspect-ratio (HAR) limitations imposed by DRIE.

6. Shock resistance, Robustness and Lifespan.

The bearing system should have sufficiently large stiffness and damping to contend with shocks and undue environmental perturbations. An ideal bearing system should have an infinitely long lifespan. It should also be reasonably robust to avoid any severe dimensional changes arising from accidental shocks or impacts.

7. Transcritical considerations.

Many macro-scale bearing systems operate subcritically. The main advantage accruing from this is that the rotor-bearing system would be spared the challenge of having to operate transcritically, during which the whirl or vibration amplitudes might attain unacceptably large values. A purely subcritical journal and thrust bearing operation would also be beneficial for the microengine. However, in view of the very high rotational speeds on the order of a million rpm, this would also require the bearings to have a natural frequency greater than the maximum operating speed which is unattainable with a gas bearing. If the bearing system selected requires mandatory transcritical operation, it should have a sufficiently high damping ratio to keep the resonant whirl amplitudes as low as possible. This is of importance for rotors having large radial imbalances resulting from DRIE etch non-uniformities and photolithographic and bonding misalignments, since large dynamic deflections preclude transcritical operation.

8. Ease of operation and controllability.

The most ideal bearing system would be one that is "hands-off" and does not require any form of control, whether manual or automatic using sophisticated feedback control systems. However, for bearing systems that are required to operate transcritically, some form of control should be included for physically navigating the domain of bearing stiffness, natural frequency and damping to facilitate transcritical operations with minimum resonance amplitudes at a sufficient low operating speed, so as to avoid a rotor crash and subsequent fracturing. However, this control scheme or strategy should be as simple as possible and should not incorporate sophisticated instrumentation and elaborate feedback control systems.

9. Cleanliness, contamination and filtration requirements.

The bearing system chosen should not lead to requirements for cleanliness that are

not reasonably achievable. But the air supply should be free from dust particles, dirt and other forms of residue which would potentially cause obstruction to the blade passages, narrow trenches and clearances with geometric dimensions ranging from tens to hundreds of microns. The air supply should also preclude foreign body contamination which may intrude into the bearing clearance, seize up the bearings and render them non-operational. If the bearings employ a fluid as the working medium, the filtration system employed should be as simple as possible.

1.6 Assessment of Available Bearing Systems Technology

It might be difficult, or perhaps impossible, to find a bearing system technology that will simultaneously satisfy the above lengthy list of requirements. In the following, the available bearing technological options are examined and their relative merits and drawbacks are examined.

Aircraft turbine engines are supported by rolling element bearings, and it is valid to address whether such bearings can be miniaturized to support the high speed rotating disks of the MIT microdevices. One advantage of rolling element bearings is that ball or tapered roller bearings are capable of performing dual duty, in the sense that they are capable of simultaneously providing radial and axial support stiffness. This has the benefit that separate journal and thrust bearing systems need not be developed for supporting the micro-rotors. Moreover, rolling element bearings are capable of supplying orders of magnitude higher stiffness than gas bearings. However, ball bearings are not easily microfabricated using DRIE. In addition, there are no known rolling element bearings available off the market which can satisfy the high DN number requirements of the bearing systems for incorporation into the microengine. The high frictional losses incurred by rolling element bearings impose a severe penalty on the output power and overall efficiency of the microengine. Most of them also have finite life spans, and might not be able to sustain the high rotational speeds for more than a few hours. Furthermore, most rolling element bearings require oil or grease lubrication, which may potentially act as a source of contamination and adversely affect the other integral components of the microsystem.

The next available choice of bearing systems are fluid film bearings, which can be further subdivided into two categories: liquid film bearings using oil, and gas bearings. The main problem with liquid film bearings is the high dynamic viscosities of liquids (which are typically 3 orders of magnitude higher than those of gases) and the associated increase in viscous drag and power dissipation due to the bearings. Moreover, the medium used for the bearings may introduce contamination issues, and elaborate filtration systems might have to be incorporated into the bearing system before the liquid can be fed into the microdevice or recycled for recirculation. Additionally, the temperature of 1000 K is significantly higher than the boiling point of most practical liquids commonly used in liquid film bearings. Granted that most liquid film bearings do operate in the presence of cavitation (thus giving rise to the well known half-Sommerfield solution for infinitely wide hydrodynamic journal bearings), the low boiling point of the liquid lubricant relative to the surrounding environment results in a bearing where massive vaporization has occurred in the bearing clearance. Furthermore additional seals would have to be incorporated to separate the liquid lubricant from the rest of the microsystem which operates in a gaseous medium.

On the other hand, gas bearings are highly compatible with the functional requirements of the microengine. They can be designed to achieve high DN numbers and consume significantly less power than liquid-film bearings. Contamination is not an issue and the bearing gas supply can simply be tapped off from some other part of the engine, thus eliminating the need for additional seals and separate filtration systems. Gas bearings are able to withstand high temperatures, although the viscosity of gases, and hence the power requirements, increase monotonically with increasing temperatures. The drawback associated with gas bearings are the low values of damping and load capacities they can provide as compared to liquid film bearings. The low natural frequencies of micro-gas journal bearings also imply that they have to be run supercritically in order to achieve the stringent high speed requirements. Hence, transcritical operation is mandatory and may be inhibited by the low levels of damping ratio available from micro-gas journal bearings. However, this can be circumvented by regulating the hydrostatic supply pressure to the journal bearing and thus the radial stiffness in order to achieve the desired high levels of damping ratio and a sufficiently low natural frequency (so that the rotor does not fracture in the event of a rotor crash) required for transcritical operation.

Magnetic bearings have two critical limitations. First, many magnetic materials have Curie temperatures significantly lower than the temperatures required for some critical microfabrication processes. Next, magnetic bearings, being inherently unstable, require sophisticated position measuring instrumentation and feedback control systems. The successful miniaturization and integration of the feedback control systems can be challenging.

Recently, compliant foil bearings (CFB) have been demonstrated to be capable of achieving DN numbers on the order of 5 million mm-rpm. However, this is still lower than the bearing requirements for the MIT microdevices. The CFB uses a combination of a gas lubricated hydrodynamic film with a foil spring flexibly supported bearing surface. The properties of the foil springs can be optimized so that the combination of air and foil supports yields an overall bearing with the desired stiffness, damping and stability requirements. CFB's are oil free and so have no lubricant contamination issues. However, the compliant foil journal bearings developed thus far have aspect ratios close to unity and it is uncertain whether the technology can be extrapolated to aspect ratios deviating significantly from one. The microfabrication of CFB's with aspect ratios close to unity has yet to be demonstrated. A CFB for radial support placed at the periphery of a high-speed spinning microrotor as shown in Figure 1-2(b) would require a very low L/D ratio to be consistent with current DRIE technology, and the CFB technology previously developed may not be directly transferable. Additionally, the fabrication and assembly of the foils is not compatible with MEMS technology.

Based on the above discussion, it is evident that as compared to the other available technological options, gas bearings satisfy most of the requirements previously stated and are hence the most suitable choice of bearing systems for the MIT power-MEMS devices.

1.7 Organization of Thesis

This dissertation documents the research efforts comprising an amalgam of analytical modeling, design, microfabrication, experimental testing and operation of micro-gas bearings for application to microturbomachinery and power-MEMS devices. The structure of the thesis is outlined as follows.

Chapter 2 focuses on the modeling and experimental investigation of micro-hydrostatic gas thrust bearings for application to micro-turbomachines. Analytical models are developed to predict the steady state performance indicators of micro-hydrostatic thrust bearings and to analyze their static and dynamic stability. Operating protocols are developed for several MIT micro-devices where significant coupling effects exist between the thrust bearings and the other integral components of the microsystem. The analytical model predictions are subsequently compared to experimental results, and the validity of the operating protocols are proven by applying them to the actual operation of several micro-devices. A simple dynamic stability criterion is also established and verified experimentally.

Chapter 3 presents a generalized micro-hydrostatic thrust bearing model based on a Green's function approach. The generalized model is subsequently applied to a wide range of applications, such as evaluating the hydrostatic direct-coupled tilting stiffness, analyzing novel thrust bearing configurations, quantifying the effects of geometric non-uniformities arising from microfabrication on thrust bearing performance and assessing coupling effects between annular thrust bearings and the turbomachinery. The roll and pitch dynamics of a rotor-thrust bearing system are also analyzed using a two degree-of-freedom rotordynamic model, where the rotordynamic coefficients are obtained using fluid dynamic models employing the generalized Green's function approach and Reynolds equation.

As mentioned previously, the MIT microdevices employ hydrostatic gas journal bearings with ultra low L/D ratios. In particular, the flow in the circumferential direction fails to become fully-developed. The effects of a non-fully-developed circumferential flow on journal bearing power dissipation and dynamic whirl stability are addressed in Chapter 4. Hydrodynamic stiffness coefficients for different journal bearing geometries and operating conditions are evaluated using Computational Fluid Dynamics (CFD). In order to rescale and potentially collapse the CFD data, an analogous problem with a known analytical solution involving the impulsive starting of a Couette flow is considered. The relevant dimensionless parameter governing the flow field is extracted and applied to rescale and successfully collapse all the available CFD data. Analytical models using an influence coefficient approach for viscous, compressible flows are developed to predict the performance of annular seals. The use of these seal models for

accurately ascertaining the rotor axial position of a micro-turbopump is demonstrated.

Chapter 5 focuses on the analysis and redesign of a microbearing test device for demonstrating repeatable high speed and high whirl-ratio microbearing operation. First, major lessons acquired from the microfabrication and testing of previous microbearing test device builds are discussed. Examples of these lessons which may potentially preclude high speed bearing operation include sources of negative radial and tilting stiffness due to coupling effects, the formation of a "fence" at the exit of the journal bearing, the existence of spikes in the journal bearing and structural integrity issues. Building upon the foundation of these major lessons learnt, the analysis and design of a new microbearing test device which aims to rectify the known design flaws of the original design are performed. The key elements and components addressed in the redesign include annular seals, multiple journal bearing plena, turbomachinery, thrust bearings, structural integrity considerations and enhancement, thrust balance considerations and device variations.

Details pertaining to the microfabrication of the redesigned bearing test device are described in Chapter 6. First, the key microfabrication process flows for the constituent wafers or layers which comprise the final six-wafer stack microbearing test device are presented. The key microfabrication challenges and strategies to overcome them are subsequently outlined. Particular attention is given to the fabrication techniques and procedures for "D^3" rotors (*d*ouble layer, *d*onor-receiver and *d*rop-in rotors).

In Chapter 7, measurement and analytical techniques for statically quantifying the radial imbalance of rotors arising from DRIE non-uniformities are presented. Experimental techniques using a high-resolution fiber optic sensor and data reduction schemes developed for determining imbalance-driven whirl amplitudes and response curves are described in detail. Salient rotordynamic quantities of micro-hydrostatic journal bearings, such as stiffness, natural frequency, damping ratio and rotor imbalance are quantified experimentally, and compared to analytical model predictions, showing favorable agreement. Alternative and simplified experimental procedures for quantifying journal bearing natural frequencies are presented. The chapter closes with experimental strategies for crossing journal bearing natural frequencies and procedures for accelerating to high speeds.

Chapter 8 presents the experimental testing results of the redesigned microbearing

rig. Static flow tests are first performed to assess whether the critical geometric dimensions and clearances have been fabricated to meet design specifications. Experiments are subsequently performed at low journal bearing hydrostatic differential pressures employing both isotropic and anisotropic journal bearing operation. Ultra high whirl-ratios in excess of 20 (even up to 43) are demonstrated repeatably for many of the tested devices. Journal bearing operation at high journal bearing hydrostatic differential pressures is subsequently explored. Appropriate operating protocols for achieving repeatable high speed operation in excess of 1.2 million rpm are mapped out. The effects of using different gases are investigated. Troubleshooting efforts for eliminating low-frequency unstable oscillations arising from flow-controllers are expounded. Controlled high-speed operation has been demonstrated up to 70% of design speed. This corresponds to a rotor rotation rate of 1.7 million rpm and a rotor tip speed of 370 m/s (equivalent to a DN number of about 7 million mm-rpm). Plausible reasons limiting even higher operating speeds from being achieved are finally suggested.

Chapter 9 provides an overall summary of the work presented in this dissertation and the contributions arising from this research. Recommendations for future research and development are also discussed.

CHAPTER 2

Modeling and Experimental Investigation of Micro-Hydrostatic Gas Thrust Bearings for Micro-turbomachines

2.1 Background and Motivation

All high speed rotating devices require thrust bearings to provide axial support and stiffness. Examples of such devices for power-MEMS applications in the MIT Microengine project are shown in Figure 2-1 and include micro-turbochargers (Savoulides [16]), micro-turbopumps (Diez [17]), and micro-turbine-generators (Steyn [18]). The thrust bearings of these micro-devices are hydrostatic, as they possess several significant advantages over their hydrodynamic counterparts. For example, hydrodynamic thrust bearings are incapable of developing a sufficiently high stiffness at low rotational speeds, since the magnitude of the stiffness arises from the relative motion between the stationary and rotating bearing surfaces. In contrast, hydrostatic thrust bearings depend on a controllable external pressure supply to generate stiffness, which depends only weakly on the rotational speed of the rotor. Furthermore, hydrodynamic thrust bearings in general require smaller clearances than their hydrostatic counterparts. This poses two major challenges in power-MEMS applications: (1) the drag penalty associated with hydrodynamic thrust bearings outweighs the penalty of pressurized air usage of hydrostatic thrust bearings, and (2) the requirement for smaller running gaps in hydrodynamic thrust bearings renders them more susceptible to failure due to geometric non-uniformities. Hydrodynamic thrust bearings are also known to possess poor stability characteristics at high speeds, as discussed by Constantinescu and Galetuse ([19,20]). In view of the above-mentioned shortcomings of hydrodynamic thrust bearings, inherent restrictor-orifice hydrostatic thrust bearings were selected to provide axial support and stiffness in the MIT MEMS-based micro-devices.

There are a number of key challenges associated with the development of micro-hydrostatic thrust bearings. The geometric dimensions of the micro-hydrostatic thrust bearings employed in the MIT microdevices are typically one to two orders of magnitude smaller than conventional macro-scale hydrostatic thrust bearings (the thrust bearing gap of the MIT microdevices is of order 3 μm). The critical dimensions of micro-thrust bearings have to be controlled to higher levels of precision to ensure an equivalent level of reliability in operation as compared to their macro-scale counterparts. The low Reynolds numbers and high pressure ratios encountered in the micro-thrust-bearings give rise to increased interactions between viscous and compressible flow effects, necessitating the development of new models to accurately predict the bearing performance and stability. In many of the micro-devices there exists a strong coupling between the thrust bearings and the other integral components of the microsystem which poses a major challenge to the stable operation of the bearings.

2.1.1 Nature of the Issues

Figure 2-1 shows three MIT micro-devices supported axially by means of hydrostatic forward and aft thrust bearings. Figure 2-1(a) depicts a micro-electrostatic turbine-generator, which is fabricated on the aft side of a 4.2 mm-diameter silicon rotor, and driven by a radial-inflow turbine etched on the forward side. In this device, the electrostatic attraction between the rotor and stator can result in a negative (destabilizing) axial stiffness[1] experienced by the spinning rotor. Operating protocols are thus necessary to ensure stable operation of the thrust bearings in the presence of electrostatic pull-in forces.

The cross-sectional view of a micro-turbopump is displayed in Figure 2-1(b). The 6 mm-diameter turbopump rotor consists of a radial-outflow centrifugal pump driven by a radial-inflow turbine, both of which are situated on the forward side of the rotor. The pump, with primary function to discharge fuel to the combustion chamber of a micro-rocket, is separated from the turbine by the forward annular hydrostatic thrust bearing. Both the turbine and thrust bearings are operated using an inert gas to reduce the viscous drag which can impose a large penalty on the overall performance of the turbomachinery.

[1] A decreasing axial gap increases the electrostatic attraction force such that the stiffness is negative.

This implies that the forward thrust bearing serves the dual role of a bearing providing axial support and stiffness and a seal to prevent the leakage of the liquid from the pump into the gas turbine. Such a configuration poses rotordynamic challenges which are manifested by the design requirements of a rotor speed of 750,000 rpm yielding pressures of 32 atm at pump outlet and 9 atm at turbine exit. It is thus important to assess the performance and dynamic behavior of the annular thrust bearing system. Furthermore, operating protocols are required to ascertain the appropriate thrust bearing supply pressure and to control the rotor axial position depending on pump outlet pressure.

Figure 2-1(c) illustrates the cross-sectional view of a micro-turbocharger. Experiments on the micro-turbochargers were initially performed with low thrust bearing supply pressures, to keep the flow through both forward and aft thrust bearings unchoked. In an attempt to increase the axial stiffness of the thrust bearings to avoid resonance issues near the natural frequency, the supply pressure to both thrust bearings was increased, operating with choked flow through the orifices of both thrust bearings. This had a detrimental effect on thrust bearing dynamic behavior and stability, which will be discussed in detail in this chapter.

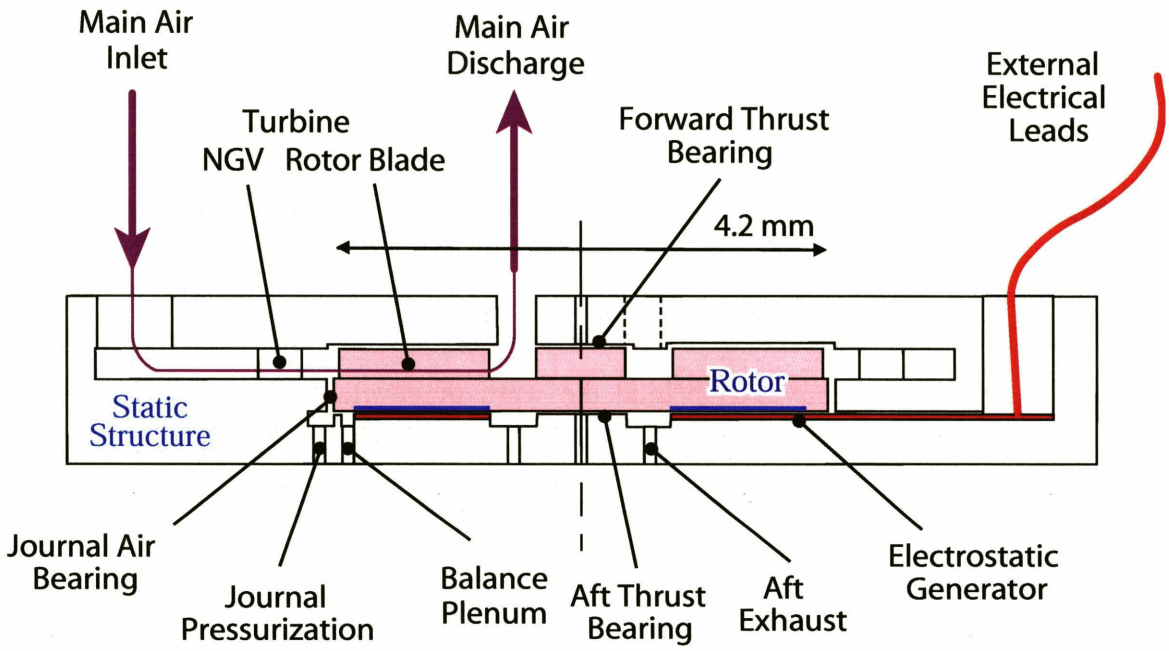

(a)

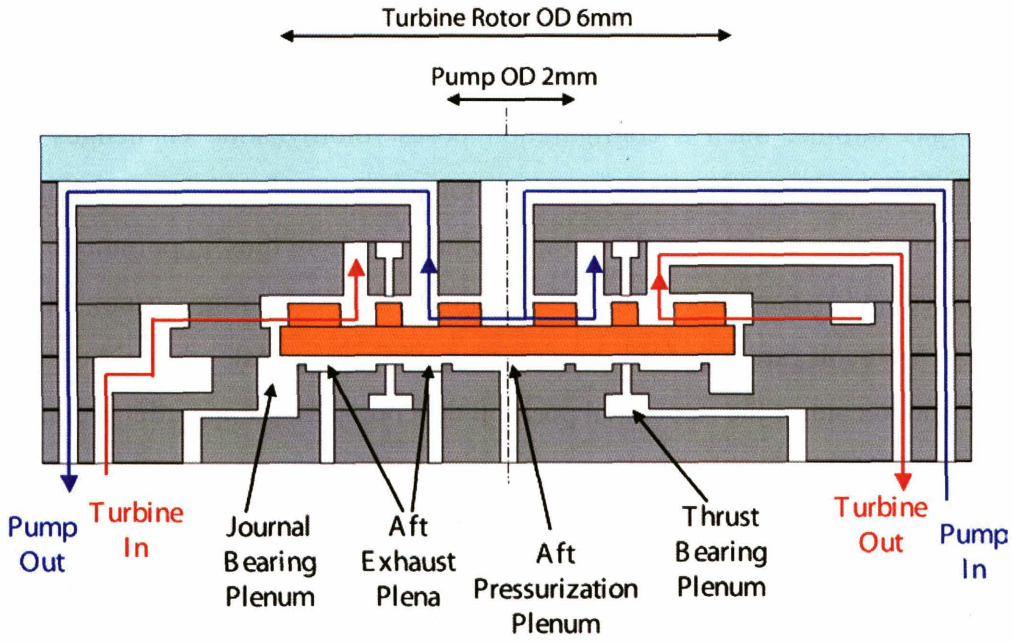

(b)

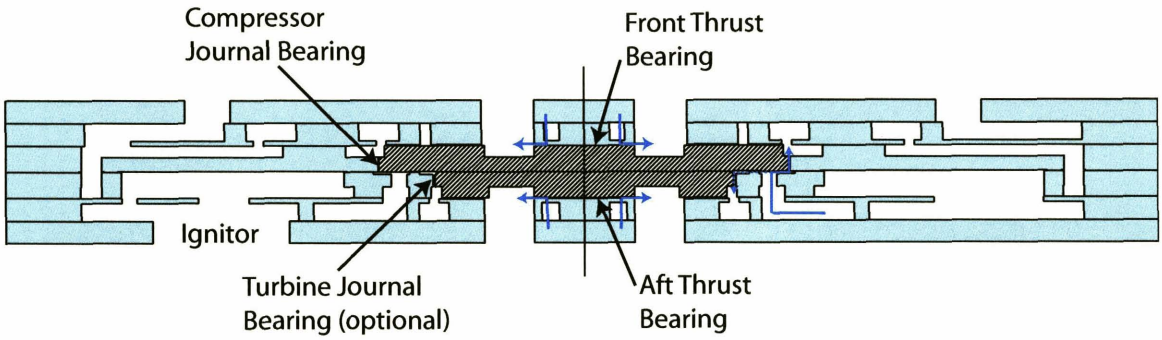

(c)

Figure 2-1: Cross Sectional View of three MIT micro-devices. (a) Micro-turbine-generator, (b) Micro-turbopump, (c) Micro-turbocharger.

The close coupling between the thrust bearings and the rest of the micro-device system is the major motivation behind the work of developing accurate and reliable analytical models. These models establish operating protocols to ensure the stable operation of the bearings under a variety of operating conditions. The developed analytical model is also capable of estimating the steady-state performance characteristics of micro-hydrostatic thrust bearings. The quantities of interest are axial stiffness, natural frequency and mass flow rates for different thrust bearing hydrostatic supply pressures. In addition, the analytical model can be used to analyze the static and dynamic stability of

these micro-thrust-bearings. For static stability considerations, it is necessary to ensure that coupling effects due to interference from other micro-device components do not introduce negative stiffness which exceed the thrust bearing stiffness. In terms of dynamic stability, the developed models capture the essential mechanisms underlying the dynamic instability phenomena and help establish design guidelines and criteria to avoid their occurrence.

2.1.2 Objectives and Scope of this Chapter

The objectives and goals of this chapter are to: (1) develop an analytical model with the above mentioned capabilities, (2) assess the accuracy of the model by comparing steady-state experimental data to analytical predictions, (3) illustrate the applicability of the model based operating protocols to the experimental testing of several of the micro-devices, (4) experimentally investigate the thrust-bearing operating conditions under which dynamic instability occurs, and (5) compare experimental results to a-priori analytical predictions to evaluate their validity and usefulness.

The chapter is organized as follows. The essential components of the newly-developed analytical hydrostatic thrust bearing model are first described in detail. The model is subsequently used to predict the steady-state performance characteristics of the MIT micro-devices and to establish operating protocols. The importance of static stability considerations is demonstrated in two micro-devices, the micro-electrostatic turbine-generator and the micro-turbopump next. Experimental results obtained from these two devices are presented to demonstrate the feasibility of the operating protocols. The models are then utilized to investigate the dynamic stability of the thrust bearings, and operating conditions under which axial oscillations occur are predicted. Finally, experiments are carried out in a micro-turbocharger to investigate dynamic stability. The experimental results are compared to a-priori model predictions and the ability to capture the underlying mechanisms is assessed. Finally, the results and conclusions of this chapter are summarized.

2.2 Analytical Model for Hydrostatic Thrust Bearings

The newly developed hydrostatic gas-thrust bearing model consists of two parts, a steady-state fluid dynamic model to predict hydrostatic thrust bearing performance and an unsteady flow model to capture the dynamic behavior and stability of the thrust-bearing-rotor system.

2.2.1 Steady-State Thrust Bearing Performance Model

Figure 2-2 shows the configuration and dimensional variables of the inherently-compensated-orifice hydrostatic thrust bearings. The bearings rely on an external source of pressurized gas supplied through a series of orifice restrictors (typically of 10 μm diameter and 100 μm length), which together with the thrust bearing gap (nominally 2 to 3 μm deep), generate the axial stiffness. The key advantage of hydrostatic thrust bearings is their ability to provide an almost constant stiffness independent of the rotational speed of the rotor. The steady state operating characteristics of the thrust bearings are modeled using a fluid resistance model, whose key components are outlined in Figure 2-2. The station numbers are also labeled in the figure and the mechanism for the generation of axial stiffness is illustrated schematically. The rotor is supported axially by means of a forward and an aft thrust bearing. When the rotor is given a slight perturbation in the axial direction and comes into closer proximity with the aft thrust bearing pad, the hydraulic resistance in the outflow region of the aft thrust bearing pad increases, thus necessitating a larger pressure difference between the outlet of the orifices and the thrust bearing exhaust (vented to atmosphere). The increase in static pressure over the aft thrust bearing pad culminates in a larger restoring axial force acting on the rotor. The opposite occurs on the forward thrust bearing, and the consequence is a net upward axial force acting on the rotor disk to restore the equilibrium axial position of the rotor.

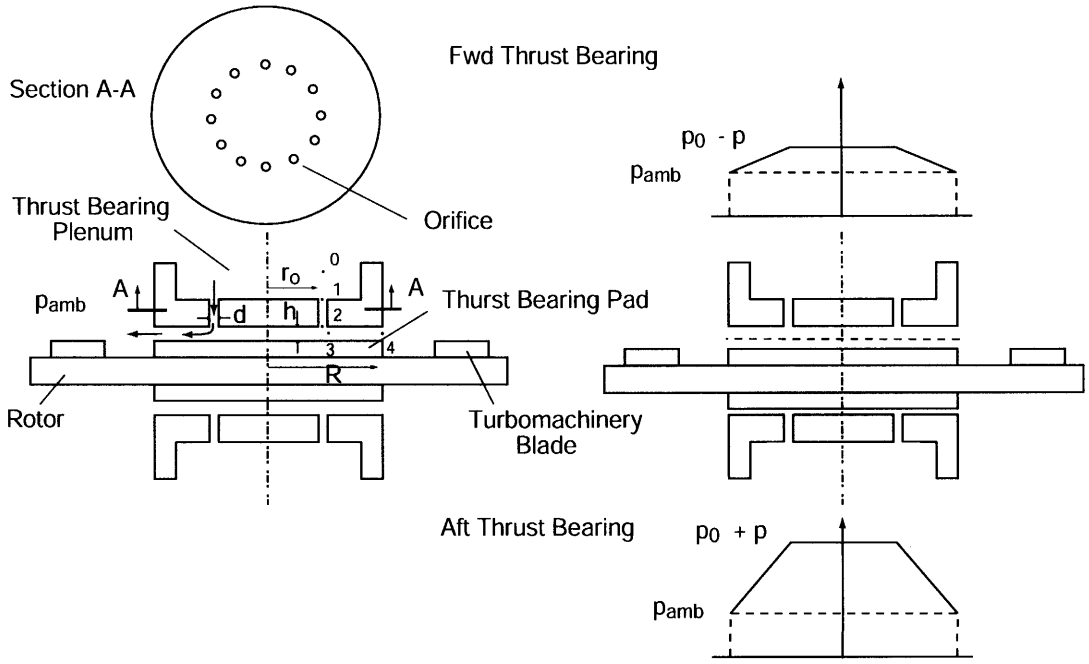

Figure 2-2: Geometric configuration of inherent-restrictor orifice hydrostatic thrust bearings. (Not to scale)

The inlet loss from station 0 to station 1 is manifested as a drop in stagnation pressure of the fluid at the entrance of each orifice. This loss can be described as

$$\frac{\Delta P_t}{P_t - P} = 0.5, \tag{2.1}$$

where the loss coefficient of 0.5 was obtained from handbooks of hydraulic resistance (Idelchik [21]), and has been verified by CFD calculations performed by Gong [22].

The flow through each of the circular orifices (from station 1 to station 2) is modeled as a compressible, isothermal, fully-developed viscous flow. In view of the high thermal conductivity of Silicon, the isothermal assumption is reasonable. The relevant equations governing such a flow are given in Shapiro [23] and can be summarized by the following expression for the corrected mass flow

$$\frac{\dot{m}\sqrt{\Re T_{t2}}}{A P_{t2}\sqrt{\gamma}} = \Phi\left(Re_d, \frac{P_{s2}}{P_{t1}}, \frac{L}{d}\right) = \Psi(M_2). \tag{2.2}$$

The corrected mass flow at the exit of each orifice depends on the Reynolds number $Re_d \equiv \frac{\rho V d}{\mu} = \frac{\dot{m} d}{A\mu} = \frac{4\dot{m}}{\pi d \mu}$, the ratio of the static pressure at the exit of the orifice P_{s2} to the

total pressure at the inlet P_{t1}, and the aspect ratio of the orifice L/d, where L and d are the length and diameter of the orifice, respectively. It should be noted that although the Reynolds number of the flow is sufficiently low so as to render the flow laminar, the effects of friction and the associated decrease in stagnation pressure tends to increase the Mach number of the flow to appreciable values, thus necessitating the effects of compressibility to be taken into account. However, in contrast to the familiar Fanno flow involving adiabatic flow through ducts, where choking occurs at a local Mach number of unity, the isothermal flow through ducts chokes at a local Mach number of $1/\sqrt{\gamma}$ (Shapiro, [23]). Furthermore, since the flow is laminar ($Re_d = O(10^2)$), viscous effects which are quantified by the friction coefficient C_f, can be related analytically to the Reynolds number Re_d via $C_f = 16/Re_d$. Also, since $C_f M^2(L/d)$ is of order one, compressibility effects have to be taken into account even though the flow is dominated by viscous effects. The viscous losses through the orifices are normally neglected in the modeling of macro scale hydrostatic thrust bearings employing orifice restrictors, as exemplified by the work of Eshghy [24]. However, since the Reynolds numbers of the flows through the orifices of hydrostatic micro-gas-thrust-bearings considered in this work are typically one order of magnitude smaller, the viscous losses are not negligible and have to be correctly accounted for.

The turning losses at the exit of the orifices (from stations 2 to 3) are modeled using the following empirical correlation by Vohr [25]

$$\frac{\Delta P_t}{P_t - P} = 0.31\left(\frac{Re_h}{2000}\right) - 0.122\left(\frac{Re_h}{2000}\right)^2 + 0.282\left(\frac{Re_h}{2000}\right)^3, \qquad (2.3)$$

where $Re_h = \dfrac{2\dot{m}}{\pi d\mu}$.

After leaving the orifices, the fluid flows outwards through the radial region between the stator and rotor, before finally being discharged into the surrounding atmosphere. This occurs from stations 3 to 4. In the radial outflow region, the static pressure distribution, which varies both radially and circumferentially, is computed numerically using a finite element method. The flow in this region is assumed to be isothermal and the mass flow $\dot{m}$ is driven by the difference in the squares of the static pressure

ΔP^2 between the exit of the orifices and the thrust bearing exhaust. This can be expressed non-dimensionally as

$$\frac{\Delta P^2}{\left(\frac{\mu \Re T \dot{m}}{h^3}\right)} = \phi\left(N, \frac{r}{R}\right), \tag{2.4}$$

where h is the thrust bearing clearance. The ratio $\Delta P^2 / \left(\mu \Re T \dot{m} / h^3\right)$ can be interpreted as a dimensionless hydraulic resistance between the exit of the orifices and the thrust bearing exhaust, and the magnitude of this resistance depends on the layout and geometrical configuration of the orifices, which in turn depend on the number of orifices, N, and the normalized radial location of the orifices, r/R. Assuming the value of h to be constant, the static pressure P in the outflow region can be obtained by solving the Laplace equation for P^2

$$\nabla^2 P^2 = 0. \tag{2.5}$$

Having identified and modeled the individual resistances leading from the thrust bearing supply plenum[2] to the thrust bearing exhaust, the objective is to iteratively solve for the mass flow rate $\dot{m}$ given a thrust bearing supply pressure and a fixed thrust bearing geometrical configuration. The static pressure distribution in the outflow region between the stator and rotor can then be integrated to yield the axial force acting on the rotor. Figure 2-3 shows the finite-element solution of the static pressure distribution on the thrust bearing pad of a micro-turbocharger, previously displayed in Figure 2-1(c). The analytical model is capable of predicting key steady-state performance parameters as a function of the hydrostatic supply pressure and thrust bearing geometry, such as bearing mass flow, axial stiffness and natural frequency. In addition to thrust bearings with circular pads, the model can also be employed to analyze the performance of thrust bearings with annular pads. Both thrust-bearing configurations have found applications in the micro-devices presented in Figure 2-1.

[2] The pressure supply to the thrust bearing supply plenum is held at a constant value, whereas the thrust bearing exhaust is nominally at atmospheric pressure.

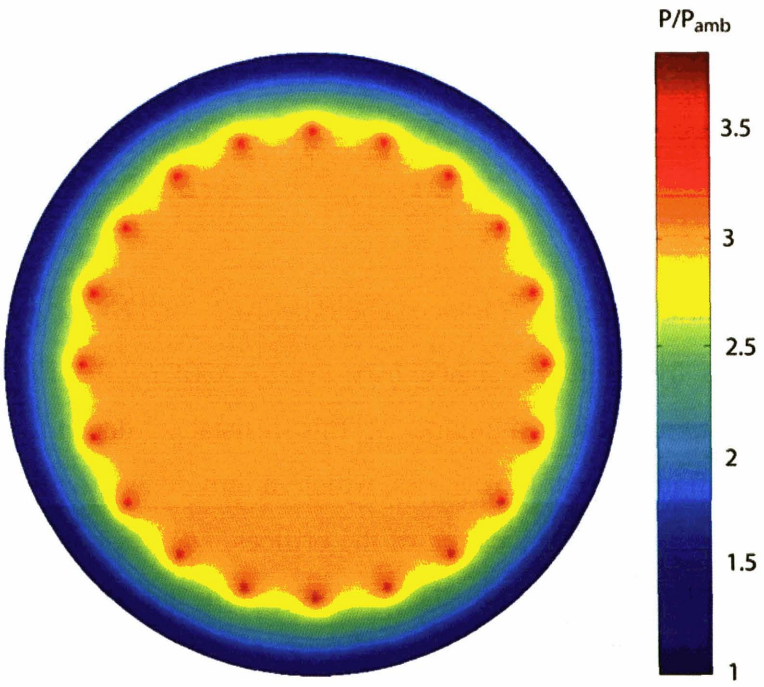

Figure 2-3: Finite element solution of the normalized static pressure distribution on the thrust bearing pad of a micro-turbocharger.

In order to verify the validity of the hydraulic resistance model, experimental results obtained from a micro-turbocharger shown in Figure 2-1(c) were compared to results predicted from the model. Figure 2-4 displays static flow test results obtained experimentally by varying the supply pressure to the aft thrust bearing and monitoring the variations in mass flow through the forward thrust bearing. In the latter the supply pressure is kept constant. The modeling results presented in Figure 2-4 match the experimental data well, both in trend and in magnitude. This indicates that the resistances in the thrust bearing system are well modeled. In view of the observation that the results presented in Figure 2-4 show an inverted S-shape, the results obtained from such a flow test will subsequently be known as "S-curves".

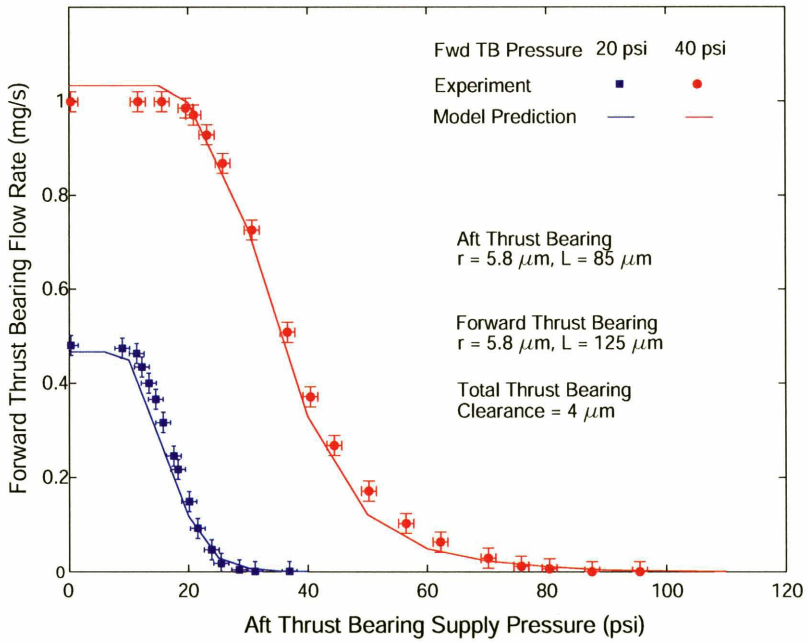

Figure 2-4: Experimental measurement and model predictions of forward thrust bearing mass flow rate as a function of aft thrust bearing pressure setting.

Analytical predictions for axial natural frequency of the micro-turbocharger thrust bearings are plotted against thrust bearing supply pressure in Figure 2-5. The results show a monotonic increase in axial stiffness and thus natural frequency with supply pressure. The figure also indicates that a supply pressure in both forward and aft bearings of at least 95 psi is required to ensure that the bearings operate subcritically up to the rotor design speed of 1.2 million rpm. This is an important consideration and avoids potential resonance effects arising from transcritical operation. The required thrust bearing mass flow rates for various thrust bearing supply pressures are also shown on Figure 2-5. The thrust bearing mass flow rates are typically 2% of the turbomachinery mass flow at design speed.

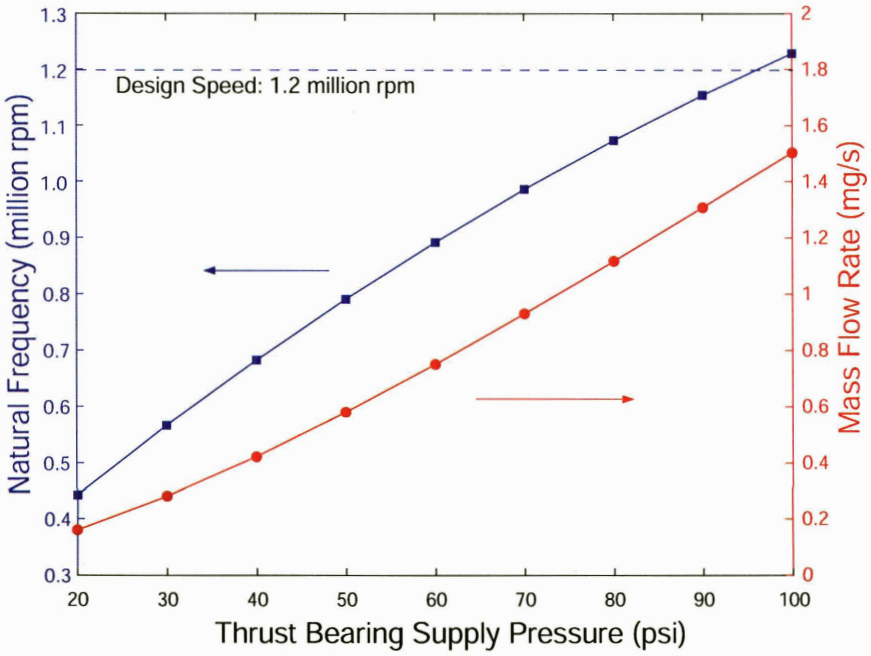

Figure 2-5: Variations of thrust bearing natural frequency and mass flow rate with supply pressure for a micro-turbocharger.

2.2.2 Dynamic Thrust Bearing System Model

Although steady-state operating characteristics are important, one issue in the design of fluid film bearings is stability. Prior to describing the details of the dynamic stability model, it is useful to highlight the essential difference between static and dynamic stability. Static instability refers to a pure divergence from the system's initial equilibrium state, and can be analyzed solely from the static or steady-state characteristics of the system at the perturbed state. On the other hand, dynamic instability corresponds to oscillations of exponentially growing amplitude, which usually have to be treated using a dynamic analysis that accounts for the temporal evolution of perturbations in the system. As an example, for a classical mass-spring-damper system with mass m, spring constant k and damping coefficient c, static instability occurs for negative values of k, whereas dynamic instability corresponds to negative values of c.

The dynamic stability of hydrostatic thrust bearings has previously been studied by Licht et al. [25] and Roudebush [27] for circular thrust bearings with a circular central recess, by Allen et al. [28] and Stowell [29] for annular thrust bearings, and by Chen and Ho [30] for capillary compensated multi-pocket thrust bearings. All of the work focused

on instabilities arising from undesirable "air-hammering" effects. The dynamic stability of one thrust bearing operating in isolation is first analyzed to elucidate the essential physics, before extending the approach to study the dynamic stability of both the forward and aft thrust bearings operating in tandem, as is the case in the MIT micro-devices. The state variables chosen for this analysis are the static pressure at the exit of the orifices, p, and the thrust bearing gap, h. Referring to Figure 2-6, small perturbations in mass flow into and out of the thrust bearing gap arise due to small perturbations p' and h' about the equilibrium states p_0 and h_0. The time rate of change of fluid mass in the bearing gap is given by the difference in the perturbed mass flow rates into and out of the thrust bearing gap:

$$\frac{dm'}{dt} = \dot{m}_{in}' - \dot{m}_{out}' = -(C_1 + C_2)p' - C_3 h', \tag{2.6}$$

where the coefficients are $C_1 = \left(\frac{d\dot{m}_{in}}{dp}\right)_0$, $C_2 = \left(\frac{\partial \dot{m}_{out}}{\partial p}\right)_0$ and $C_3 = \left(\frac{\partial \dot{m}_{out}}{\partial h}\right)_0$ respectively. It is useful to note that $\dot{m}_{in}'$ only depends on p' and does not depend on h'. This is due to the fact that the mass flow into the thrust bearing gap has to match the mass flow out of the orifices. The perturbed mass flow out of the orifices, given by Equation (2.2), is solely a function of the static pressure perturbations at the exit of the orifices since the thrust bearing supply pressure, P_{supply}, the geometry of the orifices, and the fluid medium are assumed constant.

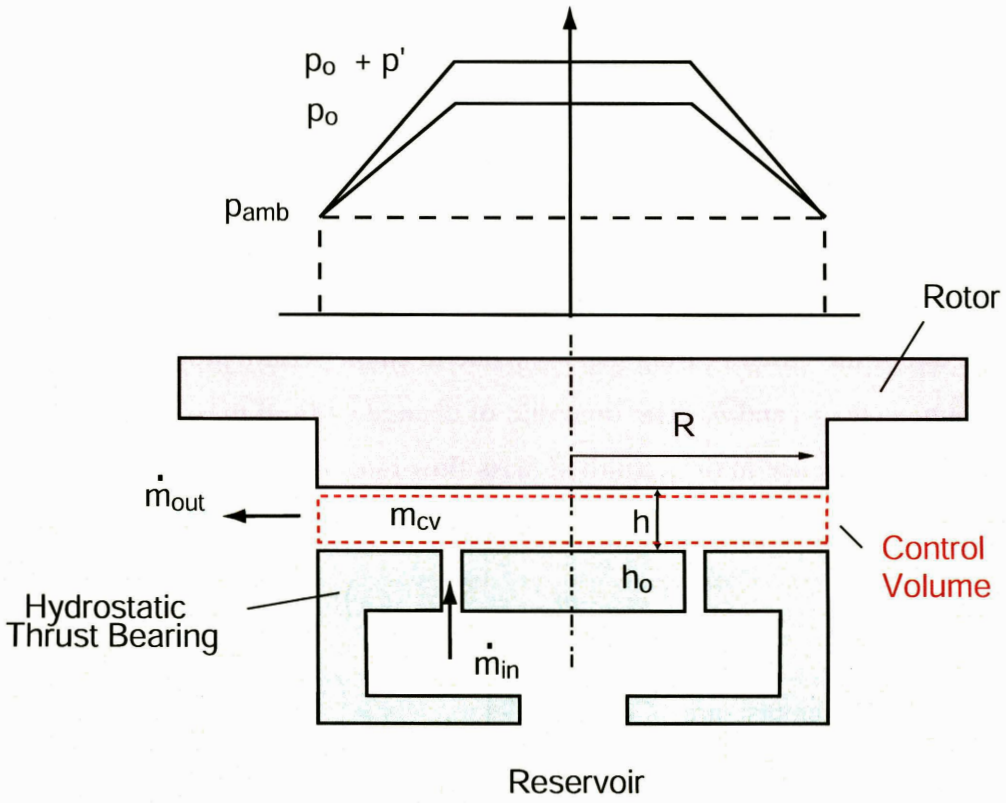

Figure 2-6: Dynamic stability model for hydrostatic thrust bearing.

Under steady-state conditions the mass of gas m_{CV} between the bearing surfaces is

$$m_{CV} = \int_0^{2\pi}\int_0^R \rho h_0 r dr d\theta = \frac{h_0}{\Re T}\int_0^{2\pi}\int_0^R p r dr d\theta, \tag{2.7}$$

which can be evaluated once the pressure at every location along the thrust bearing pad is known. Corresponding to perturbations p' and h', the time rate of change of the perturbed fluid mass between the bearing surfaces becomes

$$\frac{dm_{CV}'}{dt} = \left(\frac{\partial m_{CV}}{\partial p}\right)_0 \dot{p}' + \left(\frac{\partial m_{CV}}{\partial h}\right)_0 \dot{h}' = C_4\dot{p}' + C_5\dot{h}'. \tag{2.8}$$

From conservation of mass considerations, one can write using Equation (2.6)

$$\frac{dm_{CV}'}{dt} = \dot{m}_{in}' - \dot{m}_{out}'. \tag{2.9}$$

Hence, one obtains

$$C_4\dot{p}' + C_5\dot{h}' + (C_1 + C_2)p' + C_3h' = 0. \tag{2.10}$$

The perturbations h' and p' are also coupled by Newton's second law governing the axial motion of the rotor. This yields

$$m_R \ddot{h}' = \left(\frac{\partial F_p}{\partial p}\right)_0 p' = \frac{\Re T}{h_0} C_4 p' = C_6 p', \tag{2.11}$$

where m_R is the mass of the rotor.

Coupling Equations (2.10) and (2.11), the final ODE which governs the perturbed axial motion of the rotor takes the form

$$\dddot{h}' + \left(\frac{C_1 + C_2}{C_4}\right)\ddot{h}' + \frac{C_5 C_6}{M_R C_4}\dot{h}' + \frac{C_3 C_6}{M_R C_4} h' = 0, \tag{2.12}$$

which is a third order differential equation in h'. The stability of the system is described by the above equation and is readily analyzed by applying the Routh-Hurwitz stability criterion. This yields the following criterion for dynamic stability:

$$\frac{C_1 + C_2}{C_3} > \frac{C_4}{C_5}. \tag{2.13}$$

The values of the coefficients C_1, C_2, C_3, C_4 and C_5 can be obtained using the steady state thrust bearing model introduced earlier. Equation (2.13) reveals that one of the main factors which drives the system towards instability is a low value of coefficient C_1, which in fact becomes zero when the flow through the orifices of the thrust bearing chokes. When this occurs, the mass flow out of the orifices becomes independent of the back pressure, thus $C_1 = \left(\frac{d\dot{m}_{in}}{dp}\right)_0 = 0$. It is also of interest to note that for an incompressible fluid with constant density, C_4 becomes zero and Equation (2.12) reduces to a second order ODE in h', which can then be expressed in a more familiar fashion as

$$m_R \ddot{h}' + c\dot{h}' + kh' = 0. \tag{2.14}$$

This is the equation of motion for a linear mass-spring-damper system, with spring constant k given by $C_3 C_6/(C_1 + C_2)$ and damping constant c given by $C_5 C_6/(C_1 + C_2)$. As discussed previously, static instability ensues when k becomes negative. However, static stability is necessary but not sufficient, and in practice dynamic stability is often violated first. In the presence of dynamic effects, the phase difference between the unsteady perturbations in p' and h' may be such that in one cycle or period of the

perturbations, the net disturbance energy input into the system is positive. This causes the amplitude of h' to experience exponential growth and results in dynamic instability.

The above analysis was carried out for a single thrust bearing configuration first.[3] Since the rotors of the MIT micro-devices are axially supported by a forward and an aft thrust bearing, it is necessary to extend the preceding analysis and to couple the disturbance of the rotor axial location to the dynamics of the dual thrust bearing system (see Figure 2-1). This eventually leads to a coupled system of equations:

$$M_R \dddot{h}' + \left(\frac{C_{1a}+C_{2a}}{C_{4a}}\right) M_R \ddot{h}' + \left(\frac{C_{5a}C_{6a}}{C_{4a}} + \frac{C_{5f}C_{6f}}{C_{4f}}\right)\dot{h}' + \left(\frac{C_{2a}C_{6a}}{C_{4a}} + \frac{C_{2f}C_{6f}}{C_{4f}}\right)h' + C_{4f}\left(\frac{C_{1a}+C_{2a}}{C_{4a}} - \frac{C_{1f}+C_{2f}}{C_{4f}}\right)p_f' = 0 \tag{2.15}$$

$$\text{and } C_{5f}\dot{h}' + C_{2f}h' - C_{4f}p_f' - (C_{1f}+C_{2f})p_f' = 0. \tag{2.16}$$

The subscripts 'f' and 'a' in the above equations denote the forward and aft thrust bearings respectively. In contrast to Equation (2.12) the order of the characteristic polynomial or the number of poles for the system is now increased from three to four. The system is dynamically stable if, and only if, all the roots of the characteristic equation have negative real parts, indicating exponential decay of the oscillations.

2.2.3 Limitations of the Analytical Model

Although the analytical model adequately accounts for the effects of compressibility and the radial and circumferential variation of the static pressure in the thrust bearing pad, the model is limited to hydrostatic thrust bearings with orifices located axisymmetrically at the same radial location. The simple restrictor model is not applicable to thrust bearing configurations where several sets of orifices are arranged at different radial locations. Furthermore, the model assumes a constant thrust bearing gap, neglecting any tilting of the rotor. The model also does not address the effects of geometric non-uniformities in

[3] Most of the research reported in the literature focuses on the dynamic stability of a single thrust bearing operating in isolation.

the orifices. These limitations are further addressed and the model is extended to account for the mentioned effects in Chapter 3.

2.3 Model Applications and Experimental Investigation

The complications associated with the operation of the three micro-devices depicted in Figure 2-1 have previously been highlighted. In the following, the models are employed to study the static stability of the thrust-bearing system in these micro-devices and to establish necessary operating protocols guaranteeing stable operation. Using the operating protocols, experiments are subsequently performed to investigate their applicability.

2.3.1. Static Stability and Operating Protocol for a Micro-electrostatic turbine-generator

The issue of thrust bearing static instability arises in the micro-electrostatic turbine-generator depicted in Figure 2-1(a). In this micro-device, the electrostatic attraction between the rotor and stator is captured by the electrostatic force F_p between two parallel plate capacitors (see Figure 2-7):

$$F_P = -\frac{\varepsilon_0 \upsilon^2 A}{4g^2}, \tag{2.17}$$

where ε_0 is the permittivity of free space, υ is the voltage difference between the stator and rotor, A is the effective area of the electrodes on the stator and rotor, and g is the generator running gap. This pull-in force F_p results in a negative (destabilizing) axial stiffness, k_p, experienced by the spinning rotor

$$k_p = -\frac{\partial F_p}{\partial g} = -\frac{\varepsilon_0 \upsilon^2 A}{2g^3}. \tag{2.18}$$

The magnitude of the destabilizing stiffness increases with increasing voltage difference υ and decreasing generator gap g.

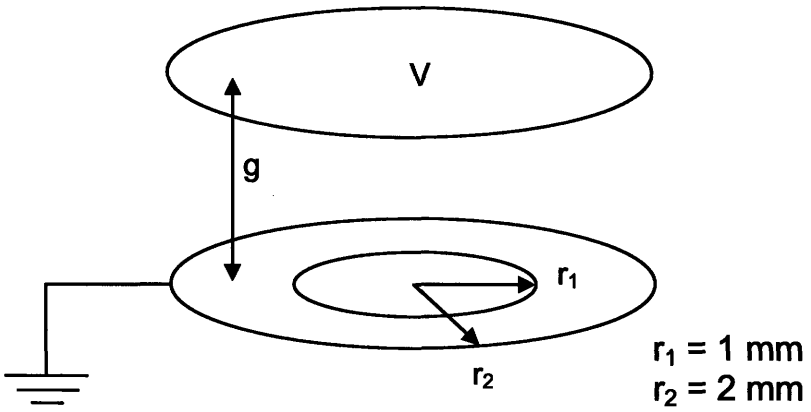

Figure 2-7: Modeling of electrostatic attraction between rotor and stator of micro-electrostatic-turbine-generator.

For static stability, the net axial stiffness must be positive such that

$$|k_B| > |k_P|, \tag{2.19}$$

where k_B is the thrust bearing axial stiffness. Using Equation (2.18), the criterion for the maximum allowable voltage between the stator and rotor becomes

$$\upsilon < \sqrt{\frac{2g^3 k_B}{\varepsilon_0 A}}. \tag{2.20}$$

In Figure 2-8, the natural frequency of the thrust bearings is plotted as a function of rotor axial position with a supply pressure of 70 psi and 50 psi applied to the forward and aft thrust bearings respectively. The total thrust bearing gap is 3 μm and a non-dimensional axial rotor position of zero implies that the rotor is axially centered between the forward and aft static structures. A positive axial rotor position indicates the rotor operating in closer proximity to the static structure on the forward side, with the rotor coming into physical contact with the static structure at a non-dimensional rotor axial position of unity. Knowledge of the axial stiffness for various rotor axial positions allows the maximum allowable voltage between the stator and rotor to be evaluated from Equation (2.20). The results are displayed in Figure 2-8 which shows that the maximum allowable voltage between the stator and rotor decreases drastically for a rotor operating in closer proximity to the static structure on the aft side. This is due to a larger destabilizing stiffness which increases strongly with a decreasing generator gap, in accordance to Equation (2.20). The maximum allowable voltage increases as the rotor

operates in closer proximity to the forward static structure and shows a peak at a rotor axial position of approximately 0.7. This dip in maximum allowable voltage is due to the softening of the thrust bearings for large positive rotor axial positions. The stiffness of each of the thrust bearings is maximum when the flow resistance due to the orifice (from station 1 to station 2 in Figure 2-3) is approximately equal to the resistance due to the radial outflow region from the exit of the orifices to the edge of the thrust bearing pad (from station 3 to station 4 in Figure 2-3). For large positive eccentricities, which correspond to small forward thrust bearing gaps, the flow resistance due to the radial outflow region dominates the resistance due to the orifice. This results in a reduction in stiffness due to the forward thrust bearings and hence a reduction in the overall stiffness of the system. It can be further inferred from Figure 2-8 that the maximum allowable voltage is approximately 350 V, corresponding to a rotor axial position of 0.7. However, it might not be desirable to operate the rotor and bearings at such high rotor axial positions. However, if only a maximum voltage of 300 V is required, it might be feasible to operate the thrust bearings at rotor axial positions close to 0.5.

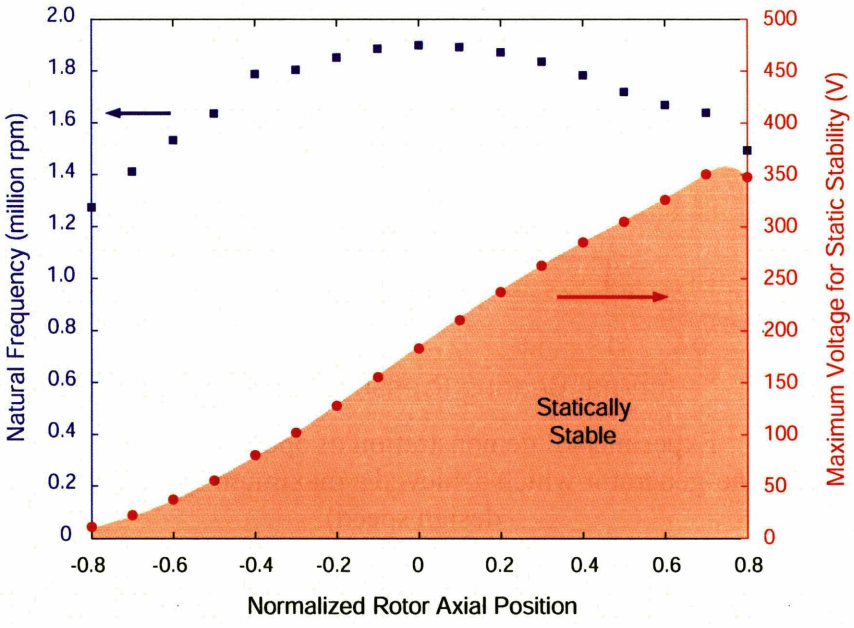

Figure 2-8: Thrust bearing natural frequency versus rotor axial position for micro-electrostatic turbine-generator.

Figure 2-8 serves as an important plot for the successful operation of the micro-electrostatic turbine-generator, as it provides information pertaining to the maximum allowable generator voltage which can be applied between the rotor and stator without resulting in static instability. It also indicates that, based on static stability considerations, the rotor should be operated closer to the forward static structure at rotor axial positions not exceeding 0.7 in order to maximize the allowable voltage between electrodes on the stator and the rotor. By careful implementation of the operating protocols, the rotors of these devices have been experimentally spun up to 850,000 rpm which corresponds to 93% design speed, as shown in Figure 2-9. Voltages of up to 120 V have been applied between the electrodes without any observable electrostatic pull-in effects.

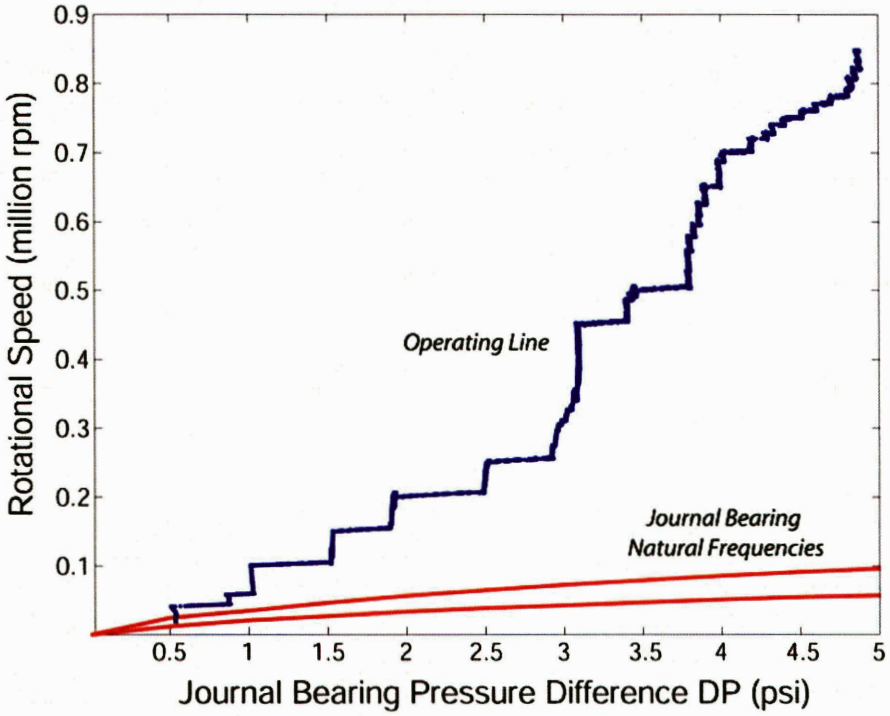

Figure 2-9: Experimental demonstration of operating schedule for a micro-electrostatic turbine-generator which achieved a maximum speed of 850,000 rpm (93% design speed).

2.3.2 Stability of Annular Thrust Bearings with Liquid-Gas Interface in Micro-Turbopumps

The analytical model also serves as a tool for establishing operating protocols in the micro-turbopump, shown in Figure 2-1(b). Referring to Figure 2-14, a simple hydrostatic analysis is performed on the liquid-gas interface at the intersection between the pump

outlet and the forward thrust bearing. The analysis reveals that the static pressure P_1 along the inner rim of the annular forward thrust bearing pad has to exceed the pump outlet pressure P_{pump} in order to support the surface tension forces due to the liquid-gas interface. For such small micron-sized thrust bearing clearances h, the surface tension forces are of great significance. The force balance at the liquid-gas interface yields

$$P_1 = P_{pump} + \frac{2\sigma \cos \alpha}{h}, \tag{2.21}$$

where σ is the surface tension and α is the contact angle of the wetting interface ($\alpha < 90°$). Equation (2.21) imposes a constraint on the allowable combinations of P_1, P_{pump} and h necessary for static equilibrium of the liquid-gas interface. Since the value of P_{pump} increases with the square of the rotational speed the value of P_1 has to increase accordingly for a fixed forward thrust bearing gap h. If P_1 is raised above its allowable value gas bubbles can enter the pump, resulting in a two-phase flow at the pump outlet. The gas bubbles tend to conglomerate into larger slugs of gas pockets which impede the liquid flow and reduce the mass flow through the pump. Conversely, if P_1 is allowed to fall below P_{pump}, liquid leaks into the annular thrust bearing pad and results in a significant increase in viscous drag and destabilizing hydrodynamic torques. However, all this is further complicated by the fact that P_1 and h are not independent, but rather, P_1 depends on both the thrust bearing supply pressure, P_{supply}, and clearance, h. The delicate nature of the equilibrium expressed in Equation (2.21) indicates the necessity for establishing an operating protocol for the appropriate combination of values of P_{supply} and h at different values of P_{pump}. The values of P_1 for given values of P_{supply} and h can be computed numerically by solving Equation (2.5) with imposed Dirichlet type boundary conditions $P = P_{ambient}$ along the outer rim of the forward thrust bearing pad and Neumann type boundary conditions $\partial P/\partial n = 0$ (corresponding to zero normal flow) along the inner rim of the forward thrust bearing pad, as shown on Figure 2-10. Having obtained P_1, P_{pump} can then be solved using Equation (2.21).

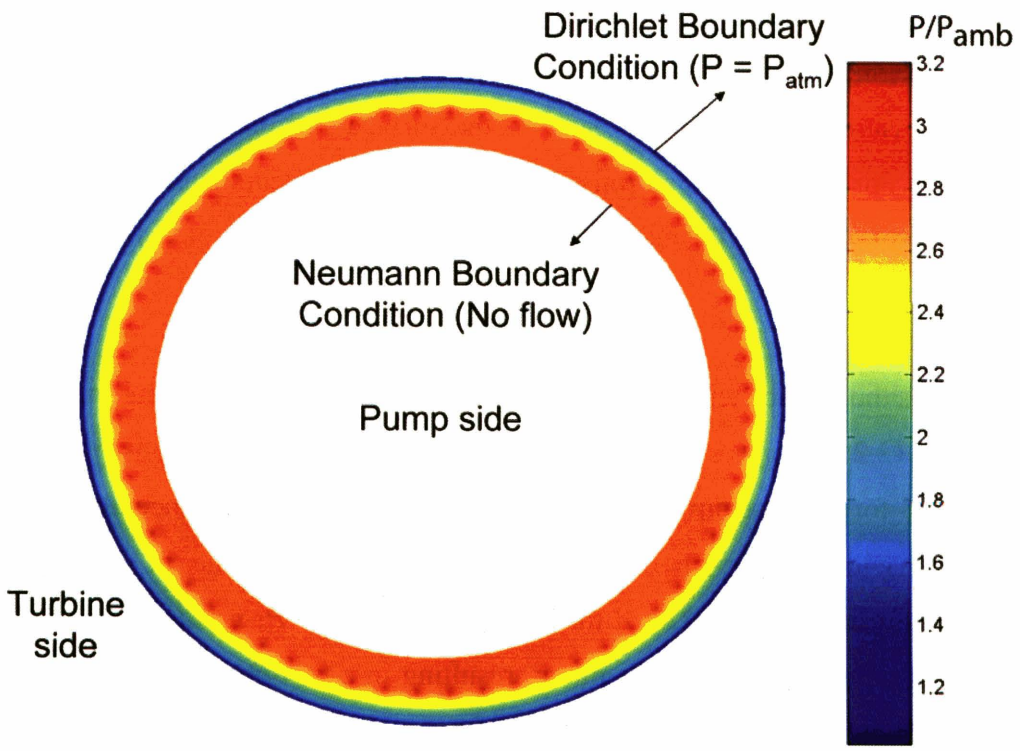

Figure 2-10: Static pressure distribution on thrust bearing pad assuming zero mass flow between pump outlet and thrust bearing.

Figure 2-11 depicts analytical predictions for the possible combinations of P_{supply} and h required for different values of P_{pump}, assuming a contact angle of $\alpha = 50°$. The same set of data has been presented in a more instructive manner on Figure 2-12. For a fixed thrust bearing supply pressure P_{supply} the allowable pump outlet pressure P_{pump} first increases with increasing values of h before reaching a maximum at $h = h_{crit}$ (marked by the dotted line) and subsequently decreases for larger values of h. The occurrence of this maximum is due to the interplay between P_1, which decreases with increasing values of h, and surface tension forces which increase significantly (as $1/h^3$) with decreasing values of h. For small values of h, the surface tension forces increase much more rapidly than P_1 as h is reduced, thus giving rise to a reduction in the allowable value of P_{pump}. Starting with the rotor in an axially centered location and with P_{supply} fixed, P_{pump} increases quadratically with the rotor speed, thus requiring a smaller forward thrust bearing gap h to maintain the static equilibrium of the liquid-gas interface. However, when h is reduced below h_{crit}, the allowable P_{pump} begins to decline. Hence, from an operational perspective, it is necessary to operate the rotor at thrust bearing clearances greater than h_{crit} for a given

value of P_{supply}. The values of h_{crit} are plotted as a function of P_{supply} and contact angle α on Figure 2-13.

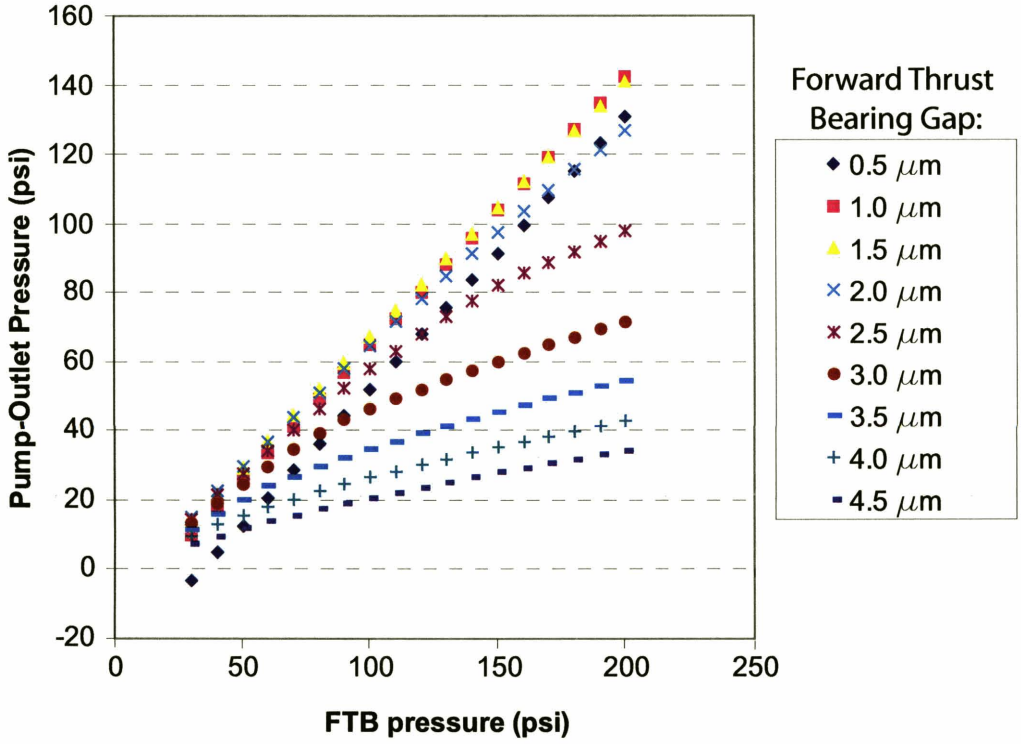

Figure 2-11 Forward thrust bearing pressure required at different pump-outlet pressures and different forward thrust bearing clearances.

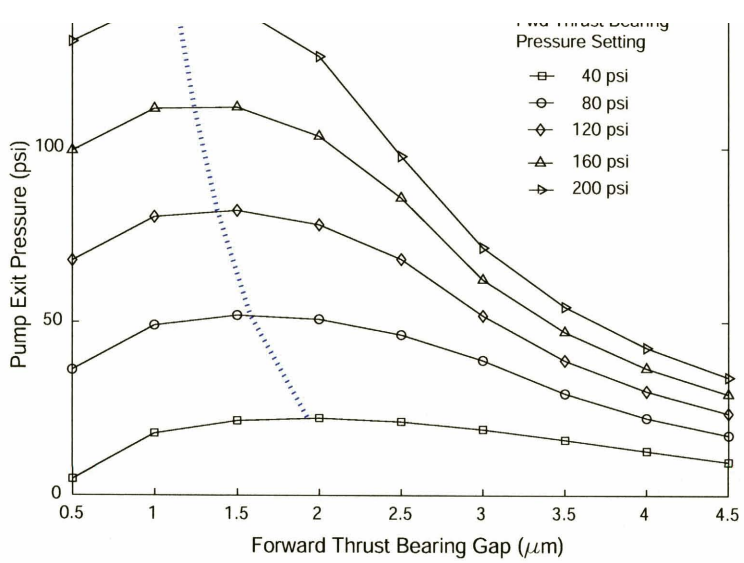

Figure 2-12: Required forward thrust bearing pressure settings for different pump-outlet pressures and different forward thrust bearing clearances.

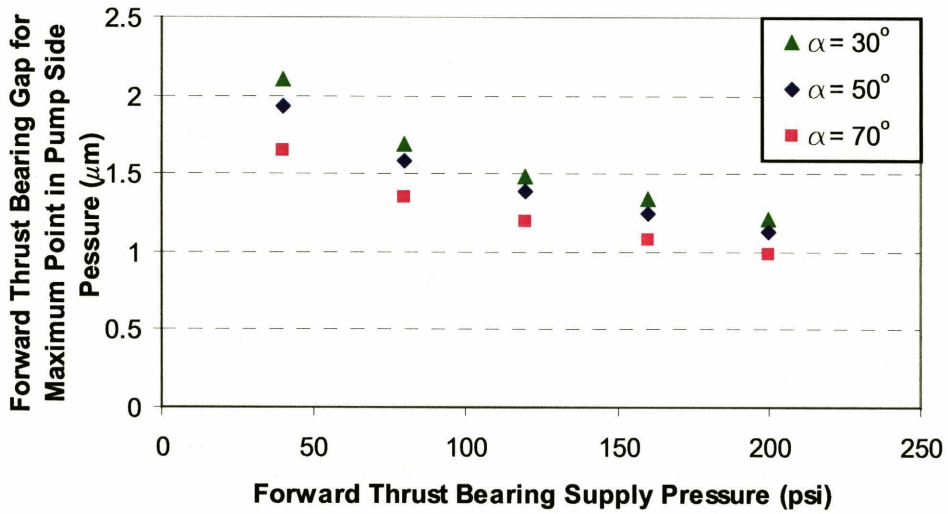

Figure 2-13 Minimum allowable forward thrust bearing gap for stable operation for different thrust bearing supply pressures and contact angles.

During actual experimental runs on the micro-turbopumps, the thrust bearing clearance h can be measured to a high degree of accuracy by monitoring the pressure drops and flow rates across the radial seals on the aft side of the static structure as shown

evaluate the validity of the operating protocols which have been generated using the analytical model. The value of P_{supply} was held constant at 50 psi and the value of h was gradually reduced until bubbles started to form in the turbopump. Values of thrust bearing clearance h which correspond to the onset of appearance of bubbles in the pump are plotted in Figure 2-14 as crosses for various values of P_{pump}. Also shown on the same figure are analytical predictions for different values of contact angle α. The experimental data are seen to fall between the analytical predictions corresponding to contact angles α between 30° and 50°, which compare favorably to values of $\alpha \approx 30°$ cited in the literature for air-water interface on Silicon (see, for example, Senturia [31]). The established operating protocols proved to be a useful guide for when operating the rotor at various speeds.

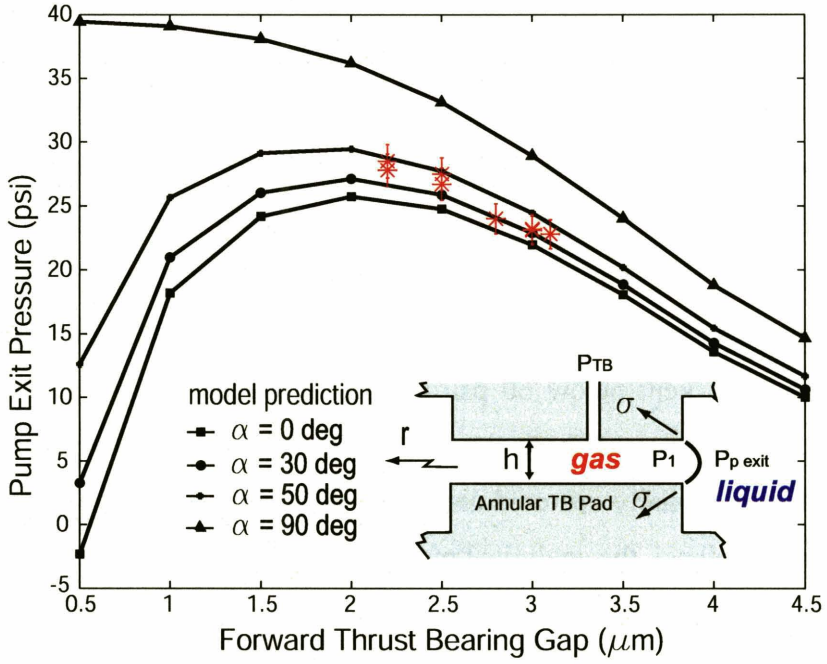

Figure 2-14: Comparison of experimental results and analytical predictions for operating protocol on micro-turbopump. Inset shows hydrostatic analysis performed on liquid-gas interface at the intersection between the turbopump outlet and the forward thrust bearing.

In view of the above complications associated with achieving the correct combination of h, P_{pump} and P_{supply}, one design guideline is to avoid using the thrust bearing for sealing purposes, whose main functional requirement is to provide axial stiffness. Furthermore, Jacobson [32] has shown that the forward thrust bearing may be subjected to Rayleigh-

Taylor instability, which is liable to destabilize high speed operation. Along the liquid-gas interface, the centrifugal force acting on the denser inbound liquid is significantly larger than that acting on the outer gas, resulting in a potentially unstable system. At low rotational speeds, where centrifugal effects are small, Rayleigh-Taylor instability can be suppressed by surface tension. However, at high rotational speeds, Rayliegh-Taylor instability ultimately sets in, causing the liquid and gas on both sides of the interface to swap sides. Therefore, another design guideline is to avoid locating the pump with the denser fluid inbound.

Although static stability is necessary, it is not sufficient for determining the overall stability of a system. To assess the overall stability of a system, dynamic stability considerations have to be made as well. This is discussed next.

2.4 Dynamic Stability of Hydrostatic Thrust Bearings

An a-priori dynamic stability analysis was carried out on the thrust bearing system of a micro-turbocharger using the analytical model described previously. The analysis predicted that the thrust bearings were dynamically stable (the roots of the characteristic equation were either real or had negative real parts) when the supply pressure to both thrust bearings was kept below 60 psi and the rotor was axially centered. Under such circumstances the orifices of both thrust bearings were essentially unchoked. However, when the rotor was axially centered and the supply pressure to both thrust bearings was increased beyond 60 psi, the analytical model predicted the onset of dynamic instability.

To further understand the nature of the dynamic instability, the roots of the characteristic equation were investigated for different rotor axial positions and a thrust bearing supply pressure of 120 psi. Figure 2-15 shows the roots of the characteristic equation for various different rotor axial positions. For every rotor axial position investigated, two of the roots are real and negative, while the remaining two roots are complex. For rotor axial positions between -0.3 and 0.3 (i.e. when the rotor is operated almost axially centered), the two complex roots have positive real parts, indicating that the system is dynamically unstable. For these rotor axial positions, it is observed that the flow through the orifices of *both* thrust bearings is choked. However, for larger positive

and negative rotor axial positions, the two complex roots have negative real parts, thus alluding that the system is dynamically stable. Under such circumstances, although the flow through the orifices of one of the thrust bearings is choked, the flow through the orifices of the other thrust bearing remains unchoked. Even though a thrust bearing operating in isolation might be dynamically unstable due to flow choking, the overall system remains stable. The other unchoked thrust bearing is capable of stabilizing the entire bearing system. This highlights the importance of analyzing the entire dual thrust bearing system as a whole, and it is misleading to draw conclusions based on the dynamic stability of each individual thrust bearing operating in isolation.

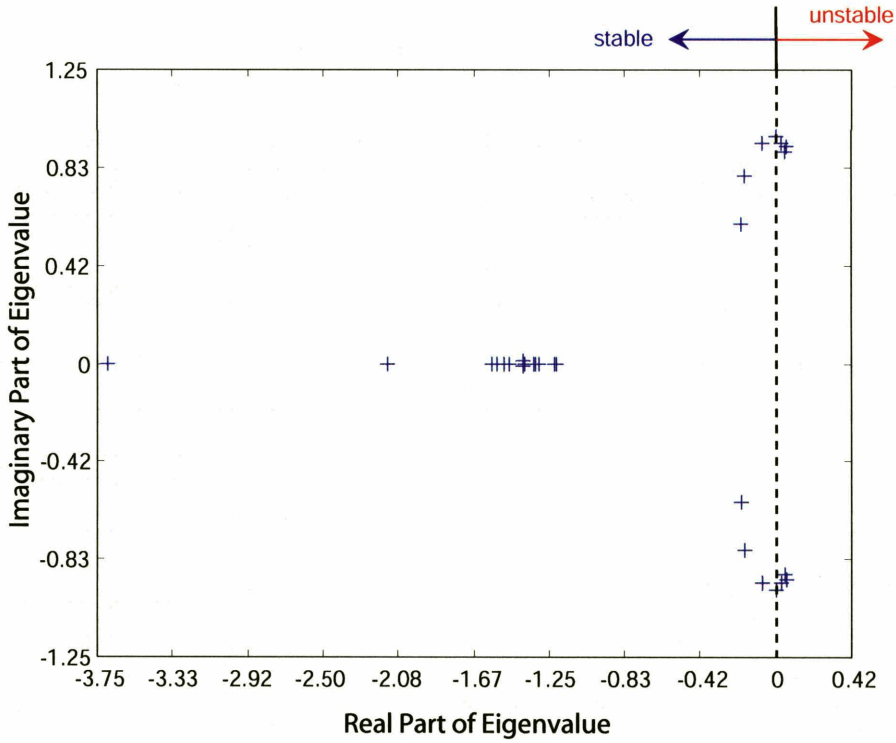

Figure 2-15: Real and complex parts of roots of characteristic equation governing dynamic stability of thrust bearings of a micro-turbocharger with supply pressures of 120 psi. Roots have been normalized using rotor design speed of 1.2 million rpm.

To test the above model prediction, experiments were subsequently performed on the micro-turbocharger. Both the rotational speed and axial position of the rotor can be measured using a Philtec D6 ultra-high frequency response fiber-optic displacement sensor overlooking a series of speed bumps etched on the surface of the rotor. When the supply pressure to both thrust bearings was increased beyond 60 psi, the fiber-optic

sensor precipitously detected a high frequency axial oscillation of the rotor, which was in fact also within the audible frequency range of the human ear. Figure 2-16(a) and 2-16(b) are comparisons of the scaled output voltages from the sensor with the supply pressures to both thrust bearings held at 60 psi and 220 psi, respectively. Figure 2-16(b) explicitly shows the presence of high frequency axial oscillations superimposed on the background voltage signal. Figure 2-17(a), (b) and (c) are comparisons of the spectral density of the output voltages from the sensor with the supply pressures to both thrust bearings held at 60 psi, 120 psi and 220 psi, respectively. Figure 2-17(b) and (c) shows the presence of high frequency axial oscillations superimposed on the spectrum of the background voltage signal. The frequency of these axial oscillations for various thrust bearing supply pressures was quantified by passing the real-time voltage signal through a spectrum analyzer, and the measured frequency of oscillations is presented in Figure 2-18. Also shown in the same figure are analytical predictions, which only occur for thrust bearing supply pressures in excess of 60 psi when the flow through the orifices of both thrust bearings is choked. Good agreement is observed between the a-priori analytical predictions and the experimental measurements, thus validating the ability of the simple model to accurately predict the frequency of the instability. The analytical model seems to capture the essential mechanism responsible for driving the system towards dynamic instability and establishes a simple criterion for thrust-bearing dynamic stability: if the flow through both forward and aft thrust bearings is choked, the system is dynamically unstable.

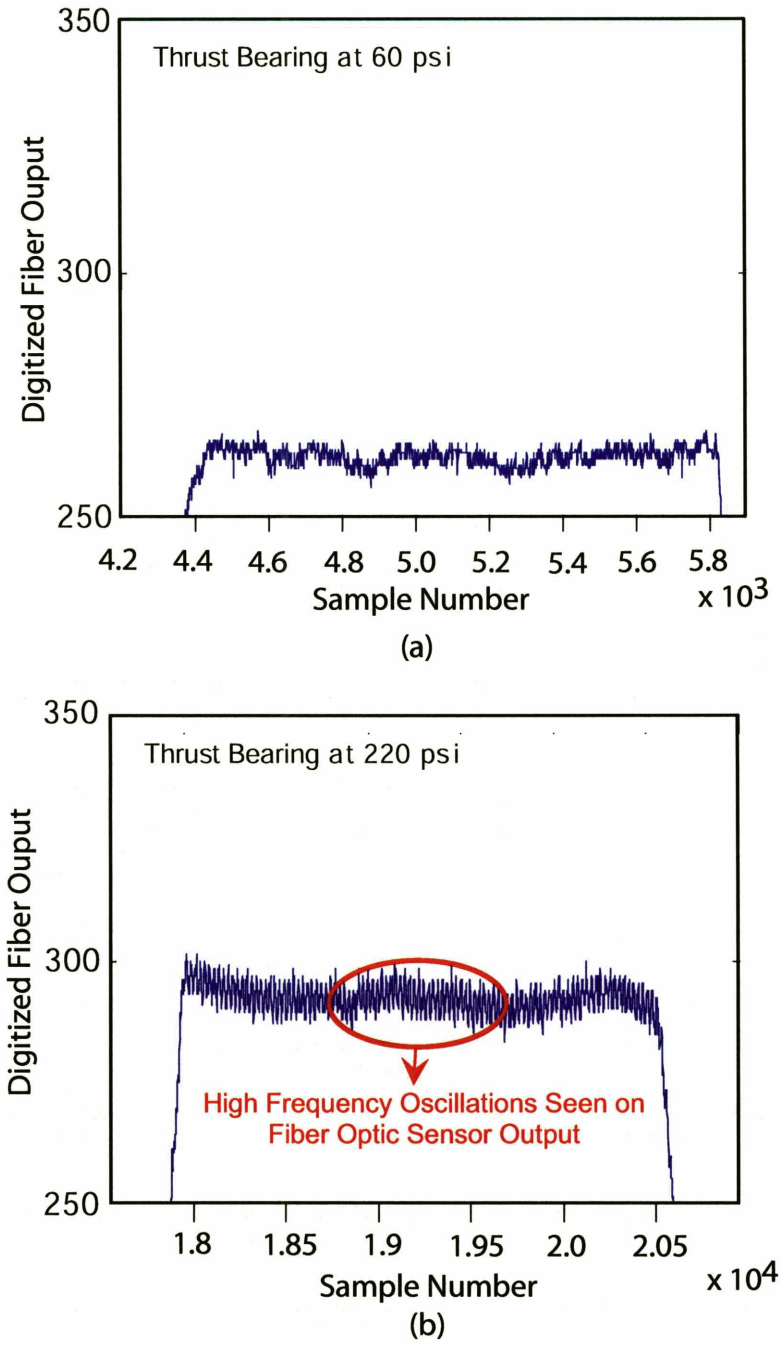

Figure 2-16: Output from fiber optic sensor for thrust bearing supply pressures of (a) 60 psi and (b) 220 psi, showing the presence of unstable axial oscillations when the orifices of both thrust bearings choke.

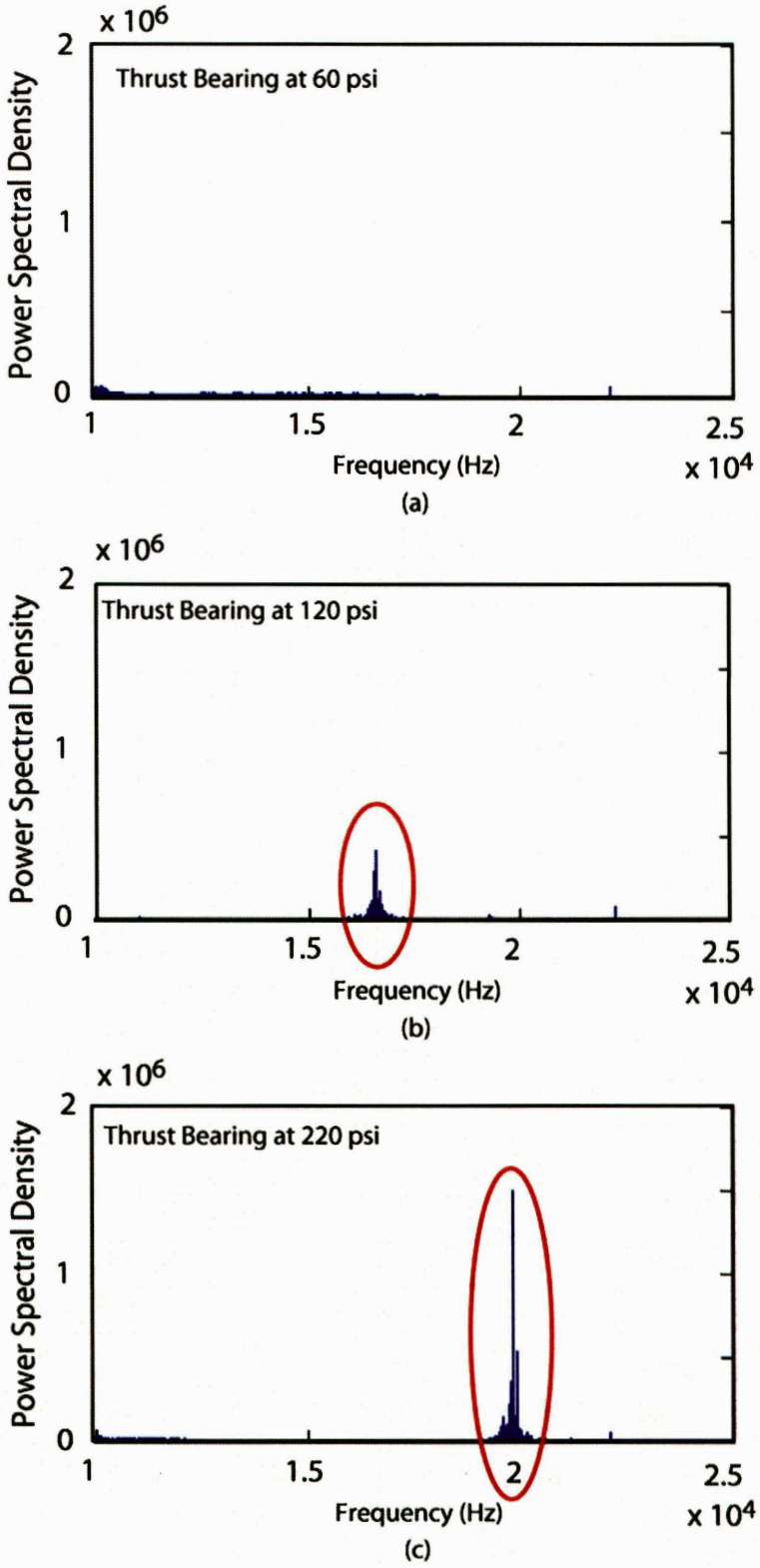

Figure 2-17: Spectral density of output voltage from fiber optic sensor for thrust bearing supply pressures of (a) 60 psi, (b) 120 psi and (c) 220 psi, showing the presence of unstable axial oscillations when the orifices of both thrust bearings choke.

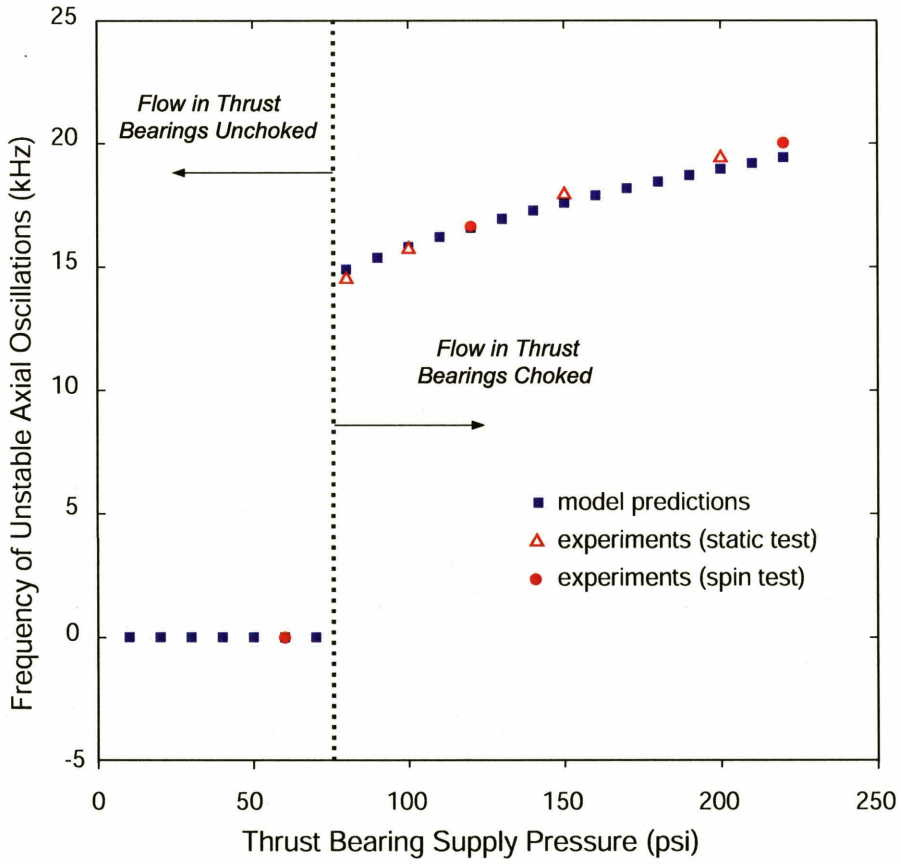

Figure 2-18: Comparison of experimental measurements and analytical predictions of the frequency of unstable axial oscillations for different thrust bearing supply pressures. The uncertainties in pressure and frequency measurements are ±1.25 psi and ±2 Hz, respectively.

2.5 Summary and Conclusions

An analytical model to predict the steady-state performance of inherent-restrictor orifice hydrostatic thrust bearings for application to micro-turbomachines has been developed. Although the Reynolds number of the flow through the bearings is low, the Mach numbers are relatively high. The effects of both compressibility and viscosity have been incorporated into the resistance model, which is capable of predicting variations in axial stiffness, natural frequency and mass flow rates as functions of the thrust bearing supply pressure. In terms of applicability, the model can be employed to analyze the

performance of thrust bearings with both circular and annular pads. Both thrust bearing configurations have been employed on the MIT micro-devices. An analytical model for analyzing thrust bearing dynamic stability was introduced and extended to dual thrust bearing systems for application to the MIT micro-devices. The model illustrates the role of choked flow in the orifices as one of the drivers of dynamic instability manifested in axial oscillations.

The analytical model was further utilized to develop operating protocols for micro-devices such as the micro-electrostatic turbine-generator and the micro-turbopump, where the coupling effects of the accompanying components within the microsystem introduce undesirable negative stiffness, subjecting the bearings to static instability. The validity and usefulness of these operating protocols have been verified during experimental testing of these micro-devices. In the micro-electrostatic turbine-generator, implementation of the operating protocols has allowed the rotors of these devices to be operated to 93% of their design speed (850,000 rpm). No observable electrostatic pull-in effects were observed for voltages up to 120 V applied between the electrodes. On the micro-turbopump, experiments performed at low pump outlet pressures have shown the validity of the operating protocols in successfully preventing the leakage of liquid from the pump outlet into the thrust bearing pads.

In addition to static stability, the thrust bearing dynamic stability of a micro-turbocharger was also addressed using the analytical model. A-priori predictions were made pertaining to the thrust bearing supply pressures required for dynamic instability. The predicted axial dynamic instability was subsequently verified and demonstrated in experiments performed on a micro-turbocharger. The frequency of unstable oscillations was found to show good agreement with the model predictions, verifying the ability of the analytical model to capture the key mechanisms responsible for dynamic instability. The combined experimental and modeling efforts further demonstrate that a criterion for the onset of dynamic instability is the occurrence of flow choking through the orifices of both the forward and aft thrust bearings.

CHAPTER 3

Analysis of Tilting Effects and Geometric Non-uniformities in Micro-Hydrostatic Gas Thrust Bearings

3.1 Introduction and Motivation

In Chapter 2, an analytical model was presented for predicting the steady-state performance characteristics of inherent-restrictor orifice hydrostatic thrust bearings for application to micro-turbomachines. The model is capable of predicting thrust bearing performance and the static and dynamic stability of the thrust bearing system. In addition the model helped establish thrust bearing operating protocols used in the experimental testing of the MIT micro-devices. The key advantage of the original analytical model, which utilizes a fluid resistance approach, is its simplicity. However, the model is limited to axisymmetric configurations with the thrust bearing orifices placed along the same radial location. The thrust bearing clearances and the geometric dimensions of the orifices were assumed uniform. In this chapter, an approach employing Green's functions is presented, which allows one to extend the applicability of the original model.

One of the primary motivations for generalizing the model is to quantify the tilting stiffness of the thrust bearings. Unlike conventional axial-flow turbomachines, where engine architecture is based on long slender shafts supporting the rotating structure, the rotors of the MIT micro-devices consist of thin disks with very low thickness-to-diameter ratios (L/D) and thrust bearings located near the center of the disk. As shown in Figure 1-2(a), conventional rotors have two bearings which can provide a radial load. In view of the fact that these two bearings are separated by a considerable distance, they are able to provide a moment reaction to counteract any rotor pitching or yawing motion. However, the single journal bearing configuration of a typical MIT microdevice shown in Figure 1-2(b) is unable to exert an appreciable torque to resist any tilting motion, and the rotors are thus more prone to unwanted tilting. The onus of providing a tilting stiffness thus lies in

the thrust bearings, and it is therefore crucial to quantify its magnitude. The tilting stiffness characteristics of hydrostatic thrust bearings have previously been studied by Al-Bender and Brussel [33] for circular centrally fed thrust bearings, by Yabe and Watanabe [34] and Yabe and Yamamoto [35] for annular pad thrust bearings, and by Nakamura and Yoshimoto [36,37] for rectangular double-pad thrust bearings.

In addition, thrust bearing performance may be compromised due to the presence of geometric non-uniformities such as orifice diameters and profiles. The lack of precise control of geometric uniformity constitutes one of the major challenges encountered during micro-fabrication. Occasionally, one has to contend with the presence of more severe defects, such as the failure of a number of orifices to etch through completely. Another anomaly which has been observed pertains to the profile of the orifices, where the diameters of the orifices are found to vary considerably along their lengths, thus resulting in tapered rather than uniform orifice profiles. The focus of this chapter is then to quantify the magnitudes of the torques and static tilting angles arising from the presence of these undesirable geometric non-uniformities and defects.

3.1.1 Objectives and Scope of this Chapter

One of the primary goals of this chapter is to generalize and extend the capabilities of the hydrostatic thrust-bearing model presented in Chapter 2, and to analyze non-axisymmetric thrust bearing configurations. More specifically the chapter addresses the following objectives: (1) quantification of the thrust bearing tilting stiffness, in addition to evaluating torques and rotor tilting angles due to geometric non-uniformities in thrust bearing clearance or orifice diameter, (2) assessment of the performance of thrust bearings with novel arrangement of thrust bearing orifices, (3) quantification of the performance of annular thrust bearings which are coupled to the turbomachinery, and (4) analysis of the pitch and yaw dynamics of a thrust-bearing-rotor system with non-zero dynamic or moment imbalance using a two degree-of-freedom rotordynamic model. This chapter also presents analytical models for annular seals and the application of these models for determining the rotor axial position.

3.1.2 Layout of Chapter

First, the Green's function formulation for generalizing the original analytical model presented in Chapter 2 is explained in detail. The modeling approach for hydrostatic and hydrodynamic tilting stiffness are also presented. The extended model is subsequently employed to predict the thrust bearing tilting stiffness in the MIT micro-devices. Variations in mass flows through the thrust bearings as a function of rotor tilting angle are quantified and utilized to indicate the tilting angle of the rotor. Next, a specific example is presented to illustrate how the generalized model can be applied to other thrust bearing configurations with novel arrangements of orifices. In addition, the model is used to predict and to analyze the performance of annular thrust bearings with variable exhaust pressures which depend on the rotational speed of the rotor. The ability to analyze the resultant torques and static tilting angles due to geometric non-uniformities (i.e. clogged orifices) is demonstrated. An influence-coefficient based approach to model the compressible, viscous internal flows through tapered orifices is then presented to illustrate the effects of tapered orifices on thrust bearing performance. The chapter then analyzes the rotordynamics in terms of pitching and yawing response of a two degree-of-freedom thrust-bearing-rotor system subjected to dynamic imbalance. Subsequently, a linear perturbation analysis in pursuit of an eigenvalue problem is performed to study the dynamic stability of the system subjected to small perturbations about its steady-state tilting angle. The influence-coefficient based approach is also utilized to model the viscous, compressible flow through annular seals. The model is applied to determine the rotor axial position in one of the MIT micro-devices. Finally, the feasibility of employing a Lomakin effect seal thrust bearing in substitution of a hydrostatic thrust bearing is investigated.

3.2 Thrust Bearing Configurations

In the design of micro-hydrostatic thrust bearings, desirable attributes which have to be taken into consideration include large axial and tilting stiffness, low mass flow and power consumption, as well as static and dynamic stability. Furthermore, the micro-fabrication processes associated with the manufacture of micro-thrust bearings have to be sufficiently robust to yield acceptably low levels of geometric non-uniformities. In

particular, the thrust bearing clearances and the geometric dimensions have to meet stringent tolerance requirements.

Figure 3-1 illustrates three possible thrust bearing configurations. Figure 3-1(a) shows the baseline thrust bearing configuration with a circular thrust bearing pad, together with 20 orifices uniformly distributed around the circumference. Figure 3-1(b) shows a novel circular pad thrust bearing configuration, with 37 orifices distributed on different radial locations so as to form a hexagonal array. For ease of reference, this configuration will be referred to as a hexagonal thrust bearing hereafter. Figure 3-1(c) shows an annular thrust bearing, with a single row of 20 orifices arranged uniformly at the mean radius.

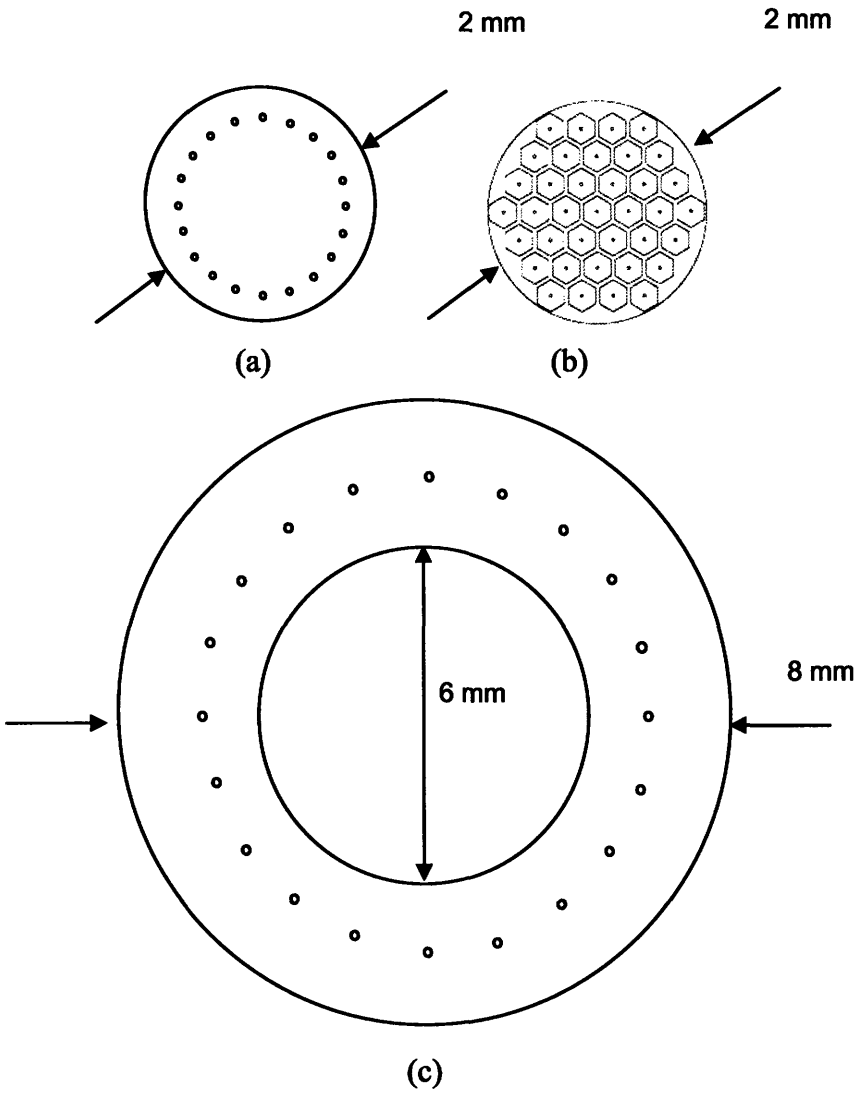

Figure 3-1: Schematic illustration of 3 different configurations of hydrostatic thrust bearings: (a) baseline configuration, (b) hexagonal configuration, and (c) annular configuration.

One useful simplification in the modeling of the baseline configuration is to assume that the flow through each orifice contributes equally to the overall stiffness of the system, thus permitting all the orifices to be modeled as springs with equal stiffness. Since the hexagonal thrust bearing has almost double the number of orifices compared to the baseline configuration, one may conjecture that the hexagonal thrust bearing possesses superior axial and tilting stiffness, in contrast to the baseline configuration. An annular thrust bearing with the same radial extent as the baseline configuration is also expected to

have larger axial and tilting stiffness, since both the effective area of the thrust bearing pad and the radial location of the orifices are larger.

In order to assess the performance of the various thrust bearing configurations shown in Figure 3-1, it is necessary to extend the capabilities of the analytical model presented in Chapter 2. In particular, to evaluate the thrust-bearing tilting stiffness, the refined model needs to be able to handle scenarios with non-uniform thrust bearing clearances. Moreover, the extended analytical model should have the attribute of simultaneously coupling the flow field through all the individual orifices and the bearing gap in an efficient manner. For instance, the flow field through each individual orifice of the hexagonal thrust bearing is strongly coupled to the flow field of the other orifices, even in the absence of tilting effects. Depending on the micro-turbomachinery application, the inner and outer radii of the thrust bearing pad may be subjected to different static pressure boundary conditions, and the model should have the capability to deal with a variety of boundary conditions.

3.3 Modeling Approach

3.3.1 Rotordynamic Model for Yaw and Pitch Dynamics

This section presents the approach used to analyze the tilting response of the rotor-thrust-bearing system in terms of yaw and pitch dynamics. Referring to Figure 3-2, in the absence of rotation, the vertical axis through the geometric center and *fixed to the rotor* is OB. This is termed the static axis. The axis *fixed to the static structure*, which coincides with the static axis OB in this configuration is OZ. The dynamic imbalance χ is the angular misalignment between the static axis OB and the principle axis OA (the principle axis corresponding to the polar moment of inertia of the rotor). When the rotor is set into motion, the static axis OB, which is fixed to the rotor, exhibits a coning motion about OZ at a small inclination angle β. Denoting the projections of β onto the x-z and y-z planes by β_x and β_y, respectively, the linearized equations of motion governing β_x and β_y are given by

$$I\ddot{\beta}_x + I_p\Omega\dot{\beta}_y + k_{xx}\beta_x + k_{xy}\beta_y + c\dot{\beta}_x = (I - I_p)\chi\Omega^2\cos\omega t, \qquad (3.1)$$

$$I\ddot{\beta}_y - I_p\Omega\dot{\beta}_x + k_{yy}\beta_y - k_{xy}\beta_x + c\dot{\beta}_y = (I - I_p)\chi\Omega^2 \sin\omega t\,. \qquad (3.2)$$

The notation for the Euler angles β_x, β_y and ϕ (where $\omega = \dot{\phi}$) follows the same convention as that used in Childs [38], where β_x is the yaw angle and β_y is the pitch angle (β_x, β_y << 1). Here, k_{xx} and k_{yy} are the thrust bearing direct-coupled hydrostatic tilting stiffness, c is the thrust bearing angular damping and k_{xy} is the cross-coupled stiffness due to hydrodynamic effects. The cross-coupled stiffness k_{xy} couples angular displacements β_x and β_y and vice versa. Note that the direct-coupled stiffness $k_{xx} = k_{yy} = K^{hs}$ and damping coefficient c can be calculated as a function of β. In addition to $k_{xy} = K^{hd}$ which couples β_x and β_y, an additional source of coupling arises due to the gyroscopic terms $I_p\Omega\dot{\beta}_y$ and $I_p\Omega\dot{\beta}_x$ in Equations (3.1) and (3.2). The non-homogeneous driving terms on the right-hand-side of each equation depend on the diametral and polar moments of inertia, denoted by I and I_p respectively, as well as the dynamic imbalance χ. In the limit of infinite rotational speeds, the inclination angle β of the conical motion approaches the dynamic imbalance χ. Physically, the polar principle axis OA aligns itself with the inertial axis OZ as a consequence of gyroscopic stiffening which becomes increasingly dominant at high speeds. If β becomes excessively large, physical contact between the rotor and static structure is liable to occur.

It is now possible to subject the rotor to small perturbations in inclination angles to analyze the linear dynamic stability of the system. This involves linearizing Equations (3.1) and (3.2) and solving them as an eigenvalue problem. The resultant fourth order characteristic polynomial then yields

$$\left(Is^2 + k + cs\right)^2 + \left(I_p\omega s + k_{xy}\right)^2 = 0\,. \qquad (3.3)$$

The real part of each of the eigenvalues carries information pertaining to the stability of the inclination motions to small perturbations about the equilibrium condition.

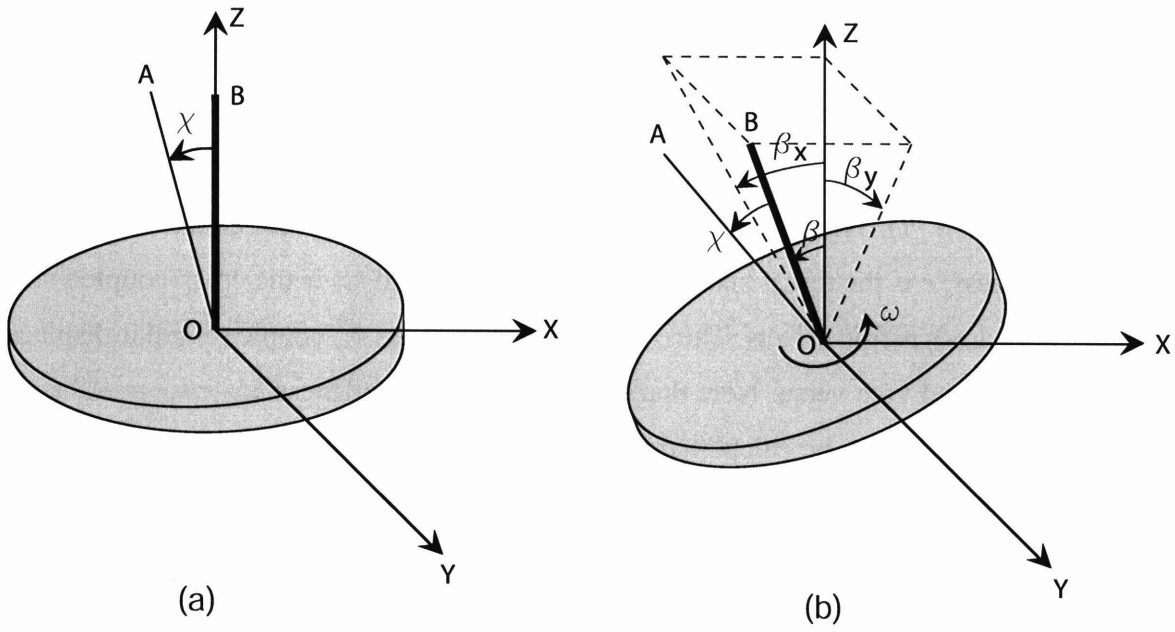

Figure 3-2: Schematic for two degree-of-freedom rotordynamic model for pitch and yaw dynamics: a) Rotor at rest. (b) Rotor spinning at speed ω.

3.3.2 Fluid Dynamic Model

The direct-coupled and cross-coupled tilting stiffness and damping coefficients need to be determined in order to calculate the dynamic behavior. This is achieved using a fluid dynamic model for the hydrostatic force, hydrodynamic force and damping force. For the micro hydrostatic gas thrust bearings analyzed in this work, the time taken for the hydrostatic fluid to flow through the thrust bearing gap is small compared to the period for one complete revolution of the rotor. Even at the maximum design speed, the reduced frequency $\hat{\omega} = \Omega L / U$ is of order 0.1, where Ω is the rotational frequency of the rotor and L/U is the mean flow through time for the hydrostatic fluid. In view of the very low reduced frequencies, it is possible to assume that the flow induced by the motion of the rotor (shown on the right of Figure 3-3) can be separated from the flow arising due to the externally applied hydrostatic pressure drop across the thrust bearing (depicted on the left of Figure 3-3).

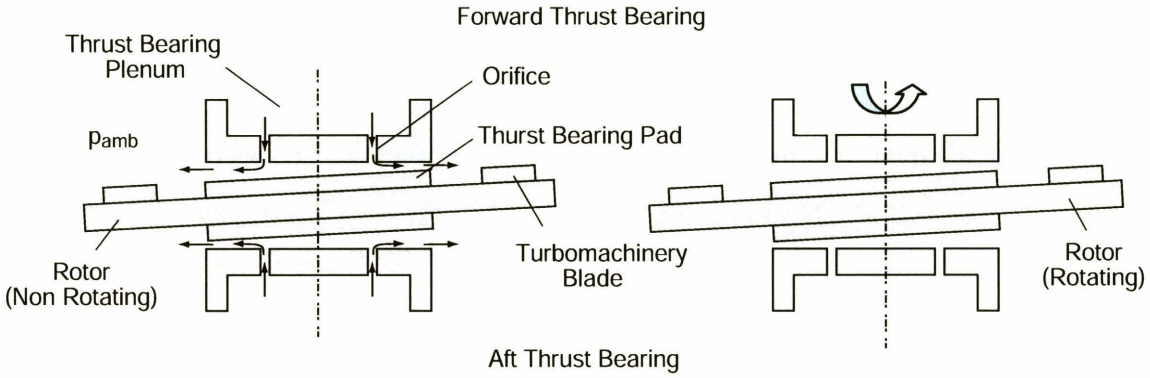

Figure 3-3: Decoupled models for hydrostatic moments (left) and hydrodynamic moments (right).

The following describes in detail the modeling approach for each of the three primary force components acting on the rotor, namely the hydrostatic force, the hydrodynamic force and the damping force.

3.3.2.1 Hydrostatic Force Model: Generalized Analytical Model Employing Green's Functions

In evaluating the forces and moments acting on the rotor due to the externally supplied hydrostatic pressure, the rotor is assumed to be stationary, as depicted on the left of Figure 3-3. In cylindrical coordinates, the continuity equation along the thrust bearing pad can be expressed as

$$\nabla\cdot(\rho\vec{q})=\frac{\partial}{\partial r}(\rho q_r)+\frac{1}{r}\frac{\partial}{\partial\theta}(\rho q_\theta)=\sum_{i=1}^{N}Q_i\delta(\vec{r}_i), \tag{3.4}$$

where $\vec{q}=q_r\hat{e}_r+q_\theta\hat{e}_\theta$ is the volumetric flow rate per unit length normal to the local direction of flow. The right hand side accounts for hydrostatic mass injection of Q_i at discrete locations $\vec{r}_i$ along the thrust bearing gap.

Assuming the flow to be locally of Poiseuille type, the pressure field P in the thrust bearing gap is related to the volumetric flow rate $\vec{q}$ via

$$\vec{q}=-\left(\frac{h^3}{12\mu}\right)\nabla P, \tag{3.5}$$

where μ is the dynamic viscosity of the fluid. Substituting (3.5) in (3.4) thus yields

$$\nabla \cdot \left(\frac{\rho h^3}{12\mu} \nabla P \right) = -\sum_{i=1}^{N} Q_i \delta(\vec{r}_i). \tag{3.6}$$

Assuming an ideal gas and the flow to be isothermal, Equation (3.6) becomes

$$\nabla \cdot \left(h^3 \nabla P^2 \right) = -24\mu \Re T \sum_{i=1}^{N} Q_i \delta(\vec{r}_i). \tag{3.7}$$

In Chapter 2, the thrust bearing gap h was assumed to be uniform. Here, this assumption is relaxed and the general situation where $h = h(r, \theta)$ is analyzed. Noting that (away from the orifices)

$$\nabla \cdot \left(h^3 \nabla \left(P^2 - P_{amb}^2 \right) \right) = 0, \tag{3.8}$$

and letting

$$p = \left(P^2 - P_{amb}^2 \right), \tag{3.9}$$

the governing equation for the pressure field becomes

$$\nabla \cdot \left(h^3 \nabla p \right) = -24\mu \Re T \sum_{i=1}^{N} Q_i \delta(\vec{r}_i). \tag{3.10}$$

Equation (3.10) is a linear equation for p. To solve this equation, the method of Green's functions is employed, where the Green's function is obtained by solving for the impulse response along the thrust bearing pad

$$\nabla \cdot \left(h^3 \nabla G(\vec{r}, \vec{r}') \right) = \delta(\vec{r}). \tag{3.11}$$

A finite-element method with the appropriate boundary conditions is used to compute the Green's function $G(\vec{r}, \vec{r}')$ numerically.

Physically, the Green's function $G(\vec{r}, \vec{r}')$ yields the pressure at the position $\vec{r}'$ within the thrust bearing pad for a unit mass flow through an orifice of diameter d placed at $\vec{r}$. Hence, at the exit of the m^{th} orifice (located at $\vec{r}_m$), the pressure $G(\vec{r}_n, \vec{r}_m)$ due to unit mass flow through orifice n (located at $\vec{r}_n$) is given by

$$\nabla \cdot \left(h^3 \nabla G(\vec{r}_n, \vec{r}_m) \right) = \delta(\vec{r}_n). \tag{3.12}$$

By superposition, the resultant pressure at the exit of the m^{th} orifice due to the combined flows through all the N orifices is given by

$$p_m = \sum_{n=1}^{N} G(\vec{r}_n, \vec{r}_m) Q_n, \; m = 1,\ldots,N, \tag{3.13}$$

where Q_n is the mass flow rate through the n-th orifice.

Note that Equation (3.13) is a set of N equations for $2N$ unknowns, p_m and Q_m, where m = 1,...,N. In order to close the system, another set of N equations is required. These are obtained from the pressure-drop-flow-rate relationship across each of the N orifices:

$$Q_m = f(p_m), \; m = 1,\ldots,N \tag{3.14}$$

A typical functional form for Equation (3.14) is illustrated in Figure 3-4. Since the flow through the orifice chokes for sufficiently low values of p_m and sufficiently high values of thrust bearing supply pressure $P_{TB}, \partial Q_m / \partial(p_m / P_{TB})$ approaches zero at low values of p_m. Note that Equation (3.14) is non-linear and one ends up with a set of coupled non-linear algebraic equations, for which the values of p_m and Q_m are to be determined.

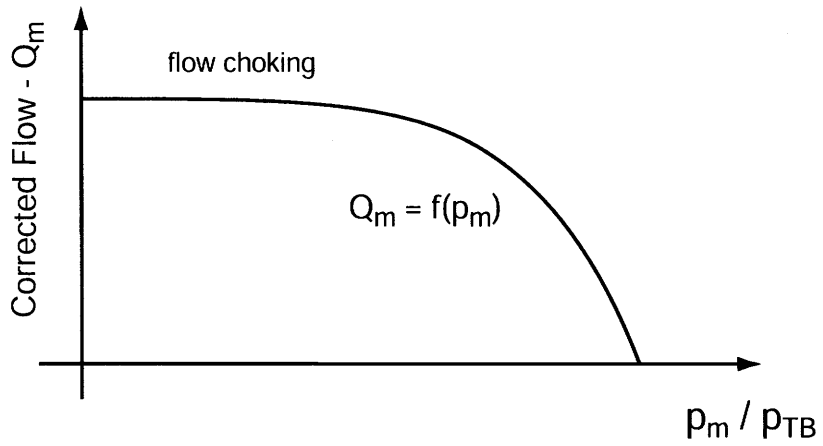

Figure 3-4: Mass flow rate versus pressure drop across thrust bearing orifice.

One common approach to solve such non-linear algebraic equations is to employ the multidimensional Newton's method with the vector of unknowns denoted by

$$\vec{w} = [p_1,\ldots,p_N, Q_1,\ldots,Q_N]^T. \tag{3.15}$$

The system of Equations (3.13) and (3.14) can then be expressed as

$$F(\vec{w}) = \begin{bmatrix} Q_1 - f(p_1) \\ \cdots \\ Q_N - f(p_N) \\ -p_1 + \sum_{n=1}^{N} G(\vec{r}_n, \vec{r}_1) Q_n \\ \cdots \\ -p_N + \sum_{n=1}^{N} G(\vec{r}_n, \vec{r}_N) Q_n \end{bmatrix} = \begin{bmatrix} 0 \\ 0 \\ 0 \\ 0 \\ 0 \\ 0 \end{bmatrix}. \tag{3.16}$$

The multidimensional Newton's method is given by

$$J_F(\vec{w})(\vec{w}^* - \vec{w}) = -F(\vec{w}), \tag{3.17}$$

where the Jacobian $J_F(\vec{w})$ is

$$J_F(\vec{w}) = \begin{bmatrix} -f'(p_1) & 0 & 0 & 1 & 0 & 0 \\ 0 & \cdots & 0 & 0 & \cdots & 0 \\ 0 & 0 & -f'(p_N) & 0 & 0 & 1 \\ -1 & 0 & 0 & G(\vec{r}_1, \vec{r}_1) & G(\vec{r}_2, \vec{r}_1) & \cdots \\ 0 & \cdots & 0 & \cdots & G(\vec{r}_n, \vec{r}_m) & \cdots \\ 0 & 0 & -1 & \cdots & \cdots & G(\vec{r}_N, \vec{r}_N) \end{bmatrix}. \tag{3.18}$$

Once the values of the $2N$ unknowns are found, the static pressure at any location $\vec{r}$ along the thrust bearing pad can be simply determined using

$$p(\vec{r}) = \sum_{n=1}^{N} G(\vec{r}_n, \vec{r}) Q_n. \tag{3.19}$$

Note that the above equation is simply a discrete version of Green's formula. Knowledge of the pressure field $p(\vec{r})$ facilitates the evaluation of the hydrostatic forces F^{hs} and moments M^{hs} acting on the rotor. The resulting hydrostatic tilting stiffness $K^{hs} = \partial M^{hs} / \partial \beta$ can then be evaluated for varying rotor tilting angles β.

The Green's function approach for analyzing the tilting effects of hydrostatic thrust bearings has previously been employed by Yabe and Watanabe [34] and Yabe and Yamamoto [35] for annular thrust bearing pads. The authors employed an analytical expression for the Green's function specifically for application to annular pad thrust bearings. However, for the approach described above and adopted in this work, the Green's function is obtained numerically. This approach is more general, as it permits a wide variety of thrust bearings with unconventionally shaped pads to be analyzed. In

particular, analytical expressions for the Green's function are only available for simple geometrical configurations.

3.3.2.2 Hydrodynamic Force Model

As a consequence of rotor tilt, the spinning motion of the rotor drags the flow along a circumferentially varying clearance, thus giving rise to hydrodynamic pressures. This can be modeled using the Reynolds Equation. For incompressible flow in cylindrical coordinates, the Reynolds equation becomes:

$$\nabla \cdot \left(h^3 \nabla P\right) = 6\mu\Omega \frac{\partial h}{\partial \theta}. \tag{3.20}$$

The forces F^{hd} and moments M^{hd} due to the hydrodynamics can thus be evaluated for varying rotor tilting angles β and rotational speeds Ω. The hydrodynamic torque M^{hd} acts in a direction which is orthogonal to the rotor tilt, and thus contributes a cross-coupled torque and hence hydrodynamic tilting stiffness $K^{hd} = \partial M^{hd} / \partial \beta$.

In order to assess compressibility effects on the modeling results, fully-compressible CFD calculations were performed. In Figure 3-5, the non-dimensional hydrodynamic moment $\zeta = M^{hd}/(P_a R^3)$ is plotted as a function of the bearing number $\Lambda = (6\mu\Omega R^2)/(P_a h^2)$ for varying normalized tip deflections (and hence rotor tilting angles). The incompressible model results compare well to the compressible CFD results and consistently yield higher values of M^{hd} at high bearing numbers. Hence, the use of an incompressible assumption leads to a marginal over-prediction of the cross-coupled hydrodynamic torques and stiffness. This in turn gives rise to more conservative modeling results, since larger magnitudes of cross-coupled hydrodynamic torques increase the system's tendency towards instability.

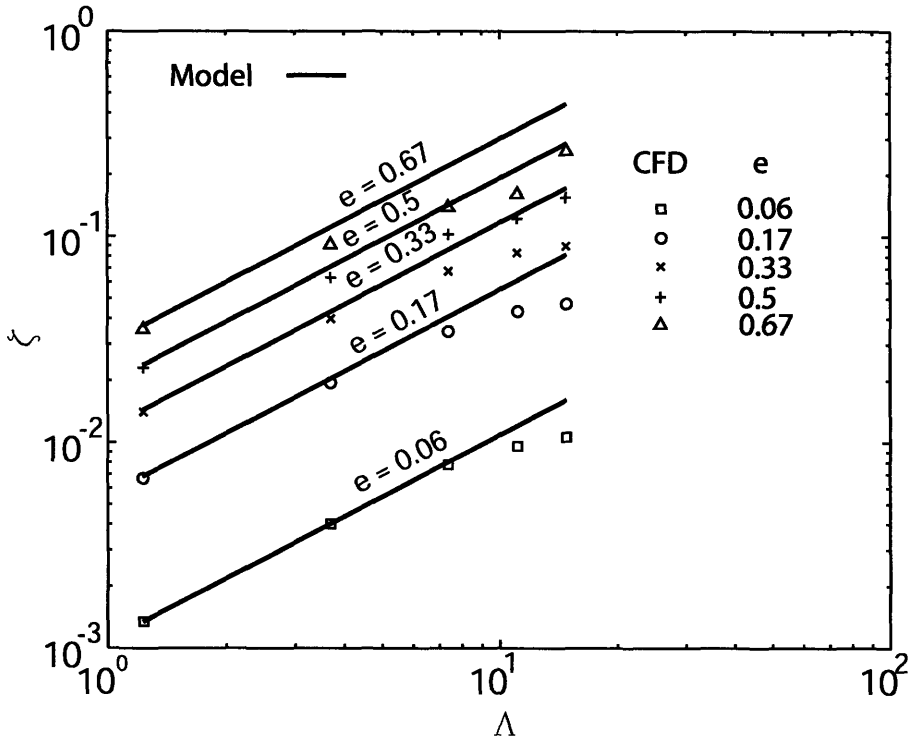

Figure 3-5: Cross-coupled hydrodynamic torque comparison between incompressible analytical model and CFD calculations.

In addition to the above-mentioned cross-coupled component, fluid compressibility results in hydrodynamic moments with a direct-coupled component. This direct-coupled hydrodynamic torque acts in a direction which opposes the rotor tilt, and hence contributes to a direct coupled hydrodynamic tilting stiffness. However, at the rotational speeds and tilting angles of interest, the direct-coupled hydrodynamic torques are negligible compared to the direct-coupled hydrostatic torques.[1]

In summary, the incompressible model enables the calculation of the resulting hydrodynamic torques which only contribute to a cross-coupled hydrodynamic tilting stiffness. As a consequence, the direct coupled tilting stiffness arises solely due to hydrostatics.

[1] For a 1 mm radius thrust bearing with a nominal clearance of 3 μm rotating at a design speed of 1.2 x 10^6 rpm, a (large) rotor tip deflection of 1.5 μm gives rise to a direct-coupled hydrodynamic torque which is approximately 20% of the direct-coupled hydrostatic torque corresponding to a nominal thrust bearing supply pressure of 4 atm.

3.3.2.3 Damping Force Model

The damping force and associated torque is determined from the pressure distribution established when the flow is squeezed through the gap and the thrust bearing orifices due to the tilting motion of the rotor. This pressure field in the gap can be obtained by solving the Reynolds equation of the form

$$\nabla \cdot \left(h^3 \nabla P\right) = 12\mu \frac{\partial h}{\partial t} \tag{3.21}$$

together with the appropriate homogeneous boundary conditions $P = 0$ at the outlet of the thrust bearing pad and at the entrance of the thrust bearing orifices. However, the tilting motion of the rotor induces different mass flow rates through the individual orifices, thus necessitating the Green's function formulation to evaluate the varying mass flows and pressures at the exit of the individual orifices. The damping forces and torques are dependent on the rotor tilting angle, the tilting rate and the bearing geometry. The damping coefficient for the tilting motion, c, can thus be determined by evaluating the pressure forces and concomitant tilting torques arising from a rotor tilt rate of $\dot{\beta}$.

3.3.2.4 Fluid Dynamic Effects of Tapered Orifices

One source of geometric non-uniformity which may arise during the micro-fabrication process is the tapering of the thrust bearing orifices. In order to model the compressible, viscous flow through an orifice with variable cross-sectional area A, a one-dimensional compressible flow with friction, heat addition and area change is employed (Shapiro [22] or Greitzer et. al. [39]). Assuming the flow through the orifices to be isothermal, the fractional change in static temperature can be expressed as

$$\frac{dT}{T} = \frac{(\gamma-1)M^2}{1-M^2}\frac{dA}{A} + \frac{\left(1-\gamma M^2\right)\left(1+\frac{\gamma-1}{2}M^2\right)}{1-M^2}\frac{dT_0}{T_0}$$

$$-\frac{\gamma(\gamma-1)M^4}{2\left(1-M^2\right)}4f\frac{dr}{D_h} = 0 \ , \tag{3.22}$$

where f is the local friction factor and D_h is the local hydraulic diameter. The fractional change in the square of the Mach number dM^2/M^2 is given by

$$\frac{dM^2}{M^2} = -2\frac{\left(1+\frac{\gamma-1}{2}M^2\right)}{1-M^2}\frac{dA}{A}$$

$$+\frac{\left(1+\gamma M^2\right)\left(1+\frac{\gamma-1}{2}M^2\right)}{1-M^2}\frac{dT_0}{T_0}+\frac{\gamma M^2\left(1+\frac{\gamma-1}{2}M^2\right)}{\left(1-M^2\right)}4f\frac{dr}{D_h} \quad (3.23)$$

and the fractional change in the static pressure dP/P can be expressed as

$$\frac{dP}{P} = \frac{\gamma M^2}{1-M^2}\frac{dA}{A}+\frac{\gamma M^2\left(1+\frac{\gamma-1}{2}M^2\right)}{1-M^2}\frac{dT_0}{T_0}$$

$$-\frac{\gamma M^2\left(1+(\gamma-1)M^2\right)}{2\left(1-M^2\right)}4f\frac{dr}{D_h} \quad (3.24)$$

In the above Equations (3.23) and (3.24), the coefficients corresponding to fractional changes in area, stagnation temperature and wall frictional effects only depend on the local Mach number and are known as the influence coefficients. Using Equation (22) to eliminate dT_0/T_0 in Equations (3.23) and (3.24) yields

$$\frac{dM^2}{M^2} = -\left[\frac{2\left(1+\frac{\gamma-1}{2}M^2\right)}{1-M^2}+\frac{(\gamma-1)M^2\left(1+\gamma M^2\right)}{\left(1-M^2\right)\left(1-\gamma M^2\right)}\right]2\frac{dD}{D}$$

$$+\left[\frac{\gamma(\gamma-1)M^2\left(1+\gamma M^2\right)}{2\left(1-M^2\right)\left(1-\gamma M^2\right)}+\frac{\gamma M^2\left(1+\frac{\gamma-1}{2}M^2\right)}{1-M^2}\right]\frac{16\mu\pi dx}{\dot{m}} \quad (3.25)$$

and

$$\frac{dP}{P} = \left[\frac{\gamma M^2}{1-M^2}+\frac{\gamma(\gamma-1)M^4}{\left(1-M^2\right)\left(1-\gamma M^2\right)}\right]2\frac{dD}{D}$$

$$+\left[-\frac{\gamma^2(\gamma-1)M^6}{2(1-M^2)(1-\gamma M^2)}-\frac{\gamma M^2\left(1+(\gamma-1)M^2\right)}{2(1-M^2)}\right]\frac{16\mu\pi dx}{\dot{m}}. \qquad (3.26)$$

Using Equations (3.25) and (3.26), the fractional change in the square of the Mach number dM^2/M^2 and the fractional change in the static pressure dP/P can be evaluated numerically along the entire length of the orifice. The resulting model is used to assess the effects of geometric non-uniformities on thrust bearing dynamic behavior.

3.4 Generalized Model Applications

3.4.1 Prediction of Thrust Bearing Direct-Coupled Tilting Stiffness for Baseline Configuration

The first application of the new model formulation is the evaluation of the direct-coupled tilting stiffness in hydrostatic thrust bearings. This is illustrated for the baseline thrust bearing configuration shown in Figure 3-1(a), which is the configuration adopted in the MIT micro-turbocharger (Savoulides [15]). In addition to providing the necessary axial stiffness, the thrust bearings have the additional onus of restoring the rotor to its equilibrium configuration when it is subjected to small tilting perturbations about its spinning axis. The model is applied to the baseline thrust bearing configuration and the computed static pressure distribution on the thrust bearing pad is shown in Figure 3-6. The radius of the thrust bearing pad is 1 mm, the supply pressure to the thrust bearing orifices is held constant at 60 psi (corresponding to a static pressure ratio $P_{supply}/P_{ambient}$ = 4) , and the nominal thrust bearing gap is 3 μm. Figure 3-6(a) illustrates the baseline situation of an untilted rotor, where the static pressure distribution is seen to be axisymmetric. Computation results obtained for a rotor tip deflection of 2 μm are displayed in Figure 3-6(b) and the static pressure on the thrust bearing pad becomes non-axisymmetric with a larger static pressure building up in regions of smaller axial gaps. The concomitant non-axisymmetric pressure distribution gives rise to a restoring torque which tends to oppose the tilting of the rotor. The monotonic increase in magnitude of the restoring torque with tilting angle thus results in a tilting stiffness, whose magnitude is non-dimensionalized and plotted on Figure 3-6 for a range of dimensionless rotor tip

deflections [2] . The dimensionless direct-coupled tilting stiffness is defined as $k^+ = k/\left(\sqrt{A}P_{supply}r^2\right)$, where k is the direct-coupled tilting stiffness, A is the thrust bearing surface area and r is the radial location of the orifices. The rotor tip deflections are normalized using the maximum allowable tip deflection. Knowledge of the tilting stiffness allows one to predict the rotordynamic behavior pertaining to the pitching and yawing of the rotor, which is discussed in a later section.

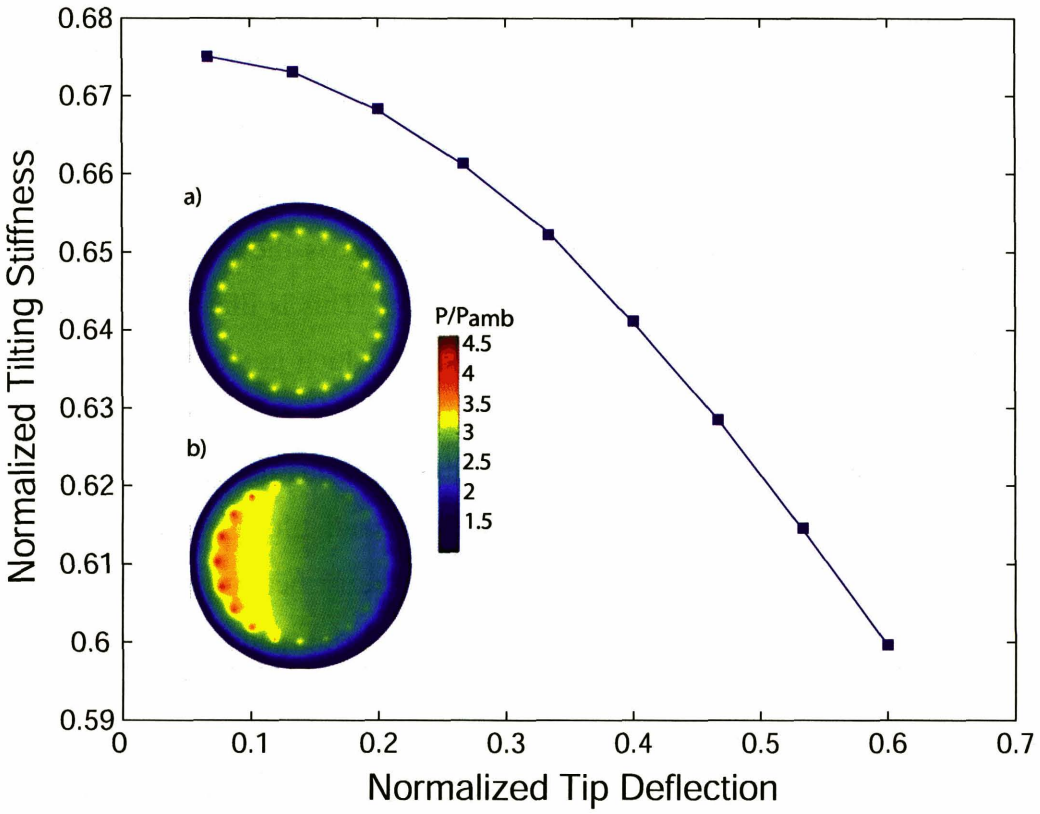

Figure 3-6: Variation of thrust bearing tilting stiffness with normalized tip deflection; baseline configuration.

3.4.2 Performance Analysis of Hydrostatic Thrust Bearings with Unconventional Orifice Arrangements

Next, the potential improvements in direct-coupled tilting stiffness of unconventional and novel thrust bearing configurations is assessed. The new model is employed to

[2] Since the thrust bearing gap is 3 μm, the corresponding maximum tip deflection of the rotor is also 3 μm.

perform a feasibility study of the hexagonal thrust bearing shown previously in Figure 3-1(b). Using the Green's function formulation, the modeling results for the static pressure distribution along the thrust bearing pad are shown in Figures 3-7(a) and 3-7(b) for cases in which the rotor is untilted and tilted with a tip deflection of 2 μm, respectively. The supply pressure to the thrust bearings was kept constant at 60 psi for all calculations presented in this section, in order to compare the results to the original baseline configuration shown in Figure 3-7(a). For the untilted case shown in Figure 3-7(a), the static pressure distribution is nearly axisymmetric. When the rotor tip deflection is 2 μm, the high pressure "pocket" shifts outwards towards regions where the thrust bearing gaps are smaller, and provides a restoring torque and direct-coupled tilting stiffness in response to angular perturbations on the rotor. The results are summarized and the two configurations are compared to one another in Table 3-1. The table also includes results for the annular thrust bearing which is discussed next.

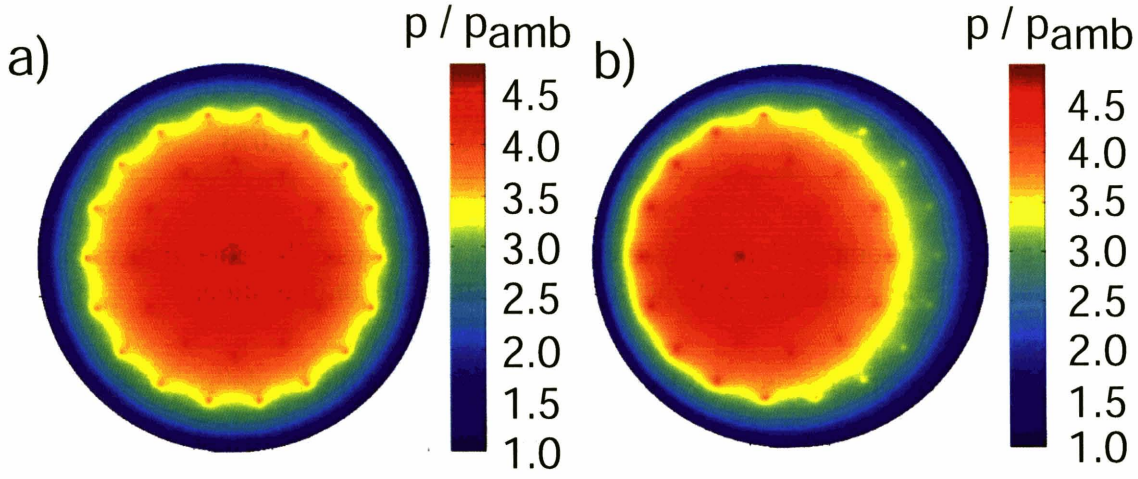

Figure 3-7: Normalized static pressure distribution on thrust bearing pad for hexagonal thrust bearing configuration: (a) untilted, (b) tilted.

Table 3-1 presents two sets of results for the hexagonal thrust bearing configuration. The total thrust bearing clearance of 5.5 μm, which optimizes the axial stiffness for the baseline case, is found to be sub-optimal for the hexagonal case. A total clearance of 7 μm maximizes the axial stiffness for the case with a hexagonal arrangement of orifices. It is apparent from the table that the hexagonal thrust bearing has a marginally lower axial

and direct-coupled tilting stiffness, as compared to the original baseline case. However, the mass flow requirement for the hexagonal thrust bearing is perceptibly higher. The hexagonal thrust bearing is thus seen to be inferior to the baseline configuration in terms of steady-state performance, even though the hexagonal thrust bearing has 37 orifices, whereas the original configuration has only 20 orifices.

Total clearance = 5.5 μm

Type	Axial Stiffness (N/m)	Mass flow (g/s)	Tilting stiffness (N-m/rad)
Original/ Baseline	2.2×10^{5}	1.00×10^{-3}	0.089
Hexagonal	1.7×10^{5}	1.19×10^{-3}	0.087
Annular	8.3×10^{5}	1.15×10^{-3}	5.0

Total clearance = 7 μm (Optimized for axial stiffness)

Type	Axial Stiffness (N/m)	Mass flow (g/s)	Tilting stiffness (N-m/rad)
Hexagonal	1.9×10^{5}	1.73×10^{-3}	0.075

Table 3-1: Comparison of key operating characteristics of baseline thrust bearing configuration with hexagonal and annular configurations.

As discussed previously, one useful simplification in the modeling of the baseline configuration is to assume that the flow through each orifice contributes equally to the overall direct-coupled tilting stiffness of the system, thus permitting all the orifices to be modeled as springs with equal spring constants. When the number of orifices is increased and located at different radial locations, one might hypothesize that the overall stiffness of the system will increase, since there is an increase in the total number of springs. However, as seen from the above results, these orifices do not contribute equally to the overall axial stiffness of the system due to the interaction between the pressures and flows for orifices placed at different radial locations. Even after optimizing the axial gap for maximum stiffness, the hexagonal thrust bearing is still inferior in performance, since

the gap is optimized for the *overall* thrust bearing system, and not with respect to individual orifices.

In summary, the Green's function approach serves as an effective modeling tool to analyze novel thrust bearing orifice configurations. Apart from modeling thrust bearing configurations with novel arrangements of orifices, the Green's function approach can be easily extended to thrust bearing pads which are not circular. As an example, the tilting characteristics of the rectangular thrust bearings considered by Kwan and Post [40] can be easily analyzed using this approach.

3.4.3 Prediction of Annular Thrust Bearing Performance Subjected to Varying Outlet Static Pressures

One further application of the Green's function formulation is to assess the design of annular hydrostatic thrust bearings. One major proposal for improving the performance of the radial-outflow compressor of the MIT micro-turbocharger is to shroud the compressor (Sirakov [41]) in order to improve the turbomachinery component efficiency. It might then be feasible to incorporate an annular thrust bearing on the shroud in replacement of the thrust bearing at the center of the rotor. However, as the rotational speed increases, the pressure rise across the compressor rotor increases quadratically with the rotational speed. This implies that the static pressure along the outer rim of the annular thrust bearing no longer remains constant while the static pressure along the inner rim is approximately at ambient pressure. It is thus of interest to investigate the effects of an increase in pressure ratio across the compressor rotor on the axial stiffness of the annular thrust bearing. This can be readily assessed using the Green's function formulation. Figure 3-8(a-c) shows the static pressure distribution over the thrust bearing pad of an annular thrust bearing for normalized static pressure ratios across the annular pad of 1, 2 and 3 respectively. The supply pressure to the thrust bearing was held fixed at 60 psig. The inner and outer rims of the thrust bearing pads are located at radial locations of 3 mm and 4 mm, respectively. The dimensionless axial stiffness of the annular thrust bearing is plotted against the static pressure ratio across the annular pad in Figure 3-8. The results show a monotonic decrease in axial stiffness with increasing pressure ratio. The dimensionsless axial stiffness is defined by $K^{+} = K/\left(\sqrt{A}P_{supply}\right)$, where K is the axial

stiffness, A is the area of the thrust bearing pad and P_{supply} is the thrust bearing supply pressure. For a static pressure ratio of roughly 3, the thrust bearing loses approximately 50% of the axial stiffness compared to a stationary rotor. Since the turbomachinery and the bearings are closely coupled, such considerations are important to the design of annular thrust bearings in micro-turbomachinery applications,.

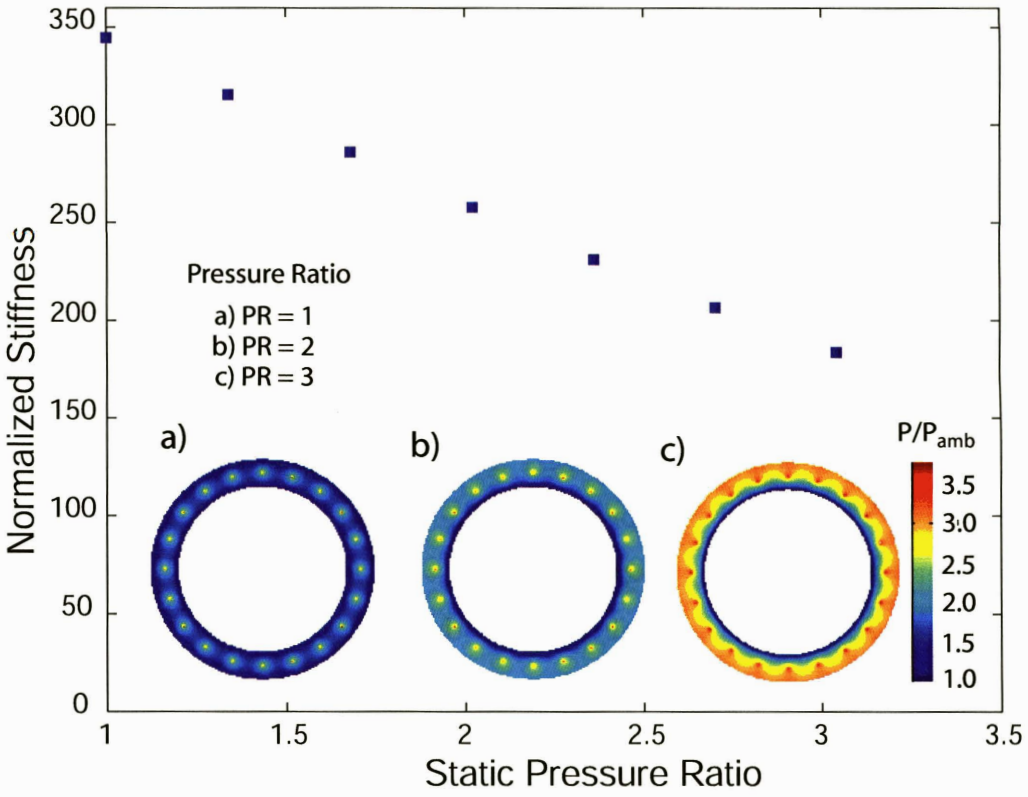

Figure 3-8: Variation of annular thrust bearing axial stiffness with compressor rotor outlet static pressure.

Next, the axial stiffness of the annular thrust bearing is compared with the baseline configuration. Although the area of the annular thrust bearing is 7 times higher than the baseline configuration, the axial stiffness is only 3 times greater and subsequently decreases for increasing static pressure ratios. A larger thrust bearing area thus does not translate into a corresponding linear increase in axial stiffness. Referring to Figure 3-8(a), for the baseline configuration, the circular array of orifices serves as a fence to maintain a high pressure near the center of the pad. This contributes significantly to the axial stiffness, since variations in the thrust bearing gap give rise to variations in static pressure in this region. This in turn contributes to the restoring force acting on the rotor. In

contrast, for the annular thrust bearing, a high pressure region is only maintained in the close vicinity of the orifices, with the static pressure dropping rapidly to ambient conditions along both the inner and outer edge of the circular pad. From a stiffness per unit thrust bearing area perspective, the baseline configuration is thus more efficient in utilizing the available area to generate axial stiffness.

In summary, annular thrust bearings are in general superior to the baseline thrust bearing configuration in terms of direct-coupled tilting stiffness. However, annular thrust bearings do not as efficiently utilize the available area to generate axial stiffness. Furthermore, coupling effects between the turbomachinery and annular thrust bearings may result in a deteriorated thrust bearing performance.

3.4.4 Experimental Prediction of Rotor Tilting Angle

A series of experiments were performed on a micro-turbocharger. Although the pressures to both the forward and aft thrust bearings were held constant during the course of the experiments, the mass flows through *both* thrust bearings were found to decrease monotonically with increasing rotor speeds. The thrust bearing mass flows for both the forward and aft thrust bearings are shown plotted against the rotor spinning speed on Figure 3-9. A purely axial displacement of the rotor would result in a mass flow increase in one of the thrust bearings and a simultaneous decrease in the other (provided the flows through the orifices are unchoked). Therefore, it was conjectured that this simultaneous reduction in mass flows through both thrust bearings must arise as a consequence of rotor tilt.

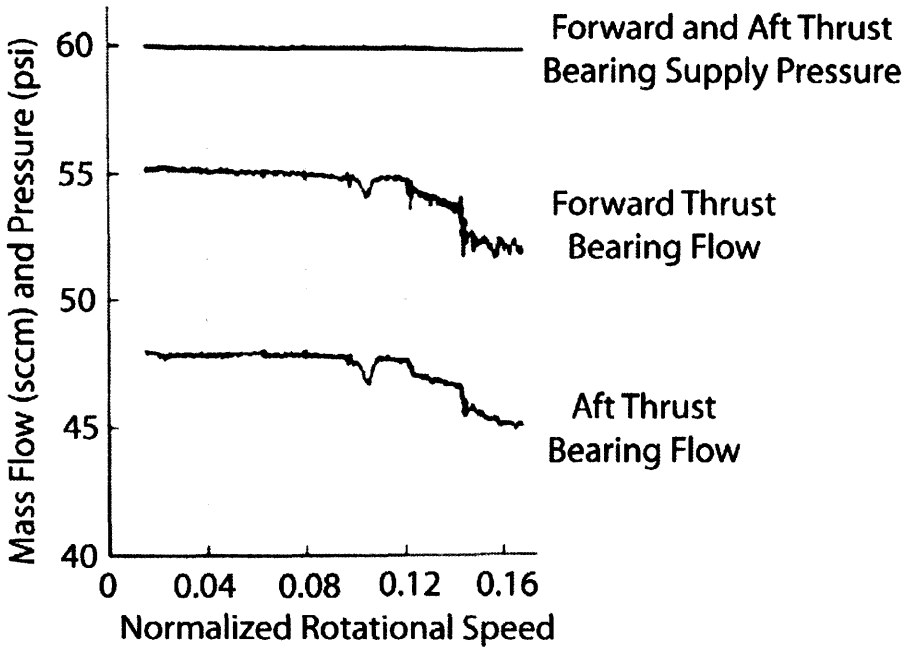

Figure 3-9: Variation in thrust bearings mass flow rates with normalized rotational speed for experiments performed on a micro-turbocharger.

The Green's function formulation has been used to test the above hypothesis and the model has been employed to compute the mass flows through each of the individual orifices as a function of the rotor tilting angle. However, from the point of view of experimentation, one is interested in the total mass flow through the thrust bearings, since this is the quantity which is physically measurable during the course of experiments. The total thrust bearing mass flow rate at each tilting angle is readily evaluated by summing up the flows through the individual orifices. An interesting observation can be seen in Figure 3-10, which illustrates the total mass flow through the thrust bearing as a function of the tilting angle of the rotor. According to the model, the mass flow through the thrust bearing decreases monotonically with increasing rotor tilting angles or tip deflections.

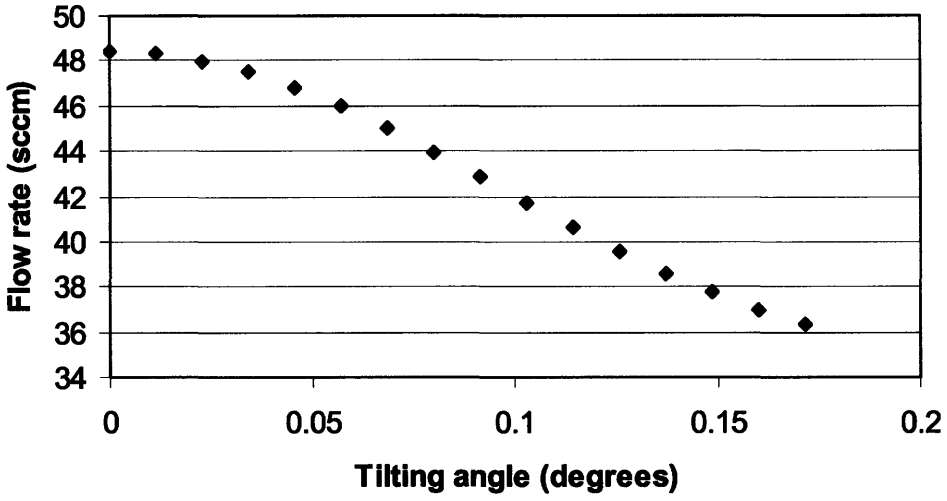

Figure 3-10: Variation of mass flow rate with rotor tilting angle.

Although intriguing at first, a simultaneous dip in mass flows through *both* thrust bearings would be consistent with the hypothesis that the tilting angle of the rotor is increasing. In addition to qualitative trends, Figure 3-10 further allows one to quantify the magnitude of decrease in mass flow to the rotor tilting angle. Hence, according to the analytical results shown in Figure 3-10, corresponding to a reduction in mass flow of approximately 3 sccm in both thrust bearings, the tilting angle of the rotor is estimated to be approximately 0.07 degrees.

In summary, using the measured decrease in thrust bearing mass flow, the model is capable of predicting the rotor tilting angle. Since it is nearly impossible to physically and accurately measure the rotor tilting angle using conventional instrumentation in the MIT micro-devices, the analytical predictions are thus invaluable for providing a quantitative estimate.

3.5 Effects of Geometric Non-uniformities in Thrust Bearing Orifices

3.5.1 Torques and Static Tilting Angles Arising from Clogged Orifices

One of the main problems arising from micro-fabrication is the precise control of the thrust bearing clearances and the orifice dimensions. In this regard, the Green's function formulation serves as a useful design tool to quantify the effects of geometric non-

uniformities arising from micro-fabrication. For example, the effects of a non-uniform clearance $h(r, \theta)$ on the direct-coupled tilting stiffness can be easily assessed, as elucidated by the calculations shown in Figure 3-6.

Variations in thrust bearing orifice diameters constitute a commonly observed geometric non-uniformity. One scenario characterizing such a geometric non-uniformity is the presence of clogged orifices, or more precisely, orifices which fail to be etched through as a consequence of photolithographic problems or breakdown of the photoresist. Figure 3-11 presents the static pressure distribution on the thrust bearing pad for two cases: one clogged orifice and seven clogged orifices in a row. The total number of orifices is 20 and the supply pressure to the thrust bearing is set to 60 psi. Two main consequences are seen to arise due to the presence of clogged orifices. First, the deviation from an axisymmetric pressure distribution results in a net out-of-plane torque acting on an untilted rotor, which is in turn counterbalanced by the thrust bearing tilting stiffness. The rotor will thus experience a net static tilting angle and a corresponding rotor tip deflection, which is plotted non-dimensionally in Figure 3-11 as a function of the number of clogged orifices. As expected, the rotor tip deflection increases monotonically with the number of clogged orifices. An excessively large tip deflection may give rise to large out-of-plane hydrodynamic torques which may in turn lead to instability.

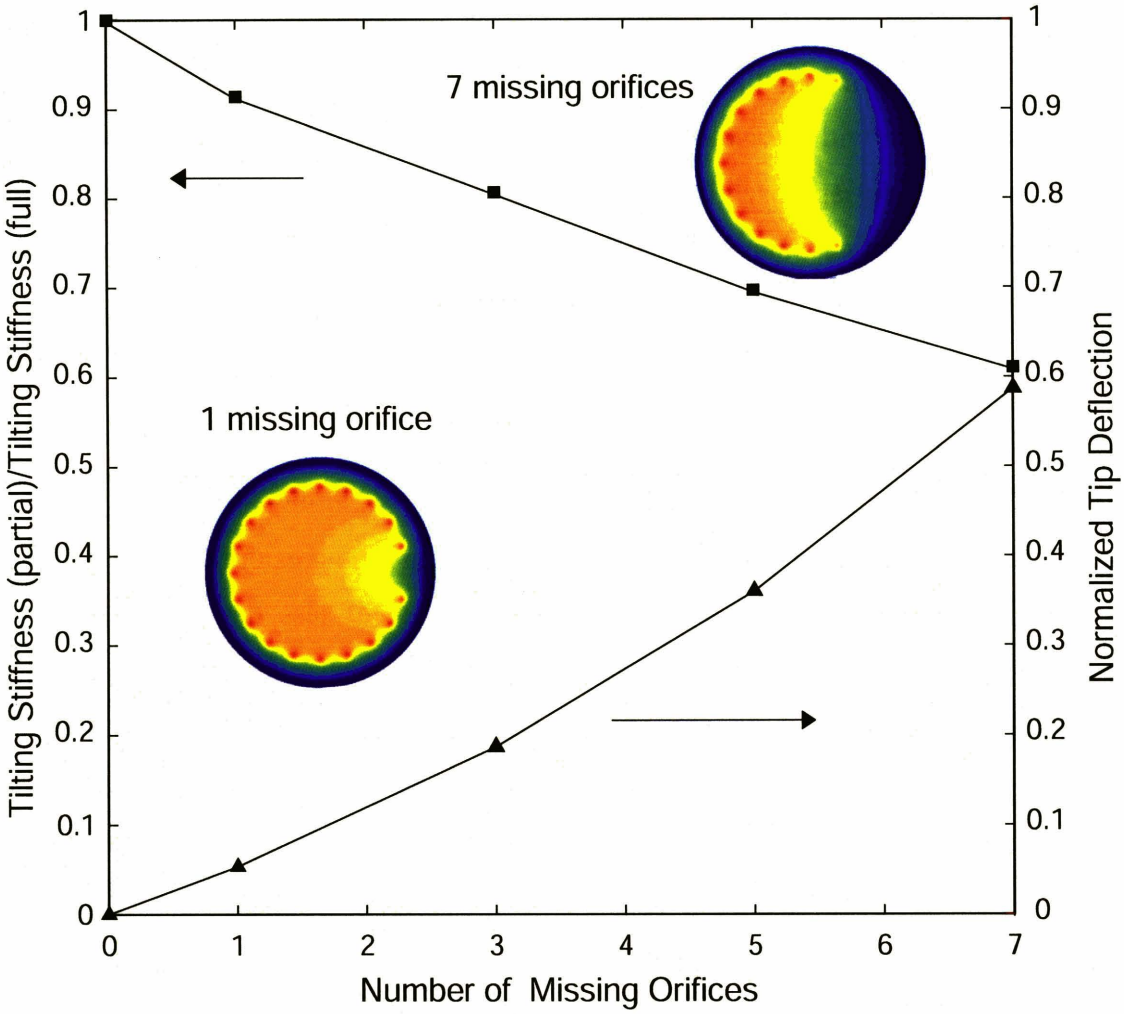

Figure 3-11: Variation in tip deflection and tilting stiffness with number of missing orifices.

A second consequence of unetched orifices is the reduction in magnitude of the direct-coupled tilting stiffness, as also shown in Figure 3-11. This arises from the fact that fewer orifices contribute to the net tilting stiffness. Although in this discussion, the approach has been to adopt the most severe scenario to illustrate the ability of the model to provide adequate predictions, the model is capable of handling other more specific and less severe cases of geometric non-uniformities such as variations in lengths and diameters of the thrust bearing orifices.

3.5.2 Effects of Tapered Orifices

Another geometric non-uniformity which tends to arise during the micro-fabrication process is the tapering of the thrust bearing orifices. The viscous, compressible flow through an orifice with variable cross sectional area can be readily handled using the influence coefficient approach described previously. The discussion here is confined to linearly tapered orifices, although the method is well suited for orifices of any general geometrical profile. The profile of such a linearly tapered orifice is given by

$$D(x) = \frac{2\overline{D}}{\sqrt{AR}+1} + 2\left(\frac{\overline{D}}{L}\right)\left(\frac{\sqrt{AR}-1}{\sqrt{AR}+1}\right)x, \tag{3.27}$$

where $\overline{D} = (D_1 + D_2)/2$ is the mean diameter of the orifice, and $AR = \sqrt{D_2 / D_1}$ is the area ratio of the outlet to the inlet of the orifice. An area ratio greater than unity ($D_2 > D_1$) denotes a negatively tapered orifice, whereas a value of less than unity ($D_1 > D_2$) represents a positively tapered orifice. Figure 3-12 depicts the dimensionless thrust bearing axial stiffness as a function of supply pressure for orifices of length L = 100 μm, an average orifice diameter $\overline{D}$ = 10 μm, and different area ratios AR. For the baseline case where the orifices are untapered (i.e. AR = 1), the flow through the orifices of both the forward and aft thrust bearings choke at a supply pressure ratio (P/P_{amb}) of approximately 6.4, where P_{amb} = 14.7 psi.

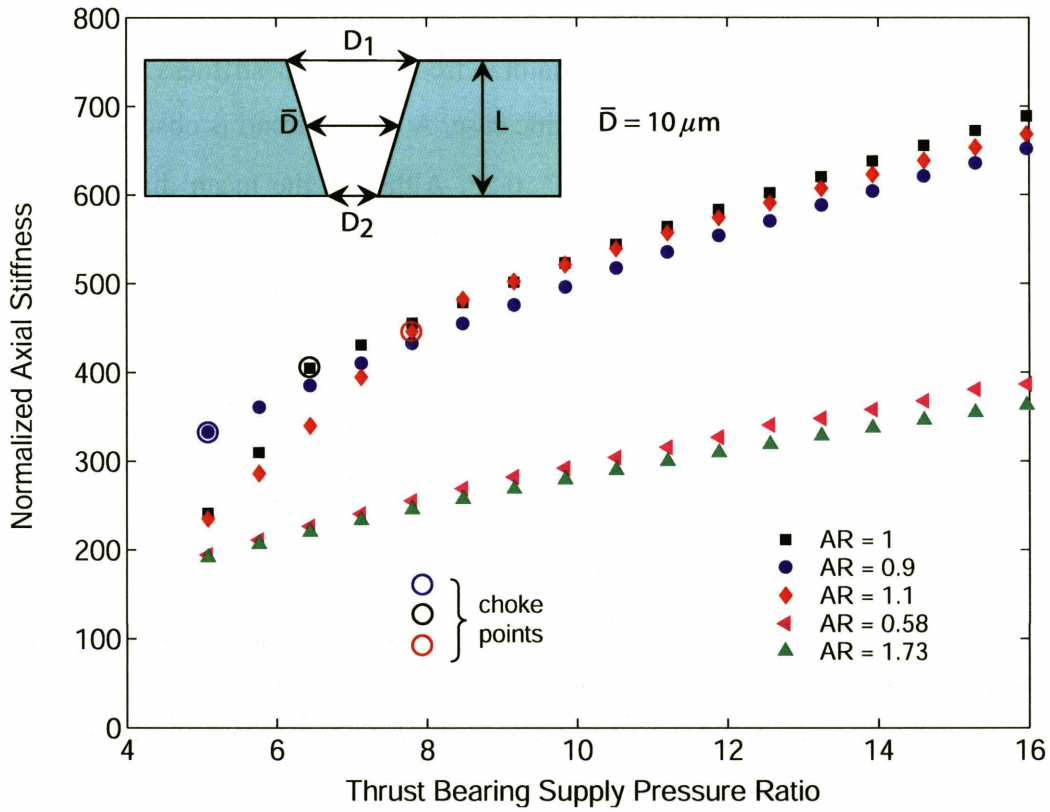

Figure 3-12: Effects of tapered orifices on normalized thrust bearing stiffness.

When the orifices have a slight positive taper $AR \approx 0.9$, the natural frequency and stiffness are greater than the baseline case with untapered orifices for supply pressure ratios ranging between 5.1 and 6.4. Note that, the presence of the positively tapered orifices causes the orifices to choke at a lower thrust bearing supply pressure ratio of 5.1. Although the static axial stiffness may be higher than the baseline case, the thrust bearings become dynamically unstable at lower thrust bearing pressures as a result of the choked flow through the orifices. A negative taper of $AR \approx 1.1$ shows an opposite trend. Compared to the baseline case, the natural frequency and stiffness are decreased for supply pressure ratios ranging between 5.8 and 7.1. Due to negative taper, the flow through the orifices has less tendency to choke and the orifices remain unchoked up to a thrust bearing supply pressure ratio of 7.8. As a consequence, slightly negative tapered orifices have the advantage of delaying the occurrence of flow choking and therefore the onset of dynamic instability (see Section 2.4 for details).

In the above scenarios, the taper ratios analyzed were relatively small. For a larger positive taper ratio of $AR \approx 1.73$, the natural frequency and stiffness are found to be significantly lower compared to the baseline case. A similar trend is observed for orifices with a large negative taper ratio of $AR \approx 0.58$. Although the mean diameter $\overline{D}$ of the orifices is 10 μm, the overall hydraulic resistance is significantly larger due to the stronger contribution from orifice sections with lower diameters. The flow resistance due to the 5.5 μm gap in the "radial" outflow region of the thrust bearing land is thus too small to match the resistance posed by the orifices. This results in low values of stiffness. Moreover, due to the flow choking near regions where the diameters are excessively small, dynamic instabilities can be triggered more easily.

In summary, the influence coefficient method for compressible, viscous orifice flows can be incorporated into the original model to assess the effects of non-uniform orifice profile on hydrostatic thrust bearing performance. The model can be used as a design tool to specify tolerance requirements related to the allowable taper ratio for a given level of thrust bearing performance, as well as to predict the thrust bearing performance based on actual geometric measurements pertaining to the profile of the orifices. For thrust bearings with orifice area ratios ranging between 0.9 and 1.1, the axial stiffness with tapered orifices are not expected to deviate significantly from the untapered case. Positively tapered orifices may, however, lead to flow choking which induces dynamic instabilties at lower thrust bearing supply pressures. Orifice area ratios which deviate significantly from unity result in a considerable reduction in thrust bearing axial stiffness.

3.6 Pitch and Yaw Dynamics of a Rotor with Dynamic Imbalance

In this section, the pitch and yaw dynamics of a rotor-thrust-bearing system is analyzed using Equations (3.1) and (3.2). For an isotropic system with $k_{xx} = k_{yy} = K^{hs}$, the yaw and pitch angles β_x and β_y are equal and the tilting angle of the rotor is simply quantified by a single parameter β. The Green's function formulation can be applied to evaluate the variation of K^{hs} and c as a function of β. The values of K^{hd} are determined using the Reynolds equation. Two primary ways of reducing the values of β at high speeds are: (1) to increase the thrust bearing direct-coupled tilting stiffness K^{hs} and (2) to

maintain low levels of dynamic or moment imbalance χ by reducing the rotor etch non-uniformity and the bond misalignment between the compressor and turbine disks. Figure 3-13(a) illustrates the variation of the inclination angle β with rotational speed for a micro-turbocharger rotor with 3 different values of dynamic imbalance χ subjected to the same thrust bearing pressures and therefore direct-coupled tilting stiffness. At a fixed rotational speed, the inclination angle β is greater for rotors with larger dynamic imbalance χ. Assuming the maximum allowable tip deflection is 3 μm[3], the model predicts that the rotor with a dynamic imbalance of $\chi = 1.5$, which corresponds to an asymptotic tip deflection of 4.5 μm, is suggested to fail at a quarter of the design speed. Without considering the effects of dynamic stability, the maximum allowable tilting angle is limited by the total thrust bearing clearance or the minimum clearances imposed by the presence of labyrinth seals. The above analysis thus implies that, in order to reduce the likelihood of physical contact between the rotor and static structure as the rotor accelerates, it is necessary to ensure that the rotor possesses a sufficiently low, normalized dynamic imbalance χ of order 0.5.

[3] This corresponds to a normalized dynamic imbalance $\chi = 1.0$.

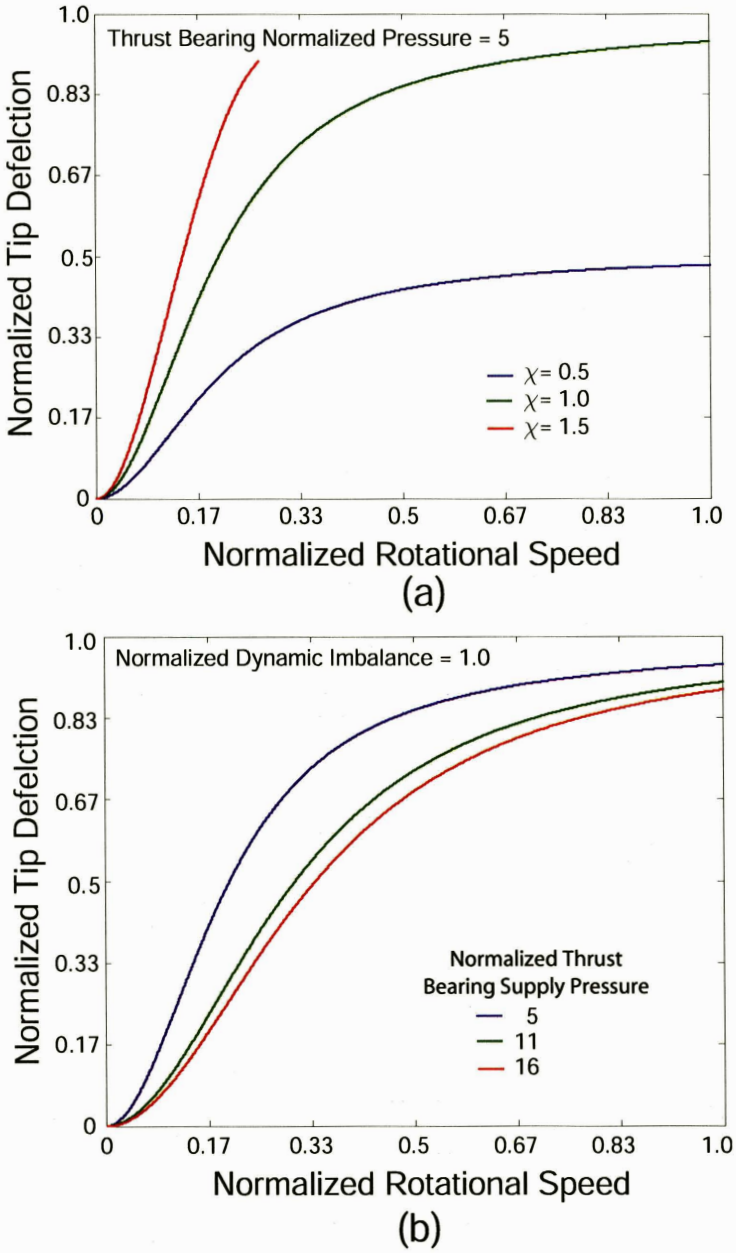

Figure 3-13: (a) Variation of tip deflection with rotational speed for different dynamic imbalance levels χ. (b) Variation of tip deflection with rotational speed for a rotor with normalized dynamic imbalance of 1.0 for different thrust bearing supply pressures.

The effect of thrust bearing direct-coupled tilting stiffness is shown in Figure 3-13(b) for rotors with a normalized dynamic imbalance of $\chi = 1$, which corresponds to 3 μm tip deflection. An increase in thrust bearing supply pressure and therefore direct coupled tilting stiffness results in smaller inclination angles β for the same rotational speed. The implication of this is that an increase in thrust bearing direct-coupled tilting stiffness has

the beneficial effect of reducing the rotor tilting angle and hence the likelihood of physical contact between the rotor and the static structure.

The above analysis implies that if it is possible to quantify the dynamic imbalance of the rotor during the micro-fabrication process, the two degree-of-freedom model for the yaw and pitch dynamics is capable to predict the steady-state inclination behavior of the rotor at different operating speeds and thrust bearing conditions.

It should also be noted that the variations of the tip deflection with rotational speed depicted in Figure 3-13 do not exhibit any peak response corresponding to the tilt mode critical frequency or rotational speed. This is unlike the response observed for the radial deflection of a Jeffcott rotor [38] which exhibits a peak corresponding to the radial mode critical frequency. The inherent difference lies in the fact that for the pitch and yaw motion, the gyroscopic stiffening effect of the spinning rotor plays a dominant role in increasing the tilting stiffness and hence the natural frequency corresponding to the tilting mode. Furthermore, unlike conventional axial-flow turbomachines (Figure 1-2(a)) where the diametral moment of inertia I is significantly greater than the polar moment of inertia I_p (i.e. $I > I_p$), the rotors of the MIT microdevices (Figure 1-2(b)) have larger polar than diametral moments of inertia (i.e. $I_p > I$). The enhanced gyroscopic stiffening effect experienced by the micro-rotors results in a tilting natural frequency which increases much more rapidly than the rotational frequency, thus giving rise to the absence of a critical frequency corresponding to the tilting mode.

It is also essential to analyze the dynamic stability of the rotor-thrust-bearing system subjected to small perturbations in rotor inclination angles. The eigenvalue problem for dynamic stability has previously been obtained in Equation (3.3). If any of the eigenvalues has a positive real part, the system is deemed to be dynamically unstable. For the specific case of the micro-turbocharger rotor with a large dynamic imbalance of χ = 1.0, and supported by the baseline thrust bearings with supply pressures of 60 psi, the eigenvalues are found to be complex conjugate pairs. The real parts of each complex conjugate pair are determined for the entire range of operating speeds. All real parts are found to be negative, implying linear stability of the inclination or coning motion. Although the real part of the eigenvalues are all negative, some of them have magnitudes close to zero (corresponding to neutral stability). Coupling effects from other components

of the system, such as the gas journal bearings located at the outer periphery of the rotor (Liu [3]), can render the eigenvalues positive and hence unstable. This is currently being investigated.

3.7 Analytical Model for Annular Seals

In the micro-turbopump and redesigned bearing rig, annular labyrinth seals comprised of a series of teeth and grooves have been employed. As will be further expounded in Section 5.2.1.2, the use of labyrinth rather than plain seals yields a major advantage. The use of a single wide annular seal may result in a negative tilting stiffness, the magnitude of which can be significantly reduced by the use of labyrinth seals. An analytical model has been developed to predict the pressure drops and mass flows through annular labyrinth seals for different seal clearances. When the pressure ratios across the seals become sufficiently large, the Mach numbers of the flow can attain values on the order of unity and compressibility effects become increasingly important. Similar to the hydrostatic thrust bearings, the enhanced interactions between viscous and compressible flow effects necessitate new models to be developed to adequately predict the flows through these seals. The inlet loss at the entrance of each tooth of the labyrinth seal is modeled as a drop in stagnation pressure of the fluid:

$$\frac{\Delta P_t}{P_t - P} = 0.5 . \tag{3.28}$$

The viscous, compressible flow through each tooth is modeled using an influence coefficient approach for computing a quasi one-dimensional compressible flow which combines the effects of friction, heat addition and area changes (Shapiro [22] or Greitzer et. al. [39]). In view of the high thermal conductivity of Silicon, the flow through each tooth is assumed to be isothermal. The fractional change in static temperature dT/T corresponding to a fractional change in cross sectional area dA/A, a fractional change in stagnation temperature dT_0/T_0 and a drop in stagnation pressure arising from viscous dissipation has previously been given by (3.22). The corresponding fractional changes in the Mach number and static pressure are given by (3.23) and (3.24), respectively. Furthermore, the fractional change in cross sectional area is given by

$$\frac{dA}{A} = \frac{dr}{r}, \tag{3.29}$$

and the local friction factor can be expressed as

$$f = \frac{\tau_w}{0.5\rho V^2} = \frac{12}{\mathrm{Re}_h}, \tag{3.30}$$

where the Reynolds number based on the seal clearance $\mathrm{Re}_h = \rho V h / \mu$. Hence,

$$4f\frac{dr}{D} = \frac{48\mu\pi r}{\dot{m}h}dr. \tag{3.31}$$

Once again, Equation (3.22) can be used to eliminate dT_0/T_0 in Equations (3.23) and (3.24), thus yielding

$$\frac{dM^2}{M^2} = -\left[\frac{2\left(1+\frac{\gamma-1}{2}M^2\right)}{1-M^2} + \frac{(\gamma-1)M^2\left(1+\gamma M^2\right)}{\left(1-M^2\right)\left(1-\gamma M^2\right)}\right]\frac{dr}{r}$$

$$+\left[\frac{\gamma(\gamma-1)M^2\left(1+\gamma M^2\right)}{2\left(1-M^2\right)\left(1-\gamma M^2\right)} + \frac{\gamma M^2\left(1+\frac{\gamma-1}{2}M^2\right)}{1-M^2}\right]\frac{48\mu\pi r}{\dot{m}h}dr, \tag{3.32}$$

and

$$\frac{dP}{P} = \left[\frac{\gamma M^2}{1-M^2} + \frac{\gamma(\gamma-1)M^4}{\left(1-M^2\right)\left(1-\gamma M^2\right)}\right]\frac{dr}{r}$$

$$+\left[-\frac{\gamma^2(\gamma-1)M^6}{2\left(1-M^2\right)\left(1-\gamma M^2\right)} - \frac{\gamma M^2\left(1+(\gamma-1)M^2\right)}{2\left(1-M^2\right)}\right]\frac{48\mu\pi r}{\dot{m}h}dr. \tag{3.33}$$

The above two equations can be used to numerically compute the fractional changes in the Mach number and static pressure along the entire length of each tooth. The static pressure along each groove has been assumed to be constant. This assumption is reasonable, in view of the significantly larger depths of the grooves as compared to the teeth, thus implying that the radial and circumferential hydraulic resistances in the grooves are negligible. The flow is assumed to lose all its dynamic head when exiting a tooth and venting into a groove. For a specified seal clearance, together with prescribed

seal inlet and exit static pressure boundary conditions, the mass flow rate through the seal can be obtained numerically.

The analytical model was experimentally verified and subsequently used in determining the rotor axial position during the testing of a micro-turbopump. Figure 2-1(b) presents a cross-sectional view of the MIT demo-micro-turbopump. Two sets of annular seals have been employed on the aft side of the micro-device. The first set of seals (hereafter termed the inner seals) which segregates the thrust balance plenum and the inner aft thrust bearing exhaust plenum consists of two sets of teeth, each spanning a radial extent of 25 μm. The teeth are separated by a groove with a radial extent of 50 μm. The outer exhaust plenum of the aft thrust bearing and the journal bearing plenum are separated by a second set of seals (hereafter called the outer seals) which consists of 4 teeth, each occupying a radial width of 25 μm. Similarly, any two neighboring teeth are kept apart by a groove occupying a radial extent of 50 μm. Static flow tests were performed on a micro-turbopump device prior to rotor release. The rotor was held in place by oxide pads and the inner and outer seal clearances had nominal design and as-fabricated values of 3 μm. Experimental values of the mass flow rate across both the inner and outer seals are plotted against the static pressure difference across them in Figures 3-14 and 3-15, respectively. Also shown on Figures 3-14 and 3-15 are the analytical predictions for the mass flow rate plotted as a function of the pressure difference across the inner and outer seals, respectively, corresponding to a seal clearance of 3 μm. Referring to these two figures, it is evident that the fully compressible analytical model, which employs the method of influence coefficients, compares favorably with the experimental data, thus vindicating the validity of the model. Also plotted on Figure 3-14 are the analytical results obtained by using a pseudo-compressible model, where the static pressures are directly coupled to the densities by invoking the equation of state. The momentum equation is employed to determine the static pressure variation along each tooth, without recourse to the energy equation[4]. For a given pressure drop across the inner seals, the pseudo-compressible model is seen to overpredict the mass flow through the seal. This overprediction is approximately 20% and corresponds to a pressure difference

[4] This should be contrasted to a perfectly incompressible model, where the density is assumed to be constant and is independent of the local static pressure.

of 8 psi. The inferior performance of the pseudo-compressible model in predicting the seal flows is not surprising, since the intimate coupling between the dynamics and thermodynamics of the compressible flow has been ignored.

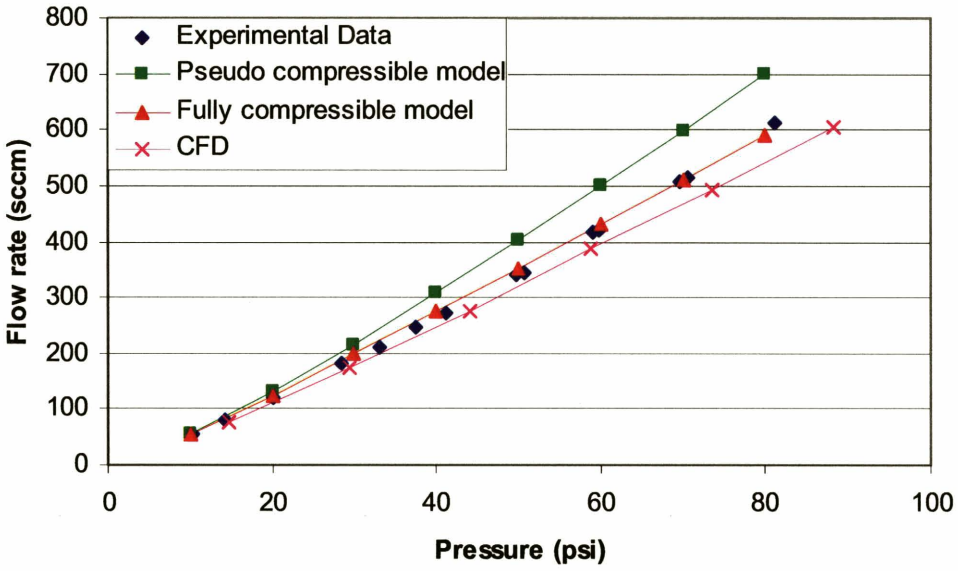

Figure 3-14: Flow rate versus pressure difference across inner seal of micro-turbopump prior to rotor release, where the nominal seal clearance is 2 μm.

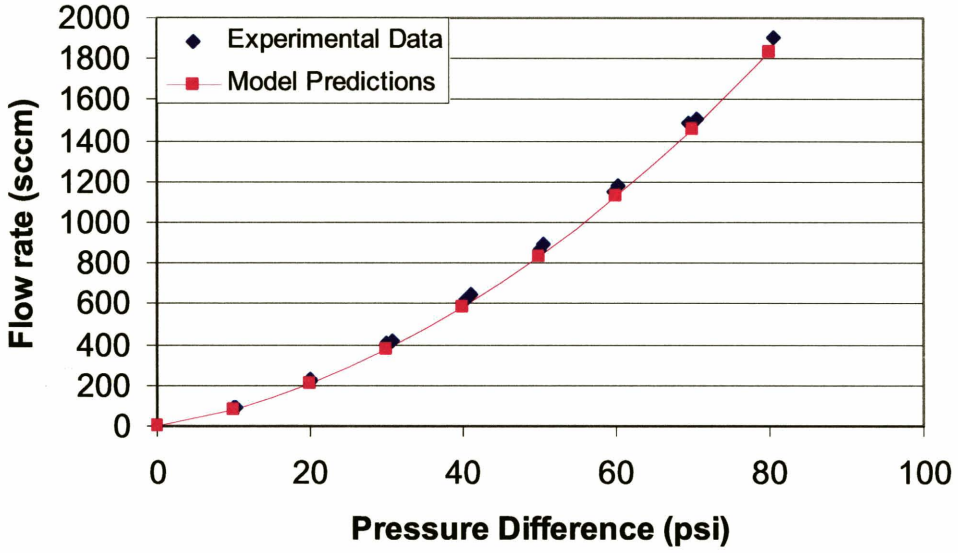

Figure 3-15: Flow rate versus pressure difference across outer seal of micro-turbopump prior to rotor release, where the nominal seal clearance is 2 μm.

3.8 Application of Annular Seal Model to Operation of Micro-Turbopump

In the previous section, the accuracy of the analytical model for predicting the flows through annular seals was verified. In this section, the analytical model is applied to determine the rotor axial position of a micro-turbopump during actual experimental testing. One of the key challenges involved in the testing and actual operation of a high-speed spinning micro-device is to experimentally ascertain the axial location of the rotor. This is of importance for the micro-turbopump due to several reasons. First, operating in close proximity to the static structure increases the likelihood of physical contact between the spinning rotor and the static structure. Furthermore, a rotor spinning excessively close to the seals and thrust bearings enhances the coupling between the tilting and radial modes of the rotor-bearings system. Based on a 4 degree-of-freedom rotordynamic model, this enhanced coupling has the detrimental effect of degrading the rotordynamic stability. Finally, as previously described at length in Section 2.3.2, the stability of the liquid-gas interface along the inner rim of the forward thrust bearing depends on the chosen combination of the forward thrust bearing supply pressure, the pump outlet pressure and the forward thrust bearing gap (which translates into the rotor axial position).

The most straight-forward and unambiguous scheme of ascertaining the rotor axial location is by monitoring the mass flow and pressure difference across the inner seals. The rotor axial location can then be deduced by invoking the analytical model. This is illustrated in Figure 3-16, which shows the mass flow plotted as functions of the pressure difference across the inner seals for various seal clearances (and hence rotor axial positions). The maximum seal clearance is 5 μm, corresponding to the rotor in immediate contact with the forward thrust bearing. Any given combination of mass flow and pressure difference across the inner seals corresponds to a unique seal clearance. The supply pressure to the balance plenum can thus be regulated to achieve the designated rotor axial location as stipulated by the operating protocol. The rotor axial location for the experimental results presented in Section 2.3.2 have been deduced by measuring the mass flow and pressure difference across the inner seals and employing Figure 3.16 to interpolate for the rotor axial position.

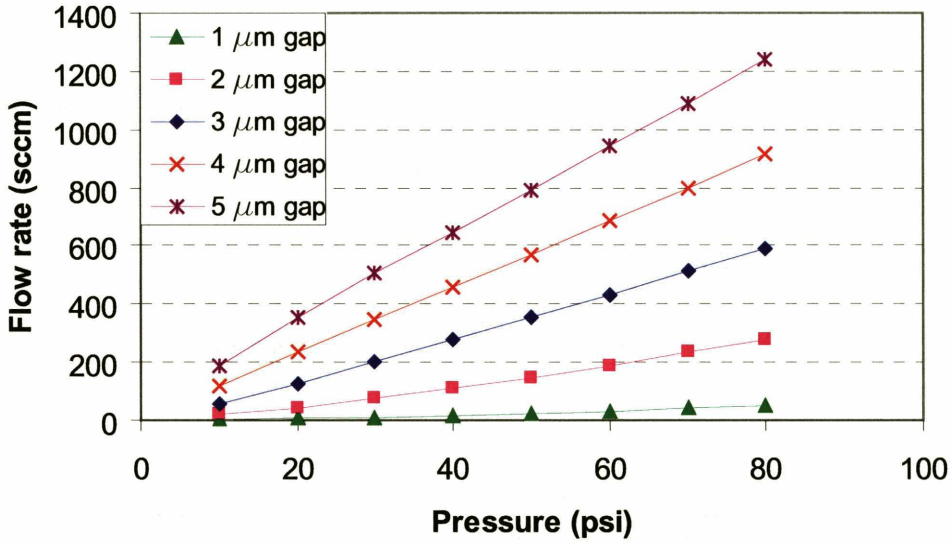

Fugure 3.16: Flow rate versus pressure difference across inner seal of micro-turbopump for various seal clearances.

3.9 Axial Stiffness of Lomakin Effect Seal Thrust Bearings

One further issue arose during the analysis of annular hydrostatic thrust bearings for application to the shrouded compressor of the MIT micro-turbocharger, which was discussed in Section 3.4.3. Recall from Section 3.7 that the overall pressure drop across a radial-inflow annular seal consists of an inlet loss component modeled using Equation (3.28) and a radial pressure drop across the face of the seal due to both viscous effects and changes in flow area, which can be modeled by applying Equation (3.33). The combined effect of the inlet pressure loss and the radial pressure gradient across the seal gives rise to a Lomakin seal effect [10], which results in a direct axial stiffness due to the annular seal.

It is thus of interest to investigate whether it is feasible to replace the annular hydrostatic thrust bearing on the shrouded compressor with an annular seal for the purpose of providing an axial stiffness to support the rotor, with the annular seal deriving its stiffness from the Lomakin seal effect. The inner and outer radii of the annular seal are 3 mm and 4mm, respectively. The axial stiffness of the annular seal is shown as a function of the static pressure ratio across the seal for different seal clearances in Figure 3-16. For the purpose of comparison, the axial stiffness due to an annular hydrostatic

thrust bearing with the same inner and outer radii and a supply pressure of 30 psi is shown on Figure 3-17 for various thrust bearing clearances. The number of thrust bearing orifices has been fixed at 20 and they are located at a radial location of 3.5 mm. A quick comparison between Figure 3-17 and 3-18 shows that hydrostatic thrust bearings are capable of providing an axial stiffness which is approximately two orders of magnitude greater than that due to the annular Lomakin effect seal thrust bearing. Hydrostatic thrust bearings are thus superior compared to annular seal thrust bearings in terms of axial support and stiffness.

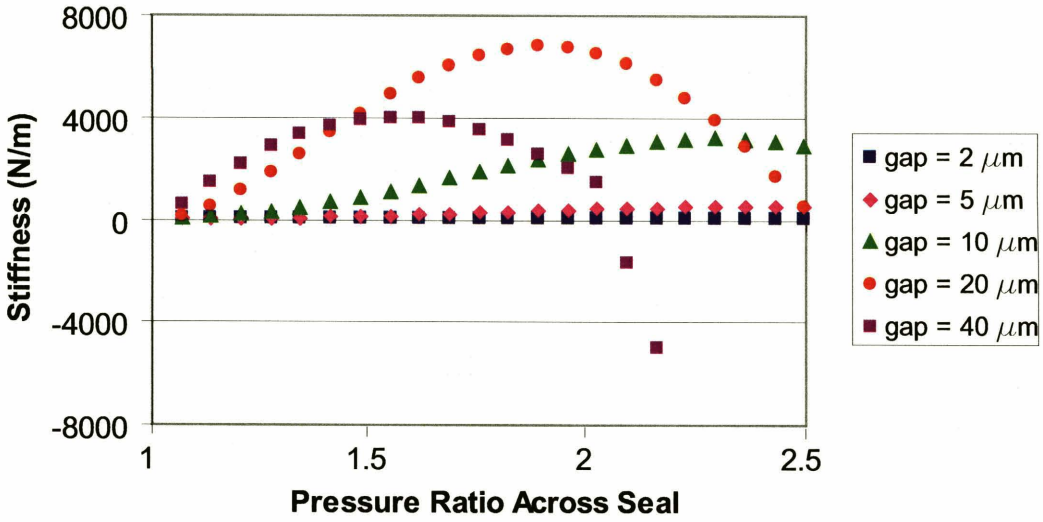

Figure 3-17: Stiffness of Lomakin effect seal thrust bearings plotted as a function of static pressure ratio across the seal for various seal clearances.

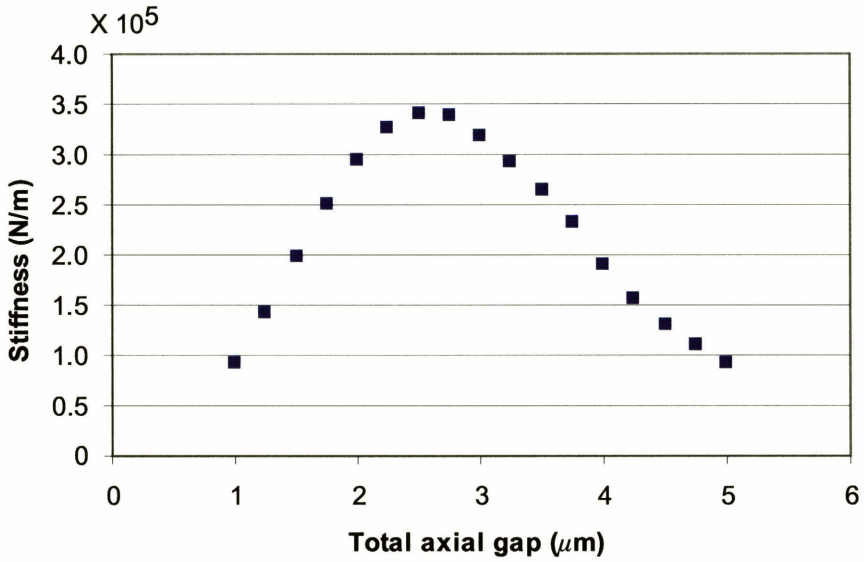

Figure 3-18: Stiffness of hydrostatic annular thrust bearings for various thrust bearing gaps.

Furthermore, several observations pertaining to the annular Lomakin effect seal thrust bearing can be observed from Figure 3-17. For the same pressure ratio across the seal bearing, an increase in seal clearance increases the axial stiffness for low pressure ratios less than approximately 1.4, where the radially inward flow through the annular seal is essentially incompressible. An increase in seal clearance results in a lower hydraulic resistance across the plane seal face. This has the effect of reducing the hydraulic or pressure drop across the seal and of increasing the inlet losses. The axial stiffness thus increases, since there is a reduction in the mismatch between the inlet loss and the hydraulic loss across the seal. For pressure ratios larger than 1.4 and for large seal clearances, compressibility effects become important and they play a significant role in reducing the stiffness arising solely from the Lomakin seal effect. According to Figure 3-17, static instability might even occur for excessively large seal clearances due to negative values of axial stiffness.

To further shed light on the effects of compressibility, the static pressure distribution across the seal is plotted non-dimensionally on Figure 3-19 for different seal clearances corresponding to a seal pressure ratio of 2.36 (this corresponds to a static pressure difference of 20 psi between the outer and inner radii of the annular seal). The

values on the horizontal axis denote the radial location along the seal normalized using the length of the seal (i.e. 1 mm), with a value of zero denoting the location of the seal inlet and a value of unity denoting the seal outlet. The static pressure on the vertical axis has been normalized using the ambient atmospheric pressure. As the seal clearance increases beyond 10 μm, the static pressure drop near the seal exit becomes increasingly non-linear due to enhanced compressibility effects. Corresponding to a seal clearance of 40 μm, the inlet losses are larger in magnitude and the static pressure drop across the seal face is smaller, as compared to the other seal clearances. However, the enhanced non-linearity of the static pressure drop near the exit of the seal due to high Mach number effects raises the static pressure level along the second half of the seal. The net consequence is an enhanced axial force (which is approximately proportional to the area under the static pressure distribution) which increases corresponding to an increase in seal clearances, thus culminating in a negative axial stiffness.

Furthermore, there is a second undesirable effect arising from compressibility. For excessively large clearances and static pressure ratios, the Mach number at the seal exit becomes sufficiently large, so that the flow through the seal chokes. When this occurs, the static pressure along the seal exit no longer corresponds to the back pressure (which equals the ambient atmospheric pressure in this case). The static pressure ratio along the inner seal radius (seal exit) becomes larger than unity. For example, corresponding to a seal clearance of 40 μm, the flow through the seal chokes and the normalized static pressure at the seal exit is 1.16 instead of unity. Although a rise in the static pressure along the seal exit further decreases the overall static pressure drop across the seal, the overall static pressure level along the face of the seal increases, which further enhances the negative stiffness arising from the effects of a choked flow.

In summary, the Lomakin seal effect may fail to contribute to a net positive stiffness for large seal clearances and pressure ratios when compressibility effects become dominant. First, an increase in Mach number increases the non-linearity of the static pressure distribution near the seal exit and increases the overall static pressure level along the seal face as the seal clearance increases. Second, when the flow through the seal chokes, the static pressure along the seal exit increases above the ambient pressure and increases the overall pressure level along the seal. The key point to note is that the

Lomakin seal effect is strictly only valid when the overall pressure drop (due to both the inlet loss and the hydraulic loss across the seal face) is kept constant. This condition no longer holds when the flow through the seal chokes.

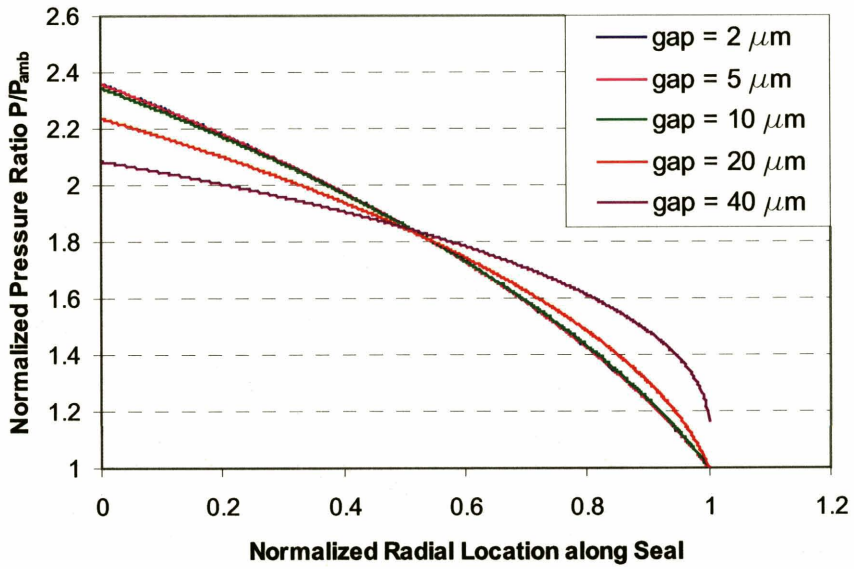

Figure 3-19: Radial variation of normalized static pressure along the seal.

It is also of interest to compare the mass flow requirements for Lomakin seal effect annular thrust bearings against their hydrostatic counterparts. Figure 3-20 shows the mass flow requirements for annular Lomakin effect seal thrust bearings corresponding to different seal pressure ratios and seal clearances. The mass flow requirements for annular hydrostatic thrust bearings are plotted in Figure 3-21 for different thrust bearing gaps. For low values of seal clearances, the mass flow requirements for Lomakin effect seal bearings are comparable to their hydrostatic counterpart. However, the axial stiffness due to Lomakin effect seal bearings is two orders of magnitude lower than that of hydrostatic annular thrust bearings, as mentioned previously. For low pressure ratios, larger axial stiffness values can be achieved for larger seal clearances (still orders of magnitude lower than hydrostatic bearings). However, for seal clearances greater than 10 μm, Lomakin effect seal bearings suffer from two major shortcomings. First, they consume significantly more mass flow than their hydrostatic counterparts. Furthermore, under conditions of high pressure ratios when compressibility

effects become dominant, they have the tendency to suffer from effects of static instability arising from a negative axial stiffness.

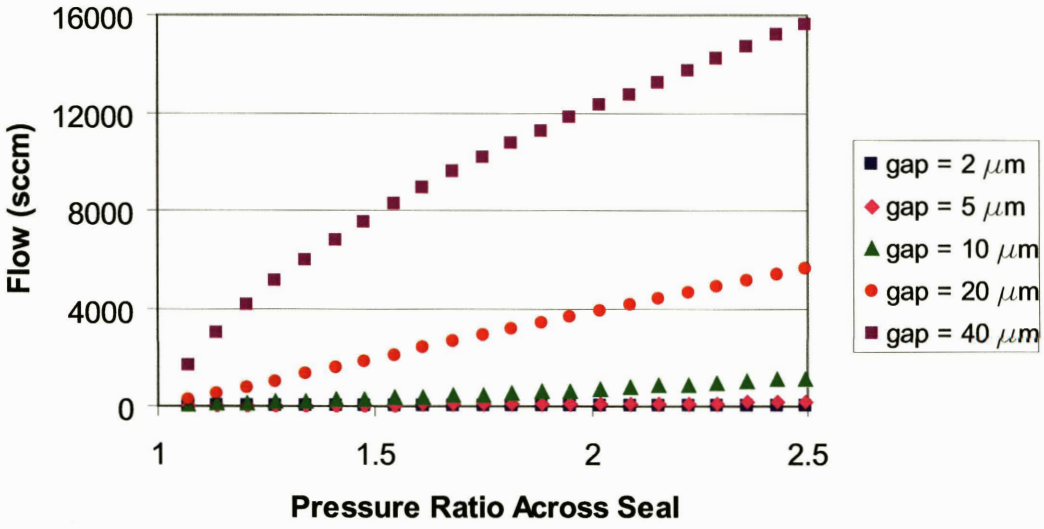

Figure 3-20: Mass flow requirements of Lomakin effect seal bearings plotted as a function of pressure ratio across the seal for various seal clearances.

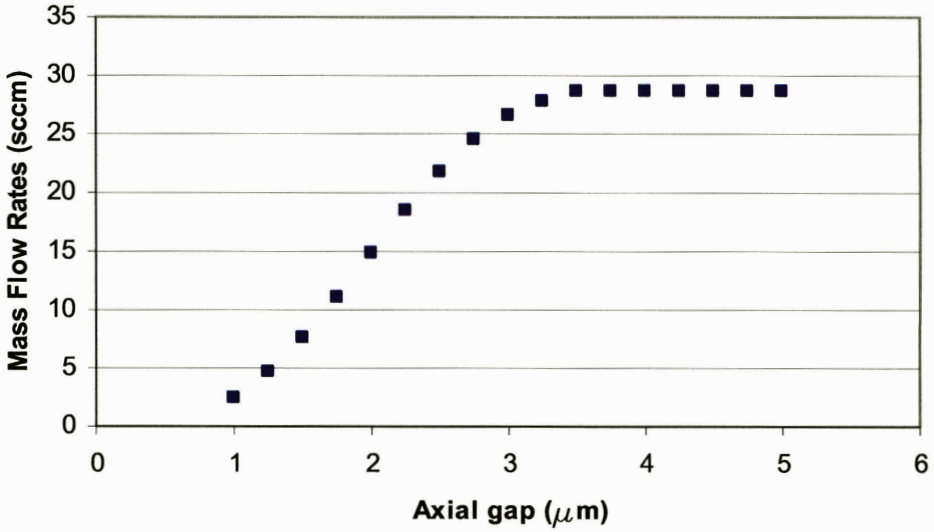

Figure 3-21: Mass flow requirements of hydrostatic annular thrust bearings for various thrust bearing gaps.

In conclusion, Lomakin effect seal thrust bearings are not suitable substitutes for hydrostatic thrust bearings in providing axial support and stiffness.

3.10 Summary and Conclusions

A Green's function approach has been employed to extend and generalize the simple analytical model presented in Chapter 2 for inherent-restrictor orifice hydrostatic thrust bearings for application to micro-turbomachinery. The hydrodynamic thrust bearing forces induced by the pumping action of the rotor rotation are determined by solving the Reynolds equation. The extended model serves as an effective tool to assess the thrust bearing tilting stiffness and the effects of geometric non-uniformities occurring in the micro-fabrication process. Other attributes and capabilities of the enhanced model include the prediction of the steady-state performance of thrust bearings with unconventional orifice arrangement, the investigation of coupling effects with the turbomachinery components in annular thrust bearings, and the quantification of the rotor tilting angles using experimentally measured thrust bearing mass flow rates. The Green's function formulation is also capable of assessing the torques and rotor tilting angles arising from geometric non-uniformities in orifice length and diameter. A wide range of micro-fabrication defects and anomalies such as the presence of unetched or missing orifices can be readily assessed. Effects of orifice taper can be dealt with by incorporating an influence-coefficient approach for modeling compressible, viscous internal flows through orifices with varying cross-sectional area.

The yaw and pitch dynamics of a rotor-thrust-bearing system with dynamic imbalance has been analyzed using a two degree-of-freedom rotordynamic model. The model is capable of evaluating the static rotor tilting angles and dynamic stability for different operating speeds and thrust bearing conditions.

For the various thrust bearing configurations investigated, the baseline configuration was found to be superior to the hexagonal configuration in terms of axial and tilting stiffness and mass flow consumption. Annular thrust bearings have the primary advantage of higher tilting stiffness, but they do not make as efficient use of the bearing land as the baseline configurations. Coupling effects between annular thrust bearings and the turbomachinery also have an adverse effect on the static performance of

the bearings. The generalized model is useful in evaluating the impact of micro-fabrication tolerances and manufacturing uncertainties on thrust bearing performance. The maximum allowable geometric non-uniformity in terms of thrust bearing clearance and orifice diameter and taper can be specified achieve the required thrust bearing performance. The maximum allowable dynamic imbalance for stable high speed operation has also been quantified.

In the final part of this chapter, an analytical model for evaluating the viscous, compressible flow through annular seals using the influence-coefficient based approach was presented. The model was employed to monitor the rotor axial position for avoiding physical contact between the rotor and stator as well as static instability in the MIT micro-turbopump. Finally, the feasibility of employing a Lomakin effect seal thrust bearing in substitution of a hydrostatic thrust bearing was investigated. Lomakin effect seal thrust bearings were found to be unsuitable for replacing hydrostatic thrust bearings in providing adequate axial support and stiffness.

CHAPTER 4

Modeling of Micro-Hydrostatic Journal Bearings for Micro-Turbomachines

In the previous two chapters, extensive analytical models have been developed to predict the performance and understand the underlying mechanisms responsible for static and dynamic instability in micro-hydrostatic gas thrust bearings. The rotors of the power-MEMS devices under development in the MIT microengine project are supported radially by micro-hydrostatic gas journal bearings. It is thus important to analyze the dynamic behavior of the rotor-journal bearing system. In this chapter, the effects of a non fully-developed circumferential flow in ultra-short hydrostatic journal bearings are investigated in detail. A simple analytical model which endeavors to capture the essential flow physics is first proposed and the results of the model are subsequently compared to CFD calculations. The implications pertaining to the non fully-developed circumferential flow are subsequently analyzed in the light of journal bearing whirl stability and power requirements.

4.1 Background of Original Journal Bearing Models Assuming Fully-Developed Circumferential Flows

The MIT microengine project utilizes hydrostatic journal bearings to provide radial support and stiffness for a rotor disk spinning at ultra high speeds. In the fluid dynamic models used to analyze these bearings, one important simplifying assumption often made is that the flows due to the hydrostatics and hydrodynamics are independent of each other, based on a low reduced frequency argument. It thus becomes possible to decouple the flow associated with hydrostatics from that due to hydrodynamics and analyze the two flow field components independently. In addition, both the axial and circumferential components of the flow through the journal are often assumed to be locally fully-developed. However, it is not trivial to invoke such an assumption for the low L/D hydrostatic journal bearing configurations employed in the MIT microengine project. The ultra short journal bearing configuration necessitates a correspondingly low axial flow-through time for a fluid particle, when a hydrostatic differential pressure is

applied axially across the journal bearing. In view of the short axial flow-through times, there is insufficient time for axial vorticity to diffuse radially outwards from the rotating surface. The circumferential flow thus fails to become fully-developed as assumed and this calls into question the validity and implications of such an assumption.

Two major implications that arise from the non fully-developed nature of the circumferential flow have to be addressed. First, the non fully-developed circumferential flow affects the magnitudes of the hydrodynamic forces and stiffness acting on the rotor. It is thus necessary to reassess the effects of a non fully-developed circumferential flow on journal bearing whirl stability, which depends strongly on the cross-coupled hydrodynamic stiffness. In addition, since the non fully-developed circumferential flow alters the wall shear stress and viscous drag acting on the rotor, effects on torque and journal bearing viscous dissipation have to be reassessed.

4.2 Review of Isotropic Gas Journal Bearing Whirl Stability Model

At this point, it is useful to review the stability theory for ultra-short hydrostatic journal bearings, previously proposed by Liu [3]. The radial imbalance of the rotor causes it to undergo a synchronous precession about its center of mass when it spins supercritically. This whirling motion drags the fluid circumferentially and sets up a Couette flow in the circumferential direction. The pressure field established by this flow induces a hydrodynamic force which acts orthogonally to the rotor displacement. Since this is a cross coupled force, journal bearing whirl instability can potentially arise. Assuming a fully-developed incompressible flow in the circumferential direction, the magnitude of the hydrodynamic force F^{hd} is given by

$$F^{hd} = \frac{\pi}{2}\mu\frac{RL^3}{C^2}\Omega\frac{\varepsilon}{\left(1-\varepsilon^2\right)^{1.5}} - 2\pi\mu\frac{R^2L}{C}\Omega\frac{1-\sqrt{1-\varepsilon^2}}{\varepsilon\sqrt{1-\varepsilon^2}}, \tag{4.1}$$

where the first term originates from the hydrodynamic pumping effect and the second term arises due to the viscous drag of the spinning rotor. In the limit of infinitesimally small radial eccentricities ε, the hydrodynamic stiffness K^{hd} is given by

$$K^{hd} = \pi\frac{\mu L(\Omega R)}{C}\left(\frac{L^2}{2C^2} - \frac{R}{C}\right). \tag{4.2}$$

The total hydrodynamic stiffness K^{hd} can also be split into a pure hydrodynamic pumping

component k^p and a pure viscous drag component due to rotor motion k^v, such that $K^{hd} = k^p - k^v$. The two components k^p and k^v act in opposite directions. The hydrodynamic force due to pumping acts in the direction of rotor rotation, thus having a tendency to induce a forward whirl, whereas the viscous drag component acts in opposition to the direction of rotor rotation and thus has a tendency to induce backward whirl. The whirl-ratio $\Re$, which is the ratio of the whirl instability speed Ω_W to the journal bearing natural frequency Ω_N, is given by

$$\Re = \frac{\Omega_W}{\Omega_N} = \frac{2}{1 - \dfrac{k^v}{k^p}} = \frac{2}{1 - W}, \tag{4.3}$$

where W is the whirl number given by [5]

$$W = \frac{k^v}{k^p} = \frac{1}{2}\left(\frac{L}{D}\right)^{-2}\left(\frac{C}{R}\right). \tag{4.4}$$

It can be seen that the whirl-ratio and hence the whirl instability speed goes to infinity when the whirl number W equals unity, or $C/R = 2(L/D)^2$. This implies that the hydrodynamic stiffness due to pumping balances the hydrodynamic stiffness due to viscous drag. Furthermore, it is worthy to note that the criterion for this singularity condition solely depends on the bearing geometry, and not on any kinematic nor dynamic quantities. In particular, the criterion for the singularity condition does not depend on the externally applied hydrostatic differential pressure DP nor the properties of the fluid.

4.3 Impulsive Startup of a Couette Flow

In view of the low L/D ratios and the correspondingly short flow-through times of the axial flow, the circumferential flow might not be fully-developed. In order to address this issue and its potential effects on journal bearing whirl stability and performance, accurate flow simulations will have to be performed. However, it is possible to gain physical insight by considering a simpler problem which resembles the nature of the issue at hand.

Consider the impulsive startup of a Couette flow between two infinite parallel plates. The problem setup is illustrated in Figure 4-1. The fluid is bounded by two rigid boundaries at $y = 0$ and $y = C$ and is initially at rest. The lower plate is suddenly brought to a steady velocity V in its own plane, with the upper plate held stationary. The velocity

distribution is governed by the equation

$$\frac{\partial u}{\partial t} = \nu \frac{\partial^2 u}{\partial y^2}, \tag{4.5}$$

with the boundary conditions

$$u(0,t) = V, \quad u(C,t) = 0 \quad \text{for } t > 0,$$

$$u(y,0) = 0 \quad \text{for} \quad 0 < y \le C.$$

The above problem admits an analytical Fourier series solution given by (see Batchelor [42], for example)

$$\frac{u(y,t)}{V} = \left(1 - \frac{y}{C}\right) - \frac{2}{\pi}\sum_{n=1}^{\infty}\frac{1}{n}\exp\left(-n^2\pi^2\frac{\nu t}{C^2}\right)\sin\frac{n\pi y}{C}. \tag{4.6}$$

The flow is unsteady and the vorticity due to the moving wall takes a finite time to diffuse across the channel.

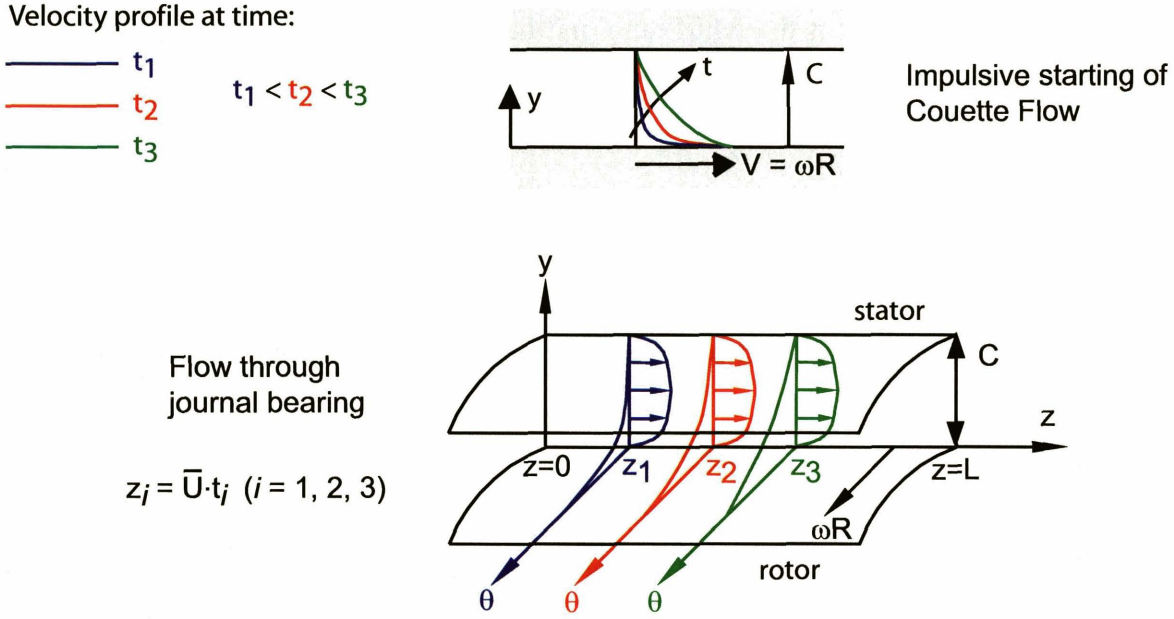

Figure 4-1: The top figure illustrates the transient fluid flow problem pertaining to the impulsive startup of a Couette flow. The transient flow is applied to elucidate the essential physical mechanisms governing the evolution of the circumferential flow in the journal bearing.

Both the impulsive startup of the Couette flow and the evolution of the circumferential flow through the journal bearing share a common concept: in order for the Couette flow to develop, the vorticity from a moving surface has to diffuse outwards across a channel towards a stationary surface. In order to relate the two flows, the

physical time t for the impulsive startup of the Couette flow can be related to the average time taken for a fluid particle to reach an axial location z along the journal bearing

$$t = \frac{z}{\overline{U}}, \tag{4.7}$$

where $\overline{U}$ is the mean axial velocity of the flow through the bearing. The circumferential velocity profile across the bearing width at this axial location z then corresponds to the velocity profile of the impulsively started Couette flow at time instant t. This has been shown schematically in Figure 4-1. Substituting the transformation (4.7) into Equation (4.6), and setting $V = \omega R$, the circumferential velocity profile at an axial location z along the journal bearing is given by

$$\frac{u_\theta(y,t)}{\omega R} = \left(1 - \frac{y}{C}\right) - \frac{2}{\pi}\sum_{n=1}^{\infty}\frac{1}{n}\exp\left(-n^2\pi^2\frac{\nu z}{\overline{U}C^2}\right)\sin\frac{n\pi y}{C}. \tag{4.8}$$

Equation (4.8) can be expressed non-dimensionally as

$$\frac{u_\theta}{\omega R} = \Psi\left(\frac{y}{C}, \frac{z}{L}, \frac{\nu L}{\overline{U}C^2}\right). \tag{4.9}$$

From the above discussion and analysis, there are inherently two time scales that govern the evolution of the circumferential flow. The first time scale is the characteristic viscous diffusion time τ_d, which scales with the kinematic viscosity ν and the journal bearing clearance C in the following manner:

$$\tau_d \sim \frac{C^2}{\nu}. \tag{4.10}$$

The second time scale is the flow-through time of the axial hydrostatic flow τ_f, which scales according to

$$\tau_f \sim \frac{L}{\overline{U}}. \tag{4.11}$$

The dimensionless variable

$$\beta_{FD} = \frac{\tau_f}{\tau_d} = \frac{\nu L}{\overline{U}C^2} \tag{4.12}$$

can thus be interpreted as the ratio of the flow-through time to the characteristic viscous diffusion time. Equation (4.8) also reveals that two different journal bearings with different widths C and lengths L are anticipated to have the same normalized

circumferential flow profile if they have the same values of β_{FD}. For values of $\beta_{FD} >> 1$, the axial flow-through time is significantly longer than the viscous diffusion time. The axial vorticity from the moving wall has sufficient time to diffuse radially across the journal bearing clearance, and the circumferential flow can be assumed to be fully-developed over a significant length of the journal bearing. On the contrary, if $\beta_{FD} << 1$, the viscous diffusion time is significantly longer than the axial flow-through time. The axial vorticity of the moving wall does not have sufficient time to diffuse radially outwards across the journal bearing clearance before the axial flow leaves the journal bearing. In this case, it is physically invalid to assume that the circumferential flow becomes fully-developed.

4.4 Evaluation of Circumferential Flow Field in Ultra-Short Gas Journal Bearings

In order to gain a deeper appreciation for the flow field through the journal bearing, CFD calculations were performed for the baseline case of a rotor which was radially centered. The absence of a rotor radial eccentricity permitted the flow to be modeled as an axisymmetric rather than a full 3-D problem, thus resulting in substantial savings in terms of computational resources and time. The CFD calculations were performed using Fluent, a commercial CFD software package which utilizes the finite-volume method to solve the governing equations for a fluid. Figure 4-2 and 4-3 show contour plots for the normalized axial and circumferential velocity components of the flow through a journal bearing of width 14 μm when an axial hydrostatic differential pressure of 5 psi is applied across the bearing with the rotor spinning at 850 000 rpm. The axial velocity has been normalized using the speed of sound, and has thus been plotted in terms of the Axial Mach number M_z in Figure 4-2. The figure shows that the axial flow through the bearing becomes fully-developed very quickly. For axial locations (normalized using the journal bearing clearance) of $z/h > 2$, the axial velocity profile becomes independent of axial location almost over the entire length of the bearing.

The circumferential velocity has been normalized using the tip speed of the rotor ωR on Figure 4-3. In contrast to the axial flow, the circumferential velocity depicted in Figure 4-3 shows significant axial variations along the length of the bearing, thus alluding to the non fully-developed nature of the circumferential flow. To further elucidate the

evolution of the circumferential flow as the hydrostatic fluid flows through the journal, the circumferential velocity is plotted non-dimensionally as a function of the normalized radial location across the width of the journal bearing in Figure 4-4. The circumferential velocity has been normalized using the rotor tip speed, and the radial distance is normalized using the journal bearing width. Each curve on the plot corresponds to a different axial location along the bearing. The normalized circumferential velocities for each curve are bound by an upper limit of unity corresponding to the surface velocity of the rotor, and a lower limit of zero corresponds to the no-slip boundary condition on the stator. If the circumferential flow is assumed to be fully-developed, the circumferential velocity varies linearly across the journal bearing clearance. However, it is evident that the curves shown in Figure 4-3 show a departure from a linear circumferential velocity profile, even near the exit of the journal bearing, indicating that the flow is not fully-developed at the exit of the journal bearing passage.

As can be seen from Figure 4-2, the axial hydrostatic flow entering the journal bearing has negligible gradients in circumferential velocity and hence axial vorticity, and the diffusion of axial vorticity occurs radially outwards from the moving wall, as the flow evolves along the length of the bearing. This diffusion process is governed by the kinematic viscosity and flow-through time of the fluid. As Figure 4-3 shows, the axial vorticity (which is equal to the magnitude of the local circumferential velocity gradient) is concentrated in the vicinity of the moving wall near the inlet of the journal bearing. The axial vorticity slowly diffuses outwards as the flow evolves along the length of the bearing, thus tending to drive the circumferential velocity profile asymptotically towards a linear one, where the axial vorticity is uniformly distributed across the bearing clearance. However, in view of the excessively short flow-through times of the hydrostatic fluid, the diffusion process does not go into completion and the circumferential velocity profile fails to be linear, even at the exit of the journal bearing.

Also plotted on Figure 4-4 are analytical results for the circumferential velocity distribution plotted non-dimensionally at different journal bearing axial locations, using Equation (4.8). Close agreement exists between the analytical results and the CFD calculations. This attests to the fact that the evolution of the non fully-developed circumferential flow is well captured by the analogous flow corresponding to the impulsive startup of a Couette flow. This is perhaps not surprising, in view of the fact that

the physical mechanisms responsible for the flow phenomena in both problems are similar, as described previously.

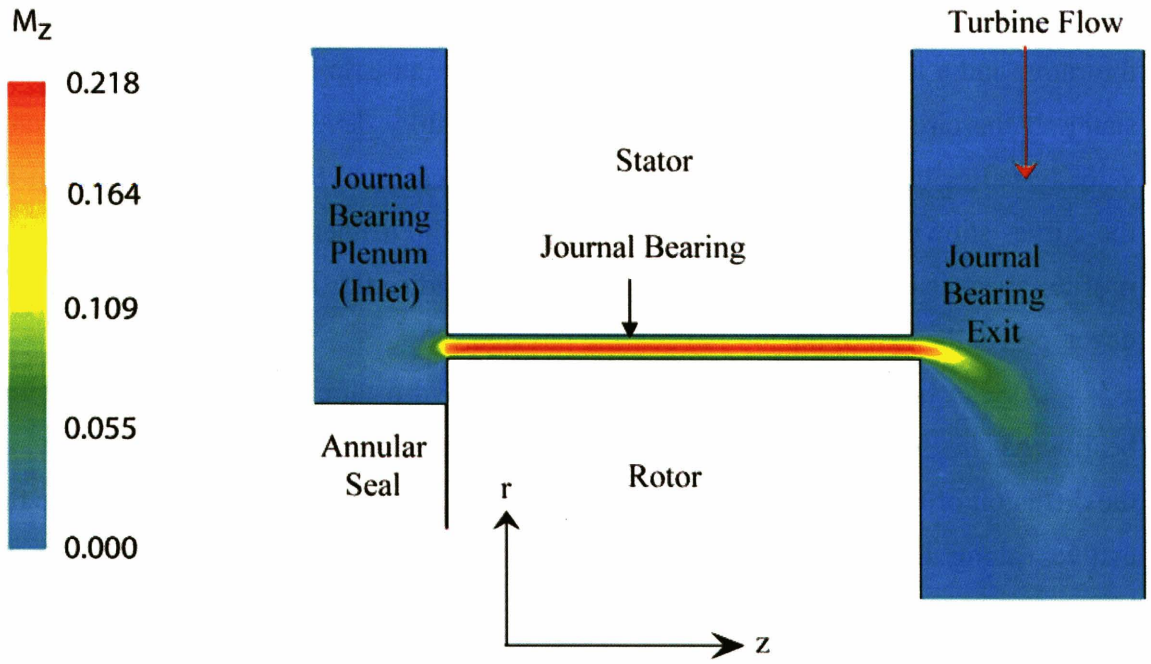

Figure 4-2: Contour plots for the axial Mach number of the flow through a journal bearing of width 14 μm when an axial hydrostatic differential pressure of 5 psi is applied across the bearing with the rotor spinning at 850 000 rpm.

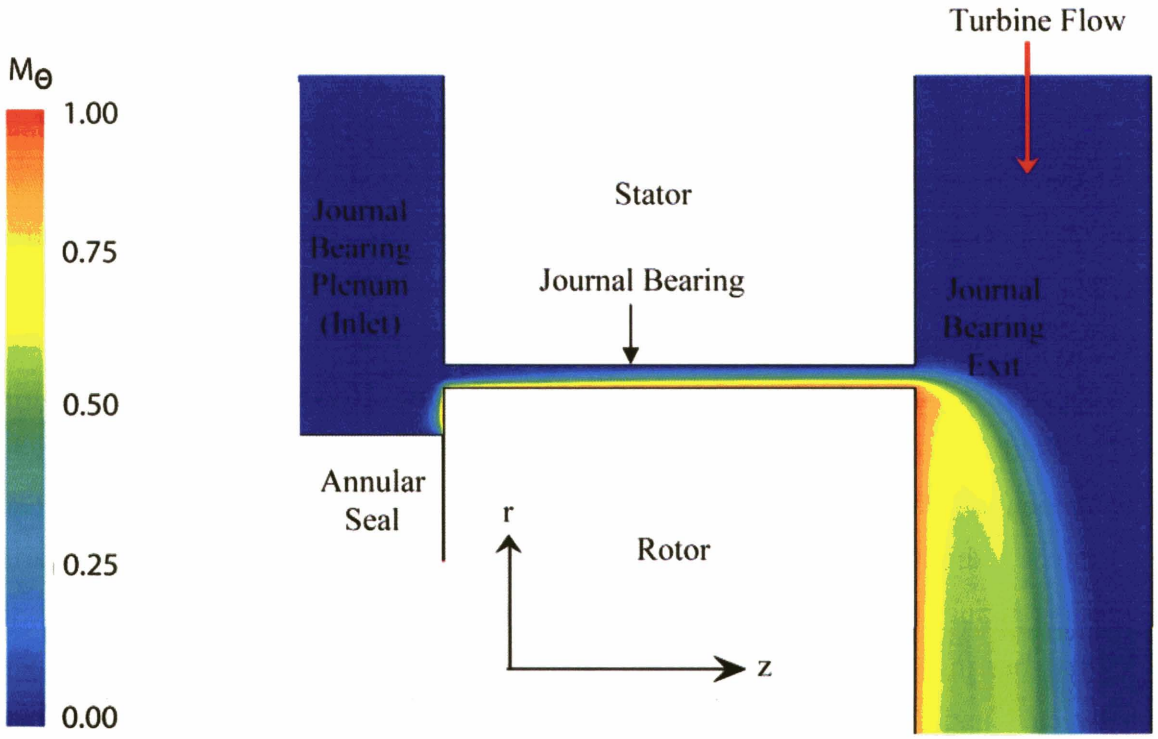

Figure 4-3: Contour plots for the normalized circumferential velocity component of the flow through a journal bearing of width 14 μm when an axial hydrostatic differential pressure of 5 psi is applied across the bearing with the rotor spinning at 850 000 rpm.

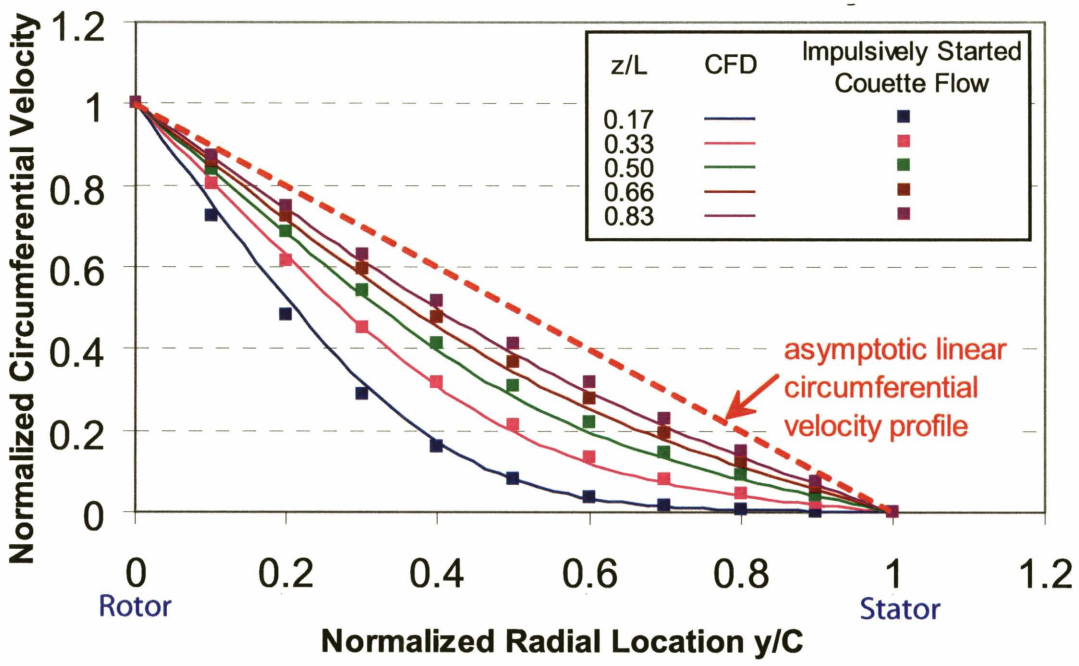

Figure 4-4: Comparison of normalized circumferential velocity profile obtained using analytical model and CFD.

4.3 Effects of Non Fully-Developed Circumferential Flow on Journal Bearing Whirl Stability

Previous expressions obtained by Liu [3] for the hydrodynamic force and stiffness assume the existence of a fully-developed circumferential flow. Since details of the kinematic flow field significantly influence the magnitudes of the hydrodynamic forces acting on the rotor, it is thus necessary to perform CFD calculations to accurately determine the values of the hydrodynamic stiffness for small radial eccentricities in the presence of a non fully-developed circumferential flow. However, the journal bearing flow field is no longer axisymmetric when the rotor is subjected to a small radial eccentricity. Hence, a full 3-D CFD calculation has to be performed to extract the required hydrodynamic forces. The calculations were performed for journal bearing widths ranging between 10 μm and 24 μm for a 2.1 mm radius rotor. The length of the journal bearing was fixed at 330 μm, and hydrostatic differential pressures ranging between 1 and 8 psi were applied axially across the journal bearing. The flow domain within the journal bearing was represented using a structured grid with 331 grid points in the axial direction, 360 grid points in the circumferential direction and 21 grid points in the radial direction (across the bearing gap), thus yielding a computational grid with more than 2 million grid points. Dirichlet boundary conditions were imposed for the static pressure at the inlet and exit of the journal bearing, and the flow was assumed to be incompressible (in view of the low axial Mach numbers $M_z < 0.3$). The rotor was subjected to a normalized radial perturbation (or radial eccentricity) of 0.1, and the viscous pumping and viscous drag components of the hydrodynamic forces acting on the spinning rotor were extracted from the converged CFD solution. The hydrodynamic stiffness components due to viscous pumping k^p and viscous drag k^v can thus be evaluated and the whirl-ratio R, which expresses the ratio of the whirl instability speed Ω_W to the journal bearing natural frequency Ω_N, can be obtained from Equation (4.3).

Although CFD is an invaluable tool to investigate fluid dynamic phenomena which are pertinent to the flow through these ultra-short journal bearings under investigation, it is computationally intensive and time consuming to perform a new set of CFD calculations whenever any changes are made to the journal bearing or rotor geometry. From a design perspective, and also from a fundamental understanding point of view, it is of great value to consolidate all the available CFD results and investigate the

possibility of collapsing the CFD data by invoking physical-based scaling arguments. In this regard, the impulsive startup of a Couette flow considered previously offers insight pertaining to the appropriate methodology for scaling the available CFD data. As mentioned previously (and referring to Equations (4.8) and (4.9)), the normalized circumferential velocity profile in the channel is given by the sum of a steady-state fully-developed term and a transient term. The key dimensionless term which governs the evolution of the circumferential flow is $\beta_{FD} = \nu L/\left(\overline{U}C^2\right)$, which can be interpreted as the ratio of the flow-through time of the axial hydrostatic flow to the characteristic viscous diffusion time. It should be noted that $\overline{U}$ depends on the hydrostatic differential pressure DP and the bearing geometry, and can be readily determined from an analytical hydrostatic flow model.

Thus all the available CFD data for the whirl-ratio R is plotted as a function of β_{FD}, as shown in Figure (4-5). It can be seen that β_{FD} serves as an effective parameter in collapsing the available CFD data pertaining to the whirl-ratio. In particular, the newly identified dimensionless parameter β_{FD} collapses all the various combinations for journal bearing width and hydrostatic differential pressure DP which yield singular whirl-ratio behavior. This is given by

$$\beta^*_{FD} = \left(\frac{\nu L}{\overline{U}C^2}\right)^* \approx 0.43. \qquad (4.13)$$

In other words, singular whirl-ratio behavior occurs when the flow-through time for the axial hydrostatic flow is approximately half of the characteristic viscous diffusion time.

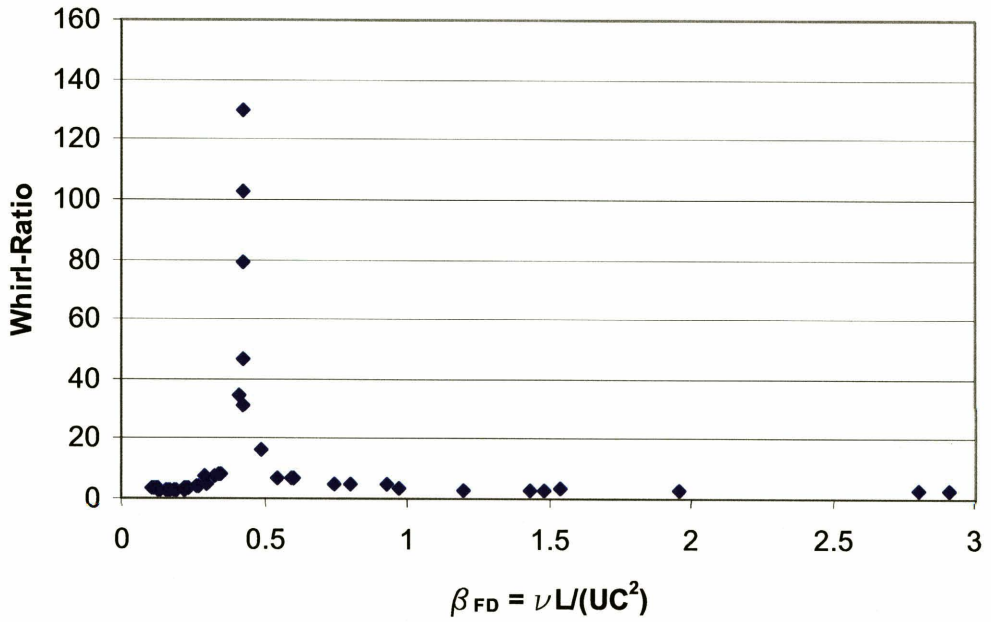

Figure 4-5: Plot of whirl-ratios as a function of β_{FD}.

The results are in agreement with the trends obtained by Liu [3], but show differences in the quantitative magnitudes of the cross-coupled hydrodynamic stiffness k^p and k^v. This indicates that the singular analytical model by Liu yields qualitatively correct results for analyzing singular whirl-ratio behavior in ultra-short gas journal bearings. The whirl-ratio becomes singular when the hydrodynamic stiffness due to viscous pumping k^p balances the hydrodynamic stiffness due to viscous drag k^v. To accurately account for the effects of a non fully-developed circumferential flow on k^p and k^v, a higher level of fluid dynamic simulations has to be performed.

Next, the effects of journal bearing clearance on journal bearing whirl stability for fixed values of hydrostatic differential pressure DP are investigated, relaxing the assumption that the circumferential flow is fully-developed.

Figure 4-6 shows values of k^p and k^v plotted against the journal bearing width for a 2.1 mm radius rotor. The journal bearing length was fixed at 330 μm and a hydrostatic differential pressure, DP, of 1 psi was applied across the bearing. Two sets of data are plotted on Figure 4-6. One set corresponds to the values of k^p and k^v obtained from the original isotropic journal bearing model of Liu [3] (hereafter called the fully-developed flow model), where the circumferential flow was assumed to be fully-developed. The second set of data was obtained from CFD calculations. The two curves corresponding to the fully-developed flow model intersect at a journal bearing clearance of 26 μm, thus

implying that the k^p matches k^v, and the net hydrodynamic stiffness is zero. This corresponds to a unity whirl number W, an infinite whirl-ratio R and an infinite whirl instability speed. The journal bearing width of 26 μm at this singularity point can also be obtained simply from the geometric criterion $C/R = 2(L/D)^2$. For bearing widths less than 26 μm, k^p exceeds k^v, the whirl-ratio R is positive and the net hydrodynamic force acts in the same direction as the rotor rotation and thus induces a forward whirl. On the other hand, for bearing widths greater than 26 μm, k^v exceeds k^p, the whirl-ratio R is negative and the net hydrodynamic force acts in a direction opposing the rotor rotation and thus induces a backward whirl. The values of k^p and k^v obtained from the CFD calculations are also plotted on Figure 4-6 as a function of the journal bearing width for a hydrostatic differential pressure of 1 psi. In contrast to the fully-developed flow model, the two curves are observed to intersect at a significantly smaller journal bearing clearance of 20 μm, which implies infinite whirl-ratio R and whirl instability speed. It is thus evident that the non fully-developed nature of the circumferential flow has a significant impact on the hydrodynamic forces and hence the values of k^p and k^v. One direct and immediate consequence is the shift in location of the journal bearing width corresponding to infinite instability speed.

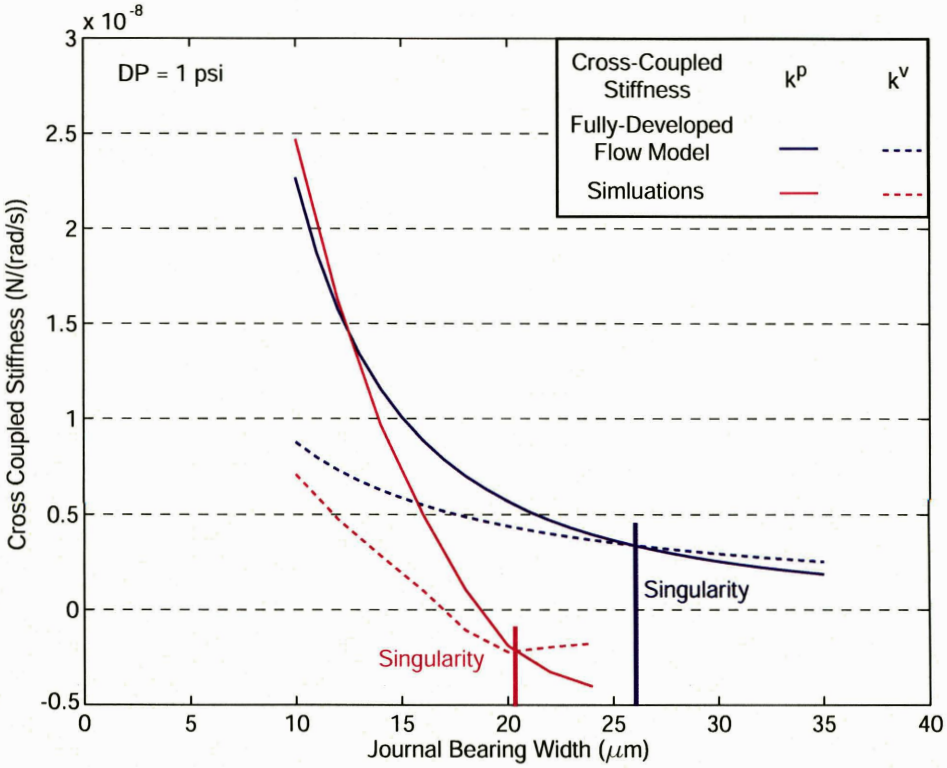

Figure 4-6: Values of k^p and k^v obtained using the fully-developed flow model and CFD for different journal bearing widths corresponding to a hydrostatic differential pressure of 1 psi.

Plotted on Figure 4-7 are the values of the viscous drag component of the hydrodynamic stiffness k^v for different journal bearing widths corresponding to a hydrostatic differential pressure of 1 psi. Two sets of data are plotted. One set corresponds to the fully-developed model, whereas the other set was obtained from CFD calculations. According to the fully-developed flow model, the viscous drag component of the hydrodynamic stiffness always tends to induce a backward whirl, and thus the sign of k^v does not change over the entire range of journal bearing widths investigated.

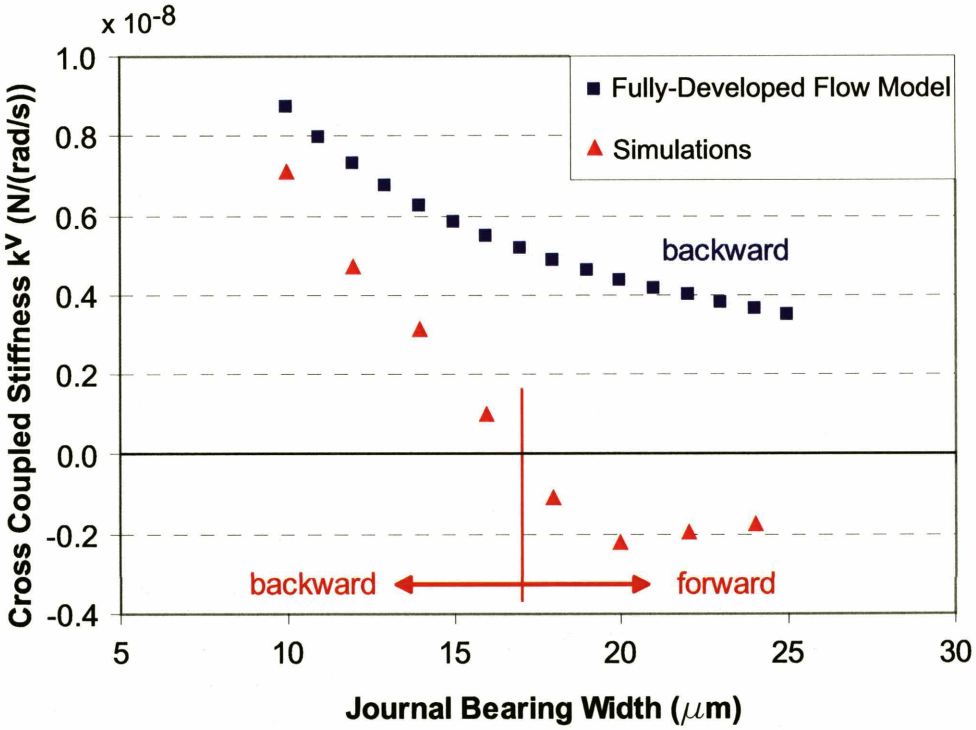

Figure 4-7: Hydrodynamic cross-coupled stiffness due to viscous drag k^v for various journal bearing widths. The rotor radius was 2.1 mm, the journal bearing length was 330 μm and a hydrostatic differential pressure of 1 psi was applied across the bearing.

In contrast, the CFD data shows that k^v does in fact change signs, and this occurs at a journal bearing width of approximately 17 μm. This implies that for small journal bearing clearances, the viscous drag component of the hydrodynamic force tends to induce a backward whirl, whereas for larger journal bearing clearances, it tends to induce a forward whirl. This might seem a little counter-intuitive at first, since the viscous drag opposes the motion of the rotor and is thus naturally anticipated to give rise solely to a backward whirl. A physical explanation why the viscous drag component is able to induce a forward whirl can be given as follows. Consider the rotor subjected to a small radial perturbation about its equilibrium position. Corresponding to regions where the journal bearing clearance has increased, one would expect that a decrease in viscous shear stress, in view of the larger clearances. However, the shorter flow-through time of the hydrostatic flow (due to higher volumetric flow rates and hence axial velocities) and the larger clearance implies that the circumferential flow becomes even less fully-developed over the entire length of the bearing in these regions. The greater departure from a fully-developed flow thus increases the magnitude of the circumferential wall

shear stress (as compared to the baseline configuration). There is thus an increase in circumferential wall shear stress corresponding to regions of large journal bearing clearance and a corresponding decrease along regions where the clearance has decreased. The above trends are qualitatively different from what the fully-developed flow model predicts. The net consequence is therefore a forward whirl inducing component arising solely from the viscous drag.

Figure 4-8 shows values of the hydrodynamic pumping component of the hydrodynamic stiffness k^p plotted against the journal bearing width for a 2.1 mm radius rotor. The journal bearing length was fixed at 330 μm and a hydrostatic differential pressure of 1 psi was applied across the bearing. Once again, two sets of data have been plotted on Figure 4-8. One set corresponds to the values of k^p obtained from the fully-developed isotropic journal bearing model. The second set of data was obtained from CFD calculations. Several interesting observations can be made from Figure 4-8. According to the fully-developed flow model, the hydrodynamic force due to pumping always tends to induce a forward whirl, and thus the sign of k^p remains invariant regardless of the journal bearing width. In contrast, the CFD data shows that k^p does in fact switch sign, and this occurs at a journal bearing width of approximately 19 μm. This implies that for small journal bearing clearances, the hydrodynamic pumping effect tends to induce a forward whirl, whereas for larger journal bearing clearances, it tends to induce a backward whirl.

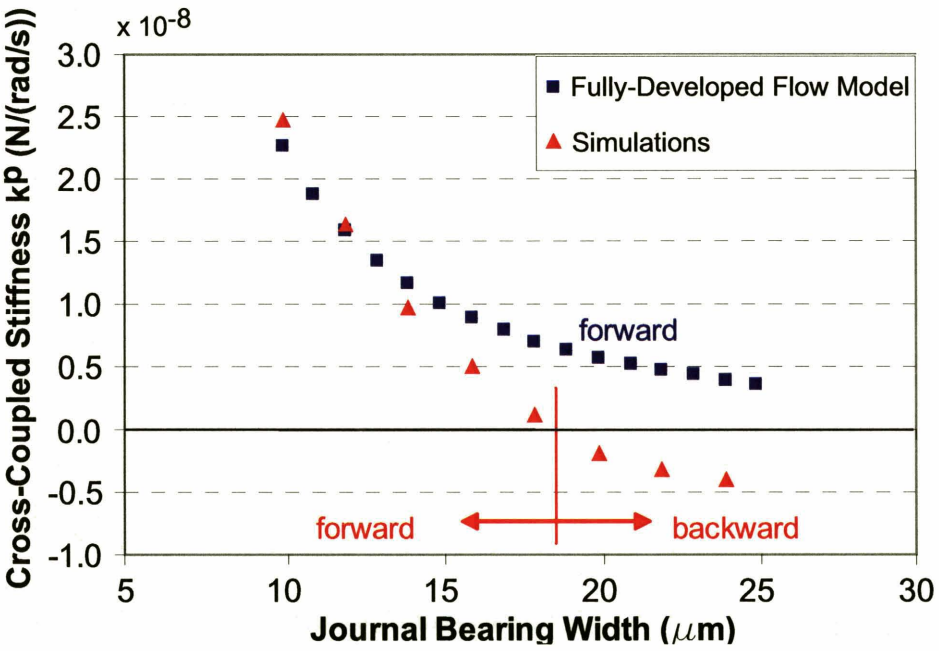

Figure 4-8: Hydrodynamic cross-coupled stiffness due to viscous pumping k^p for various journal bearing widths. The rotor radius was 2.1 mm, the journal bearing length was 330 μm and a hydrostatic differential pressure of 1 psi was applied across the bearing.

Recall that the fully-developed flow model predicts that for a fixed rotor radius and journal bearing length, the journal bearing width that yields infinite whirl-ratios is determined solely by the geometric criterion $C/R = 2(L/D)^2$, and is independent of the hydrostatic differential pressure DP. One issue yet to be reconciled is whether this holds true for a non fully-developed circumferential flow. Figure 4-9 shows the CFD results for k^p and k^v plotted as functions of the journal bearing width corresponding to hydrostatic differential pressures of 2 psi, 3 psi, 4 psi and 5 psi, respectively. The rotor radius was fixed at 2.1 mm and the journal bearing length was held constant at 330 μm. From these figures, it is evident that corresponding to each journal bearing differential pressure DP and in the presence of a non fully-developed circumferential flow, there still exists a journal bearing width for which singular whirl-ratios occur. However, for a fixed rotor radius and bearing length, the bearing width for which such singular behavior occurs varies strongly with DP, which is qualitatively different from what the fully-developed flow model predicts.

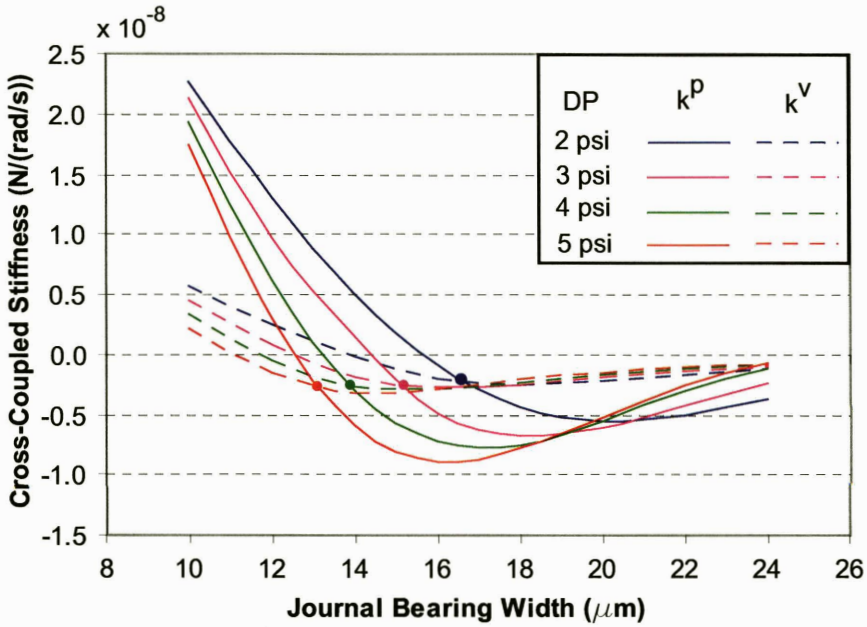

Figure 4-9: Values of k^p and k^v obtained using CFD for different journal bearing widths corresponding to a hydrostatic differential pressures of 2 psi, 3 psi, 4 psi and 5 psi.

The crucial fluid dynamic mechanism left out in the fully-developed model is the diffusion of axial vorticity from the moving or spinning wall of the rotor across the journal bearing gap. The rate at which axial vorticity diffuses outwards towards the stationary journal bearing sidewall is in turn related to the flow-through time of the axial hydrostatic flow, which thus depends on the hydrostatic differential pressure DP. The journal bearing width corresponding to singular behavior thus depends strongly on DP. According to Figure 4-9, an increase in the value of DP corresponds to a decrease in the journal bearing width at which singular behavior occurs. The journal bearing clearance at which infinite whirl-ratio occurs decreases from approximately 20 μm for a DP of 1 psi, to approximately 13 μm corresponding to a DP of 5 psi. Furthermore, from Figure 4-9, it is apparent that in addition to the intersection between k^p and k^v at approximately 13 μm, a second intersection between k^p and k^v occurs at a larger journal bearing width of 24 μm.

From the point of view of actual journal bearing operation, it is useful to determine how the whirl instability rotor speed or stability boundary varies with the hydrostatic differential pressure DP for a given journal bearing geometry and rotor radius. Figure 4-10 presents the isotropic journal bearing stability boundary plotted as a function of DP for 4 different journal bearing clearances of 14 μm, 16 μm, 18 μm and 20

μm, respectively. The journal bearing length is fixed at 330 μm, and the rotor radius is held constant at 2.1 mm. These dimensions are chosen, as they correspond to the geometric dimensions of the rotor and journal bearing in the redesigned microbearing test device. The experimental results for the redesigned microbearing test device are discussed in detail later in Chapter 8. Referring to Figure 4-10, corresponding to an increase in journal bearing clearance, there is a decrease in the value of DP at which the whirl-ratio becomes singular. The stability boundary goes to infinity at a DP of 4 psi for a 14 μm wide journal bearing, whereas the same singular behavior occurs at a significantly lower DP of 1 psi for a 20 μm wide bearing.

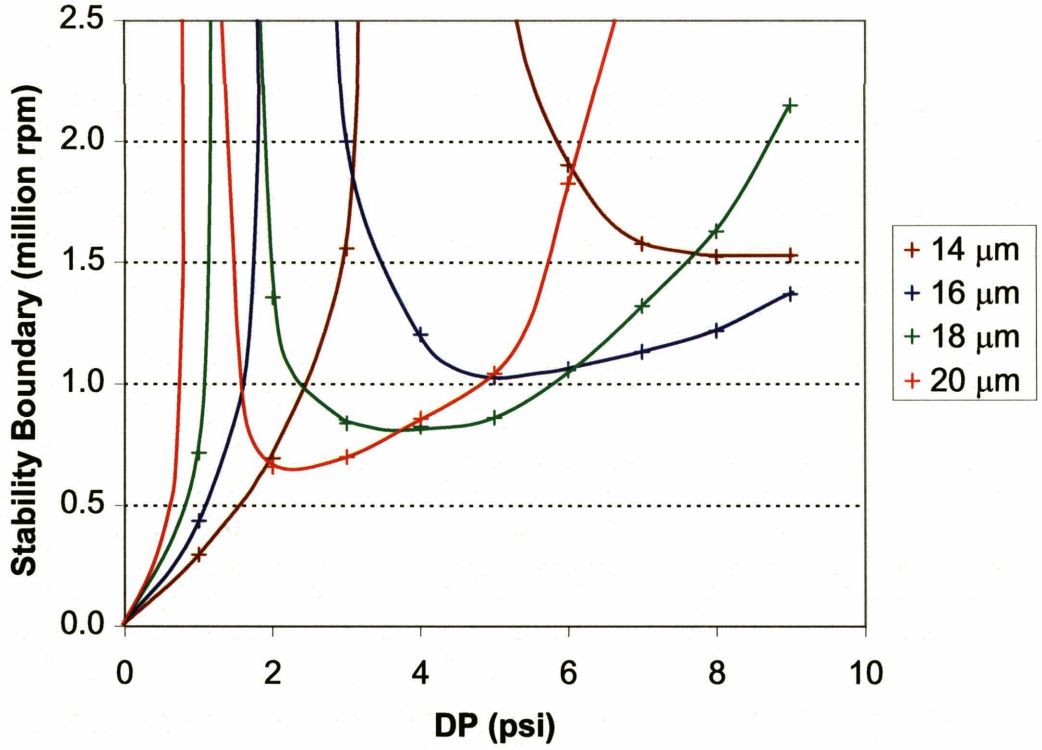

Figure 4-10: Stability boundary for journal bearing of four different widths for different values of hydrostatic differential pressure DP.

4.4 Effects of Non Fully-Developed Circumferential Flow on Journal Bearing Torque and Power Requirements

One of the dominant sources of power dissipation in the MIT microengine arises from the viscous losses due to the journal bearing. Since the journal bearing is located at

the outer periphery of the rotor disk, the large circumferential velocities on the order of 500 m/s, coupled with the small clearances of the journal bearing (typically on the order of 15 μm) both contribute directly to the large viscous stresses and hence the viscous dissipation losses. Considerations of power dissipation are vital for the microengine, since the net power output available from a closed Brayton cycle operating on the micro-scale is of the same order of magnitude as the power consumed by the journal bearing.

As shown previously in Figure 4-4, due to the non fully-developed nature of the circumferential flow, the circumferential velocity gradient immediately adjacent to the rotating wall is higher than that corresponding to a fully-developed linear circumferential velocity profile. Since the magnitude of the wall shear stress scales linearly with the circumferential velocity gradient at the wall and hence the torque and power required for overcoming the viscous dissipative losses, the actual power consumed by the journal bearing is expected to be greater than that obtained when a fully-developed circumferential flow assumption is invoked.

The Fourier series expression for the local rotor wall shear stress at any axial location z along the journal bearing can be obtained from Equation (4.8) by differentiation:

$$\tau = \frac{\mu\omega R}{C}\left(1+2\sum_{n=1}^{\infty}\exp\left(-\frac{n^2\pi^2\nu z}{\bar{U}C^2}\right)\right). \tag{4.14}$$

Figure 4-11 depicts the rotor wall shear stress plotted as a function of the journal bearing axial location for the above-mentioned rotor and bearing geometry and rotational speed. The wall shear stress has been normalized using the reference wall shear stress $\tau_{normalized} = \frac{\mu\omega R}{C}$, which corresponds to the wall shear stress for a locally fully-developed flow. From Figure 4-11, it is evident that the local wall shear stress is higher than the reference value along the entire length of the bearing. The local wall shear stress rises monotonically and precipitously towards the entrance of the journal bearing. The non fully-developed flow in the immediate vicinity of the journal bearing entrance thus contributes significantly to the viscous drag, and hence the torque and power consumption. The actual required torque and power consumption due to viscous losses in the journal bearing are plotted as functions of the rotational speed in Figures 4-12 and 4-13, respectively. Also shown on both graphs are the torque and power requirements

corresponding to a fully-developed flow assumption, which assumes a linearly varying circumferential velocity profile at every axial location. Corresponding to a fixed rotational speed, the actual torque and viscous dissipation in the journal bearing are approximately double the values which would be obtained by invoking a fully-developed flow assumption. As mentioned previously, the journal bearing power consumption constitutes one of the major sources of losses in the microengine. The non fully-developed nature of the circumferential flow has to be taken into account in order to gain a more accurate depiction of the torque and power requirements of the journal bearing. Since the simple analytical model of the impulsively started Couette flow has been demonstrated to be capable of capturing the salient features of the non fully-developed circumferential flow (as shown in Figure 4-4), it can thus be used in lieu of resource-intensive CFD calculations to obtain realistic estimates for the torque and power requirements of the journal bearing.

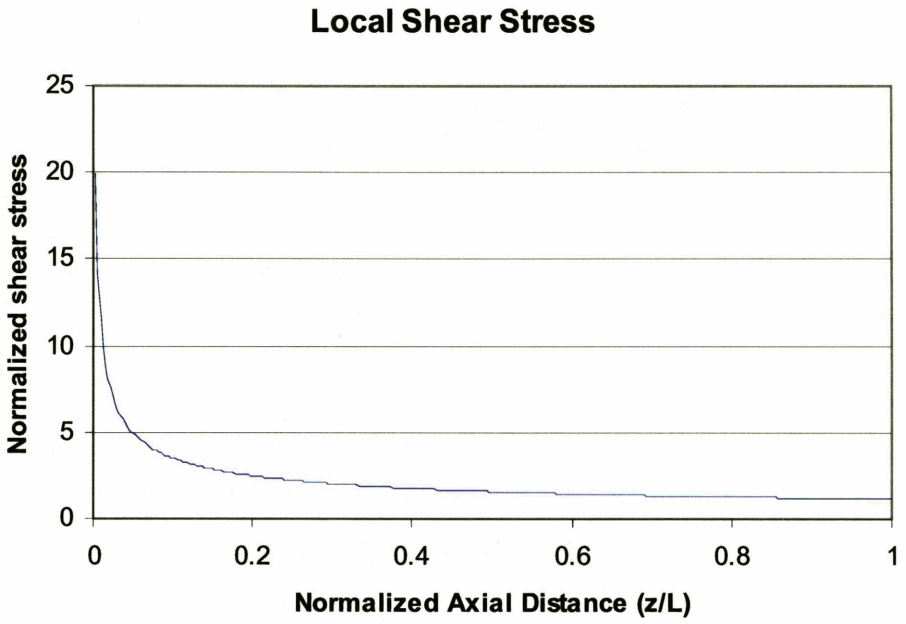

Figure 4-11: Normalized local circumferential wall shear stress along the length of the journal bearing.

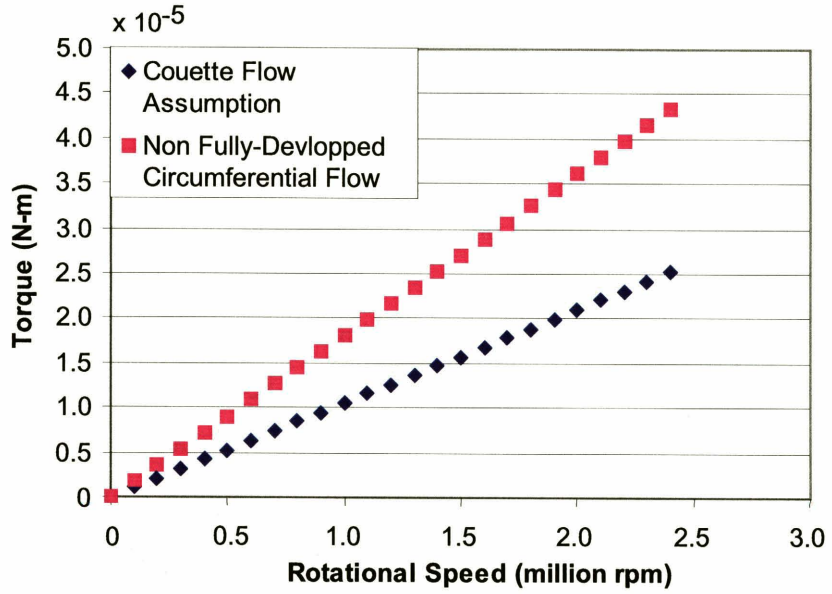

Figure 4-12: Comparison of torque requirements obtained using fully-developed and non fully-developed analytical flow models.

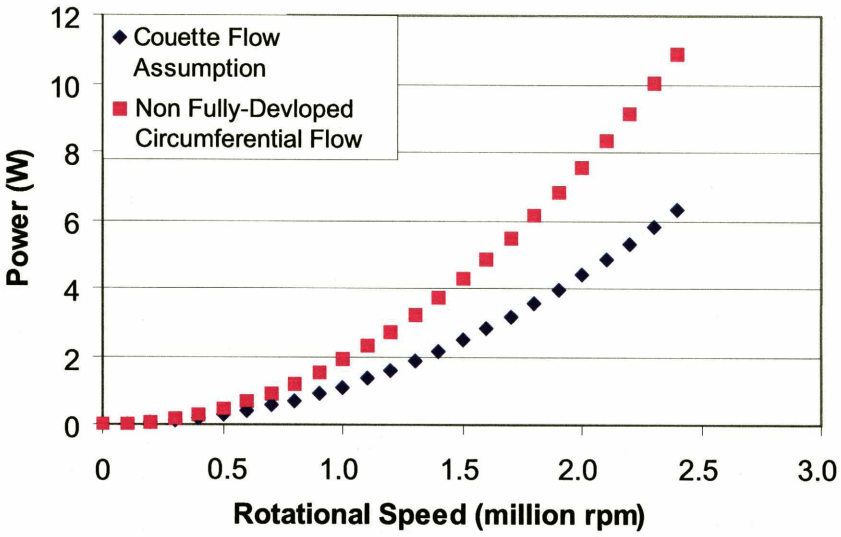

Figure 4-13: Comparison of power requirements obtained using fully-developed and non fully-developed analytical flow models.

4.5 Summary and Conclusions

In this chapter, the development of the circumferential flow in ultra short (low *L/D*) micro-hydrostatic journal bearings was investigated. The impulsive startup of a

Couette flow was employed to elucidate the essential fluid dynamic mechanisms responsible for the evolution of the non fully-developed circumferential flow. A dimensionless parameter $\beta_{FD} = \nu L / \left(\overline{U} C^2\right)$, which characterizes the ratio of the flow-through time of the axial hydrostatic flow to the viscous diffusion time, was identified to govern the evolution of the circumferential flow field. In particular, there was good agreement between CFD calculations and the predicted circumferential flow field. Journal bearing whirl stability was reassessed using CFD, and the dimensionless parameter β_{FD} was found to be capable of collapsing all the available CFD data for the whirl-ratio. Singular whirl-ratio behavior was found to occur when the flow-through time of the axial hydrostatic flow was approximately half of the characteristic viscous diffusion time. The criterion for the singular whirl-ratio behavior depends on the hydrostatic axial differential pressure DP and the fluid properties. This is in contrast to the fully-developed circumferential flow model, where the criterion for singular whirl behavior depends solely on bearing geometry. Finally, the increase in journal bearing torque and viscous power dissipation due to a non fully-developed circumferential flow have been quantified.

CHAPTER 5

Analysis and Redesign of High-Speed and High Whirl-Ratio Gas Bearings for MEMS Devices

This chapter focuses on the research efforts targeted towards the redesign of a microbearing test device for demonstrating repeatable high speed and high whirl ratio microbearing operation. In the first part of this chapter, major lessons acquired from the microfabrication and testing of previous microbearing test device builds are presented and discussed. Building upon the foundation of these major lessons learnt and the new insight gained on microfabrication, rotordynamics and structural integrity issues, the analysis and design of a new microbearing test device which aims to improve the original design are presented in the second portion of this chapter.

5.1 Lessons Learnt from Previous Builds

In this section, the major lessons acquired from previous builds of microbearing rigs are summarized. These lessons are discussed in the context of three different issues that play vital roles in the overall system performance of a microbearing test device, and they include microfabriation-related issues, rotordynamic issues and structural issues. These lessons learnt and the insight gained shed light on the essential issues that have to be addressed in the redesign of the original microbearing test device.

5.1.1 Microfabrication Issues

Three different microfabrication-related issues are discussed in this section. They include the formation of a "fence" at the exit of the journal bearing, the presence of spikes along the journal bearing sidewalls and the use of drop-in rotors to replace a previous "snap-off tabs" rotor retention technology, which proved to be unreliable and gave rise to cleanliness issues.

5.1.1.1 "Fence" at Exit of Journal Bearing

In this subsection, the effects arising from the presence of a Silicon "fence" protruding into the main turbine flow passage at the exit of the journal bearing are discussed. Microfabrication solutions are subsequently proposed to eliminate this "fence".

5.1.1.1.1 Effects on Sideloading and High-Speed Operation

Several peculiarities in journal bearing behavior were observed during the testing of the devices from Build 9. Figure 5-1 shows the performance of one particular device when the nominal pressure difference across the journal bearing (DP) was approximately 0.6 psi. In the absence of any flow from the balance plenum[1], an anomalous drop in DP was seen to occur at 40,000 rpm, with the rotor subsequently crashing at a speed of 80,000 rpm. However, when a supply pressure of 5 psi was applied to the balance plenum, no such anomalous decrease in DP was observed, and the rotor crash occurred at a speed of approximately 150,000 rpm. The device was still operable after the crashes at 80,000 rpm and 150,000 rpm.

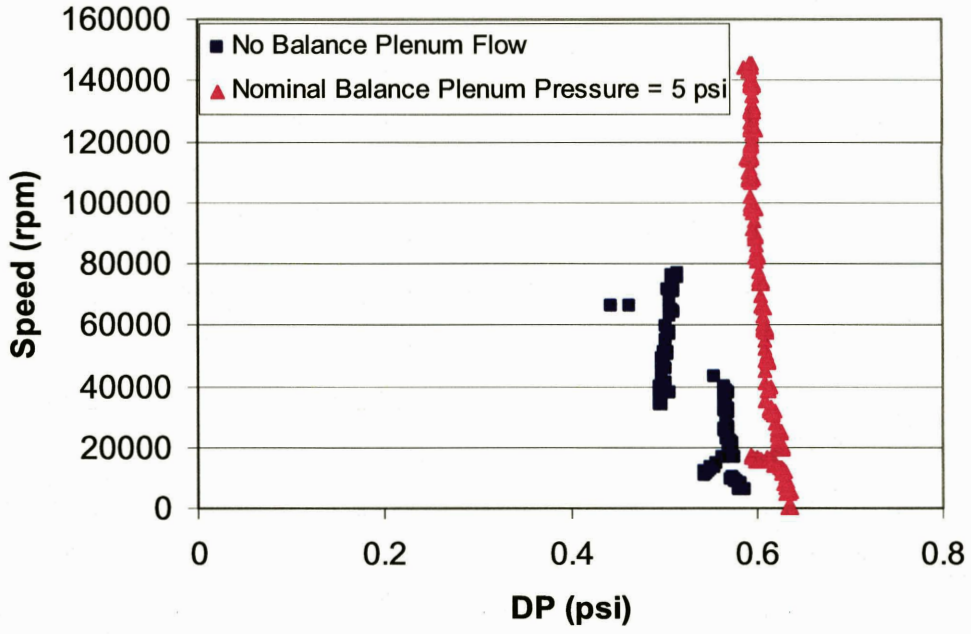

Figure 5-1: Bearing performance in the presence and absence of a supply pressure to the balance plenum.

[1] The supply to the balance plenum was blocked, so the balance plenum pressure was set by the internal leakages.

It is of interest to systematically investigate the effect of varying the balance plenum supply pressure on the crash speed of the rotor. The results for such an investigation performed on another device is plotted in Figure 5-2, with the pressure difference across the journal bearing DP held at a nominal value of 0.7 psi. As indicated by the solid black line, it is apparent that there is a general trend of increasing rotor crash speed with increasing balance plenum supply pressure.

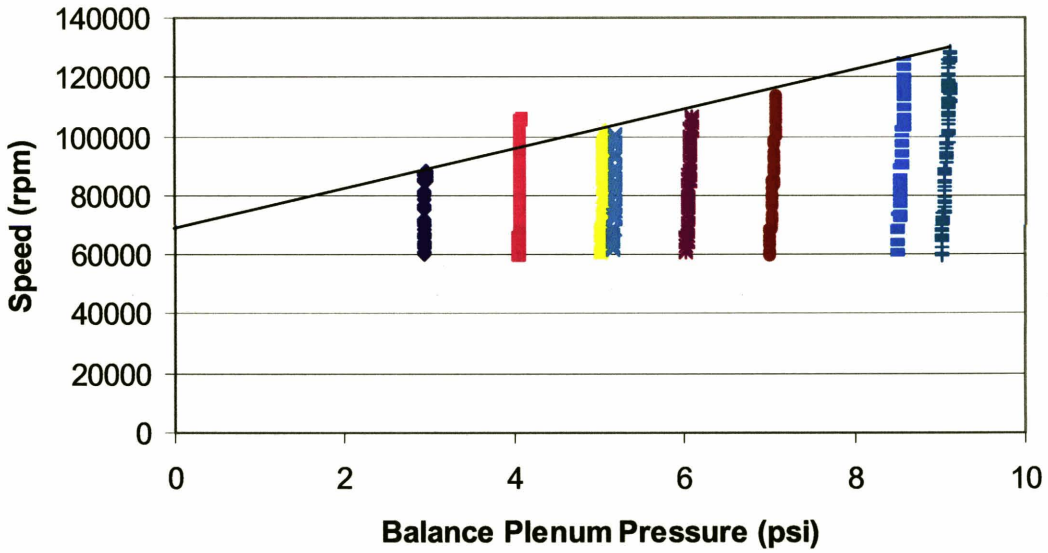

Figure 5-2: Variation of crash speed with balance plenum supply pressure corresponding to a journal bearing differential pressure DP of 0.7 psi. Different colors represent testing performed on the same device, but at different settings of balance plenum supply pressure.

Furthermore, in the absence of any flow to the balance plenum, a peculiar bi-stable radial mode was often observed. An example of such a bi-stable behavior is depicted in Figure 5-3. Although the mass flows to both journal bearing supply plena were kept constant throughout the course of the experiment, the pressure in each plenum was seen to alternate between two different values. The rotational speed of the rotor was also observed to switch between two relatively distinct levels, in tandem with the alternations occurring in the journal bearing supply pressures. Figure 5-3 also shows that the switching from one bi-stable mode to another occurred in an unpredictable fashion, and the time spent in any bi-stable mode was very nearly stochastic.

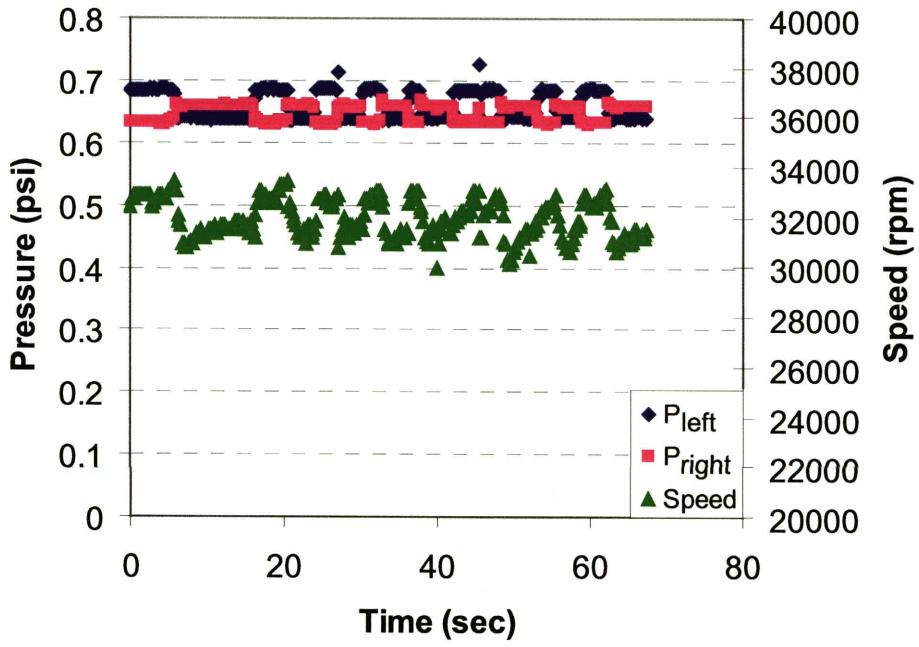

Figure 5-3: Bistable behavior exhibited by a typical device from Build 9.

To further investigate the cause for this anomalous behavior, one device was ground down using Rotorpol, which consists of a piece of sandpaper mounted on a rotating disk spinning at 300 rpm. Upon grinding down Levels 1 and 2, Level 3 was exposed, comprising the turbine blades. The rotor was subsequently removed, thus exposing the outer sidewalls of the journal bearing. The remaining static structure was analyzed in detail under a scanning electron microscope (SEM). One prominent feature of particular interest is the existence of a "fence" at the exit of the journal bearing, as depicted in the micrographs of Figure 5-4. The fence was observed to protrude by a lateral distance of approximately 50 μm into the turbine blade passage, thus interfering with the rotational flow emerging from the nozzle guide vanes (NGV's). It is worth noting that the height of the fence is approximately one-third of the height of the turbine blades, which are nominally 150 μm tall, and approximately three times the width of the journal bearing clearance, which is nominally 18 μm. The interference of the flow exiting from the journal bearing with the turbine flow is analogous to a jet in a cross flow. However, in view of the fact that the geometric dimensions of the fence are not negligible compared to the blade height and the journal bearing width, the presence of the fence is

conjectured to alter the details of the mixing between the journal bearing and turbine flows, thus giving rise to the anomalous radial behavior of the rotor as observed during the experiments.

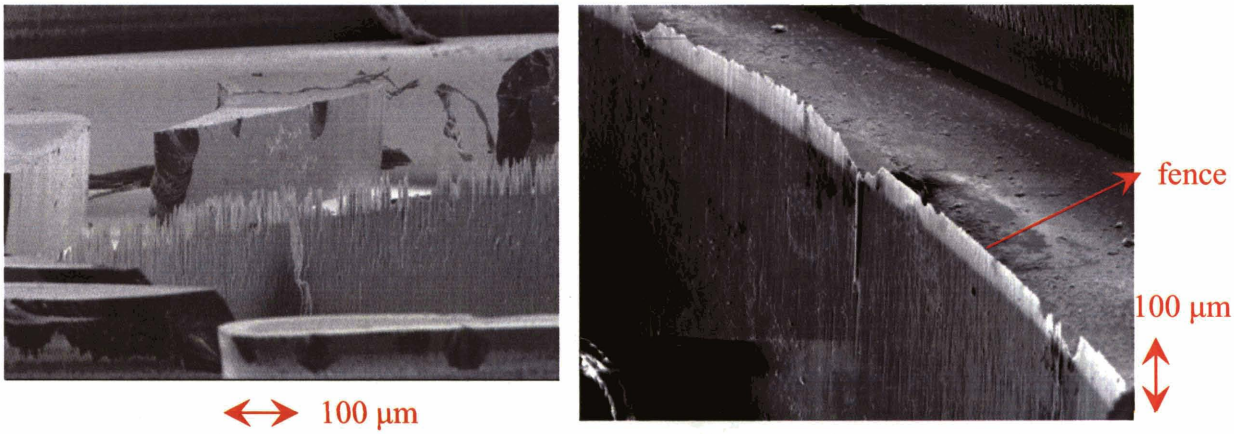

Figure 5-4: SEM micrographs showing the presence of a "fence" at the exit of the journal bearing extending into the blade passage.

A CFD calculation was performed to investigate the effects of the presence of the fence on the mixing flow field. A full three-dimensional CFD calculation requires the detailed flow through the turbine to be computed. In order to simplify the computations and elucidate the essential physics due to the existence of the fence, a simple axisymmetric jet in a cross flow problem is analyzed, where the cross flow is modeled using the radially inward shear flow along an annular passage. Referring to Figure 5-5, the hydrostatic fluid is supplied to the journal bearing via two diametrically opposite supply plena, each subtending an angular extent of 110°. The two plena are in turn separated by a "bridge" on each side. Anisotropy in the journal bearing stiffness is thus achieved due to the concomitant difference in radial stiffness in the x- and y- directions.

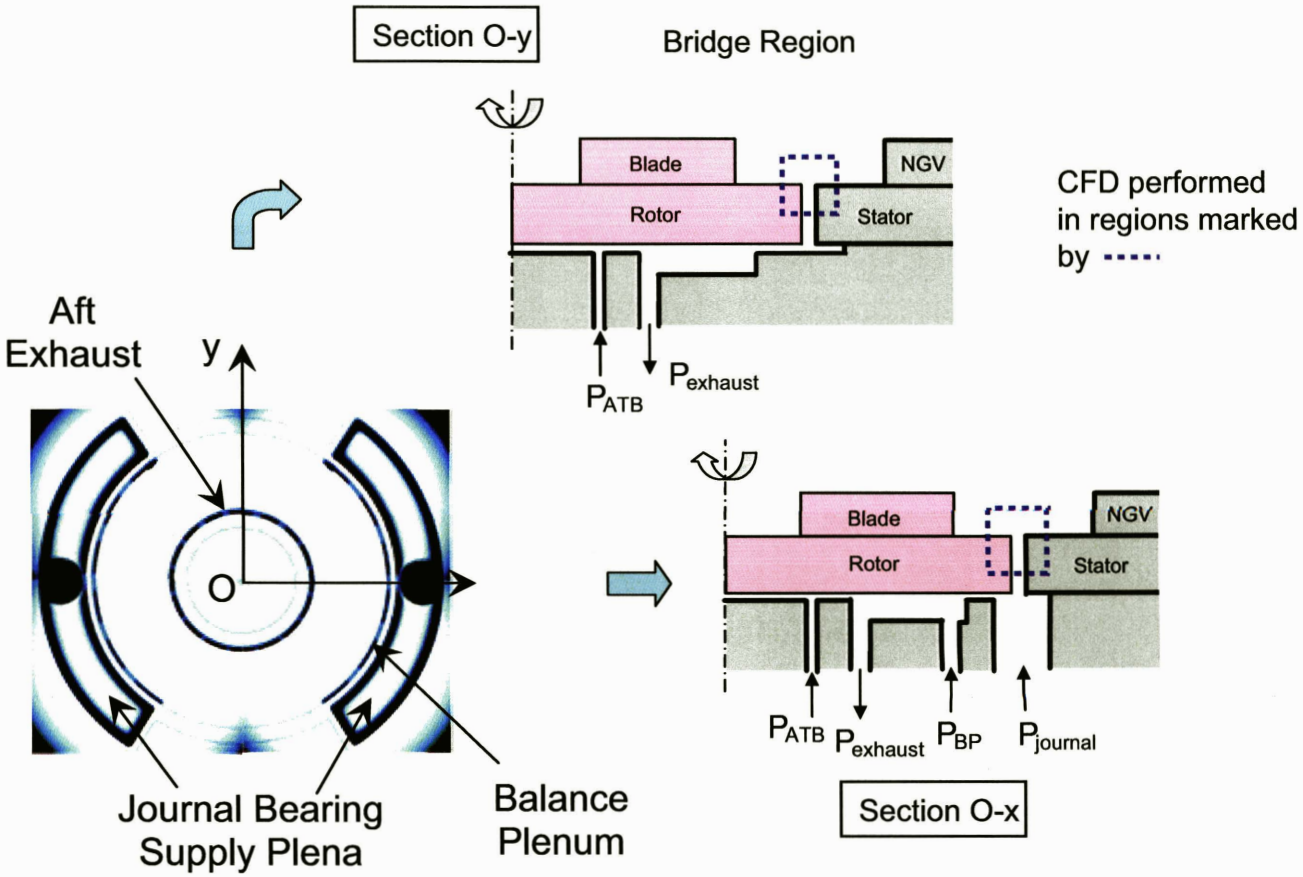

Figure 5-5: Schematic showing the arrangement of the journal bearing plena to achieve anisotropy in journal bearing direct-coupled hydrostatic stiffness.

Sample results of the CFD calculations for the journal bearing and turbine mixing flow in the x-direction are shown in Figure 5-6. Figures 5-6(a) and (b) show contour plots for the velocity magnitude in the vicinity of the mixing region in the absence and presence of the fence, respectively. Similar contour plots for the static pressure are displayed in Figures 5-6(c) and (d), corresponding to the absence and presence of the fence, respectively. Similar results for the mixing flow in the y-direction, where there is no hydrostatic fluid supplied to the journal bearing, are presented in Figure 5-7. It is evident that the presence of the fence causes the turbine flow to separate in the vicinity of the journal bearing exit. In addition, due to the substantially lower base pressure in the separated flow region, the overall pressure level within the journal bearing is diminished in the presence of the fence. This is especially pronounced along circumferential regions of the journal above the "bridge" region, due to the near absence of any axial hydrostatic pressure gradient. The above implies that a sideload is liable to be generated if the

distribution of the fence is not circumferentially uniform. The maximum static deflection of the rotor arising as a consequence of the sideload in the x- and y-directions are plotted as a function of the turbine inlet Mach number in Figure 5-8, assuming the worst case scenario of a continuous fence extending over a 180° circumferential extent which overlaps or coincides with an entire supply plenum and "bridge". Assuming a DP of 5 psi across the journal bearing, the stiffness in the x- and y-directions are 1151 N/m and 288 N/m, respectively. The stiffness values are obtained from an analytical model which models the direct stiffness arising from the inlet loss or Lomakin seal effect. It can be inferred from the figure that the detrimental effect of the sideload due to the fence is more pronounced in the y-direction. This is due to two reasons. First, the journal bearing stiffness in the y-direction is approximately 4 times less than that in the x-direction. Furthermore, as mentioned previously, the absence of any axial pressure gradient or hydrostatic flow along the journal above the "bridge" region causes the low pressure in the separated flow region behind the fence to extend into the journal, thus yielding a suction force on the rotor. It may further be argued that when increasing pressures are applied to the balance plenum, a larger mass flow leaks through the seals in the bridge region into the journal bearing, which increases the journal bearing stiffness in the y-direction, and mitigates the undesirable of the pressure depreciation due to the fence. This substantiates the experimental observation that the crash speeds increase monotonically with increasing balance plenum pressures. The bi-stable behavior of the rotor, as described previously, might be attributed to the unsteady nature of the flow separation behind the fence.

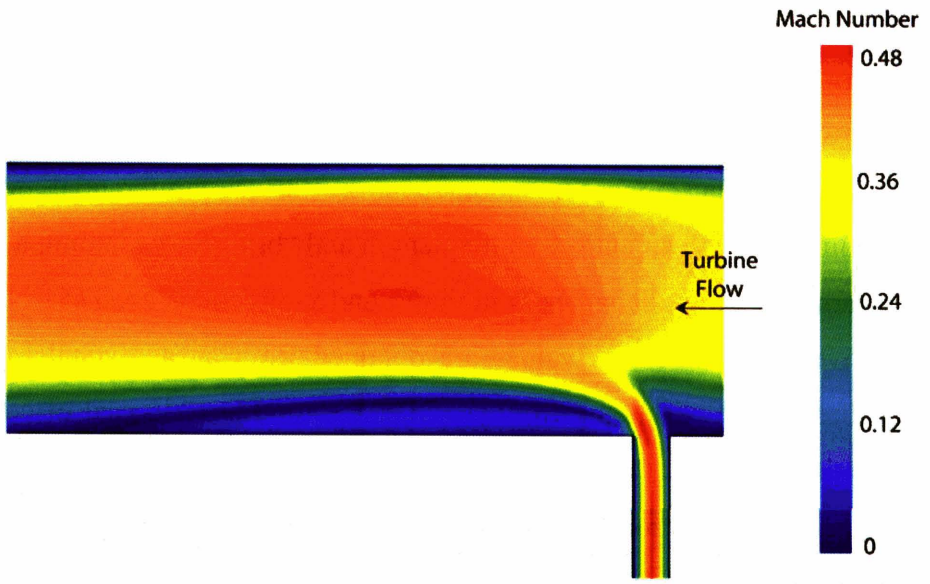

Figure 5-6(a): Contour plot for the Mach number in the vicinity of the mixing region in the absence of the fence.

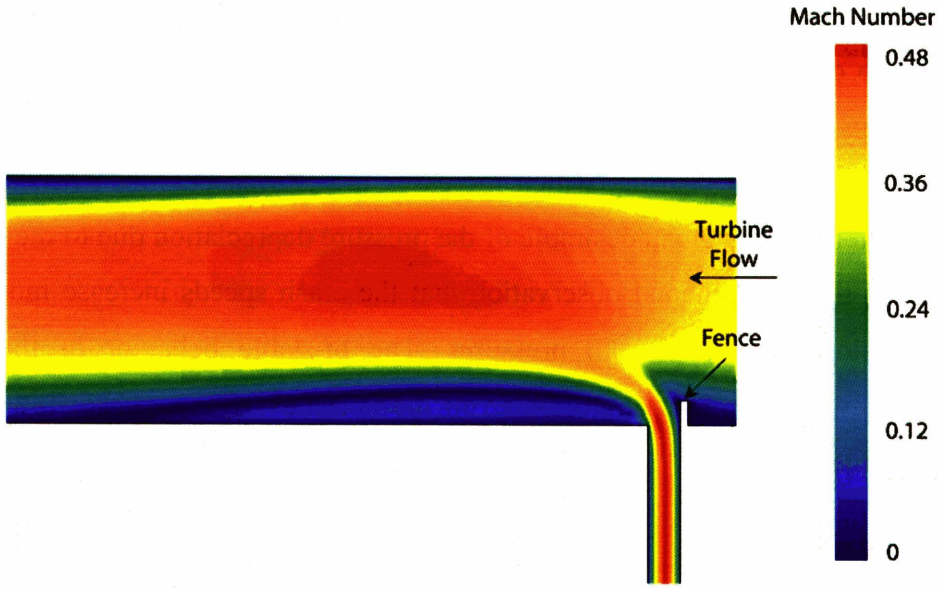

Figure 5-6(b): Contour plots for the Mach number in the vicinity of the mixing region in the presence of the fence.

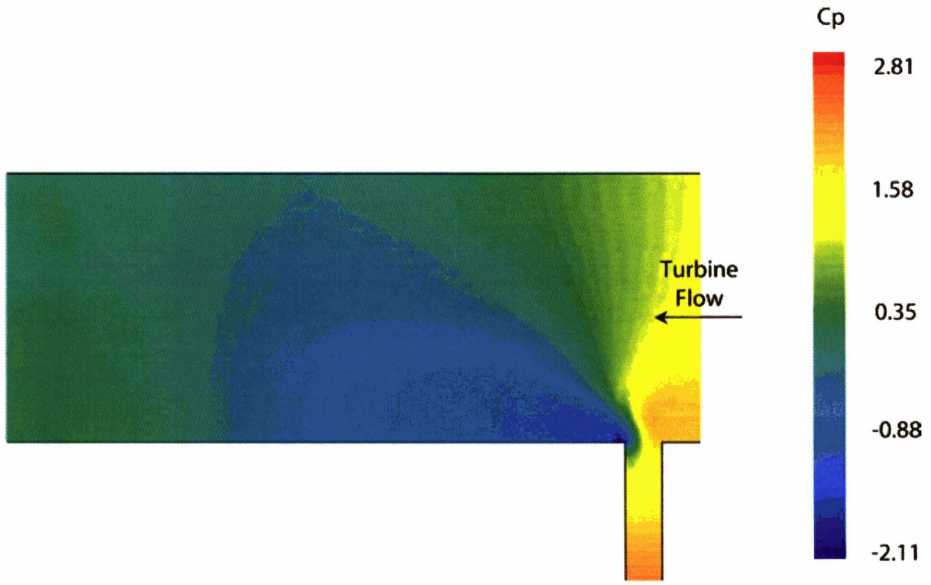

Figure 5-6(c): Contour plots for the pressure coefficient in the vicinity of the mixing region in the absence of fence.

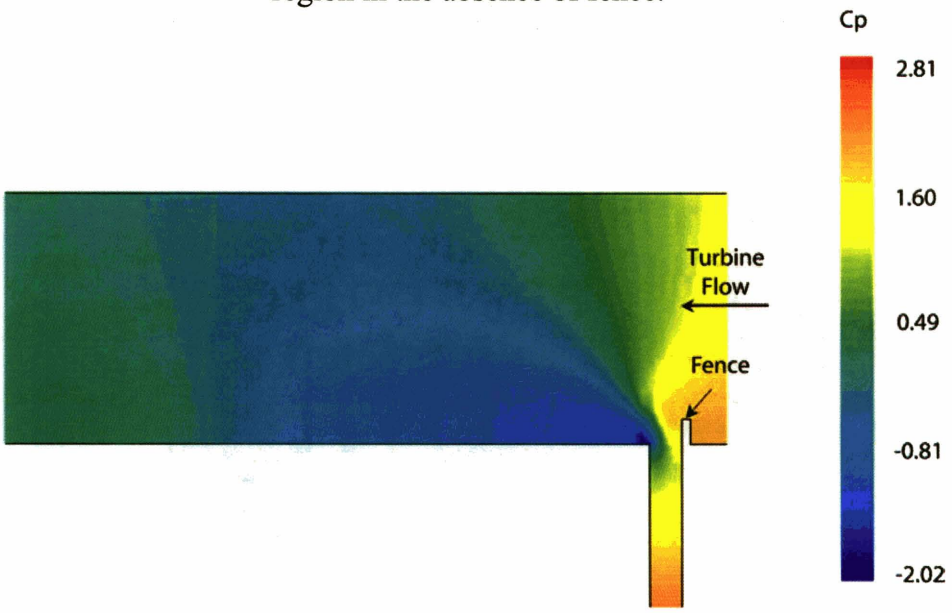

Figure 5-6(d): Contour plots for the pressure coefficient in the vicinity of the mixing region in the presence of fence.

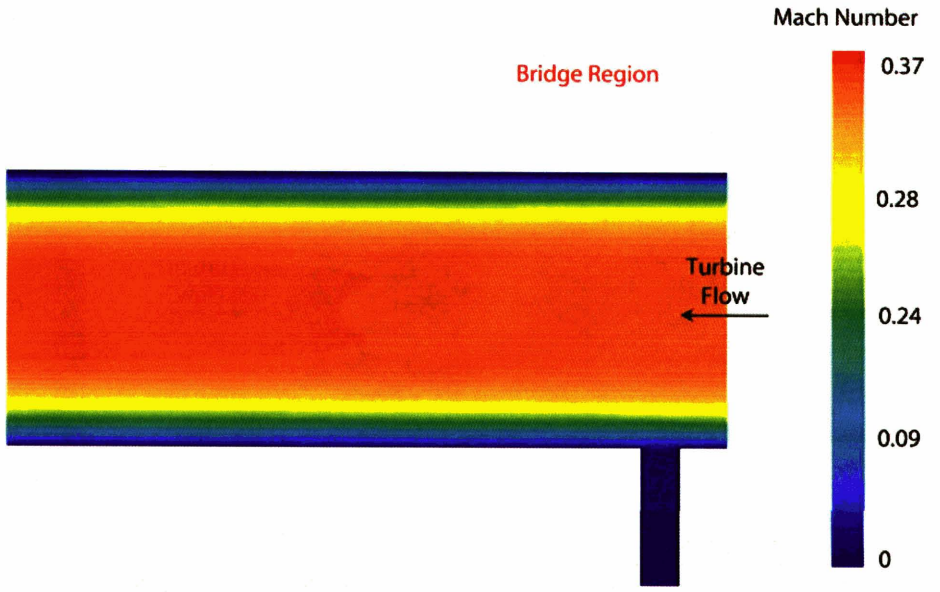

Figure 5-7(a): Contour plot for the Mach number in the bridge region in the absence of the fence.

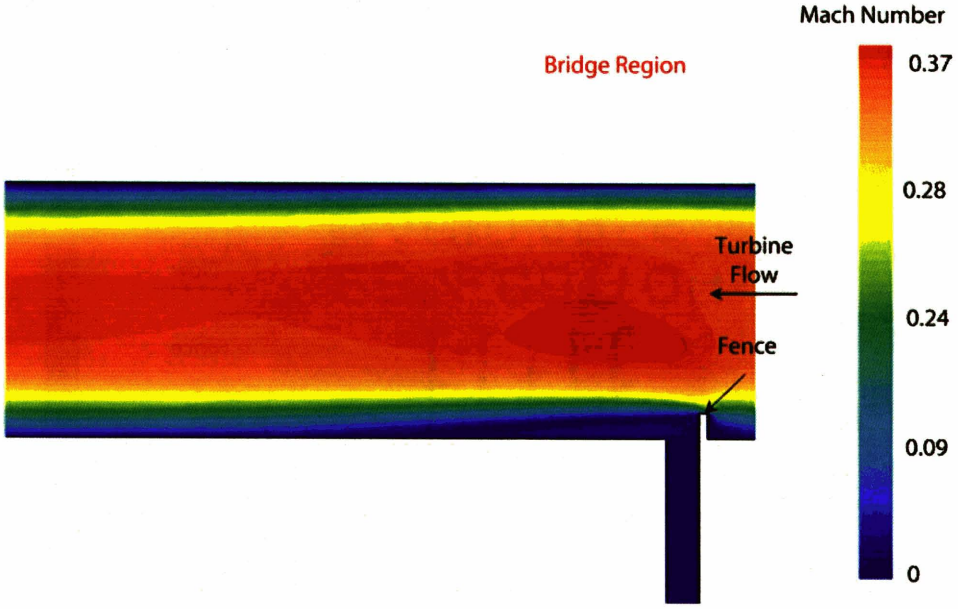

Figure 5-7(b): Contour plot for the Mach number in the bridge region in the presence of the fence.

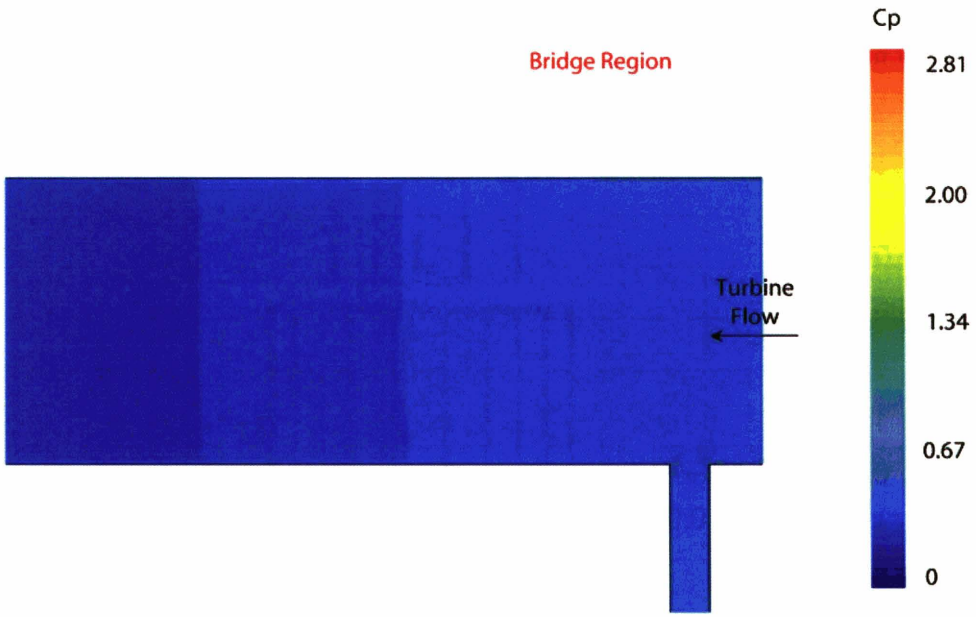

Figure 5-7(c): Contour plot for the pressure coefficient in the bridge region in the absence of the fence.

Figure 5-7(d): Contour plot for the pressure coefficient in the bridge region in the presence of the fence.

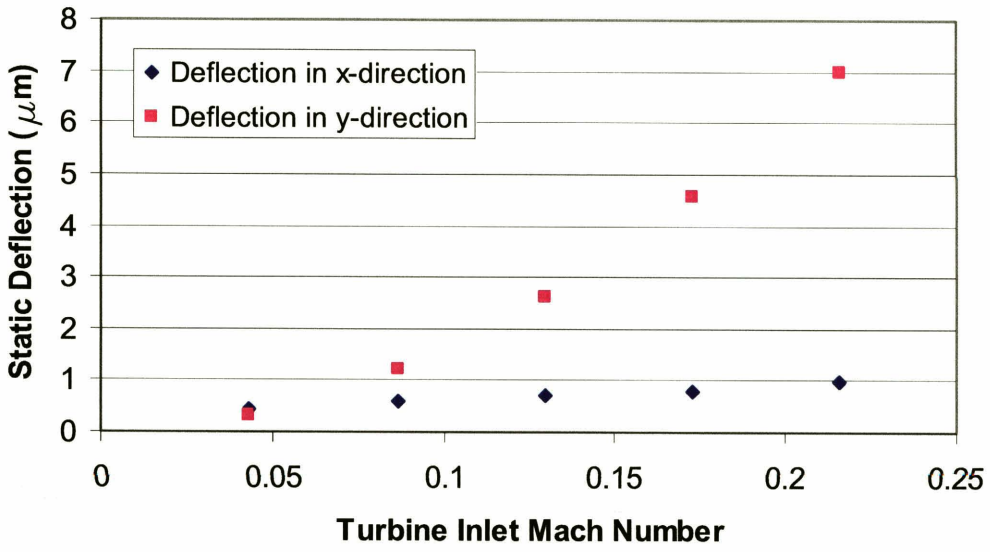

Figure 5-8: Maximum static deflection in the x- and y-directions. The journal bearing clearance for the devices in this build was estimated to be 18 μm. The "fence" was assumed to have a circumferential extent of 180°.

5.1.1.1.2 Microfabrication Solutions Using Isotropic DRIE

According to Li [43], the presence of the "fence" arises from micro-masking effects due to the Silicon dioxide which is thermally grown to protect the journal bearing. Prior to this microbearing test device build, the blades on the rotor were always etched prior to the Deep-Reactive-Ion-Etching (DRIE) of the journal bearing. However, since the journal bearing DRIE process was the most challenging step in the entire process flow, it was advantageous to etch the journal bearing before DRIE of the blades. This allowed the journal bearing etch to be performed on a fresh new piece of wafer. However, subsequent to the journal bearing DRIE, the sidewalls of the journal bearing had to be protected using thermal oxide. The wafer was then inverted for the DRIE of the blades to be carried out until the target blade height was reached and the journal bearing was etched through. When this occurred, the thermal oxide protecting the journal bearing sidewall was exposed. In the presence of a negative journal bearing taper, the exposed oxide acted as a micro-mask, preventing the Silicon beneath it from being dry etched by the plasma. When the thermal oxide was finally removed using HF or BOE, the Silicon masked by the oxide remained and result in the formation of the "fence".

Microfabrication solutions have been proposed to eliminate the undesirable "fence". Since the thickness of the "fence" is at most several microns, it can potentially be removed using an isotropic dry etch recipe which etches sideways as well. Figure 5-9 shows the presence of a "fence" at the exit of the journal bearing protruding into the blade passage of the NGV's, without performing an isotropic etch at the end of the blade DRIE. Details near the exit of the journal bearing, after carrying out an isotropic etch for one and a half minutes subsequent to the blade etch, are shown in Figure 5-10. It is evident that the "fence" is no longer present and has been successfully eliminated by performing the isotropic etch.

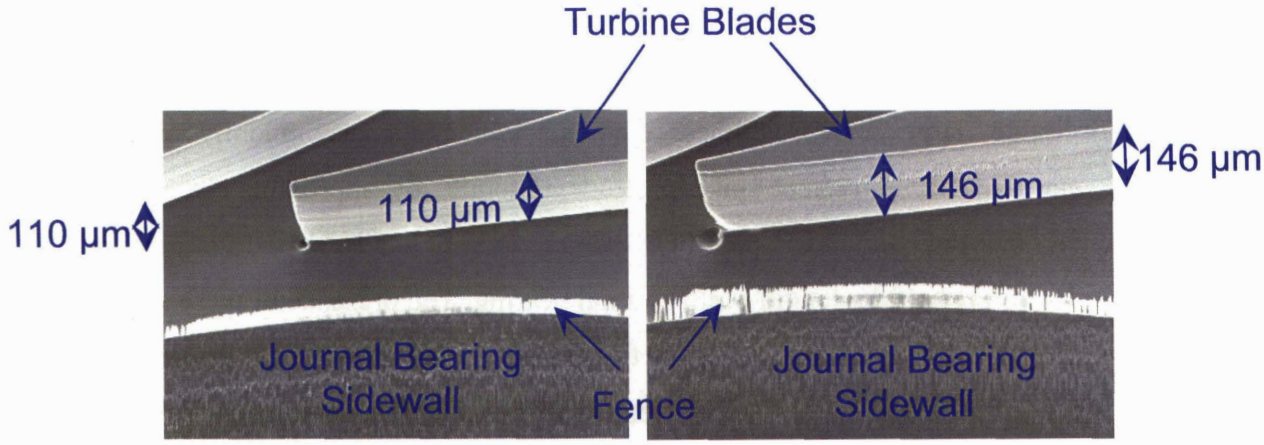

Figure 5-9: Evolution of "fence" and "dimple" at trailing edge blade root.

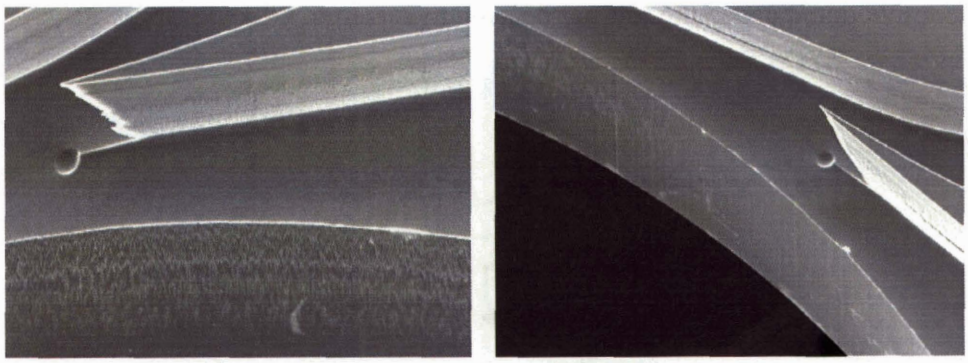

Figure 5-10: Use of isotropic DRIE to eliminate "fence".

One other interesting feature which is evident in Figures 5-9 and 5-10 is the presence of a "dimple" near the blade's trailing edge. The effects of such "dimples" on the structural integrity of the rotor are further discussed in Section 5.1.3.2.

5.1.1.2 "Spikes" on Journal Bearing Walls

One other undesirable feature which was observed is the presence of "spikes" appearing on the sidewalls of the journal bearing. An SEM photograph depicting the occurrence of such a spike is shown in Figure 5-11. A typical journal bearing has a sidewall roughness consisting of longitudinal striations which develop predominantly during the second half of the journal bearing DRIE process. These roughness elements are located near the journal bearing exit and have a lateral spacing of approximately 1 μm and a longitudinal extent of almost 100 μm. On the other hand, spikes are atypical, undesirable, large scale roughness elements which appear randomly on the journal bearing sidewall. A typical spike protrudes laterally by approximately 5 μm into the journal bearing and can possibly extend longitudinally by 150 μm, which is approximately half the length of the journal bearing. The presence of these spikes reduces the journal bearing distance-to-contact, especially when a spike on the rotor intercepts another spike on the stator. The presence of the spikes may also alter the details of the hydrodynamic flow field and hence influence the stability characteristics of the journal bearing. Spikes which fall off due to a rotor collision with the static structure may become trapped and cause the journal bearing to seize up.

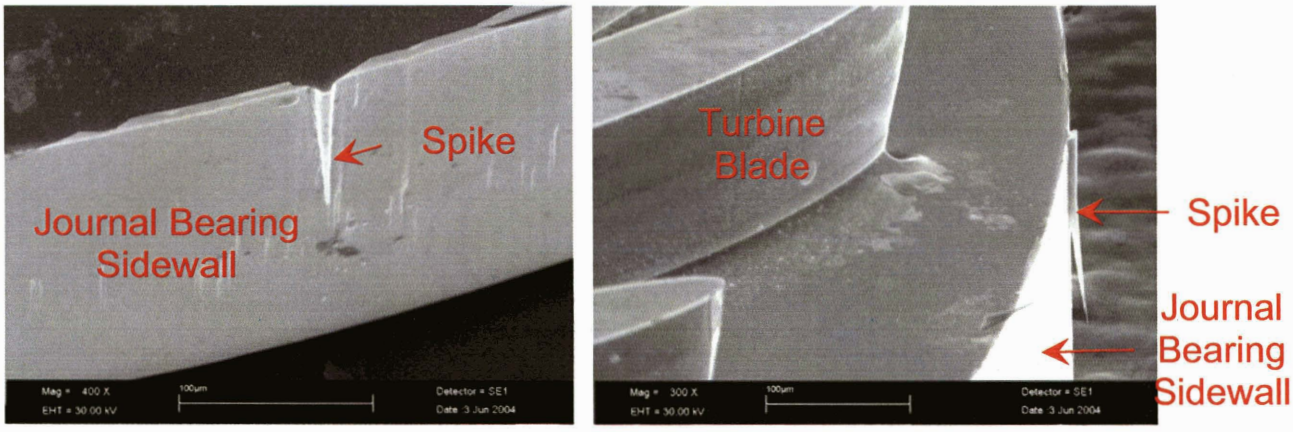

Figure 5-11: SEM micrograph showing the presence of spikes appearing on the sidewalls of the rotor.

However, it has been observed that spikes are less likely to form in journal bearings with profiles which are negatively tapered as compared to those with positively tapered profiles. It is conjectured that in the presence of a positively tapered journal bearing profile, spikes are more susceptible to form due to micromasking by small specks of photoresist [43]. A journal bearing with a negatively tapered profile also has substantially less sidewall roughness than one with a positive taper. Hence, it is apparent that the number of spikes can be reduced, or perhaps even eliminated, by etching journal bearings with negatively tapered profiles. However, the detrimental side effect of this lies in journal bearing operation. A journal bearing with an excessive negative taper experiences negative radial stiffness at low journal bearing differential pressures DP [3]. This renders transcritical operation difficult or impossible at low values of DP. When the radial stiffness becomes positive at higher values of DP, the damping ratio might be insufficient to facilitate transcritical operation without rotor collision.

5.1.1.3 Drop-in Rotors

In the original microbearing test device, the rotor blades were first being etched on the top side of Level 3, before being bonded to Level 2, which constituted the forward thrust bearing plenum and orifices (see Appendix A for a detailed cross-sectional view of the microbearing test device). The journal bearing was subsequently patterned and etched on the bottom side of Level 3. When the journal bearing was completely etched through, the free rotors on each device was retained by means of snap-off tabs on the bottom of Level 2 which were bonded to bonding pins on the blade side of the rotor. This procedure was originally devised to hold the freed rotors onto Level 2. The bonded Levels 2 and 3 stack was subsequently bonded to Levels 1, 4 and 5 to form the complete 5-layer microbearing test device wafer stack. Prior to experimental testing, the 4 snap-off tabs which held onto the rotor of each device had to be broken by means of microfabricated Silicon needles inserted through the turbine exhaust [12]. The snapping off of these tabs was a highly undesirable process, as substantial amount of debris originated from the fractured tabs, some of which potentially got into the forward thrust bearing gap or the journal bearing, thus seizing up the bearings and interfering with the smooth operation of the device.

Even more importantly, during the journal bearing DRIE process, it was difficult to ascertain whether the journal bearing had been completely etched through or not. In fact, there was one entire microbearing test device build which had to be discarded, in view of the fact that there were no spinnable devices, as the journal bearing on every device failed to etch through completely.

One other challenging issue stemmed from the quality of the bonding surfaces. There was often severe undercutting on the bonding surface of the bonding pins subsequent to the blade etch process, thus culminating in a weak bond between the bonding pins and the snap-off tabs. As a consequence, rotors were often being lost during wet chemical cleaning and spin-drying processes. The severe lack of reliability and cleanliness of the "snap-off tab" rotor retention scheme led to its abolishment and prompted a reassessment of the alternative procedures available for the proper handling and retention of the freed rotors.

A new "drop-in rotor" scheme has been proposed. In this scheme, rotor ID's are first patterned and shallow etched on the bottom surface of each rotor. The journal bearing is subsequently patterned and dry etched. Thermal oxidation is then performed so as to protect the side-walls of the journal bearing. This is followed by the patterning and DRIE of the rotor blades. The rotors which are freed after this process are retained by either photoresist or KAPTON tape. These rotors are subsequently allowed to fall off and to separate from the rest of the wafer, before they are collected and cleaned individually. Teflon tweezers are employed to handle these rotors to minimize any physical damage to the rotors. The rotor ID's permit the original locations of the individual rotors to be easily identified. The rotors can then be dropped into their appropriate destinations during the bonding of the 5-wafer stack. Apart from the advantage that the "drop-in rotor" scheme permits the dropping off, collection and cleaning of the rotors to be achieved in a controllable fashion, it is also consistent with a process flow which allows the journal bearing to be patterned and etched first. In the original "snap-off tab" scheme, the most crucial journal bearing etch had to be performed last, which introduced considerable complications arising from the mounting and protection of the wafers. Furthermore, due to etch variation effects, the journal bearing for some of the devices was etched through first. Over-etching occurs on these devices by the time the journal bearing for all the

devices had eventually etched through. This over-etching resulted in damage to the bottom surface of Level 2.

However, the "snap-off tab" scheme had one significant advantage over the "drop-in rotor" scheme. If the "snap-off tab" scheme was successful, the rotors would be held fixed by the tabs and it was possible to perform static flow tests to determine the clearance of the journal bearing, assuming that bonding misalignments were small. The "drop-in rotor" scheme did not allow static flow tests to be performed per se, although it was still possible to back out the journal bearing clearance from spinning tests, provided the rotational speeds were significantly below the natural frequencies or subcritical, so that it was valid to assume that the rotor was spinning about its geometric center.

It is further of interest to compare the yield in terms of the actual number of operational devices available from one microbearing test device build using the "drop-in rotors" scheme, versus the conventional "snap-off tab" rotor retention scheme. For Build 11 (which corresponded to the last build incorporating the original microbearing test device design), a total of 11 devices were tested, all of which were capable of achieving speeds on the order of half a million rpm or even higher, as can be seen from Figure 5-12. This was unlike builds incorporating the "snap-off tab" technology, where the yield of spinnable devices was at most 50% for each build, with many of these devices being unable to cross the journal bearing natural frequency, in view of the large mass imbalance of the rotors. The substantial increase in yield attests to the vast improvement in reliability accruing from the "drop-in rotor" scheme. It was possible to attribute this to the fact that in the "drop-in rotor" scheme, the freed rotors that had fallen off implicitly implied that the journal bearing had been completely etched through. However, it was impossible to ascertain this if the "snap-off tab" scheme was adopted. Furthermore, it was possible to subject the freed rotors which were collected to comprehensive cleaning processes, thus reducing the likelihood of bearing seizure due to foreign particle contamination. On the other hand, for the "snap-off rotor" scheme, cleaning of the rotors was a challenging task, since the chemicals might not be capable of thoroughly penetrating the narrow bearing clearances and flushing out any foreign particles trapped within the narrow trenches. Furthermore, cleaning out any liquids held by surface tension forces in the bearings would pose a significant challenge.

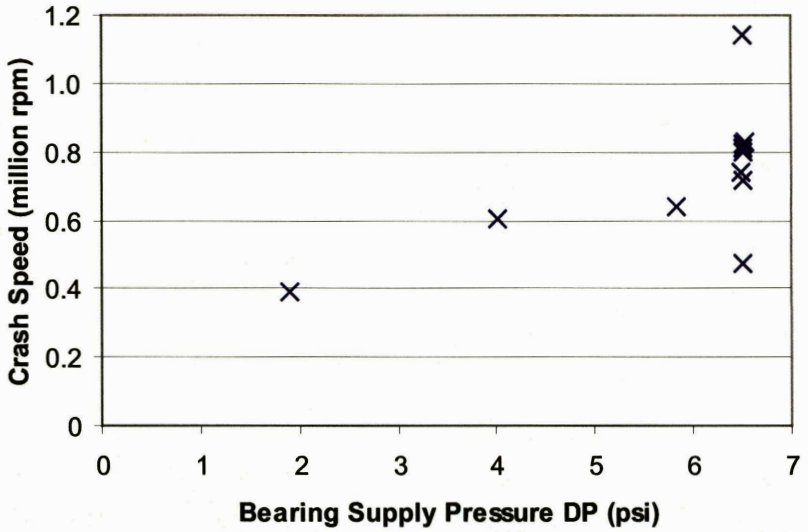

Figure 5-12: The high yield associated with the drop-in rotor technique is manifested by the ability of all the tested devices in Build 11 to achieve speeds on the order of half a million rpm.

Finally, as discussed above, debris arising from the fracturing of the snap-off tabs might potentially find their way into the bearing gaps, thus jamming the bearings and rendering the device non-operational.

In summary, the vast improvement in device yield attests to the reliability of the "drop-in rotor" technology and the effectiveness of the procedures employed for the cleaning of the rotors. In the redesigned microbearing test device, the rotors will be fabricated using a double layer wafer scheme which adopts the drop-in rotor technology. In fact, the drop-in rotor approach further includes a donor-receiver scheme to allow devices with different journal bearing widths to be microfabricated. Further details regarding the new approach for microfabricating the rotors are presented in Section 6.3. Furthermore, to avoid the formation of spikes, the journal bearings on the redesigned microbearing test device will be etched with a slight negative taper.

5.1.2 Rotordynamic Issues

The original microbearing test device had two problematic sources of negative stiffness. The first was a negative radial stiffness, and the second was a negative tilting stiffness.

5.1.2.1 Negative Radial Stiffness

It was found that the cause for the negative radial stiffness was due to the nature of the flow in the bridge region (see Figure 5-5). Under normal operating conditions, hydrostatic supply pressures were applied to the two journal bearing plena, each subtending a circumferential extent of 110°, as shown in Figure 5-5. There was a net positive mass flow upwards through the journal bearing from the journal bearing hydrostatic supply plena to the turbine inter-blade row. In the absence of any mass flow supplied to the balance plenum, the inter-blade row pressure was higher than the pressure in the balance plenum. Along the bridge region, this difference in static pressure drove a mass flow from the turbine inter-blade row into the balance plenum. This flow occurred downwards through the journal bearing before flowing radially inwards into the balance plenum via a seal. Figure 5-13 serves to explain schematically how a negative radial stiffness developed due to flow reversal through the journal bearing in the bridge region. Figure 5-13(a) shows the baseline configuration for a radially-centered rotor, where there is no net radial force acting on the rotor in the y-direction, with a static pressure difference of 5 psi between the turbine inter-blade row and the balance plenum. However, when the rotor is given a small perturbation in the y-direction, as shown in Figure 5-13(b), there is an increase in pressure drop or hydraulic loss across the journal along regions corresponding to a decrease in journal bearing clearance, and a decrease in pressure drop across the journal along regions where the journal bearing clearance increases. There is hence a higher overall static pressure in regions where the journal clearance has increased, and a lower overall pressure along regions corresponding to a decrease in journal clearance. Along the bridge region, the concomitant radial force thus acts from the region of larger journal clearance towards the region of smaller journal clearance, thus having a tendency to displace the rotor even further from its radially centered position. It is evident that the cause of this negative radial stiffness is due to the coupling of the flow through the journal bearing and the seal. The hydraulic resistance of the seal which occurs in series with the hydraulic resistance due to the journal bearing contributes to a negative radial stiffness when reversed flow through the journal bearing occurs along the bridge region. Figure 5-14 shows the magnitude of the negative stiffness generated for different

values of rotor eccentricity, corresponding to different values of seal clearance, when the pressure along the inter-blade row is 0.5 psi higher than that in the balance plenum. It can be observed that the magnitude of the negative stiffness is very sensitive to the seal clearance, and becomes generally large for large values of rotor eccentricity. Figure 5-15 plots the magnitude of the negative stiffness generated in the y-direction as a function of the rotor eccentricity for varying values of static pressure difference between the turbine inter-blade row and the balance plenum, fixing the seal clearance at 2 μm. Once again, the magnitude of the negative stiffness increases rapidly at large eccentricities and rises monotonically with increasing static pressure difference between the inter-blade row and the balance plenum.

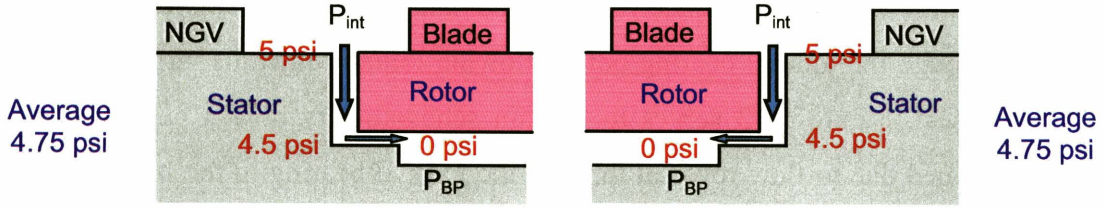

(a)

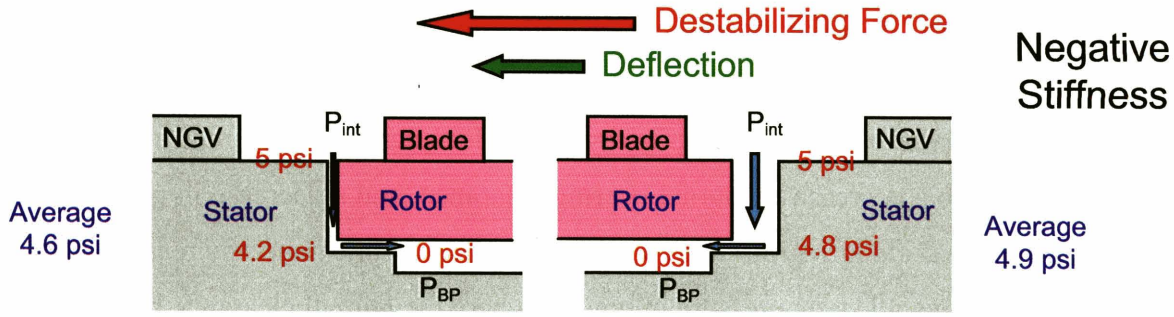

(b)

Figure 5-13: Schematic illustrating how a negative radial stiffness arises due to flow reversal through the journal bearing in the bridge region.

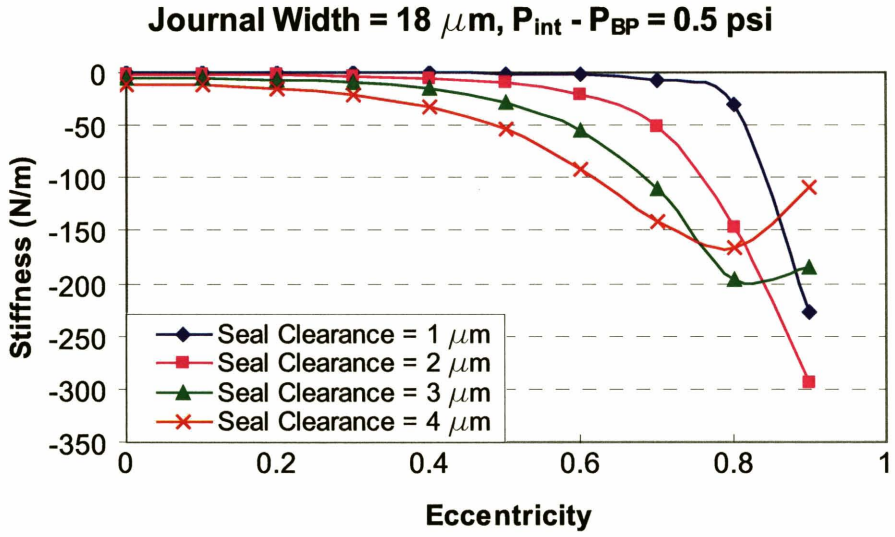

Figure 5-14: Negative radial stiffness for different rotor eccentricities, corresponding to different seal clearances, when the inter-blade row pressure is 0.5 psi higher than that in the balance plenum.

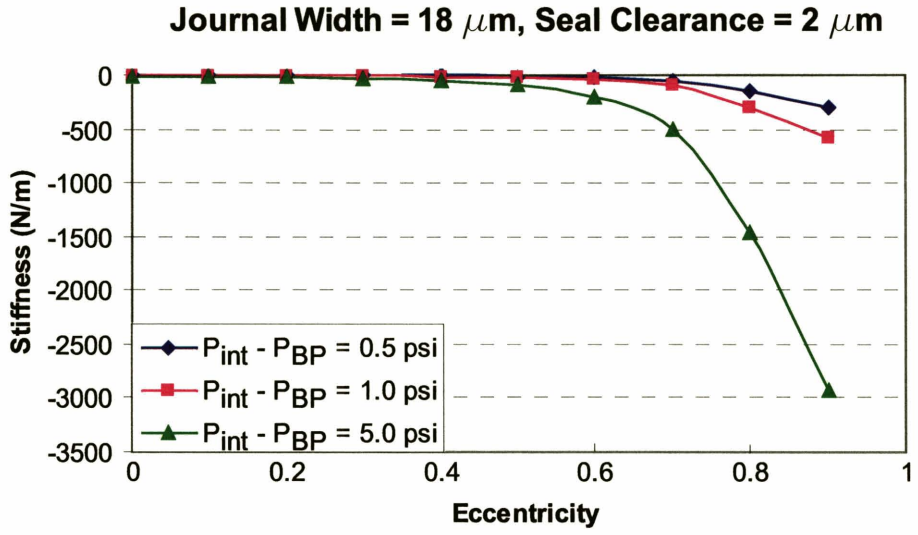

Figure 5-15: Negative radial stiffness corresponding to different rotor eccentricities for varying values of static pressure difference between the turbine inter-blade row and the balance plenum, fixing the seal clearance at 2 μm.

Since the negative stiffness arises as a consequence of the flow reversal through the journal bearing, the negative stiffness is potentially alleviated by maintaining the static pressure of the balance plenum above that of the inter-blade row. Figure 5-16 depicts such a scenario, where the static pressure of the balance plenum is kept 5 psi

higher than the inter-blade row pressure. Figure 5-16(a) illustrates the baseline situation of a radially-centered rotor, whereas Figure 5-16(b) shows the configuration of a rotor which has been subjected to a small perturbation in the y-direction. Repeating the same arguments as those used in the previous analysis, it can be concluded that the forward flow through the journal contributes to a positive radial stiffness. This corroborates the results shown earlier in Figure 5-1, where it is observed that bearing stability is enhanced when the balance plenum is held at a positive static pressure with respect to the turbine inter-blade row, as indicated by the magenta triangles. It thus appears from the above argument that it is beneficial to keep the static pressure in the balance plenum as high as possible to maintain a net positive radial stiffness in the y-direction. However, this has two potential shortcomings. First, the positive radial stiffness contribution in the y-direction decreases the journal bearing anisotropy, thus decreasing the journal bearing stability boundary for the same journal bearing hydrostatic differential pressure. Second, there exists an upper bound to the static pressure that can be applied to the balance plenum. The basic purpose of the balance plenum is to provide an axial upward force to balance the downward force of the turbine pressures. An excessively large balance plenum pressure ultimately yields an unacceptably large upward force on the rotor and brings the rotor into close proximity with the forward thrust bearing, thus increasing the likelihood of physical contact between the rotor and the forward thrust bearing.

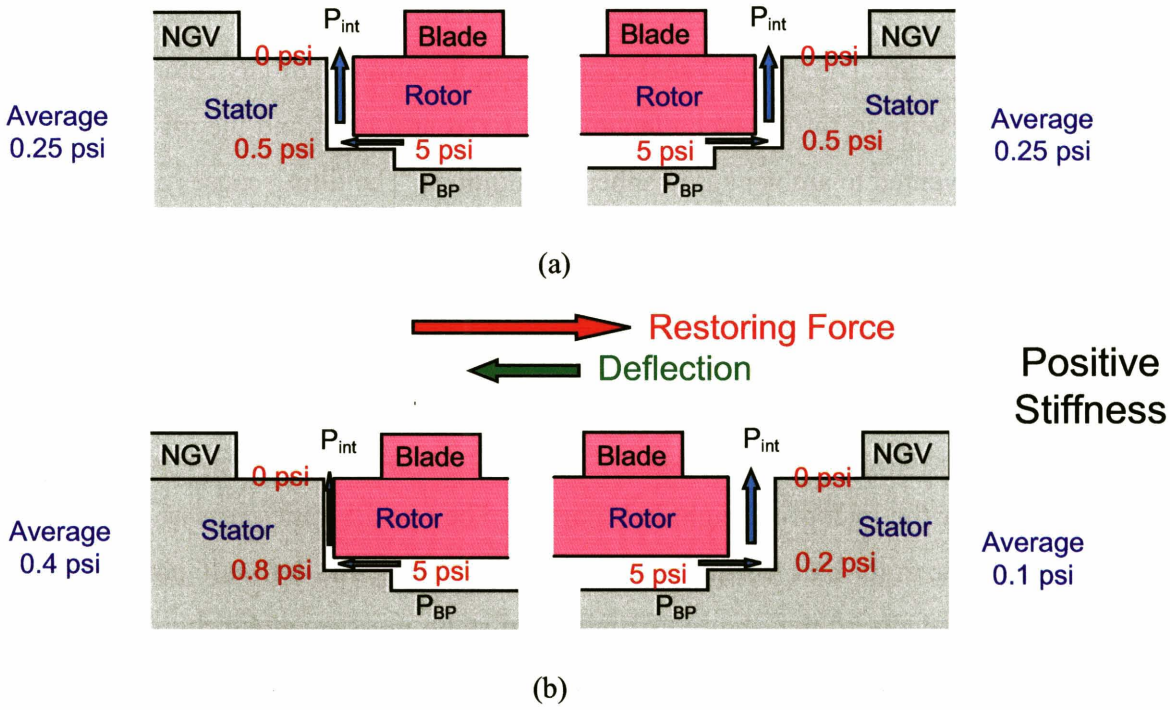

Figure 5-16: Schematic illustrating how a positive radial stiffness arises due to a positive flow through the journal bearing in the bridge region.

Several design implications arise from the above negative radial stiffness analysis. As far as possible, the journal bearing must not be directly connected in series with any hydraulic resistance, so as to avoid any undesirable negative radial stiffness due to flow reversal through the journal. These factors have to be taken into consideration in the redesign of the microbearing test device.

5.1.2.2 Negative Tilting Stiffness

The other category of negative stiffness encountered in the original microbearing test device is a negative tilting stiffness arising from the radially inward flow from the balance plenum to the aft-side exhaust, as depicted in Figure 5-17. When the rotor is subjected to a small tilting perturbation about its equilibrium configuration, a radially and circumferentially varying gap exists between the balance plenum and the aft exhaust. Since the hydraulic resistance at any location scales inversely with the cube of the local gap or clearance, the varying gap due to a rotor tilt is anticipated to give rise to static pressure distributions with strong axial gap dependencies. Figure 5-17 depicts the static pressure distribution along the seal separating the balance plenum from the aft-exhaust,

corresponding to a rotor tilting angle of -0.0006 radians about the y-axis and a rotor tip deflection of 1.3 μm. The nominal seal clearance in the absence of any rotor tilt is 3 μm. The supply pressure to the balance plenum was fixed at 5 psig, and the aft exhaust was assumed to be vented to ambient atmospheric conditions. The tilting causes a reduction in axial gap along the left-half portion of the seal, and an increase along the right-half portion. Regions of increased hydraulic resistance have thus shifted towards the balance plenum inlet along the left-half portion, whereas regions of reduced hydraulic resistance have shifted towards the balance plenum inlet along the right-half portion. The static pressure thus decreases much more rapidly near the inlet of the left-half portion and much less rapidly near the inlet of the right-half portion. The overall static pressure level is thus higher along the right-half portion of the seal than along the left-half portion. It can immediately be deduced that the redistribution in static pressure along the seal causes a net yawing or pitching torque to act on the rotor. This torque is destabilizing because it acts in a direction which tends to further increase the rotor tilting angle.

The magnitude of the destabilizing torque is plotted as a function of the rotor tilting angle in Figure 5-18. Two plots are shown, one corresponding to a rotor tilt about the y-axis, and the other corresponding to a rotor tilt about the x-axis. The plots are almost linear, and the magnitudes of the negative tilting stiffness can thus be estimated conveniently from the slope of the graphs. The negative tilting stiffness about the y-axis is approximately 50% higher in magnitude than that about the x-axis. Given that the thrust bearing hydrostatic tilting stiffness is approximately 0.03 N-m/radian, the magnitude of the negative tilting stiffness about the y-axis is thus approximately 20% of the available tilting stiffness due to the thrust bearings. It should further be noted that the magnitude of the negative tilting stiffness is very sensitive to the nominal clearance of the seal between the balance plenum and the aft-exhaust. This is depicted in Figure 5-19 for the same pressure ratio across the seal, where it is evident that the magnitude of the negative tilting stiffness increases monotonically with decreasing seal clearances. This is one plausible cause for the rotor crash previously experienced in a micro-electrostatic turbine-generator device. Both the original microbearing test device and the micro-electrostatic turbine-generator share similar configurations in terms of bearings and seals. One key difference between the two devices is the clearance of the seal between the

balance plenum and the aft-exhaust. In the original microbearing test device, this clearance was typically 12 μm, whereas in the micro-electrostatic turbine generator, this clearance was significantly lower at a nominal value of 3 μm (in view of the fact that the electrostatic generator required small axial gaps between the rotor and stator for purposes of power generation). From Figure 5-19, corresponding to the same pressure ratio across the seal, the turbine-generator is expected to experience a negative stiffness five times that experienced in the microbearing test device. When experiments were previously performed on a turbine generator at a rotor speed of 850,000 rpm, the pressure difference across the seal was 5 psi. This corresponds to a negative stiffness of 0.03 N-m/rad, which is approximately equal in magnitude to the thrust bearing direct-coupled tilting stiffness. There is thus a high possibility that the rotor crash can be attributed to the negative tilting stiffness arising from the radially inward flow through the seal.

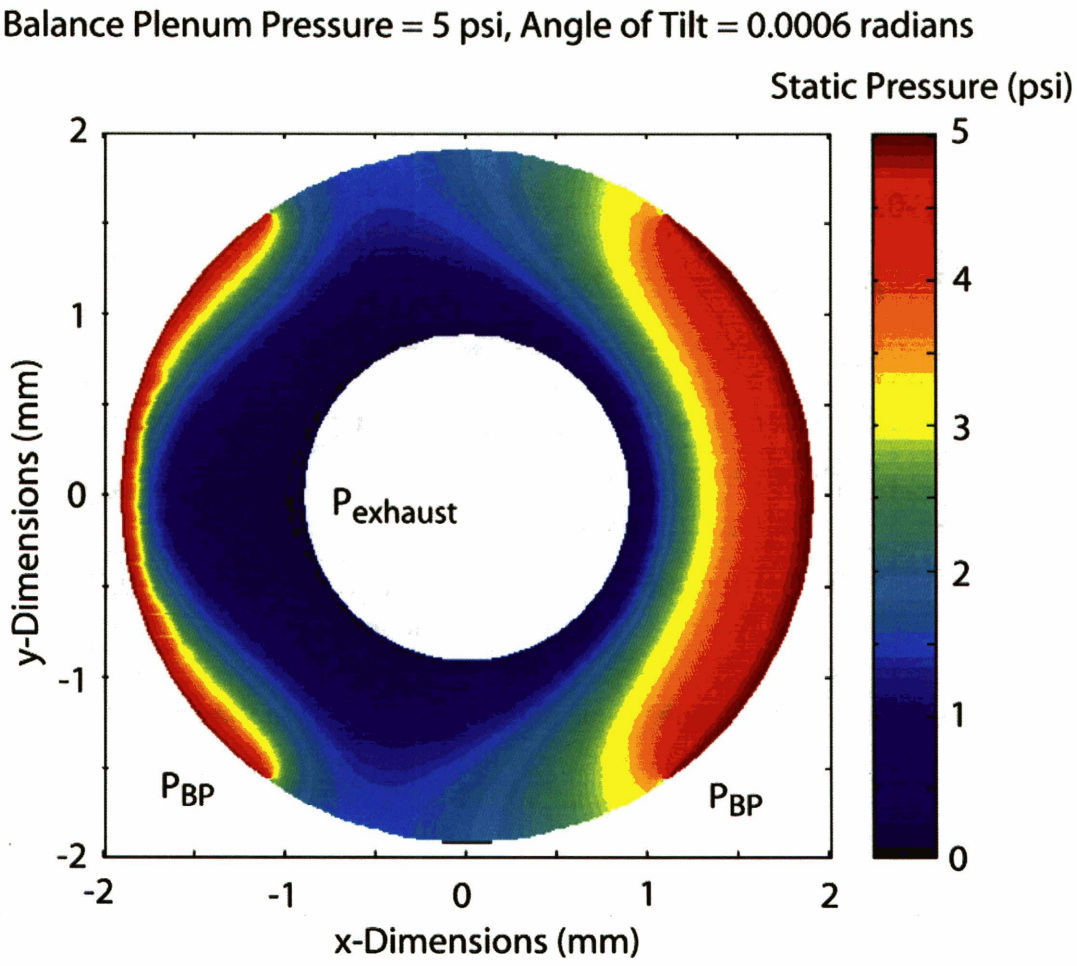

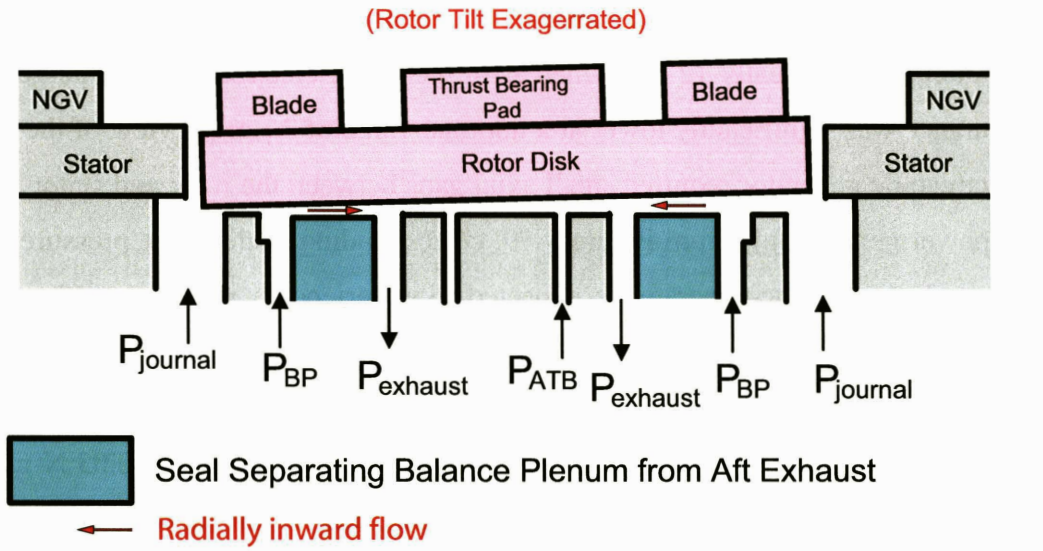

Figure 5-17: Static pressure distribution along the seal separating the balance plenum from the aft-exhaust, corresponding to a rotor tilting angle of -0.0006 radians about the y-axis.

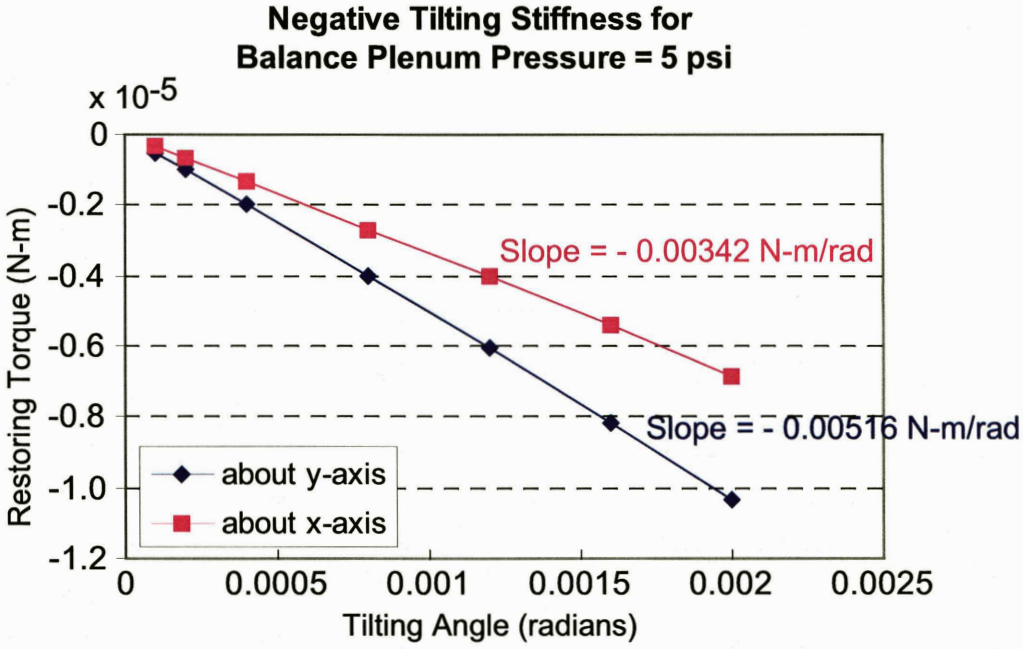

Figure 5-18: Destabilizing torque plotted as a function of rotor tilting angle.

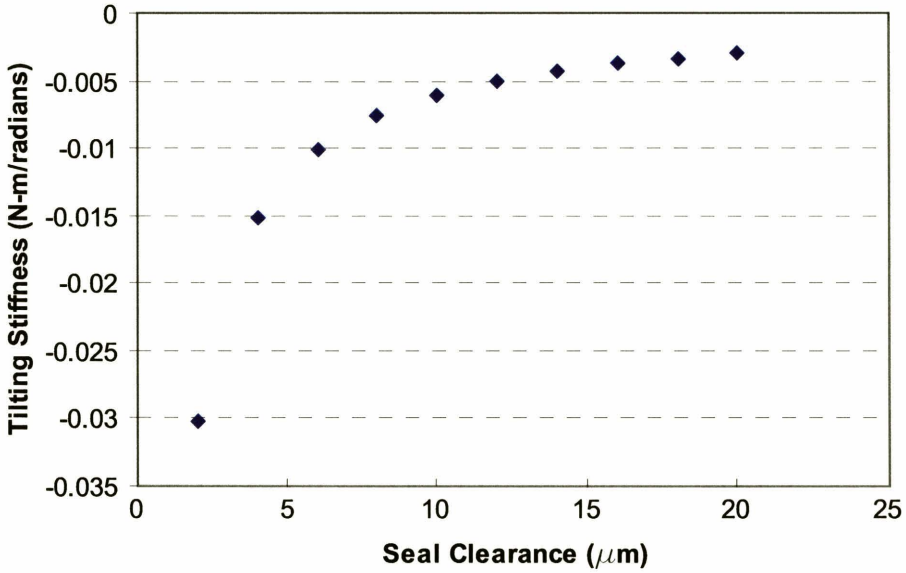

Figure 5-19: Variation of negative tilting stiffness with seal clearance.

As mentioned previously, a high static pressure in the balance plenum has the benefit of reducing the negative radial stiffness due to flow reversal through the journal bearing in the bridge region. However, the magnitude of the negative tilting stiffness also increases for excessively large balance plenum pressures.

For the redesign of the microbearing test device, the seal clearance separating the balance plenum from the aft exhaust will be chosen to be sufficiently large so that issues pertaining to negative tilting stiffness does not arise.

5.1.3 Structural Integrity Issues and Challenges

In this subsection, structural integrity issues with regard to the forward thrust bearing and the rotor blades are examined.

5.1.3.1 Structural Integrity of Forward Thrust Bearing

Several structural integrity issues were uncovered during the course of testing devices incorporating the original microbearing test device design. The most common structural integrity failure involved the supporting structures for the forward thrust bearing. On several occasions, the structures supporting the forward thrust bearing were

blown off in the midst of a high-speed run, and it was imperative to identify the plausible causes for these structural failures. In particular, there were several locations in the vicinity of the forward thrust bearing where etched features were in close proximity to one another. For example, the turbine exhaust and the port for the insertion of the fiber optic sensor for speed measurements were only separated by 40 μm. Since the forward thrust bearing has to withstand pressures on the order of several atmospheres, the presence of features separated by very thin sidewalls can potentially compromise the forward thrust bearing's structural integrity.

The forward thrust bearing plenum has a "scalloped" configuration, with the recesses of the "scallops" housing the thrust bearing orifices. The sidewalls enclosing the plenum have been designed to have a minimum thickness of 100 μm, which suggest several potential hazards. The sidewalls might be too thin to support the large pressures that the thrust bearing are subjected to. Moreover, the thin sidewalls might not offer adequate room for a sufficiently strong bond to form between the thrust bearing plenum (Level 2 of the final bonded stack of wafers, see Appendix A) and the forward foundation plate (Level 1). Bonding of poor quality is subsequently manifested by excessive forward thrust bearing flow leakages experienced during testing. Additionally, the above numerical values for the separation distance between critical features and sidewall thicknesses are upper bounds.

Effects of undercutting arising from DRIE further reduce the minimum separation between features and affect the quality of the fusion bond. Such undercuts arise due to negatively tapered through-etches of the turbine exhaust performed from the aft side of Level 2. The above issues also plague the channel supplying the hydrostatic thrust bearing flow from the forward foundation plate to the thrust bearing plenum, which is nominally separated from the turbine exhaust by 100 μm. Figure 5-20 shows photographs of the interface between Levels 1 and 2 which have been taken under an infra-red microscope for two different builds of the original microbearing test device (Builds 9 and 11). Devices from the build corresponding to Figure 5-20(a) were found to suffer from large flow leakages in the forward thrust bearing, whereas devices from the build corresponding to Figure 5-20(b) had no noticeable forward thrust bearing leakages. This is corroborated by the observation that Figure 5-20(a) shows substantially more

significant undercutting in the bonding surfaces surrounding the turbine exhaust and the thrust bearing plenum and supply channel.

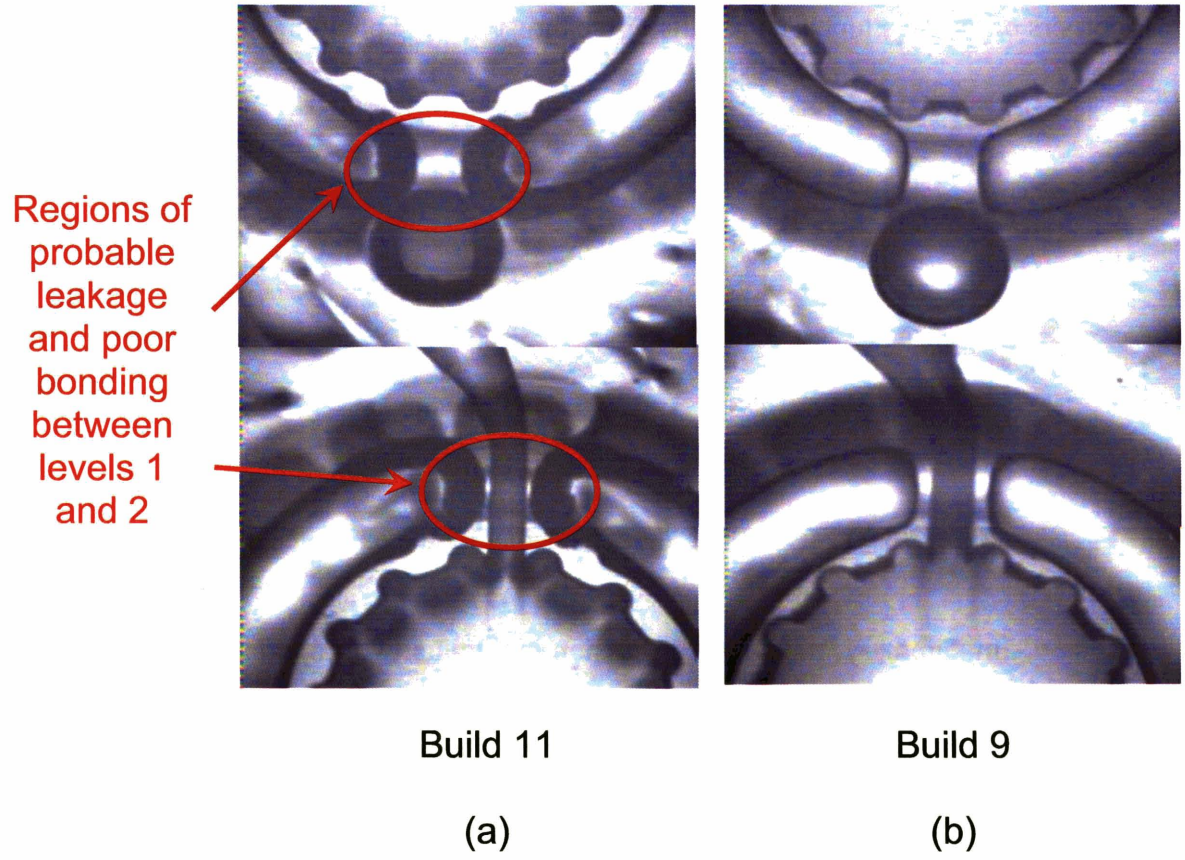

Figure 5-20: Infrared photographs showing interface between levels 1 and 2 for microbearing test device builds with (a) major forward thrust bearing flow leakages, (b) no forward thrust bearing flow leakages.

Another undesirable feature which was observed from scanning electron microscope (SEM) pictures of devices with forward thrust bearing failure was the presence of "dimples". Figure 5-21 illustrates the presence of "dimples" formed around the sharp corners of the channel supplying hydrostatic fluid to the forward thrust bearing plenum. According to Li [43], the presence of these "dimples" is suspected to be due to charging effects on features with small radii of curvature, which result in excessive burrowing by the plasma in the neighborhood of these features. The diameter of these "dimples" is approximately 50 μm, with a depth on the order of 30 μm. The presence of these "dimples" reduces the sidewall thickness of the thrust bearing plenum from a nominal value of 100 μm to 70 μm. Furthermore, they aggravate the levels of stress

concentration around sharp features, which by themselves already serve as localized regions of stress concentration. "Dimples" were also observed to form around sharp corners of the "scalloped" sidewalls of the thrust bearing plenum.

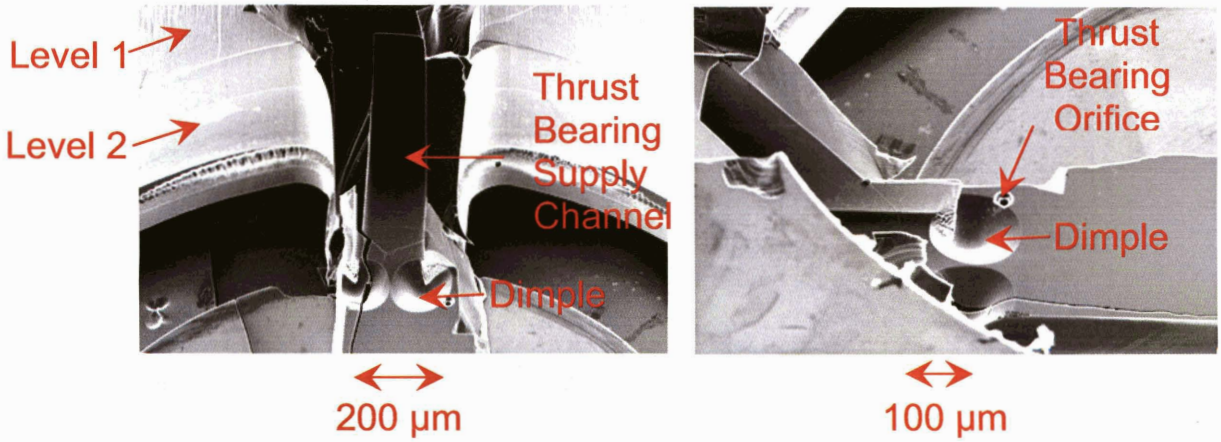

Figure 5-21: SEM micrographs depicting the existence of "dimples".

In summary, the above discussion highlights two important structural integrity considerations. First, critical features have been designed to be separated by sidewalls of at least 200 µm. This provides some allowance for sidewall undercutting, and offers more area for a strong bond to form between wafers. Second, precautions have been made to avoid the use of features with small radii of curvature. These not only act as sites of stress concentration, but also lead to the formation of "dimples", which further weaken the structure.

5.1.3.2 Structural Integrity of Rotor Blades

The structural integrity of the rotor blades is a source of great concern, since the blade roots are subjected to tremendous levels of centrifugal stresses. The problematic "dimples" which permeate the forward thrust bearing also show up in the vicinity of the blades' trailing edges, as shown in Figure 5-22. The culprit responsible for the formation of these "dimples" can again be traced to features with excessively low radii of curvature, which in this case arise from the sharp trailing edges of the blades.

Furthermore, it is evident that the trailing edges of the blades suffer from significant undercutting, which renders an unacceptably small blade root thickness near the trailing edge. The evolution of the "dimples" and undercut as the DRIE progresses

can be seen in Figure 5-9. The absence of a decent fillet greater than 25 μm at the root of the trailing edge, coupled with the thin blade root thickness and "dimples", give rise to significant stress concentrations. It should further be pointed out that subsequent to the DRIE of the blades, an isotropic etch is performed to remove the "fence" along the exit of the journal bearing. Since this isotropic etch attacks the exposed Silicon uniformly in all directions, the profile of the blades' trailing edges will further deteriorate, which is apparent by comparing Figures 5-9 and 5-10. The trailing edge roundness has completely vanished subsequent to the isotropic etch. This highlights one important aspect of microfabrication: solutions devised to solve a problem frequently give rise to other secondary, unforeseen and malignant effects or consequences.

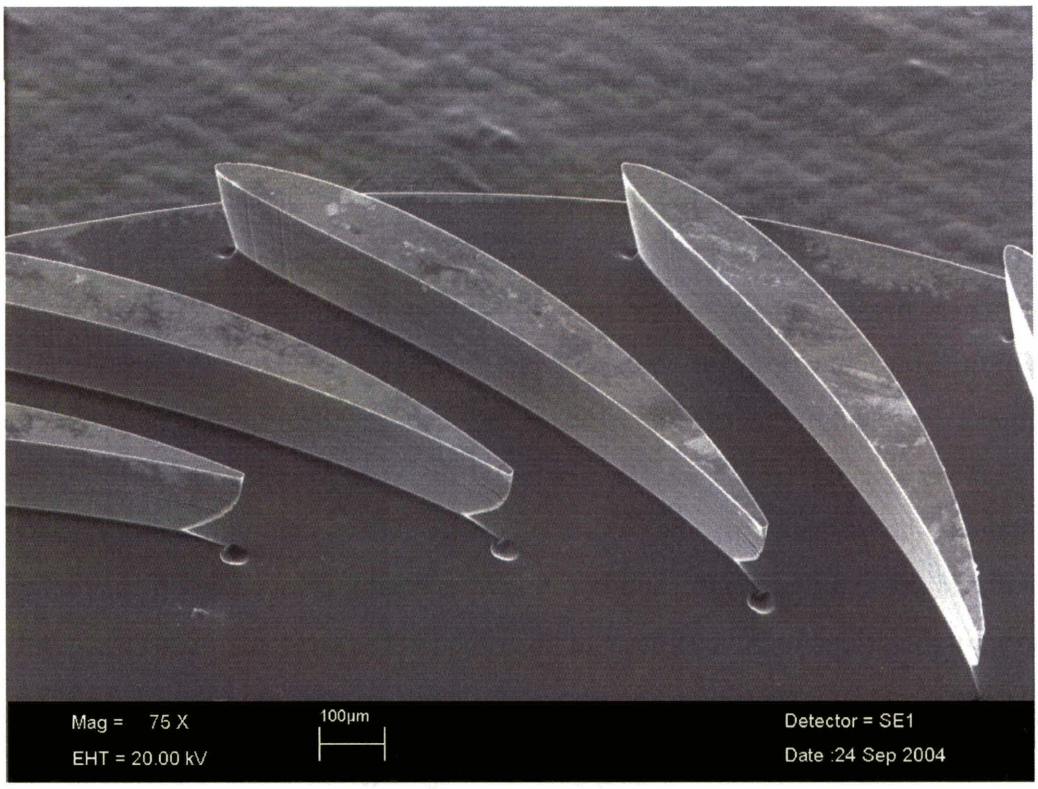

Figure 5-22: SEM micrograph depicting "dimples" and undercutting forming at the blade root of the trailing edges.

5.2 Analysis and Design of New Microbearing Rig

The major lessons acquired from previous experimental testing and analysis of the original microbearing test devices are subsequently applied to the design of a new

microbearing test device. In this section, the salient design considerations are described in detail, including rotordynamic, power and structural considerations.

5.2.1 Rotordynamic Considerations

The key rotordynamic considerations which are addressed in this subsection include analysis and design efforts for the journal and thrust bearings, as well as the annular seals. Provisions are made in the redesign to enable both isotropic and anisotropic journal bearing configurations to be subjected to experimental testing. Variations in journal bearing width are also introduced to facilitate the investigation of journal bearing clearance on bearing stability and performance.

5.2.1.1 Four Plena Journal Bearing Design

In the original microbearing test device, anisotropy in journal bearing stiffness was achieved by supplying the hydrostatic flow via two diametrically opposite plena, each subtending a circumferential extent of 110°. However, as described previously, the presence of the seal in the bridge region results in a negative radial stiffness in the y-direction. Since the origin of the negative stiffness is due to the presence of a flow resistance (the seal in this case) in series with the journal bearing, the most direct remedy to overcome the issue of a negative radial stiffness is to eliminate all unwanted flow resistances in series with the journal bearing. This can simply be achieved by reconfiguring the bridge region and introducing two additional supply plena to the journal bearing in the bridge region, so that the journal bearing essentially opens up or will be fed by plena of approximately uniform static pressures. In addition to overcoming negative stiffness, an increase in the number of journal bearing plena from two to four yields several other significant advantages. First, it allows development of anisotropic stiffness and allows different magnitudes of hydrostatic pressures or flows to be "dialed" into the two newly introduced plena. Isotropic journal bearing operation is thus rendered possible by supplying the four plena with approximately the same hydrostatic supply pressure. On the other extreme, maximum anisotropy can still be achieved by blocking off the flow to the two newly added plena. However, in order to avoid setting up any radial negative stiffness, these two plena have to be physically connected to the inter-blade row pressure

tap so as to minimize any flow through the journal bearing along circumferential regions overlooking the two plena. Furthermore, anisotropy levels between these two limits can also be achieved by supplying a hydrostatic pressure whose magnitude lies in between the supply pressure to the other two journal bearing plena and the inter-blade row static pressure. Such an arrangement permits different levels of anisotropy to be introduced, thus facilitating the investigation of journal bearing performance subjected to varying levels of anisotropy. In the original microbearing test device, there was no direct way to neither monitor nor control any sideloads arising in the y-direction. The introduction of these two new plena minimizes the amount of sideloading in the y-direction when the two plena are connected to the same pressure source. Furthermore, a sideload in the y-direction can also be deliberately introduced for research purposes if the need arises.

The use of four journal bearing supply plena instead of two also fortuitously gives rise to one other benefit. According to the analytical results of Liu [3,15], the whirl instability speed of an anisotropic journal bearing system is approximately given by

$$\Omega_w^2 = -\frac{C_x C_y}{k_{xy} k_{yx}} \left(\frac{K_{xx} - K_{yy}}{C_x + C_y} \right)^2 , \tag{5.1}$$

where K_{xx} and K_{yy} are the anisotropic direct coupled hydrostatic stiffness values in the x- and y-directions, respectively, k_{xy} is the cross coupled hydrodynamic stiffness, C_x and C_y are the damping coefficients in the x- and y-directions respectively. Equation (5.1) shows that for a given set of values for K_{xx}, K_{yy} and k_{xy}, the maximum stability boundary is achieved by choosing the ratio C_x/C_y to be unity. The subtle point to note is that in order to maximize the stability boundary, the anisotropy in direct coupled stiffness has to be maximized, while the anisotropy in the damping coefficients has to be minimized. This implies imposing isotropic static pressure boundary conditions for the pressure field of the fluid flow which contributes to the damping forces. The four plena system is the most ideal mechanism for achieving such an objective, since the elimination of the "bridges" imposes an isotropic and homogeneous boundary condition for the pressure field associated with the damping forces. As mentioned previously, maximum anisotropy in direct-coupled stiffness can be achieved by simply supplying the two opposing plena of 110° circumferential extent with the same static pressure, whilst blocking off the flow to the other two opposing plena.

Although there are many advantages associated with the four plena design, the main shortcoming of such a design lies in the fact that the flows and pressures to the four different plena have to be monitored individually when the journal bearing is not operated in the maximum anisotropic configuration. This requires additional mass flow controllers and metering valves to be introduced to the plumbing or gas-handling system. Furthermore, simultaneous regulation and monitoring of the static pressures and mass flows to the four plena increases the complexity associated with the operation of these micro devices.

5.2.1.2 Design of Seals

The design of the annular seals for isolating the journal bearing plena, the thrust balance plenum and the aft side exhaust are discussed in this section. Efforts are taken to ensure that negative values of radial and tilting stiffness do not arise due to the coupling effects between the seals and the other components of the microsystem. Other important considerations for sizing the seals include the thrust balancing capability of the seals, effects of rotor tip axial deflections at high rotor spinning speeds, and the precision to which the rotor axial position can be controlled.

5.2.1.2.1 Negative Stiffness Considerations

One of the main objectives for the redesign of the seals is to rectify the shortcomings of the original seal design in the microbearing test device. Ideally, the seals have to serve the following crucial roles. First, it has to serve as an isolation between the journal bearing plena and the balance plenum, and has to minimize the amount of flow between them. Furthermore, a well-designed seal has to play an active role in the thrust-balancing of the rotor. Since the turbine pressures increase monotonically with the rotor spinning speed, the downward forces acting on the rotor due to the turbine pressures are expected to increase with speed as well. If the seals are capable of setting up a pressure field on the aft side of the rotor which increases with the spinning speed of the rotor, so as to yield a net upward force whose magnitude approximately matches that of the downward pressure force acting on the rotor, simplification in terms of operation can be achieved. If it was possible for thrust balance to be automatically achieved by the seals

over a wide range of operating speeds, the amount of regulation required for the flows through the balance plenum could be minimized. This relieves the operator from the painstaking task of having to closely monitor the flows through the balance plenum to achieve thrust balancing of the rotor and maintain the rotor in an essentially axially centered configuration.

However, as shown previously, a negative tilting stiffness might result if a single plane annular seal is used. This is a consequence of the static pressure redistribution over the face of the annular seal as the rotor tilts over and a net destabilizing torque acts on the rotor. In the redesign, a labyrinth annular seal configuration has been proposed. By splitting up a single radially wide plain seal into a series of labyrinth seals consisting of an array of several teeth and slots (or grooves), the negative tilting stiffness can be significantly reduced. The annular grooves in between any two teeth serve to even out any static pressure non-uniformities in the circumferential direction, since each groove has negligible hydraulic resistance in the circumferential direction as compared to the teeth. Since the magnitudes of the pressure variations in the circumferential direction are significantly reduced due to the presence of the grooves, the net torques and, as a consequence, destabilizing tilting stiffness experienced by the rotor are appreciably reduced.

A simple hydraulic resistance model has been constructed to elucidate this effect. The labyrinth seal configuration under investigation consists of 4 sets of annular teeth, each of width 50 μm. Each neighboring set of teeth is separated by a groove of width 100 μm. The nominal seal clearance (axial gap separating the teeth and the bottom surface of the rotor) is 2 μm, and each groove has a depth of 300 μm. The outer radius of the outermost tooth is 2.05 mm, whereas the inner radius of the innermost tooth is 1.55 mm. The outer radius of the outermost tooth is open to the four journal bearing plena, while the inner radius of the innermost tooth is exposed to the balance plenum. Anisotropic journal bearing operation is assumed, and a pressure difference of 1 psi is assumed to exist between the two opposing journal bearing plena of 110° circumferential extent and the balance plenum. The remaining two opposing journal plena are assumed to be kept at the same static pressure as that of the balance plenum. Figure 5-23 depicts the circumferential variation of the normalized static pressure along the outermost, center and

innermost groove. The static pressure on each plot has been normalized using the mean static pressure along the entire groove. Plotting in this manner permits the non-uniformity in static pressure along any groove to be assessed. It can be seen that the static pressure non-uniformity is greatest along the outermost groove, and minimum along the innermost groove. Even along the outermost groove, there is only a less than one percent variation in static pressure, thus attesting to the fact that the negligible hydraulic resistance along the circumferential direction of the groove fulfills the role of alleviating any circumferential static pressure non-uniformity. The corresponding mass flow through the outermost and innermost teeth are plotted in Figure 5-24, where a positive mass flow denotes a radially inward flow and a negative mass flow denotes a radially outward flow. Once again, the mass flow non-uniformity is maximum along the outermost tooth and minimum along the innermost tooth.

It is next of interest to evaluate what happens when the rotor tilts over by 0.0005 radians (corresponding to half the maximum allowable tilting angle when physical contact between the rotor and the outermost tooth occurs). The normalized circumferential static pressure variation along each of the three grooves are shown in Figure 5-25, and the mass flow rate through the outermost and innermost teeth are depicted in Figure 5-26. From Figure 5-25, it can be seen that although the tilting of the rotor has resulted in a larger circumferential variation in static pressure along the outermost groove, this variation is still on the order of one percent. The concomitant destabilizing tilting torque acting on the rotor is evaluated to be 2.2×10^{-8} N-m, and this corresponds to a negative tilting stiffness on the order of 4.4×10^{-5} N-m/radian. Such a four teeth, 3 grooves labyrinth seal configuration is thus much more effective, and yields a significantly smaller negative tilting stiffness than the case when a single tooth spanning 200 μm in radial extent is employed. The deep grooves interrupting the teeth serve to even out any static pressure non-uniformity along the circumferential direction and hence prevents huge "pockets" with high and low static pressure from building up and thus reduces the magnitude of the negative tilting stiffness.

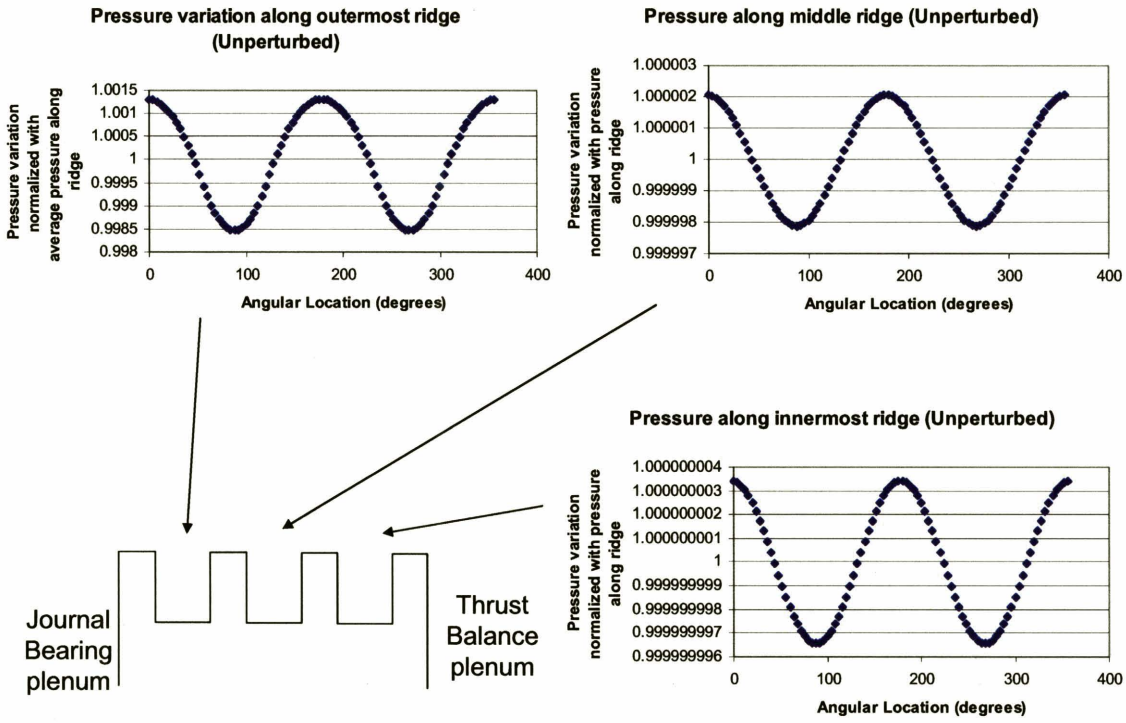

Figure 5-23: Normalized static pressure variation along outermost, center and innermost groove for an untilted rotor.

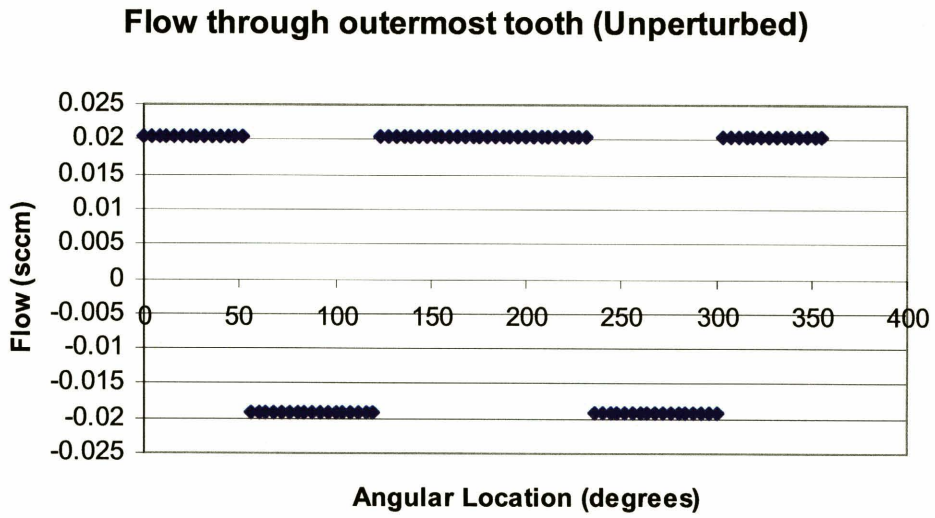

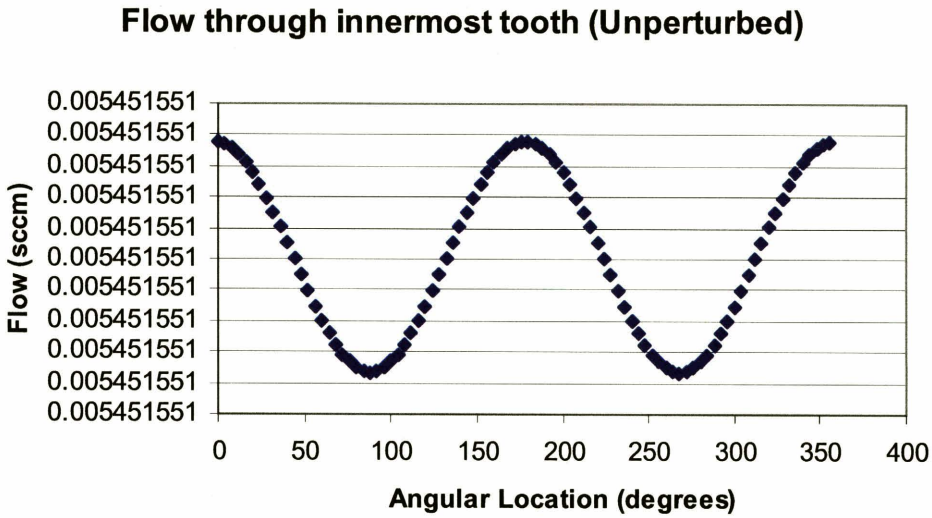

Figure 5-24: Mass flow rate through the outermost and innermost teeth for the case of an untilted rotor.

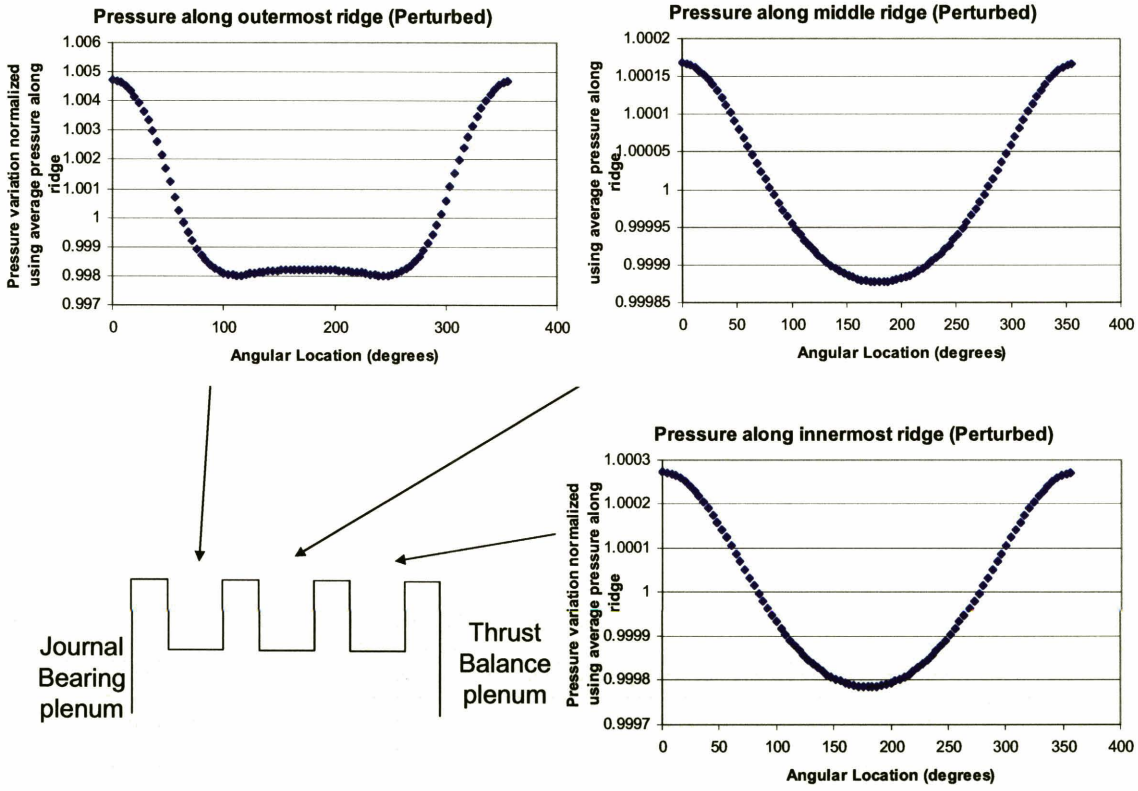

Figure 5-25: Normalized static pressure variation along outermost, center and innermost groove corresponding to a rotor tilting angle of 0.0005 radians.

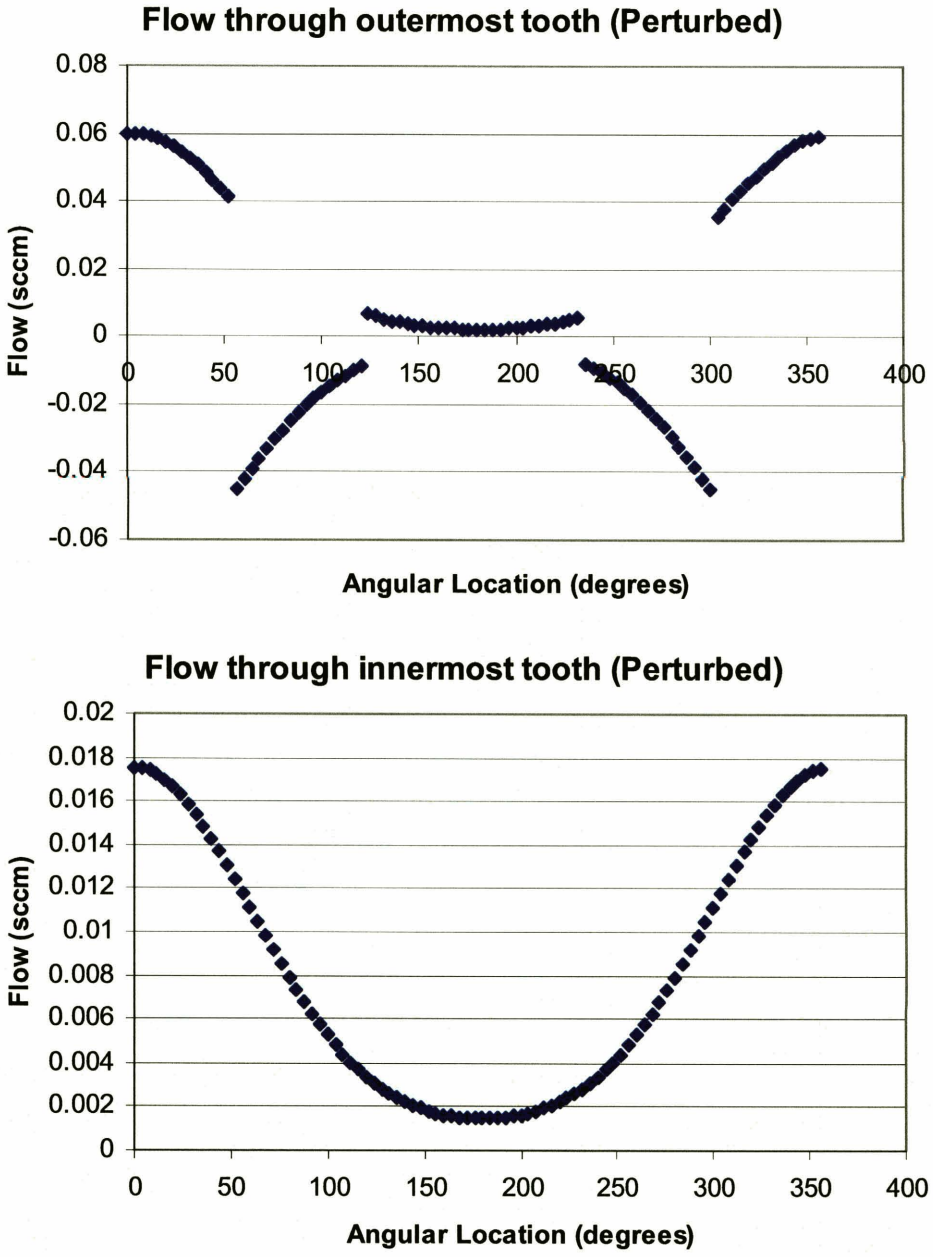

Figure 5-26: Mass flow rate through the outermost and innermost teeth for a rotor tilting angle of 0.0005 radians.

5.2.1.2.2 Thrust Balance Considerations

It is also interesting to compare the thrust balancing mechanism on the original microbearing test device with the redesigned microbearing test device. In the original microbearing test device, most of the pressure drop between the journal bearing plena and aft exhaust occurs across the seal separating the journal plena from the balance plena. In

the absence of any flow through the balance plenum, the pressure across the annular region between the aft exhaust and the balance plenum is almost uniform and marginally higher than the exhaust pressure. There is thus negligible upward force acting on the rotor to counteract the downward force acting on the rotor due to the turbine pressure force, in the absence of any balance plenum flow. As the rotor speed increases, the flow through the balance plenum has to be increased simultaneously to establish a larger pressure drop across the annular seal separating the balance plenum from the aft exhaust, and thus a larger upward pressure force acting on the aft side of the rotor. In the modified design incorporating the labyrinth seals, regions or pockets of high pressure are trapped in the grooves separating the teeth. These high pressure regions can thus serve the useful role of augmenting the upward force acting on the rotor and thus reduce reliance on the balance plenum for thrust balancing purposes.

5.2.1.2.3 Seal Clearance for Outer Labyrinth Annular Seals

In sizing the seal clearances for the outer seals, several conflicting requirements have to be taken into consideration. First, the seal clearance has to be sufficiently small to isolate the journal bearing plena from the balance plenum, and to prevent excessive flow from leaking between the journal bearing plena and the thrust balance plenum. However, two factors limit the minimum clearance which can be implemented. Liu [3] has previously established a four degree-of-freedom rotordynamic model which serves to analyze the dynamic stability of a rotor when its radial motion is coupled to its tilting motion. The four degree-of-freedom model imposes a lower bound on the allowable seal clearance, since an excessively small seal clearance culminates in excessive hydrodynamic torques acting on the rotor. This enhances coupling effects between the radial and tilting modes of the rotor, thus degrading the stability boundary of the overall rotor-bearing-seal system. According to the analytical results of Liu, the minimum outer seal clearance which can be adopted without causing the system to become dynamically unstable for the full range of operating speeds is 4 μm. The other factor which imposes a limit to the minimum allowable seal clearance arises from structural considerations. As the spinning speed of the rotor increases, the rotor blades are subjected to centrifugal forces of increasing magnitudes. Apart from introducing large centrifugal stresses at the

roots of the blades, these centrifugal effects cause a net bending moment to act circumferentially along the rotor disk, thus deforming the rotor disk into the shape akin to an umbrella at high speeds. This "umbrellaing" of the rotor results in a non-zero tip deflection, which in turn renders a monotonic decrease in seal clearance as the rotational speed increases. As will be discussed subsequently in Section 5.2.4.1, the rotor tip deflection is anticipated to be approximately 6 μm at the design speed of 2.4 million rpm. Including the 4 μm minimum clearance which is required to ensure that the rotor-bearing-seal system remains dynamically stable, a total nominal or as-fabricated seal clearance of at least 10 μm is required to ensure that both the structural and dynamic stability requirements are simultaneously met.

Hence, in the redesigned microbearing test device, two nominal values of outer seal clearance have been selected, namely 10 μm and 12 μm. The dynamic stability analysis yields results which are extremely sensitive to the outer seal clearance. A variation in outer seal clearance is thus deemed to be necessary to assess its effects, if any, on the overall system performance. Just like the variations in journal bearing clearance, a difference of 2 μm is necessary to ensure that the microfabrication uncertainties do not outweigh the variation deliberately imposed.

5.2.1.2.4 Seal Clearance for Inner Seal

Similar to the outer seal clearance, several considerations have to be taken in sizing the seal clearance for the inner seals as well. A small inner seal clearance or longer inner seal requires a smaller mass flow supplied to the balance plenum in order to maintain a fixed pressure in the balance plenum for thrust balancing purposes. However, in terms of controllability and operability, a larger inner seal clearance or shorter seal length is desirable, since a larger mass flow rate is necessary to bring about changes in the balance plenum pressure and hence the rotor axial position. This will lead to a design which allows the operator to attain a fine and precise control of the rotor axial position, which is highly desirable from the microbearing test device point of view. Since one of the main objectives of the microbearing test device is to investigate bearing dynamics and stability, it is invaluable to have the capability of controlling the rotor axial position to high levels of precision. Penalties associated with larger mass flow rates are acceptable,

since mass flow consumption is not of paramount concern in the design of the microbearing test device.

A simple analytical model was constructed to assess the mass flow and pressure requirements for the balance plenum. A schematic showing the aft side of the rotor, together with the associated outer labyrinth seals, inner seals and aft thrust bearing, is shown in Figure 5-27. At design conditions, the inter-blade row static pressure was estimated to be 45 psig, and a hydrostatic journal bearing differential pressure of 5 psi was assumed to be applied across the bearing. The journal bearing supply plena was thus assumed to have a static pressure of 50 psig, and the aft side exhaust was assumed to be vented to atmosphere. Assuming an outer seal clearance of 4 μm, it was possible to ascertain the mass flow through the outer seal as a function of the balance plenum static pressure. Given a inner seal clearance, the mass flow through the inner seal can also be determined as a function of the balance plenum static pressure. Knowledge of the mass flow requirements through the outer and inner seals for different balance plenum static pressures then allows the mass flow through the balance plenum to be evaluated as a function of the balance plenum static pressure, by invoking mass conservation or continuity. Figure 5-28 shows analytical results for the net upward force exerted by the seals and balance plenum plotted against the mass flow supply to the balance plenum. Three sets of curves have been shown, each corresponding to a different inner seal clearance. The net downward force exerted on the rotor due to the flow through the turbine is estimated to be 1.2 N. It can be observed from Figure 5-28 that a larger inner seal clearance implies a larger mass flow supply to the balance plenum to balance out the downward force of 1.2 N due to the turbomachinery. However, as discussed above, controllability and operability play a more dominant role than mass flow requirements in dictating the exact configuration to adopt. From Figure 5-28, it can also be seen that a larger inner seal clearance yields a smaller slope, thus implying a smaller axial force sensitivity corresponding to the same change in mass flow to the balance plenum. It should be noted that the mass flow to the balance plenum is regulated by means of metering valves. A smaller force sensitivity thus implies finer or more precise control, since a larger change in mass flow (translating to a larger change in the metering valve setting) is required to bring about the same variation in axial force and hence rotor axial

position. There is also one further disadvantage arising from selecting a smaller inner seal clearance from the operability point of view. Referring again to Figure 5-28, the balance plenum mass flow can attain both positive and negative values. Positive balance plenum mass flows implies a net positive flow supplied into the balance plenum from some external source, whereas negative values imply suction or mass flow extraction out of the balance plenum to some external sink. If the inner seal clearance is excessively small, the balance plenum mass flow might alternate between positive and negative values around the vicinity corresponding to an axial force of 1.2 N, thus manifesting an alternation between blowing and suction being applied to the balance plenum. This is clearly undesirable, as it introduces additional complications to the testing and operating procedures, in addition to the fact that suction entails additional equipment like a vacuum pump, valves and other accessories. Furthermore, since the value of 1.2 N is only a rough estimation yet to be verified from detailed experimental testing, a more robust design results from selecting a larger inner seal clearance. This is because even if the axial downward force due to the turbomachinery departs significantly from 1.2 N, thrust balancing and regulation of rotor axial position can still be achieved solely by means of blowing, without having to resort to suction.

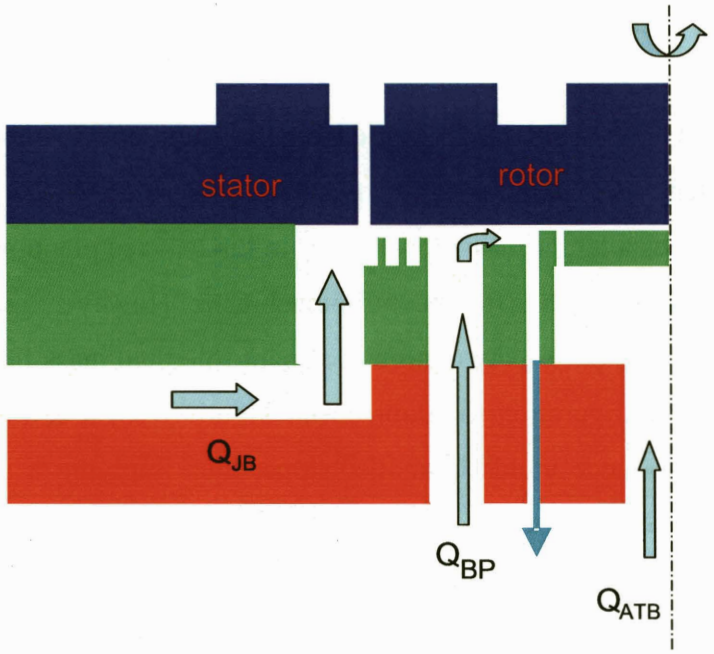

Figure 5-27: Schematic showing the aft side of the rotor, together with the associated outer labyrinth seals, inner seals and aft thrust bearing.

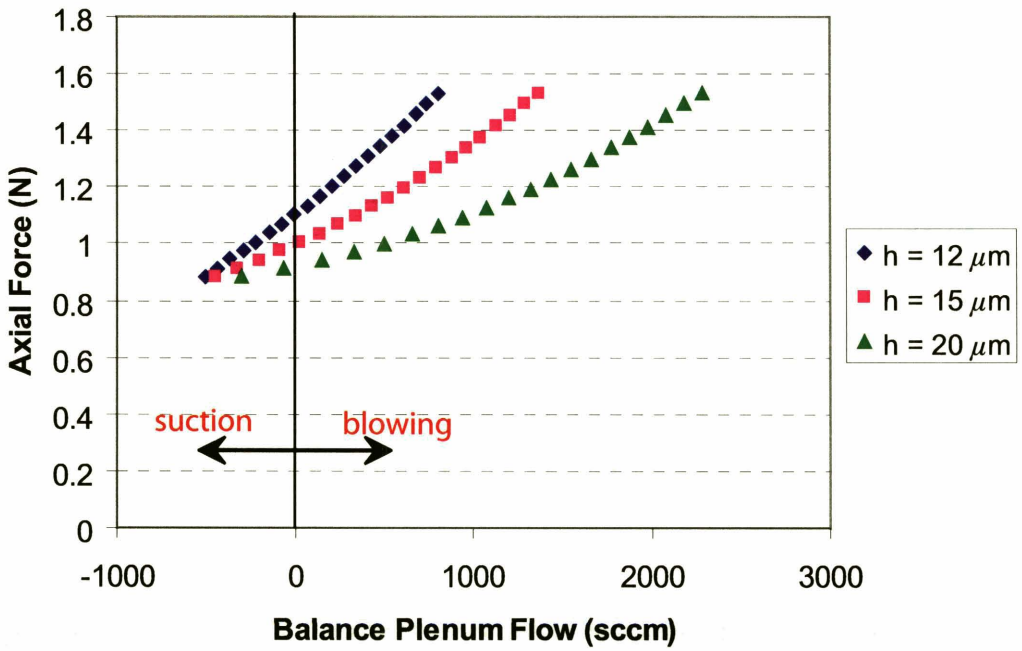

Figure 5-28: Analytical results for the net upward force exerted by the seals and balance plenum plotted against the mass flow supply to the balance plenum for different inner seal clearances.

As shown previously, issues pertaining to negative axial and tilting stiffness may arise when the flows through the seals choke due to the effects of compressibility. It is thus necessary to assess the adverse impact of flow choking on the overall axial and tilting stiffness of the system. Figure 5-29 shows the balance plenum static pressure plotted against the balance plenum mass flow for different values of inner seal clearance. The corresponding tilting stiffness due to the inner seal is plotted as a function of the balance plenum supply pressure in Figure 5-30. For a inner seal clearance of 20 μm, the flow through the inner seal chokes when the balance plenum pressure is approximately 17 psi. Using a smaller inner seal clearance requires larger balance plenum supply pressures to be applied before flow choking occurs and thus delays the onset of flow choking. However, larger magnitudes of negative stiffness are liable to occur after flow choking sets in for smaller inner seal clearances. This is another consideration that discredits smaller inner seal clearances.

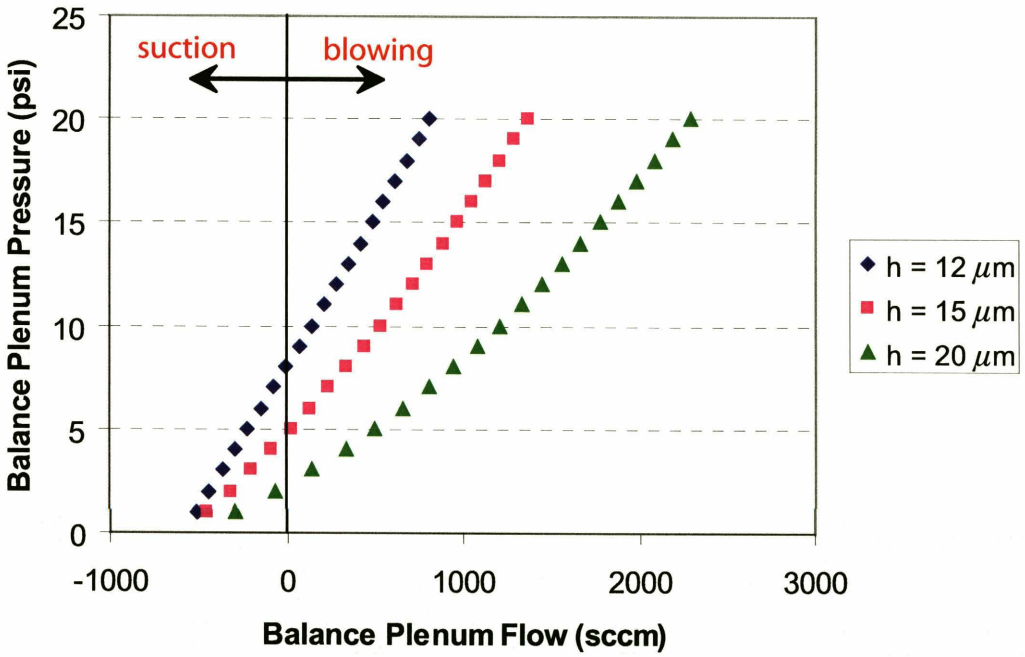

Figure 5-29: Balance plenum static pressure plotted against balance plenum mass flow for different values of inner seal clearance.

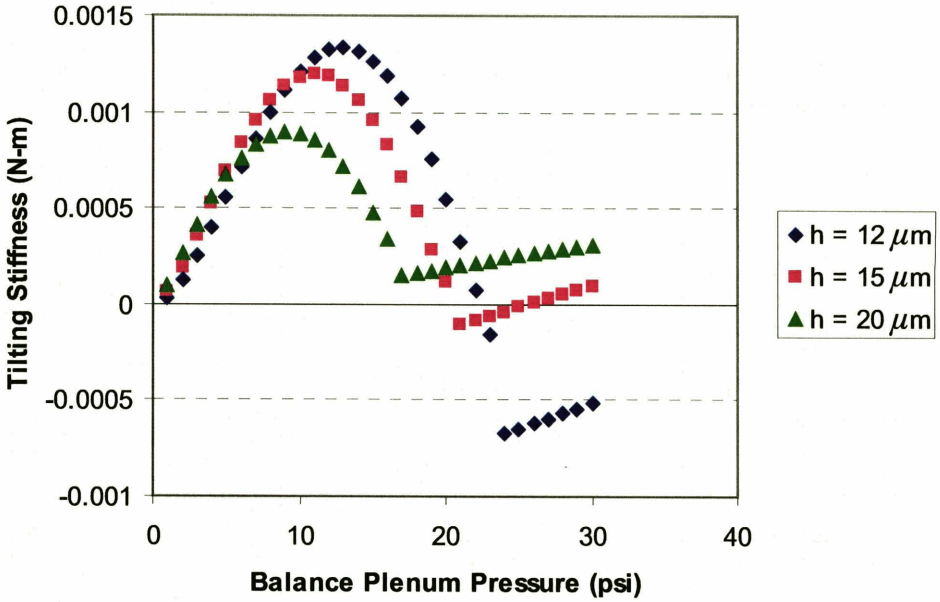

Figure 5-30: Tilting stiffness due to inner seal for different values of inner seal clearance.

Based on the above analyses and discussion, the inner seal clearance has been selected to be 20 μm.

5.2.1.3 Thrust Bearing Design

The original microbearing test device had forward and aft thrust bearings with different geometric configurations. The forward thrust bearing had an outer radius of 0.7 mm and consisted of 14 orifices evenly distributed at a radial location of 0.55 mm. On the other hand, the aft thrust bearing had an outer radius of 0.9 mm and consisted of 18 orifices uniformly distributed at a radial location of 0.75 mm. All orifices had a nominal diameter and length of 10 μm and 100 μm, respectively. The design specification for the total thrust bearing clearance was chosen to be 3 μm.

On the redesigned microbearing test device, the forward and aft thrust bearings have been designed to be geometrically similar. Both thrust bearings have an outer radius of 0.9 mm and consist of 18 orifices evenly distributed along a radial location of 0.7 mm. The length and diameter of the orifices are maintained at 100 μm and 10 μm, respectively. The geometry of the orifices are unchanged, since the associated microfabrication processes have been shown to be capable of yielding orifices which meet the design specifications. Increasing the aspect ratio of the orifices by either increasing the length or reducing the diameter of the orifices may require considerable resources to be invested in sourcing for an etching recipe which is able to yield orifices which meet the required specifications. Figure 5-31 shows the thrust bearing axial natural frequency plotted against the total thrust bearing gap, corresponding to a supply pressure of 60 psi applied to both thrust bearings having the above geometric configuration. A value of 5.0 μm has been selected for the total thrust bearing clearance to maximize the axial stiffness. Corresponding to a total thrust bearing gap of 5.0 μm, analytical results for the axial natural frequency have been plotted against the thrust bearing supply pressure in Figure 5-32.

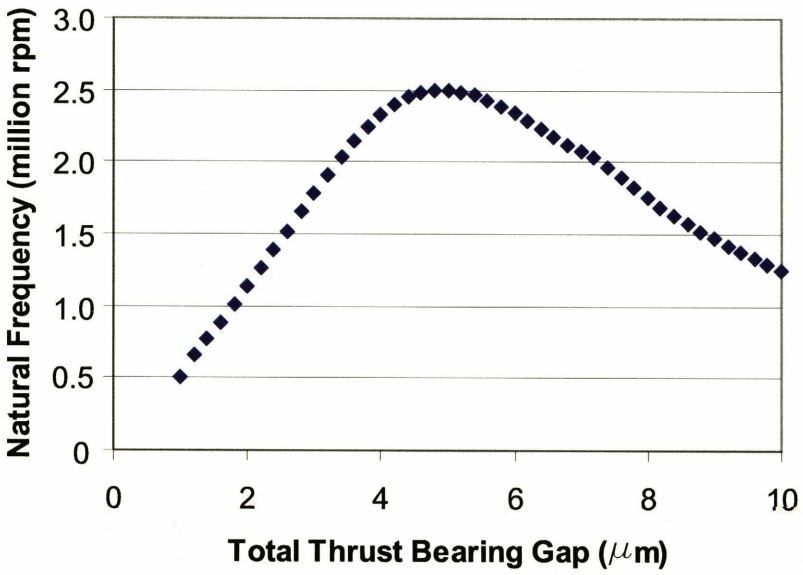

Figure 5-31: Thrust bearing axial natural frequency plotted against total thrust bearing gap, corresponding to a supply pressure of 60 psi applied to both thrust bearings.

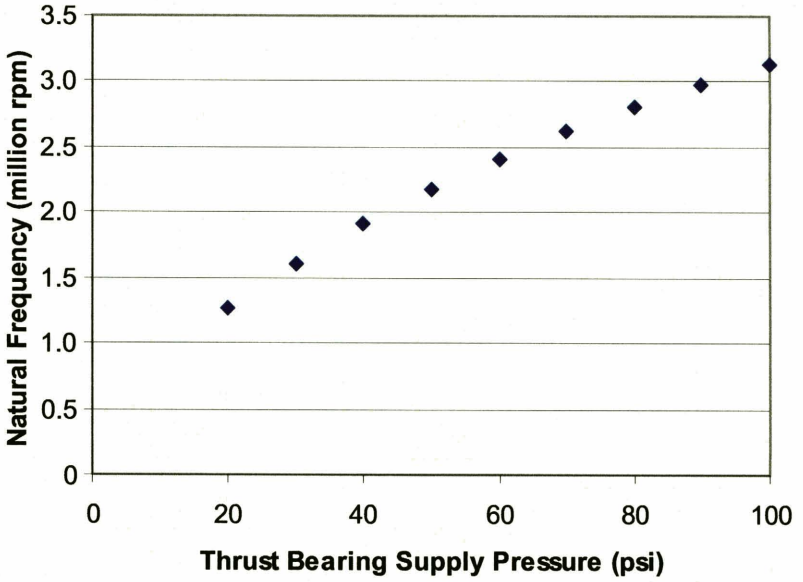

Figure 5-32: Thrust bearing axial natural frequency plotted against thrust bearing supply pressure for a total thrust bearing gap of 5 μm.

The modifications adopted for the design of the thrust bearings are motivated by several factors. Unlike the original microbearing test device, the forward and aft thrust bearing geometries are chosen to be identical on the redesigned microbearing test device. This provides an invaluable and convenient avenue for maintaining the rotor in an axially centered position due to the following reasons. The pressure distribution and hence the axial force acting on either the forward or aft thrust bearing pad depend solely on the

bearing clearance, the mass flow, the fluid viscosity and the bearing geometry. Consider a rotor supported axially solely by the thrust bearings. In the absence of any axial force arising from the flow through the turbine, the annular seals and the balance plenum, the upward force exerted on the rotor by the aft thrust bearing must balance the downward force due to the forward thrust bearing. Since both thrust bearings have similar geometries, the static pressure distribution along both thrust bearing pads must be identical as well. In addition, if both thrust bearings have identical mass flows, the forward and aft thrust bearing axial clearances must then be identical, thus implying that the rotor is axially centered. The corresponding mass flow rate is noted and during the course of the experiments when the rotor is accelerated to high speeds, the rotor can be maintained in an axially centered location by regulating the flow to the balance plenum to maintain the same thrust bearing mass flow. The above technique is also applicable even if both thrust bearings have different orifice dimensions arising from DRIE etch variations. In this case, the supply pressures to both thrust bearings differ, but the mass flows through both bearings still have to be identical to maintain the rotor in an axially-centered location. However, the above argument is no longer valid when both thrust bearings do not have the same geometric configuration, as in the original microbearing test device. In that case, it is impossible to ascertain whether the rotor is axially centered or not by simply matching the mass flows through both bearings. In summary, using thrust bearings of identical geometries allows the axial centering of the rotor to be achieved much more easily.

As compared to the original microbearing test device, the redesigned microbearing test device has a larger forward thrust bearing. This has the direct beneficial effect of increasing the total axial and angular or tilting stiffness of the overall thrust bearing system.

The total thrust bearing axial clearance in the original microbearing test device was selected to be 3 μm, which raises several disconcerting issues. First, the total thrust bearing gap of 3 μm is found to be suboptimal, based on the results of the analytical model, which has been plotted in Figure 5-33. The axial stiffness of the overall thrust bearing system is found to maximum for a total thrust bearing clearance ranging between 4 to 5 μm. Corresponding to a total thrust bearing gap of 3 μm, the axial natural

frequency is approximately 1.3 Mrpm, which is significantly lower than the design speed of 2.4 Mrpm. The other issue of grave concern is the allowable rotor tip deflection. The total 3 μm thrust bearing clearance is formed on the original microbearing test device by performing a shallow etch of 1.5 μm depth on the bottom side of level 2 and a similar 1.5 μm shallow etch on the forward side of level 4. The latter shallow etch of 1.5 μm depth is performed concurrently with the seal clearance for the annular seal separating the journal bearing plena from the balance plenum. At the design speed of 2.4 million rpm, the rotor tip deflection is anticipated to be on the order of 3 μm. If the rotor is axially centered between both thrust bearings, the nominal seal clearance of 1.5 μm is clearly inadequate to accommodate the 3 μm tip deflection of the rotor. On the redesigned microbearing test device, the shallow etch for the thrust bearing clearance is performed separately from that for the seal clearance. The seal clearance has also been selected to accommodate for the anticipated rotor tip deflection.

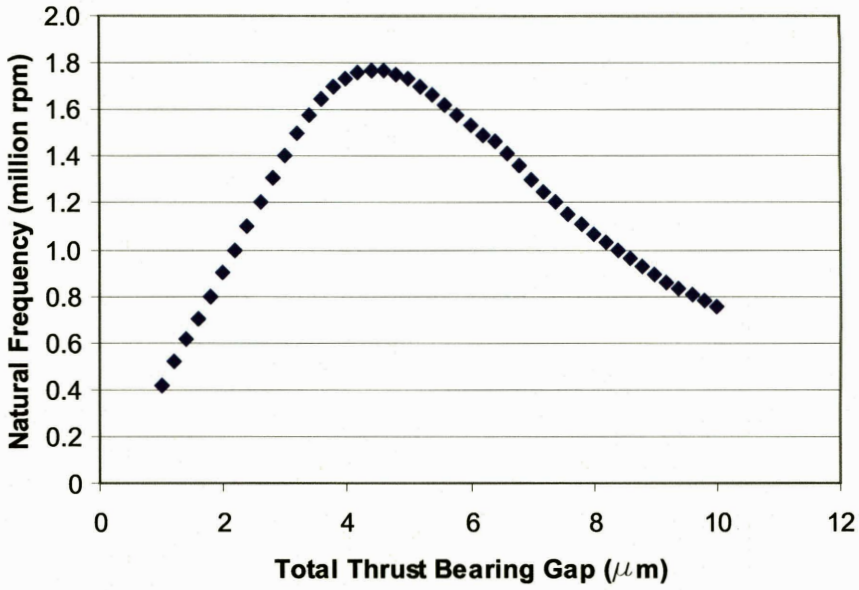

Figure 5-33: Thrust bearing axial natural frequency plotted against total thrust bearing gap for original microbearing test device.

5.2.1.4 Device Variations

One special feature of the redesigned microbearing test device is the provision for purposeful variations in key dimensions to be incorporated into different devices on the

same wafer, so as to facilitate the systematic study and investigation of the effects of various critical geometric parameters on bearing performance. Two main factors have rendered this possible. The first arises from the use of 6-inch wafers, which allows a total of 48 devices to be simultaneously microfabricated on the same build. This is in stark contrast to the original microbearing test device which was fabricated on 4-inch wafers, with a total of at most 12 operational devices for each build. A four-fold increase in the number of potentially available devices thus justifies the incorporation of several variations, since the likelihood of obtaining a sufficient number of devices for each variation is significantly increased.

The use of double-layer, donor-receiver, drop-in rotors serves as a second impetus for geometric variations to be introduced. According to the analytical models proposed by Liu [3], one of the key parameters affecting journal bearing performance and stability is journal bearing width or clearance. The redesigned microbearing test device thus has to incorporate such variations, which were not easily achievable previously. On the original microbearing test device, variations in journal bearing width necessitated features of different clearances to be patterned and etched. However, accurate profile control of the journal bearing proved to be challenging, since a journal bearing etch recipe which optimized the profile for one particular width often yielded unacceptable profiles for other widths. This was circumvented by using a new rotor fabrication scheme proposed by Li [43]. In this new scheme, annular rings of varying inner and outer diameters constituting the journal bearing are patterned and etched. However, the etched widths or clearances of the journal bearings are held constant, so that the same etching recipe can be simultaneously applied to all the annular rings. After the rotors have fallen off subsequent to the blade-etch process, variations in journal bearing width are achieved by swapping neighboring rotors with one another. The rotor originating from a hole with a particular diameter is inserted into a neighboring hole with a different diameter. Devices with varying journal bearing widths are thus achievable by employing this "donor-receiver" scheme.

Several factors have to be further considered in deciding the actual variations in journal bearing width to be incorporated. Previous microfabrication experience has shown that the journal bearing width varies by ± 1 μm from device to device, even when

all the devices from the same build are designed to have identical nominal journal bearing widths, and the same journal bearing etch recipe is used. Therefore, it is not statistically meaningful to deliberately incorporate variations in journal bearing width of less than 2 μm, since this is within the range of the fabrication tolerance or uncertainty achievable using current DRIE technology. As alluded to in the previous discussion, an excessive number of variations has to be avoided, so that there is a sufficient number of devices available for testing of each variation. Based on damping considerations, a smaller journal bearing clearance is beneficial to journal bearing performance. However, there exists a minimum clearance below which dynamic instability sets in below the design speed of 2.4 Mrpm when a journal bearing hydrostatic differential pressure of 5 psi is applied across the bearing. Based on the modeling results of Liu [3], the minimum journal bearing clearance required for stable operation up to the design speed is 14 μm. Hence, three different journal bearing widths were selected for the redesigned microbearing test device, namely 14 μm, 16 μm and 18 μm. Liu [3] has further shown using a 4 degree-of-freedom rotordynamic model that dynamic stability is compromised due to increasing coupling effects between the radial and tilting motions of the rotor. For the microbearing test device, the greatest source of this coupling arises from the seals segregating the journal bearing plena and the balance plenum. An excessively small seal clearance accentuates the cross coupling and promotes dynamic instability. A seal clearance of at least 4 μm is required to ensure dynamic stability.

Furthermore, the centrifugal forces acting on the blades result in a bending moment acting on the rotor disk, which causes the disk to deform into an "umbrella" like configuration, having a shape which is concave downwards. As is shown subsequently in the calculations presented in Section 5.2.4.1, the rotor tip is anticipated to deflect downwards by 6 μm at the design speed of 2.4 Mrpm. This implies that a minimum as-fabricated seal clearance of 10 μm is required to simultaneously prevent rotor contact with the static structure, as well as to ensure dynamic stability. Once again, the analytical 4 degree-of-freedom model indicates that the stability characteristics are very sensitive to the seal clearance. It is thus reasonable to allow for variations in seal clearance, in view of fabrication and modeling uncertainties. As a consequence, two different seal clearances of 10 μm and 12 μm were selected. The difference of 2 μm was chosen to

ensure a discernible difference in seal clearance, beyond the inherent etch variations arising from the DRIE process. With a total of three different variations for the journal bearing width and a total of two sets of variations for the seal clearance, this amounts to a total of six different variations for the 48 devices in the redesigned microbearing test device.

Figure 5-34 shows how the 6 different variations are being spread out among the 48 devices on a 6-inch wafer. Three devices have been shown hatched on the bottom right hand corner of the wafer in Figure 5-48. These three devices essentially retain the original microbearing test device design on the aft side, as well as the original turbine blade design. The original intention for the incorporation of these devices was to use them as a basis or standard to assess the improvements, or lack thereof, due to modifications which have been incorporated on the other 45 devices.

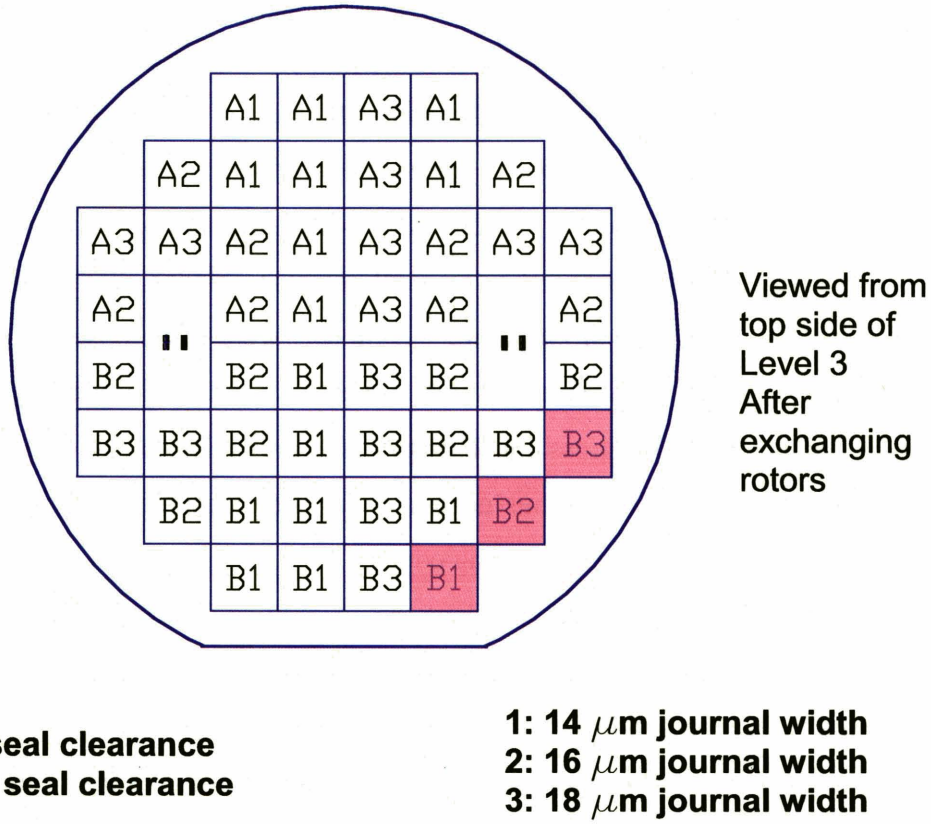

Figure 5-34: Arrangement of 48 devices with 6 major device variations.

5.2.2 Power Requirements

In this section, the efforts undertaken to redesign the turbine blades using CFD are described. The torque and power output of the turbine are evaluated to ensure that the turbine will be able to satisfy the torque and power requirements of the bearings and seals.

5.2.2.1 Turbine Redesign

Turbomachinery analysis and design also constituted one major facet in the redesign of the microbearing test device. It was imperative to analyze the performance of the turbine so as to ensure that the power output from the turbine was *adequate to* overcome the power dissipation associated with the viscous drag due to the thrust and journal bearings, as well as the labyrinth seals. One other motivating factor for the redesign of the turbine blades arises from structural integrity considerations. The newly proposed double-layer rotor concept required a blade height that was approximately twice the height of the blades in the original design. If the original turbine blade design was incorporated in the modified rig, the principal stresses at the root of the turbine blades would approximately quadruple at the same rotational speed. It was thus necessary to examine the various available options and configurations for reducing the turbine blade root stresses. Furthermore, the original turbine blades had trailing edges with unacceptably small radii of curvature. "Dimples" were often observed in the vicinity of the trailing edges as a consequence. The presence of these "dimples" was undesirable, as they serve as regions of stress concentration and thus compromise the structural integrity of the turbine blades. It was thus necessary for the redesigned turbine blades to achieve larger radii of curvature at the trailing edges.

One approach adopted to reduce the centrifugal stresses acting on the rotor blades was to shift the blades radially inwards. This had the effect of alleviating the centrifugal force and hence the bending moment acting on each blade. Another approach was to use thicker blades in order to increase the second moment of area about the bending axis of each blade and thus reduce the bending stresses experienced by the blades. The turbine stator and rotor blades were designed with the assistance of Gong [21]. A plan view of the new turbine design is shown in Figure 5-35(a), which can be compared to the original

turbine design shown in Figure 5-35(b). In order to reduce the undesirable effects of stress concentration and the formation of "dimples", the radius of curvature of the leading and trailing edges of the rotor blades was increased from 15 μm in the original turbine blade design to more than 35 μm in the modified design.

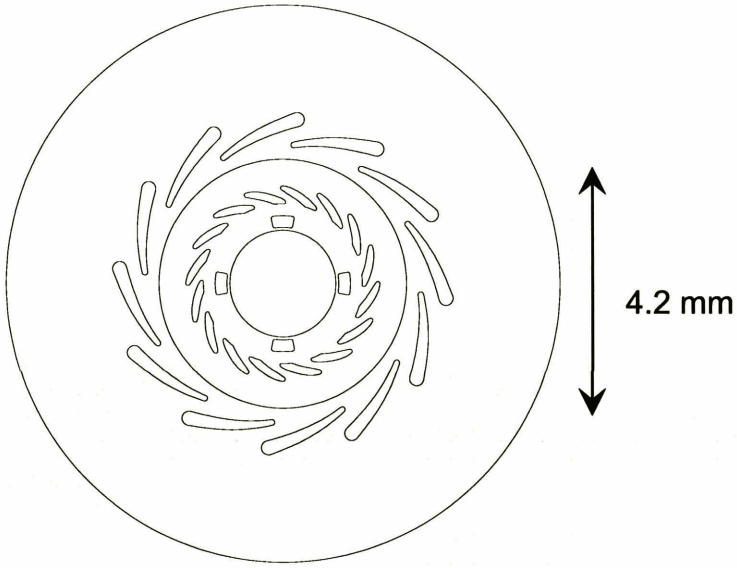

(a)

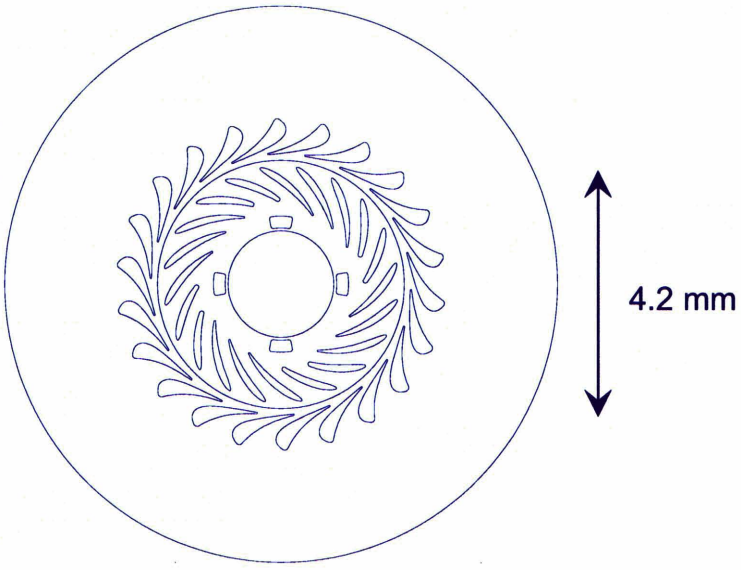

(b)

Figure 5-35: (a) New turbine design and (b) Original turbine design.

The flow through the nozzle guide vanes (NGV's) was assessed using a 2D cascade code MISES [44]. It is a finite-volume code based on a viscous-inviscid model that solves the Euler equations coupled with the integral boundary-layer equations. One issue of concern was the large inlet flow angle or blade angle near the leading edge of the NGV's, which might give rise to leading edge separation of the incoming turbine flow. This leads to the undesirable consequences of flow blockage, losses in stagnation pressure and a drop in efficiency of the turbine. The cambering direction of the NGV's was incorporated to implement a "free-vortex" design. The computational grid near the leading edge of the NGV's is shown in Figure 5-36. Figures 5-37 and 5-38 show contours of the static pressure and Mach number along the NGV's corresponding to design conditions, where the mass flow rate through the stator was matched with that through the rotor blades obtained from another CFD calculation, details of which will be described shortly. The exit Mach number of the flow from the NGV's was found to be approximately 0.34. From the contour plots, it was apparent that the flow through the NGV's was devoid of shocks, which was crucial, since the presence of shocks deteriorate the overall turbomachinery performance, in addition to giving rise to unstable turbine performance due to the extreme sensitivity of the shock location. In order to evaluate the extent of any flow separation on the suction surface near the leading edge, the skin friction coefficient C_f is plotted along the suction and pressure surfaces, as shown in Figure 5-39. Regions of flow separation are simply represented by locations with negative values of C_f. It can be seen that flow separation is only limited to a small region along the suction surface near the leading edge. The flow rapidly reattaches and the separation bubble is not seen to have a detrimental effect on the overall flow through the rest of the NGV and its performance.

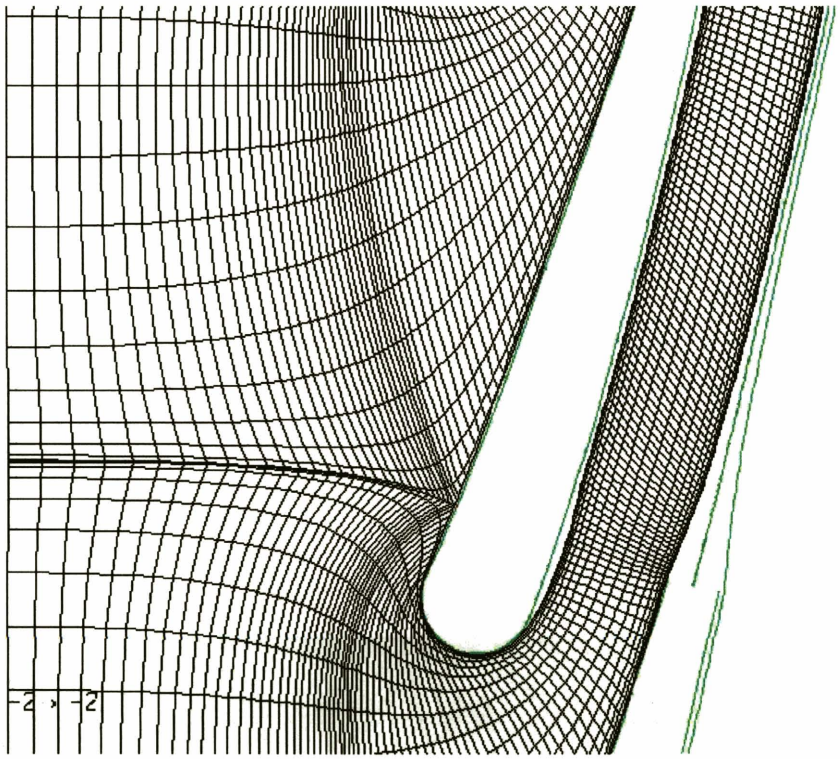

Figure 5-36: Computational grid near leading edge of NGV. Note the (m', θ) transformed coordinate system adopted by MISES [44].

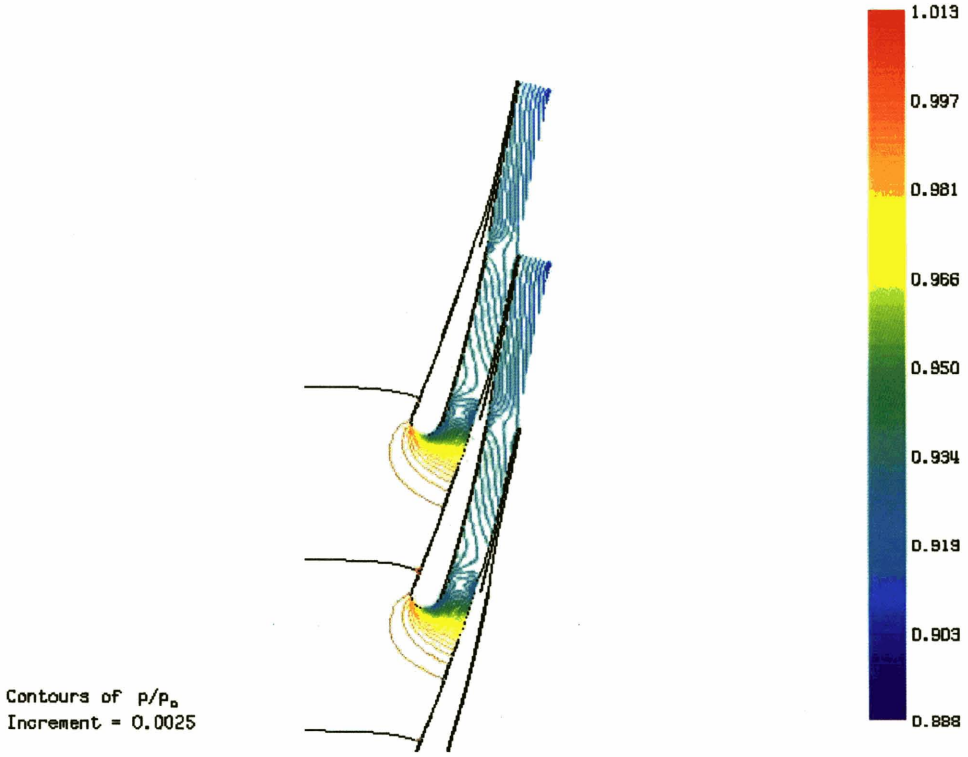

Figure 5-37: Contour plot of static pressure along NGV's in (m', θ) coordinate system of MISES.

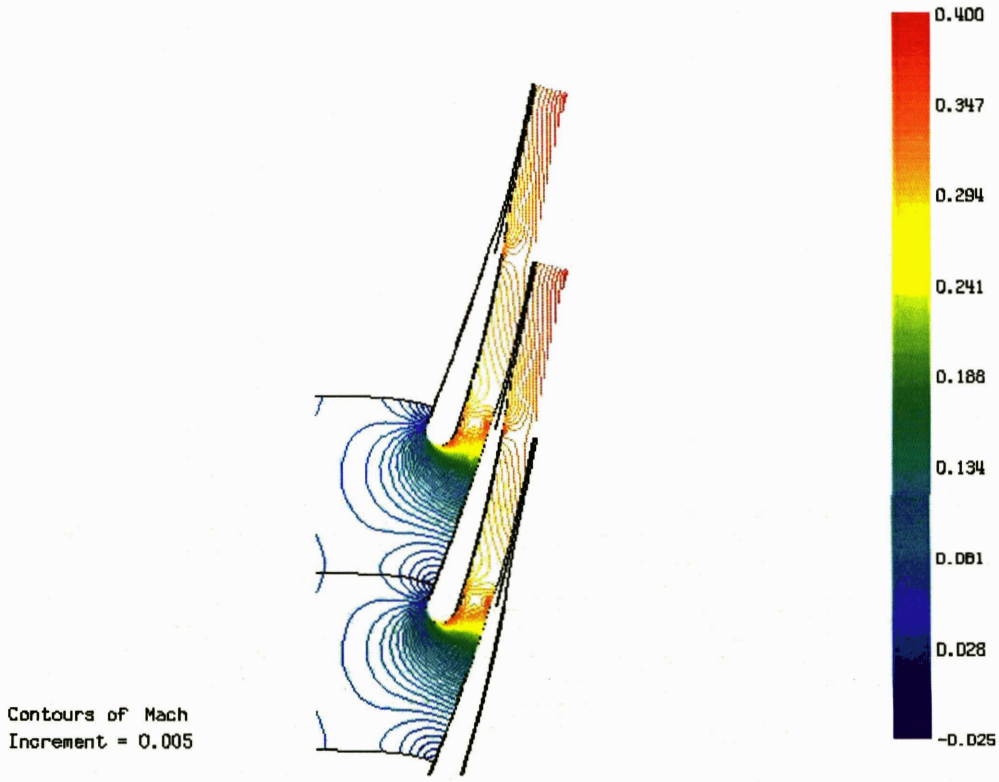

Figure 5-38: Contour plot of Mach number along NGV's in (m', θ) coordinate system of MISES.

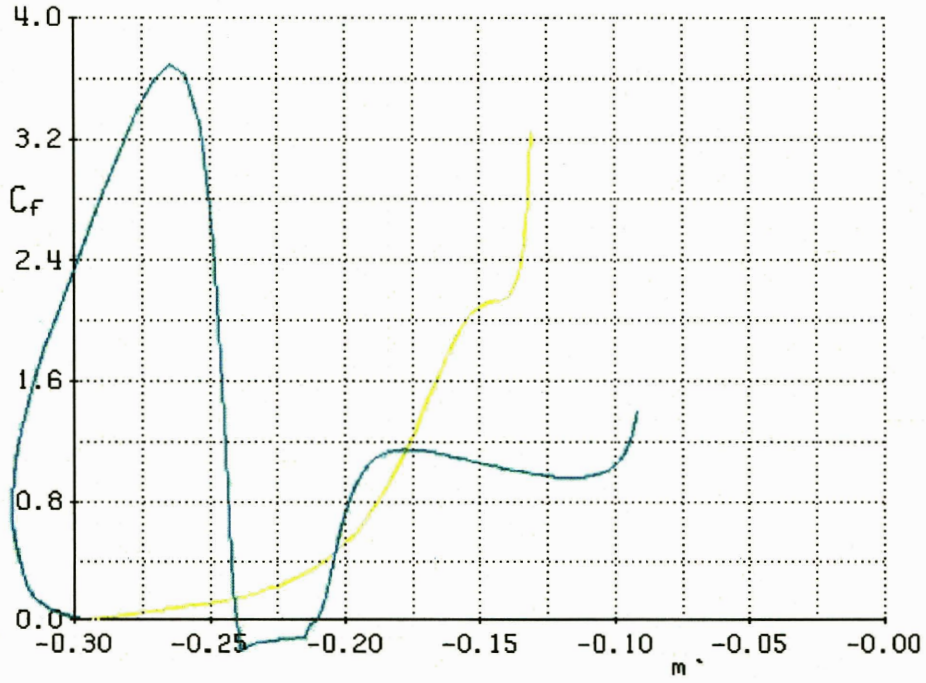

Figure 5-39: Skin friction coefficient along suction and pressure surfaces of NGV's. The horizontal axis m' is a dimensionless coordinate system used in MISES [44].

The flow through the rotor was analyzed using the commercial CFD package FLUENT. The absolute and relative Mach numbers of the flow through the rotor at the design speed are depicted in Figures 5-40 and 5-41, respectively. In the vicinity of the rotor blades, the maximum relative Mach number is only limited to values marginally above unity. Strong shocks are thus not anticipated to form and adversely affect the flow through the rotor and the overall performance of the turbine.

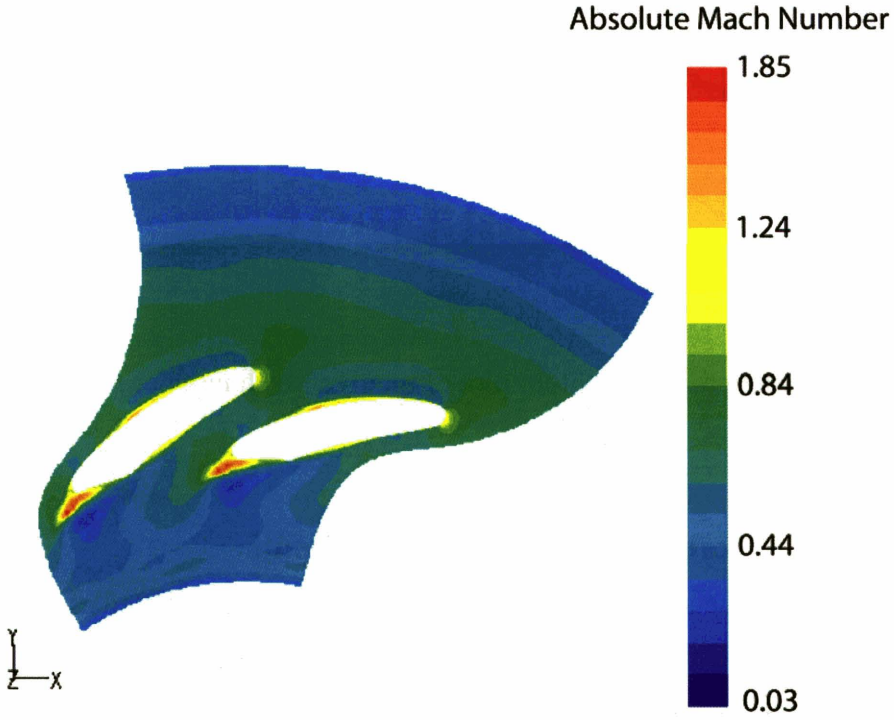

Figure 5-40: Contour plot of absolute Mach number for turbine rotor.

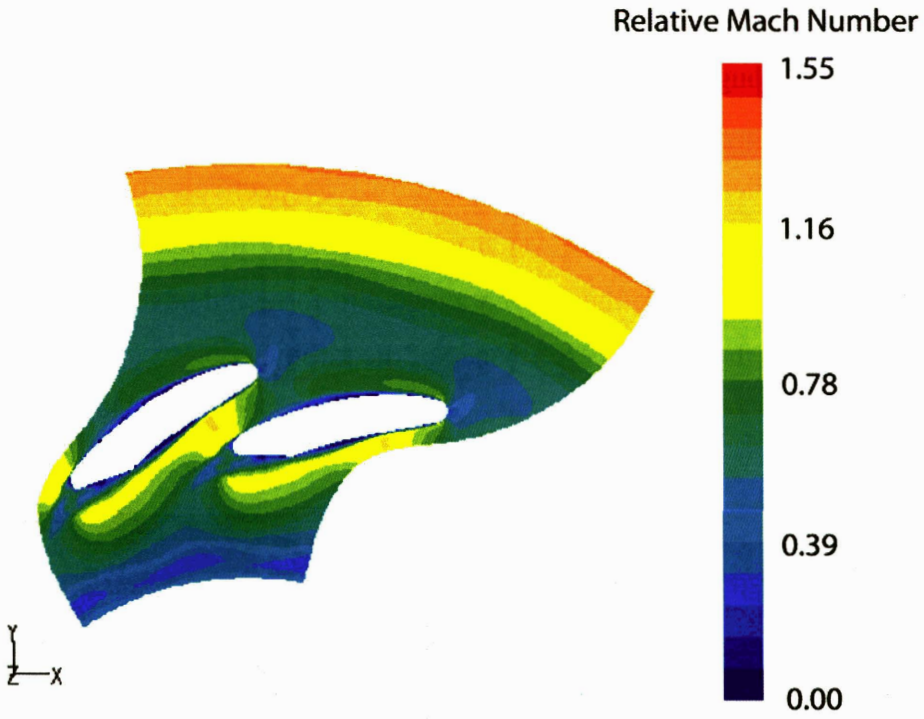

Figure 5-41: Contour plot of relative Mach number for turbine rotor.

5.2.2.2 Torque and Power Requirements

The torque and power output from the turbine are plotted as functions of the rotor corrected speed in Figures 5-42 and 5-43, respectively, for two different inlet pressure conditions. Plotted in Figure 5-44 are the estimated torque requirements for overcoming the viscous losses in the bearings and seals for various corrected turbine speeds. Several conclusions can be drawn from these figures. First, at the design speed, the required turbine inlet pressure is expected to be approximately 3 atm (gage). Furthermore, the torque required to overcome the torques arising from viscous losses in the bearings and seals increases monotonically with speed, whereas the torque-speed characteristic of the turbine decreases monotonically with speed for a given turbine inlet pressure. This implies that the design point is statically stable. A small increase in rotor speed increases the torque required for viscous dissipation, but decreases the torque due to the turbine. The net consequence is a decrease in rotor speed and hence a restoration of the rotor back to its equilibrium spinning speed.

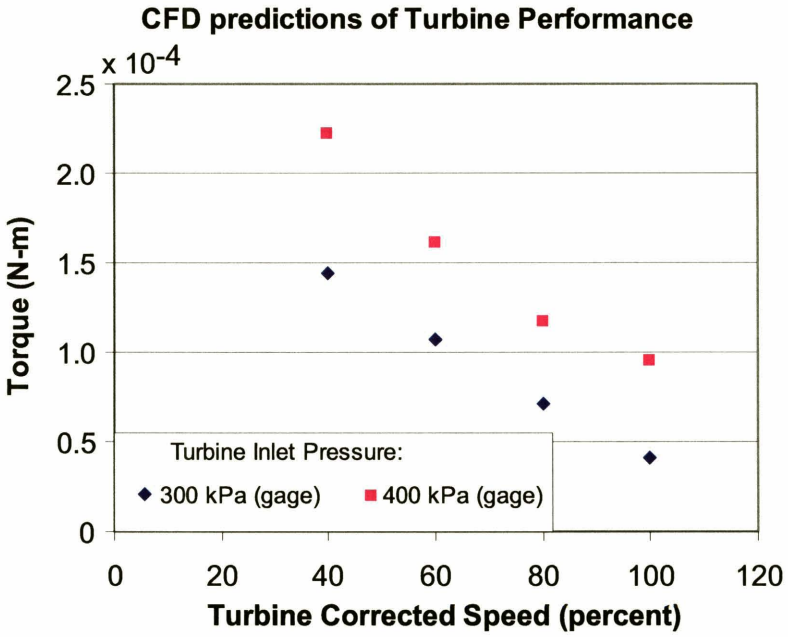

Figure 5-42: Turbine torque plotted against turbine normalized speed for two different turbine inlet pressures.

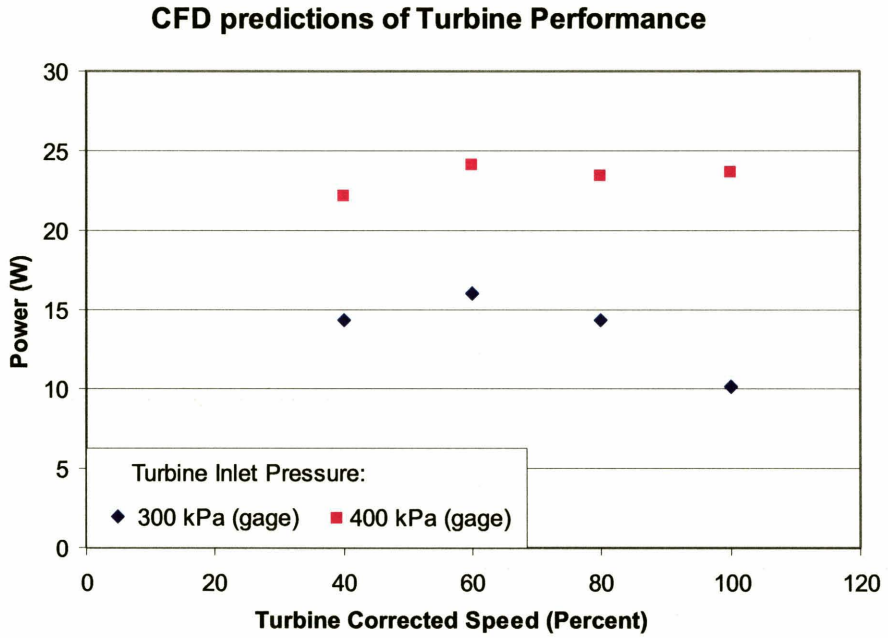

Figure 5-43: Turbine output power plotted against turbine normalized speed for two different turbine inlet pressures.

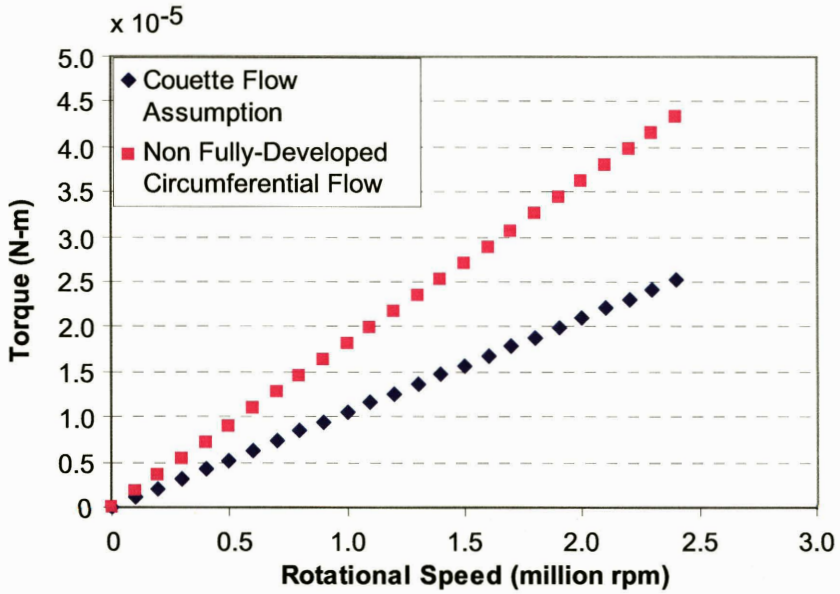

Figure 5-44: Torque requirements for overcoming the viscous losses in the bearings and seals for various turbine speeds.

5.2.3 Forward Thrust Bearing Structural Enhancement

As discussed previously in Section 5.1.3.1, structural failures associated with the forward thrust bearing were frequently encountered when high speed tests were performed on devices incorporating the original microbearing test device design. One of the suspected causes for the occurrence of these structural failures was the inadequate separation distances between critical features. One example exemplifying this is the separation distance between the port for the fiber-optic sensor and the turbine exhaust on layer 1. In the original microbearing test device, this distance was nominally 40 μm (i.e. the separation distance was 40 μm on the glass mask). Layer 1 was fabricated via one single deep etch through the entire 450 μm wafer performed on the aft side. However, a majority of the deep etch recipes resulted in profiles with negative tapers. As a consequence, after performing a DRIE of 450 μm depth through the entire wafer, the separation distance between the fiber optic port and the turbine exhaust was less than 5 μm in certain instances. The excessively thin sidewalls separating the two features might fail structurally when the fiber optic sensor was inserted or extracted from the port. Cracks might further initiate and propagate through the structure and result in the "blow-

off" of the forward thrust bearing. In the redesigned microbearing test device, the deep etches were performed from both sides of the wafer for several reasons. One of them was to mitigate the effects of the extreme negative taper which culminated when the wafer was solely etched from one single side. Two separate glass masks were used for patterning the features on Layer 1, one for the forward side and another for the aft side. The minimum distance between the port for the fiber optic sensor and the turbine exhaust was increased to 150 μm on the forward side (see Figure 5-45) and 260 μm on the aft side (see Figure 5-46).

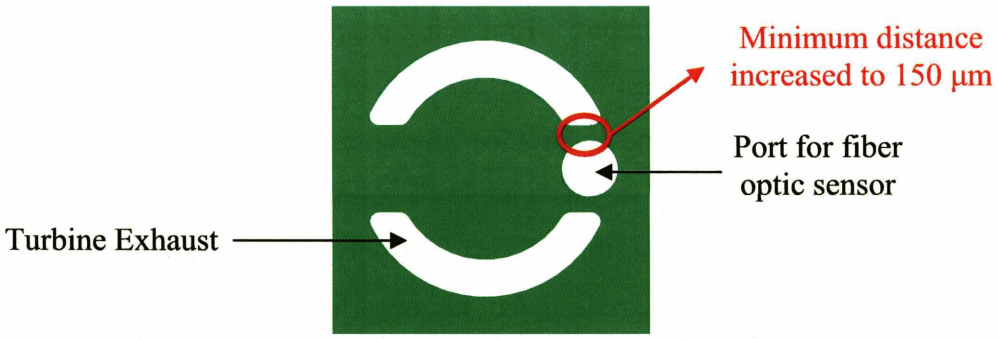

Figure 5-45: Details of mask on forward side of Layer 1.

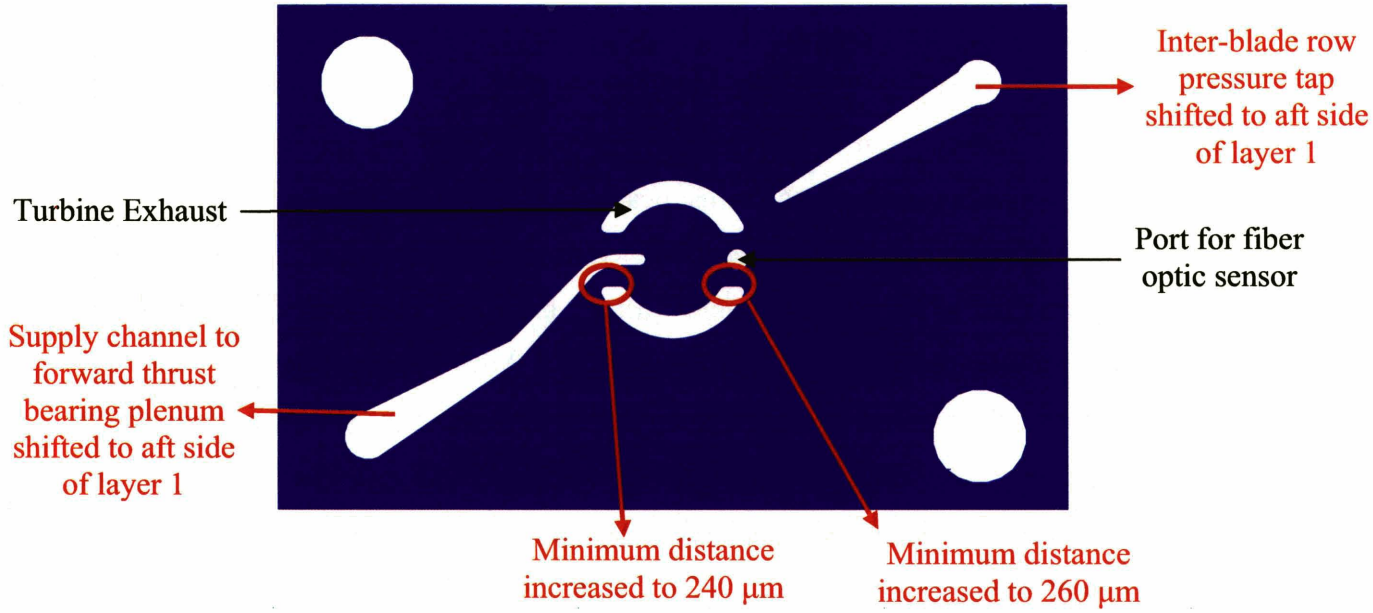

Figure 5-46: Details of mask on aft side of Layer 1.

There is also a strong correlation between design flaws culminating in thrust bearing structural failures and flow leakage. As an example, the minimum distance

between the turbine exhaust and the supply channel leading from layer 1 to the forward thrust bearing plenum on layer 2 was 100 μm on the original microbearing test device. This distance was deemed to be too small, and the surrounding region was often plagued with bonding issues. This was also a critical region, since a large pressure difference on the order of 100 psi existed between the forward thrust bearing supply channel and the turbine exhaust. A weak bond or any other bonding defects culminate in excessive flow leakages between the supply channel and the turbine exhaust. Even worse, a bonding failure shorts out the forward thrust bearing supply channel and the turbine exhaust, preventing sufficiently high pressures from being supplied to the forward thrust bearing plenum. This leads to the disastrous consequence of the forward thrust bearing being totally incapacitated and unable to provide any appreciable axial nor tilting stiffness. Since the successful bonding in this vicinity is of utmost importance, the minimum separation distance between the thrust bearing supply channel and the turbine exhaust was increased to 240 μm in the redesigned microbearing test device, as shown in Figure 5-46.

Another undesirable feature was the formation of "dimples" in the vicinity of sharp corners. It was thus imperative to identify features with excessively low radii of curvature on the original microbearing test device and to attempt to eliminate or redesign them to avoid the formation of undesirable "dimples". As shown previously in Section 5.1.3.1, the intersection between the thrust bearing plenum and the supply channel on the forward side of layer 2 resulted in the existence of 2 sharp corners which subsequently led to the formation of two large "dimples" after a deep etch of 350 μm was performed. In order to circumvent this design flaw, the forward thrust bearing supply channel was shifted from the forward side of layer 2 to the aft side of layer 1, as shown in Figure 5-46. This immediately eliminated the possibility of "dimples" being formed, since the two features are now located on separate wafers and are thus not etched simultaneously. A similar design philosophy was adopted for the newly introduced plenum for the inter-blade row static pressure tap and the existing channel communicating it with layer 1. As illustrated in Figure 5-46, the said channel was relocated from the forward side of layer 2 to the aft side of layer 1, once again to avoid the DRIE of acute features. Another source of "dimples" was the sharp corners of the "scallops" defining the perimeters of the

forward thrust bearing plenum on the original microbearing test device. These were completely eliminated by converting the "scallop" into a circle on the redesigned microbearing test device, as shown in Figure 5-47. The presence of the "scallops" resulted in a minimum separation distance or sidewall thickness of 100 μm between the high pressure forward thrust bearing plenum and the low pressure turbine exhaust. The full circle replacing the "scallops" enabled a minimum separation distance of 200 μm to be maintained between the high pressure thrust bearing plenum and low-pressure turbine exhaust (see Figure 5-47). This also culminated in a substantial increase in available bonding area between layers 1 and 2.

In order to further beef up the structural integrity of the forward thrust bearing, a central post of diameter 800 μm shown in Figure 5-47 was introduced into the forward thrust bearing plenum. The presence of this central post further increased the available bonding area between layers 1 and 2. The forward thrust bearing plenum was thus rendered sturdier. It should also be mentioned that the thickness of the sidewall along the base of the forward thrust bearing plenum was approximately equal to, and limited by, the length of the thrust bearing orifices, which was typically 100 μm. The base of the forward thrust bearing plenum which housed the thrust bearing orifices was thus structurally similar to a membrane, which potentially warped and deformed axially into an umbrella shape if an excessively large pressure difference existed between both sides of the membrane. Such warping or deformation was thus alleviated by introducing a central post which rigidly attaches the base of the thrust bearing plenum to the aft side of layer 1.

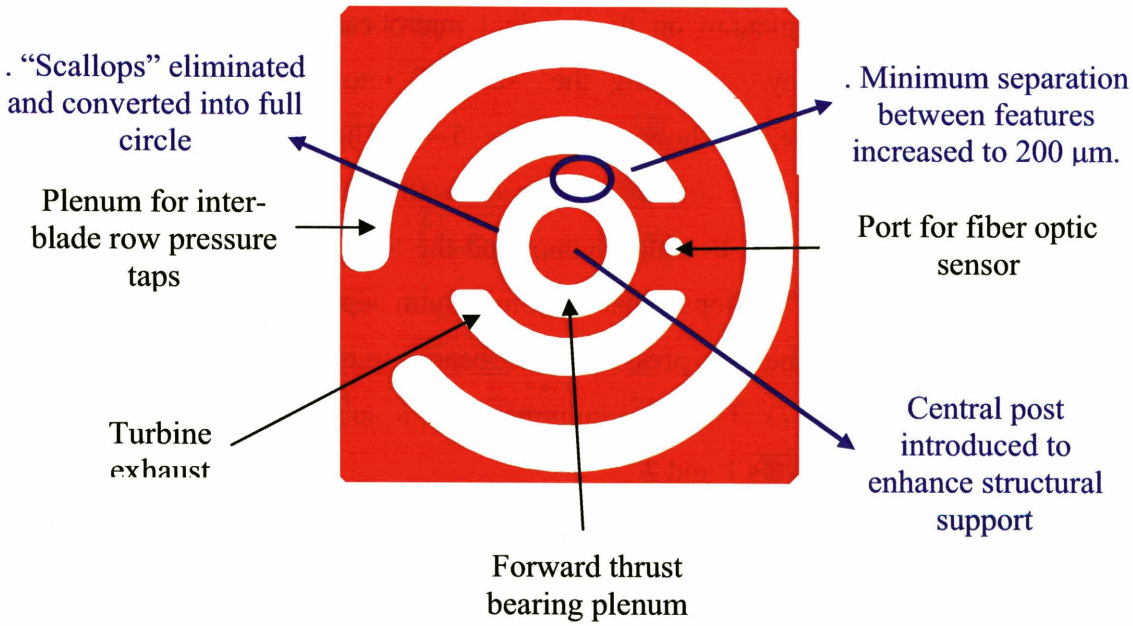

Figure 5-47: Details of mask showing features on forward side of Layer 2.

5.2.4 Modified Turbocharger Design versus Stand-Alone Bearing Rig Design

Two vastly different options arose during the redesign of the microbearing test device. The first option involved transforming the redesigned micro-turbocharger into a microbearing test device (which will be referred to subsequently as a turbocharger microbearing test device (TCMTD)). The other option was to build an entirely new and stand-alone device which was purely dedicated to the study and understanding of rotordynamics and bearing performance and stability (this option will be referred to as the stand-alone microbearing test device (SAMTD)). It was thus necessary to assess the relative advantages and disadvantages of both designs.

The micro-turbocharger consists of a stack of eight wafers. In order to convert the micro-turbocharger into a microbearing test device for the TCMTD, it was possible to retain three of the layers or wafers in the original turbocharger stack, namely the forward foundation plate, the forward thrust bearing plenum and the aft foundation plate. Since significant amounts of time and manpower had already been devoted to the fabrication of the micro-turbocharger, one of the main benefits accruing from the TCMTD was the savings in terms of manpower and time on wafer processing and technology development. Since the turbocharger wafer inventory had available spare wafers for the three common

layers shared by the turbocharger and the proposed TCMTD, only the remaining TCMTD layers comprising the rotors and the aft thrust bearing plenum and seals had to be fabricated. This potentially saves an enormous amount of time, since almost half of the wafers required for a complete TCMTD stack was already available. Furthermore, there was also synergy in terms of technology development for the TCMTD. Since completely different wafers had to be used on the SAMTD, additional time and manpower had to be devoted towards technology development and fabrication of the entirely new wafers.

The TCMTD also has a significant advantage over the SAMTD in terms of cost. The SAMTD required the procurement of a total of 16 photo-masks, whereas the TCMTD only required 7, since it shares several common layers with the turbocharger. One other benefit of the TCMTD arises from the fact that knowledge and experience gained from testing the TCMTD is more relevant and directly applicable to the successful operation of the micro-turbocharger. There are also a greater number of static pressure ports available for tracking purposes on the TCMTD than the SAMTD. This is due to the larger dimensions of each TCMTD device, which directly translates to larger areas available for pressure tappings to be made into the interior of the device. These pressure taps are invaluable for accurately monitoring the actual pressures at different locations within the device. Since significant pressure drops might occur along the tubings, fittings and bends supplying fluid to the device, static pressures measured far upstream outside the package may not accurately represent actual pressure levels within the device.

On the other hand, the larger geometric dimensions of each TCMTD device implies that each wafer or successful TCMTD build is only able to accommodate a smaller number of devices, as compared to the SAMTD. Each TCMTD build yields a maximum of 19 devices, whereas each SAMTD is capable of yielding 48 devices. Each build of SAMTD is thus equivalent to two and a half builds of TCMTD. The significantly fewer number of devices on each TCMTD build further implies that a smaller number of devices will be available for each variation in journal bearing width or seal clearance, if the same number of variations is adopted for both the TCMTD and the SAMTD.

Structural mechanics considerations also play a role in deciding whether the TCMTD or the SAMTD configuration should be adopted. These have been assessed in terms of the out-of-plane rotor tip deflections and centrifugal stresses in the blade roots in

the following section. It is also worthwhile considering the journal bearing dynamic parameters for both the TCMTD and the SAMTD. Applying the scaling laws for micro-hydrostatic journal bearings developed by Spakovszky & Liu [5], corresponding to the same hydrostatic differential pressure across the bearing and the same bearing width, the journal bearing of the TCMTD has double the stiffness of that for the SAMTD. However, in view of the four fold increase in rotor mass for the TCMTD, the natural frequency for the TCMTD is 30% lower than that of the SAMTD. However, since the design speed of the TCMTD is 1.2 Mrpm, which is half of that corresponding to the SAMTD, the whirl ratio at the design speed corresponding to the TCMTD is approximately 30% lower than that for the SAMTD. On the other hand, the journal bearing damping ratio for the TCMTD is expected to be 30% lower than that for the SAMTD. This implies that for the same level of rotor imbalance, journal bearing transcritical operation is anticipated to be more challenging for the TCMTD than the SAMTD. One further drawback of the TCMTD is the lack of any baseline to assess the improvement (or lack thereof) in performance due to the redesign. This is in contrast to the SAMTD, where a direct comparison can be made between the redesigned microbearing test device and the original one in order to assess any improvement in performance culminating from the redesign.

One other critical factor which strongly guides the final decision towards whether a SAMTD or TCMTD should be built is the coupling effect between the annular seals and the journal bearing. Liu has performed analytical predictions using a 4 degree-of-freedom analytical model for assessing the radial and tilting dynamic stability of a system encompassing the journal bearing, annular seals and the rotor [3]. He concluded that for the SAMTD, a minimum outer seal clearance of 4 μm is necessary for ensuring a dynamically stable system over the entire range of operating speeds. However, for the TCMTD, a minimum outer seal clearance of more than 8 μm is necessary for achieving the same goal. This is in view of the fact that the coupling coefficient between the radial and tilting modes is directly proportional to the cube of the radial location of the annular seals, and inversely proportional to the square of the seal clearance. A larger radial location of the annular seals on the TCMTD thus translates into larger seal clearances, in order to achieve a similar level of coupling as that encountered on the SAMTD.

Furthermore, as is shown in the following section, the TCMTD is expected to experience a rotor tip deflection which is 4 times that experienced on the SAMTD. Assuming a rotor tip deflection of 6 μm on the SAMTD, the corresponding rotor tip deflection experienced on the TCMTD is thus anticipated to be 24 μm. The minimum nominal or as-fabricated outer seal clearance on the TCMTD will thus have to be more than 32 μm. At low rotational speeds, during which the rotor tip deflections are marginal, the excessively large seal clearance will result in an enormous flow leakage between the journal bearing plena and the balance plenum, thus rendering the seal ineffective at low operating speeds. A large fraction of the mass flow supplied to the journal bearing plena will leak through the annular seals instead of flowing through the journal bearing. More elaborate instrumentation will also have to be incorporated to deduce the actual flows passing through the journal bearing.

From the above discussion and analyses, it is appropriate to suggest that the SAMTD has relatively more advantages than the TCMTD, in terms of journal bearing operability, coupling effects between the journal bearing and the annular seals, as well as the number of available devices and the number of geometric variations that can be incorporated. A final decision was thus made to proceed with the fabrication and testing of the SAMTD.

5.2.4.1 TCMTD vs SAMTD: Structural Considerations

One issue which cropped up during the debate on whether the TCMTD or SAMTD should be adopted was with regard to structural considerations. Essentially, two questions had to be addressed. First, how should the TCMTD be designed to maximize its structural performance? Second, is the TCMTD more superior than the SAMTD based on structural considerations? In order to answer these questions, a simple structural model was constructed and simple, approximate scaling laws for pertinent structural quantities were derived to shed light on the problems at hand. These scaling laws serve as useful first-order approximations to provide guidelines on how the rotor has to be designed to maximize its structural performance, without having to resort to complicated and laborious and computationally intensive Finite Element (FEM) calculations. A similar structural analysis has previously been performed by Chen [45]. Consider a rotor

spinning at a rotational speed ω. Assuming each blade to be a point mass of mass m located at a radial location r_0 from the center of the spinning disk, the centrifugal force acting on each blade is given by $m\omega^2 r_0$. If the height of each blade is t, the moment arm due to this centrifugal force is t/2. The total moment acting on the disk due to n blades is thus

$$M = n\frac{t}{2}m\omega^2 r_0. \tag{5.2}$$

The average circumferential bending moment per unit length M_0 acting on the disk along the radial location r_0 is given by

$$M_0 = \frac{M}{2\pi r_0} = \frac{ntm\omega^2}{4\pi} = \frac{ntm}{4\pi}\left(\frac{V}{b}\right)^2, \tag{5.3}$$

where b is the radius of the rotor disk and the rotor peripheral speed V is assumed to be constant at 500 m/s. This bending moment results in a deflection of the disk into an umbrella-like shape. If the disk is modeled as a circular disk subjected to a uniform bending moment per unit length M_0 at radial location r_0, the axial tip deflection of the disk δ can be evaluated using the following expression [46]:

$$\delta = \frac{6M_0 r_0^2}{\left(Eh^3\right)/(1-\nu)}\left(\frac{1}{1+\nu} + \ln\frac{b}{r_0}\right), \tag{5.4}$$

where E is the Young's modulus, ν is the Poisson's Ratio and h is the thickness of the disk, respectively. Simplifying (5.4) using (5.3) yields

$$\delta = \frac{3ntm\omega^2 r_0^2}{2\pi Eh^3}\left(\frac{1}{1+\nu} + \ln\frac{b}{r_0}\right)(1-\nu). \tag{5.5}$$

The blade root bending stress arising from a bending moment M' is given by

$$\sigma = \frac{M'a}{I} = \frac{Ma}{nI} = \frac{m\omega^2 r_0 ta}{2I} = \frac{mr_0 ta}{2I}\left(\frac{V}{b}\right)^2, \tag{5.6}$$

where a is half the maximum blade thickness, and I is the second moment of area of the cross section of the blade profile about its bending axis passing through the centroid. In terms of structural dynamics, the fundamental vibration frequency of a blade can be evaluated by modeling each blade as a cantilever. This fundamental vibration frequency is given by [47]

$$f = \frac{1.8751^2}{2\pi t^2}\sqrt{\frac{EI}{\rho A}}, \tag{5.7}$$

where A is the cross sectional area of each blade. This fundamental frequency has to be kept above the maximum operating speed of the rotor in order to avoid any resonance issues associated with the blades.

Next, four potential strategies for altering the structural mechanics of the rotor disk are proposed and analyzed for their effectiveness in reducing the rotor disk tip deflection, blade root stress and increasing the blade vibrating frequency.

First, the effect of using a thicker rotor disk, while keeping other parameters constant, is assessed. According to the above simple model, upon varying the disk thickness h, the direct effect on the rotor tip deflection is given by $\delta \alpha 1/h^3$. Increasing the rotor disk thickness h thus has the beneficial effect of reducing the rotor tip deflection. However, the rotor disk thickness has no direct effect on the blade root stress and the blade vibrating frequency, since there is no change to the blade profile or configuration. It should however be noted that there are severe limitations associated with adjusting the rotor disk thickness to reduce the tip deflection, since the thickness is equivalent to the journal bearing length. Although a thicker disk favors lower rotor tip deflections, microfabrication constraints may impose an upper limit to the maximum journal bearing length that can be fabricated using DRIE.

Next, the effect of varying the radial location r_0 of the blades is assessed. The rotor radius b and hence the radial location of the journal bearing are assumed to be invariant. The rotational speed of the rotor ω also remains unchanged, so that the rotor tip speed remains constant at 500 m/s. It is also assumed that the geometric dimensions of the blades (except the blade height t) are scaled accordingly corresponding to shifts in their radial locations. Hence, the mass of each blade scales as $m \propto r_0^2$ and the bending moment per unit length acting on the disk scales as $M_0 \propto r_0^2$, assuming that the number of blades n and the rotor speed ω remain unchanged. This implies that the rotor tip deflection scales approximately as $\delta \propto r_0^4$, although there is a weak counteracting effect due to the $\ln(b/r_0)$ term which increases as r_0 decreases. The significance of this scaling is that given the same rotor radius b, and within the limits of the assumptions made,

shifting the blades radially inwards has the rather strong and beneficial effect of reducing the rotor tip deflection. As for the blade root stresses, since the blade mass scales as $m \propto r_0^2$, the bending moment acting on each blade scales according to $M' \propto r_0^3$. Since geometrically similar blades are assumed, the second moment of area about a blade's centroidal axis is assumed to follow the scaling relationship $I \propto r_0^4$, and the blade maximum half-thickness a is assumed to scale according to $a \propto r_0$. Putting everything together yields the scaling law $\sigma \propto r_0^0$, i.e. the blade root stress is approximately independent of the radial location of the blades, assuming geometrically similar blades. As for the blade natural frequency, since $I \propto r_0^4$ and $A \propto r_0^2$, $f \propto r_0$. Hence, shifting the blades inwards towards a lower radial location r_0 has the detrimental effect of reducing the blades' fundamental vibrating frequency.

In the following, the effects of simultaneously varying the radial location r_0 of the blades and the rotor radius b are evaluated. This is useful for making comparisons between the TCMTD and the SAMTD, since they have different rotor radii and the blades have different geometrical dimensions and are located at different radial locations. For simplicity, the rotor radius b is assumed to scale linearly with the radial location of the blades, i.e. $b \propto r_0$, thus implying geometric similarity of the entire rotor disk and blades. Note that the rotational speed ω of the rotor is no longer a constant in this case, since the rotor radius is allowed to vary. In order to maintain a fixed rotor periphery speed, ω has to scale as $\omega \propto 1/b \propto 1/r_0$. Since the blade mass $m \propto r_0^2$, the bending moment per unit length acting on the disk remains approximately constant. Furthermore, since $b \propto r_0$, b/r_0 is approximately invariant, and the rotor tip deflection scales according to $\delta \propto r_0^2$. This implies that a rotor with a smaller radius experiences a significantly smaller rotor tip deflection. Therefore, from the point of view of rotor tip deflection, the SAMTD (with a rotor radius of 2.1 mm) is advantageous over the TCMTD (which has a rotor radius of 4 mm). Within the limits of the assumptions made, the TCMTD is anticipated to experience approximately four times the rotor tip deflection of the SAMTD. The larger rotor tip deflections of the TCMTD translate into larger nominal or as-

fabricated seal clearances required for avoiding rotor contact with the static structure due to the "umbrella-ing" of the rotor at high rotational speeds. At low operating speeds, the larger seal clearances result in excessive flow leakages from the journal bearing plena to the balance plenum, thus rendering it challenging to decouple the journal bearing supply pressures from the balance plenum pressure. Next, the effect of simultaneously varying the blades' radial location and the rotor radius on the blade root stress is assessed using the simple structural model. Assuming geometrically similar blades, $m \propto r_0^2$ and $a \propto r_0$, whereas $I \propto r_0^4$. Hence, the resulting scaling law for the blade root stress is given by $\sigma \propto 1/r_0^2$. This scaling relationship sheds some light on the relative advantage of the TCMTD over the SAMTD in reducing the blade root stresses. For the same rotor tip speed, the blade root stresses on the SAMTD are thus expected to be approximately four times greater than those on the TCMTD. In terms of blade fundamental vibration frequency, since $I \propto r_0^4$ and $A \propto r_0^2$, the resulting scaling law is $f \propto r_0$. Once again, the TCMTD is superior over the SAMTD in terms of blade vibrating frequency. The fundamental vibrating frequency of the blades on the TCMTD is expected to be approximately two times higher than that on the SAMTD.

Finally, the effect of blade height variations on rotor structural performance is assessed. The original microbearing test device had blades with a nominal height of 150 μm. The redesigned microbearing test device or SAMTD will incorporate a double layer rotor structure, where the rotor disk and blades are fabricated on separate wafers. The blade height will be governed by the thickness of the wafer used for the blades. However, a minimum wafer thickness is required to avoid the wafers from being excessively fragile and thus not amenable to handling using tweezers during the microfabrication process. A minimum wafer thickness of 330 μm was deemed to be sufficiently robust for common wafer handling procedures to be performed [43]. It is thus of interest to evaluate the consequences of almost doubling the blade heights on the structural integrity of the rotor. Keeping all other factors constant, the mass of each blade scales with the blade height t according to $m \propto t$. The bending moment per unit length acting on the rotor disk scales as $M_0 \propto t^2$. Therefore, the rotor tip deflection is governed by the scaling law $\delta \propto t^2$.

Hence, a doubling of the blade height leads to a four-fold increase in the rotor tip deflection, which is clearly undesirable. With regard to blade root stresses, since the blade mass $m \propto t$, the resulting scaling law is thus $\sigma \propto t^2$. Hence, one additional detrimental consequence of doubling the blade height is the four-fold increase in blade root stresses. As for the blade fundamental natural frequencies, the scaling law is given by $f \propto 1/t^2$. This implies that a doubling of the blade height has the adverse effect of causing a four times reduction in the blades' fundamental vibrating frequency. The above simple scaling laws thus allude to the detrimental effects of doubling the blade height from a structural perspective. Doubling the blade height increases the rotor tip deflection and the bending stresses and decreases the blade natural frequency. Despite the undesirable consequences of doubling the blade height, this was deemed to be necessary for the double-layer rotor microfabrication technique required for achieving the sufficiently low levels of rotor imbalance for 48 devices simultaneously fabricated on a 6 inch wafer.

The axial tip deflection for the SAMTD rotor disk incorporating the newly designed turbine blades has been plotted as a function of the blade height in Figure 5-48 for a design speed of 2.4 Mrpm. As can be deduced from the figure, a blade height of 330 μm results in a rotor tip deflection of approximately 6 μm. The variation of the blade root stresses with blade height is displayed in Figure 5-49. It should be noted that the results shown in this figure are only meant to illustrate qualitative trends. They do not account for the presence of stress concentration due to excessively small fillet radii at the blade roots. Figure 5-50 shows the blade natural frequency plotted as a function of the blade height. Although increasing the blade height from 150 μm to 330 μm leads to a corresponding decrease in blade natural frequency from approximately 8 MHz to 2 MHz, the blade natural frequency is still way above the design speed of 2.4 Mrpm, and is thus not expected to be an issue of serious concern.

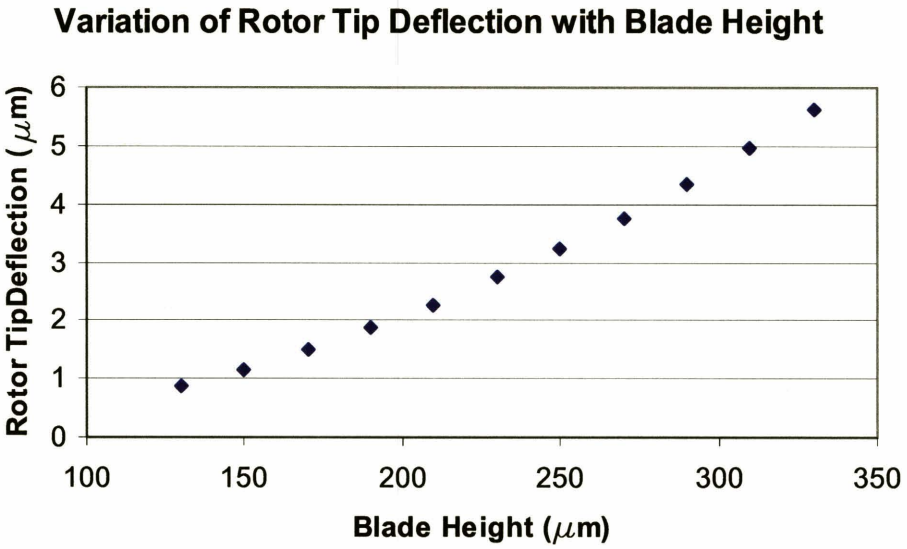

Figure 5-48: Variation of rotor tip deflection with blade height, SAMTD.

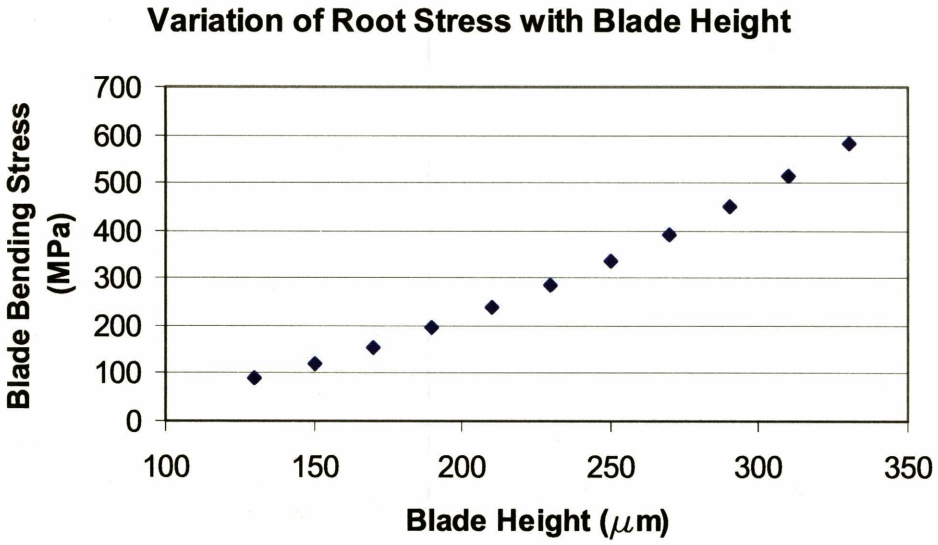

Figure 5-49: Variation of blade root stress with blade height, SAMTD.

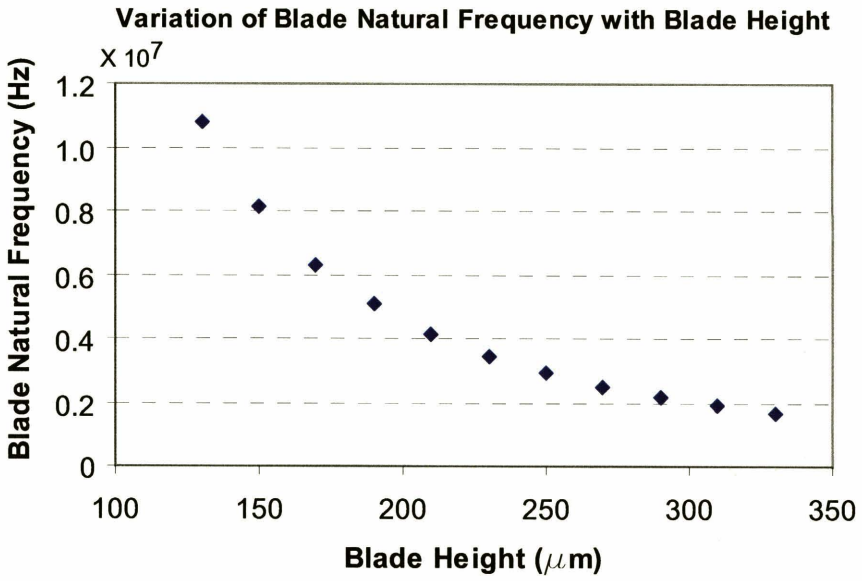

Figure 5-50: Variation of blade natural frequency with blade height.

5.2.5 Other Design Considerations and Layout of Masks

- Inter-blade row pressure tap

In the original microbearing test device, the inter-blade row pressure tap only measured the static pressure at one single point along the entire circumference of the journal bearing exhaust (which coincided with the annular region separating the turbine NGV's and the turbine rotor blades). This was reconfigured in the redesigned microbearing test device to allow the static pressure at more points along the circumference of the journal bearing exhaust to be monitored. This was achieved by etching more holes on the aft side of layer 2 along the circumference overlooking the journal bearing, as shown in Figure 5-51. The holes were subsequently allowed to communicate via a continuous plenum etched on the forward side of layer 2. This facilitates the average inter-blade row static pressure to be monitored, rather than the pressure at one single point which might not accurately depict the actual mean pressure along the exhaust of the journal bearing.

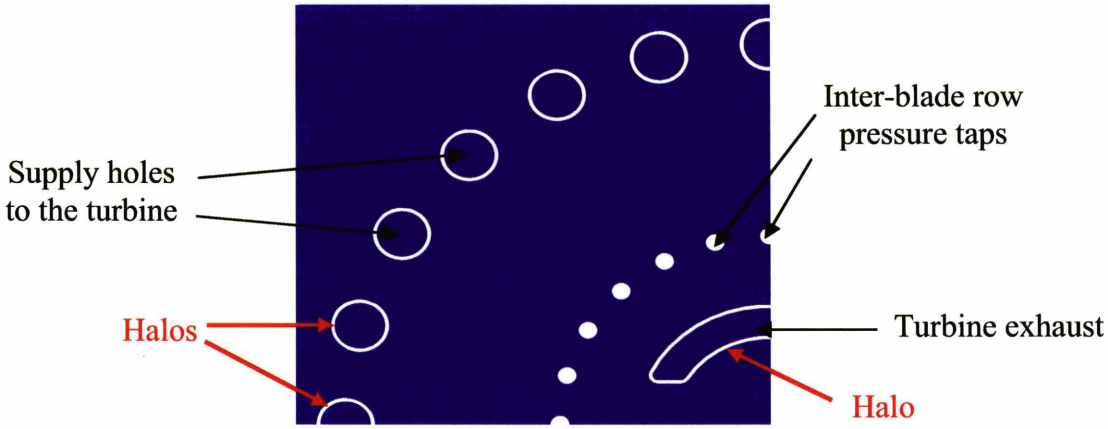

Figure 5-51: Details of mask showing features on a portion of the aft side of Layer 2. Note that the thrust bearing orifices of 7 μm diameter are too small to be seen.

- Halos

Microfabrication of the aft side of layer 2 involved the DRIE of features with vastly different geometric dimensions. The smallest features constituted the forward thrust bearing orifices, which were nominally 10 μm in diameter. However, several other features, such as the supply holes to the turbine and the turbine exhaust, were significantly larger, on the order of hundreds of microns. The DRIE etch rates for these geometrically dissimilar features were anticipated to be different, thus resulting in large differences in the time taken for these features to etch through completely. Since higher etch rates were associated with larger features, it was necessary to devise a scheme to decelerate the rate of etching for the larger features. This was accomplished by defining the outlines of these features using halos on the glass mask, as shown in Figure 5-51. Instead of dry-etching the entire large feature, the halo defining the perimeter of the said feature was etched instead. This decreased the loading of the dry-etch and since the width of the halo was geometrically more similar to the size of the thrust bearing orifices, the disparity in etch rates and hence the difference in time taken for them to etch through were reduced considerably. When the halo was etched through, the large remaining unwanted feature simply detaches itself from the rest of the wafer.

- Turbine exhaust area

The turbine exhaust area for the redesigned microbearing test device was increased to be more than double that of the original microbearing test device. The purpose of this was to accommodate the larger turbine mass flow rates due to the increase

in turbine blade heights, as well as to reduce the potentially undesirable consequences of flow blockage due to an excessively small turbine exhaust area.

- Conversion of features into full circles

On the original microbearing test device, the turbine tip clearance etch performed on the aft side of layer 2 and the rotor running gap etched on the forward side of layer 4 had features with sharp corners. Photoresist coverage of these acute corners during the "nested mask" process might be challenging due to the presence of these corners. These features were converted into full circles on the redesigned microbearing test device, in part to rectify the above shortcoming, as well as to improve symmetry.

- Redesign of balance plenum

The balance plenum on the original microbearing test device consisted of two narrow slits, each subtending an angular extent of 110°. On the redesigned microbearing test device, the two slits were replaced by a full annular plenum. The redesigned balance plenum had a cross sectional area which was more than 8 times larger than the original one.

- Considerations of symmetry

All features on the redesigned microbearing test device were ensured to be as symmetric as possible, so as to avoid any undue sideloads or tilting moments from arising due to the lack of symmetry. This was exemplified by the design of the channels on the forward surface of level 5. Figure 5-52 depicts the configuration of these channels on the original microbearing test device. One of these channels supplies the fluid to the balance plenum, whereas another channel vents the fluid from the aft-side exhaust. For the former channel, there is simultaneous circumferential flow along the channel and axial flow out of the channel into the balance plenum. Due to hydraulic losses due to friction as the fluid flows circumferentially along the channel, the fluid which exits into the balance plenum on one side of the channel might be at a significantly different static pressure from the fluid leaving on the opposite side. A tilting torque on the rotor is thus liable to occur as a consequence of this static pressure asymmetry. In the redesigned microbearing test device, symmetry was significantly improved by allowing the flow to leave axially into the balance plenum at two diametrically opposite locations. A similar lack of symmetry arises for the flow along the channel for the aft exhaust. However, in the redesigned

microbearing test device, a compromise had to be made, since allowing the flow to leave at only two diametrically opposing locations significantly reduces the available flow area and thus give rise to undesirable blockage issues. Having an adequate flow area was thus deemed to be a more critical requirement for this case, and the quest for symmetry had to be sacrificed. However, achieving perfect symmetry did not appear to be a dire requirement for this case due to two reasons. First, since the channel is located at a smaller radial location, any static pressure asymmetry results in smaller tilting moments. Moreover, the smaller radial location also implies a smaller circumferential extent, less hydraulic losses due to friction and hence smaller static pressure asymmetries. Other potential sources of asymmetry are the lateral channels leading towards each of the two channels mentioned above on the forward side of level 5. These channels were not designed to be radial in the original microbearing test device. As the fluid splits into two different paths at the intersection between a lateral channel and a circumferential channel, there might be a difference in the turning losses for each path, which culminates in asymmetry. On the redesigned microbearing test device, these lateral channels are designed to be radial, so that the turning losses are ideally equal when the fluid splits into two separate paths at the flow intersection.

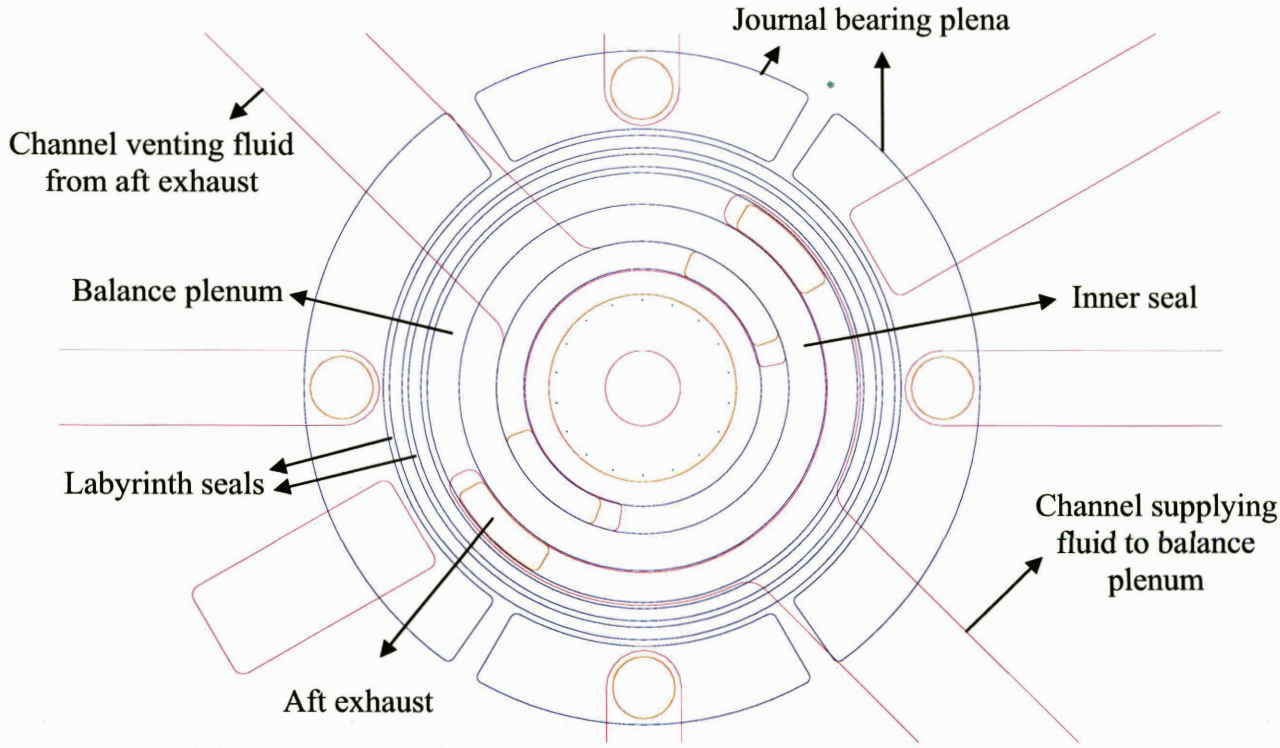

Figure 5-52: Layout of features on the aft side of the rotor, showing how the features have been designed to be as symmetric as possible to eliminate issues arising from sideloading.

- Improving structural integrity in vicinity of aft thrust bearing

Similar to the forward thrust bearing, the aft thrust bearing plenum on the original microbearing test device had a "scalloped" configuration. The minimum thickness of the vertical sidewalls separating the recesses of the "scallops" from the aft-side exhaust was 100 μm. In the redesigned microbearing test device, the "scallops" were eliminated and were converted into a full circle. The sidewall thickness partitioning the aft thrust bearing plenum from the aft-exhaust was also increased to a uniform value of 200 μm. This was performed to increase the available bonding area in the vicinity of the aft thrust bearing plenum between levels 3 and 4. This was deemed to be critical, since a bonding failure results in excessive flow leakages between the aft thrust bearing plenum and the aft-exhaust. Furthermore, the aft-exhaust and the aft thrust bearing plenum might be "shorted out", thus preventing appreciable pressures from being applied to the aft thrust bearing plenum. The aft thrust bearing then loses its functionality, since it is incapable of developing any appreciable stiffness. Furthermore, structural failure issues might arise as a consequence of a weak bonding.

- Speed bumps

A total of 4 speed bumps are incorporated on each rotor of the redesigned microbearing test device. The main motivation leading towards the use of 4 speed bumps rather than 2 arises from analyzing the effects of harmonics on upstream influence. Higher order harmonics decay much more quickly and have a smaller upstream influence than harmonics of lower order [39]. The upstream influence due to 4 speed bumps is thus anticipated to be significantly less than that due to 2 speed bumps. The speed bumps are also designed to be identical in order to render the rotor configuration as symmetrical as possible, so as to avoid imbalance and sideloading issues from arising. Additionally, since there is no intention to perform any sort of dynamic balancing on the rotor, no reference features (which inadvertently destroy the symmetric arrangement of the speed bumps) are required.

5.3 Summary and Conclusions

In the first part of this chapter, major lessons acquired from the microfabrication and testing of previous microbearing test device builds were discussed and analyzed. Examples of these lessons which potentially had adverse effects on high speed bearing operation included sources of negative radial and tilting stiffness due to coupling effects, the formation of a "fence" at the exit of the journal bearing, the existence of spikes in the journal bearing and structural integrity issues. The second part of this chapter focused on the analysis and design of a new microbearing test device which aims to rectify the known design flaws of the original design. The key elements and components addressed in the redesign include annular seals, multiple journal bearing plena, turbomachinery, thrust bearings, structural integrity considerations and device variations.

CHAPTER 6

Microfabrication of High-Speed and High Whirl-Ratio Gas Bearings for MEMS Devices

Having provided details pertaining to the redesign of the microbearing test device in the previous chapter, the microfabrication of the redesigned microbearing test device is described in this chapter. First, the key microfabrication process flows for the constituent wafers or layers which comprise the final six-wafer stack microbearing test device is presented. Next, the main microfabrication challenges and the strategies adopted to overcome them are outlined. Particular attention is given to the novel fabrication techniques and procedures for "D^3" rotors (*d*ouble layer, *d*onor-receiver and *d*rop-in rotors), with the dual objectives of achieving low imbalance rotors and devices with varying journal bearing clearances.

6.1 Key Process Flows

A cross-sectional view of the redesigned microbearing test device is shown in Figure 6-1. There are a total of 5 levels of layers. Layer 3, which corresponds to the rotors, consists of 2 wafers: layer L3B which constitutes the turbine blades and layer L3J which consists of the rotor disk and journal bearing.

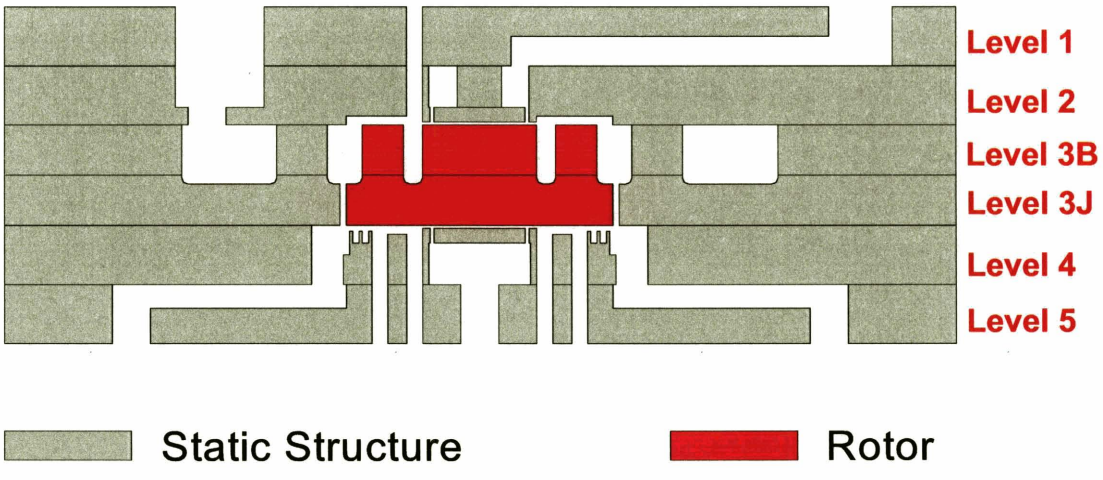

Figure 6-1: Cross section of bonded wafer stack (not to scale).

The salient steps in the process flow are illustrated in Figures 6-2 to 6-6 corresponding to layers 1 to 5, respectively. An exploded view showing the individual layers of the device is presented in Figure 6-7.

1. DRIE aft side for pipings and channels to forward thrust bearing, turbine, forward exhaust and inter-blade row pressure tap (Mask A2B).

2. DRIE forward side for pipings and channels to forward thrust bearing, turbine, forward exhaust and inter-blade row pressure tap (Mask A1F).

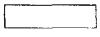

Figure 6-2: Process flow for level 1.

1. Shallow etch forward thrust bearing gap (2.5 μm, Mask B1B).

2. Pattern features for forward tip clearance on 0.5 μm thermal oxide (Mask B2B).

3. Pattern thrust bearing orifices, forward exhaust and turbine plenum on photoresist (Mask B3B).

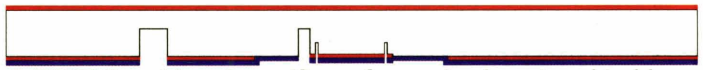

4. DRIE thrust bearing orifices, forward exhaust and turbine plenum.

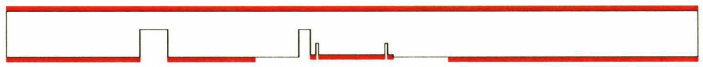

5. Remove photoresist to reveal nested oxide mask.

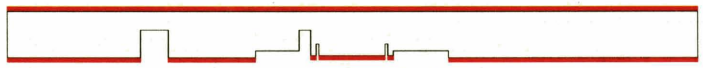

6. DRIE forward tip clearance (14 μm).

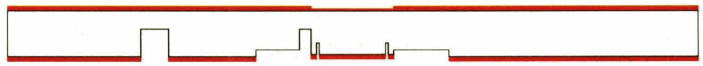

7. BOE 0.3 μm thermal oxide using Mask B1B.

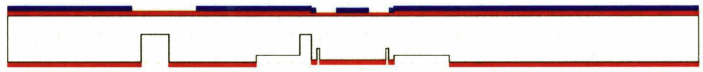

8. Pattern features for forward thrust bearing and turbine plena (Mask B4F).

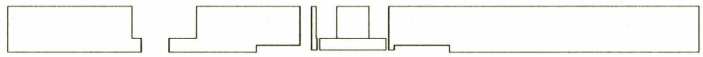

9. DRIE forward thrust bearing and turbine plena.

Figure 6-3: Process flow for level 2.

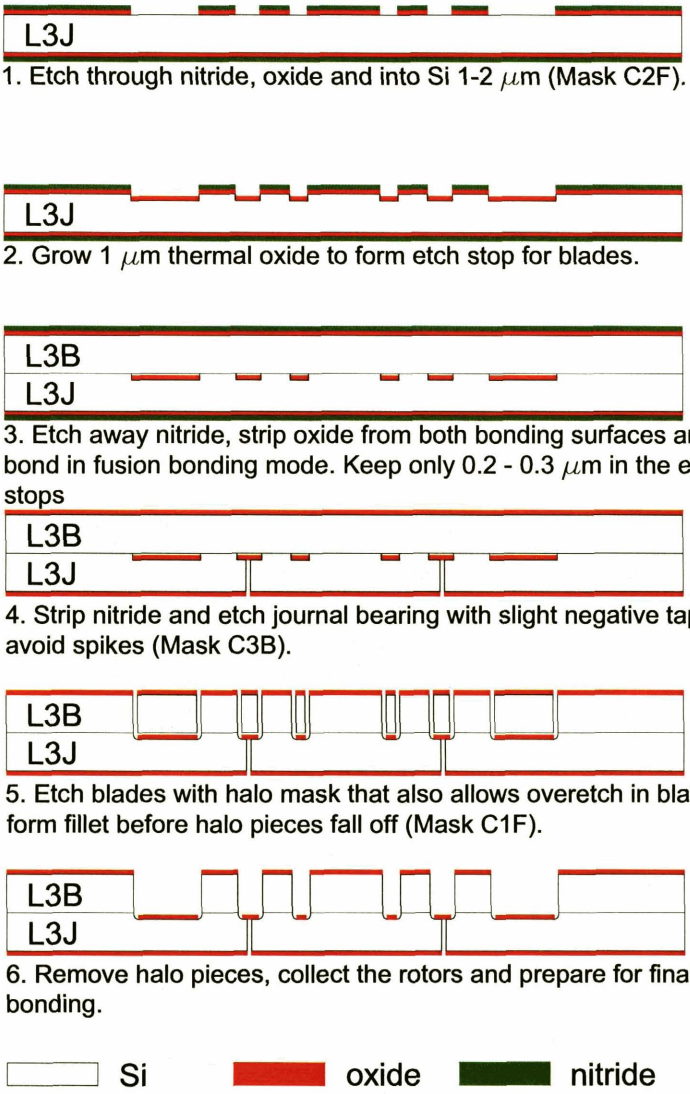

Figure 6-4: Process flow for level 3. Process flow courtesy of Li [43].

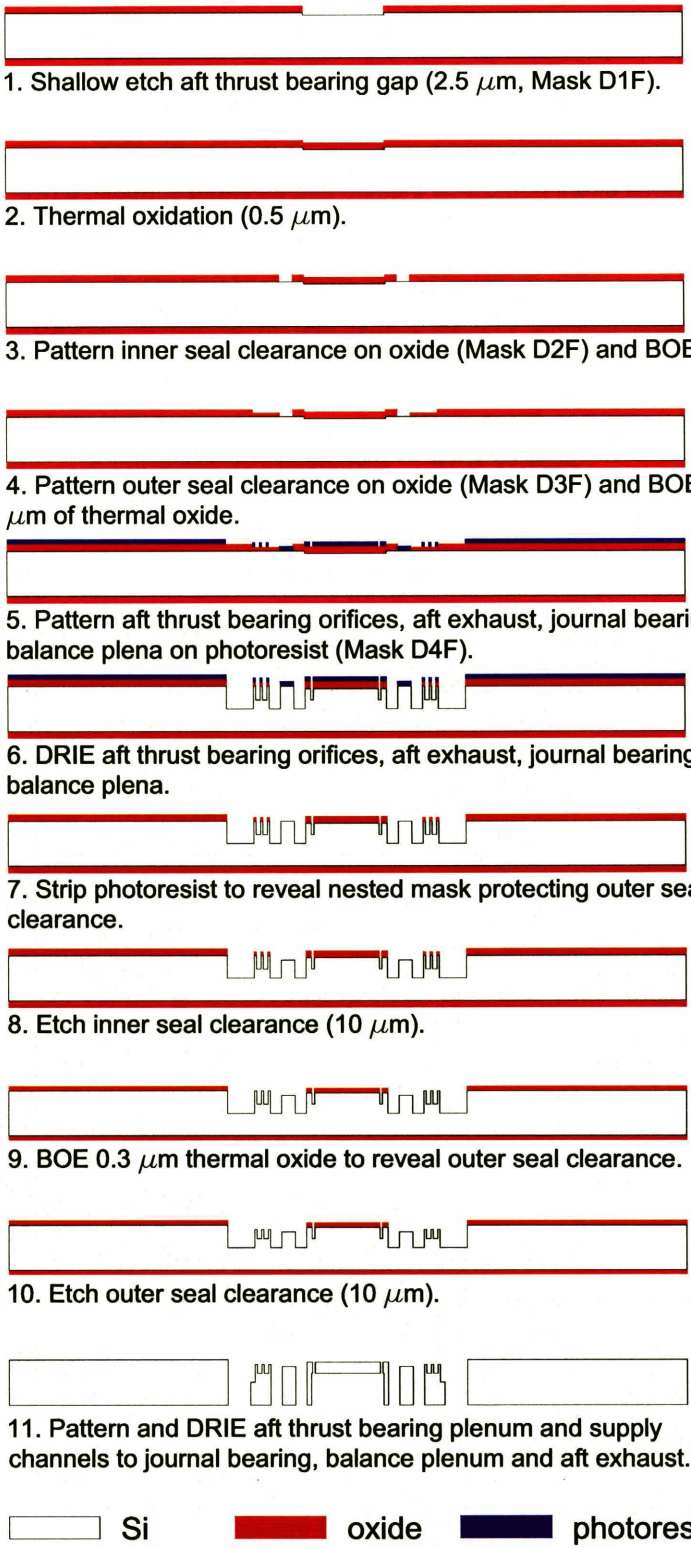

Figure 6-5: Process flow for level 4.

1. DRIE forward side for pipings and channels to aft thrust bearing, journal bearing, balance plenum and aft exhaust (Mask E1F).

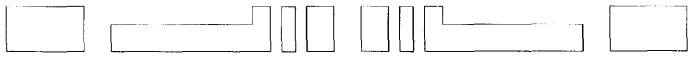

2. DRIE aft side for pipings and channels to aft thrust bearing, journal bearing, balance plenum and aft exhaust (Mask E2B).

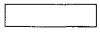 Si

Figure 6-6: Process flow for level 5.

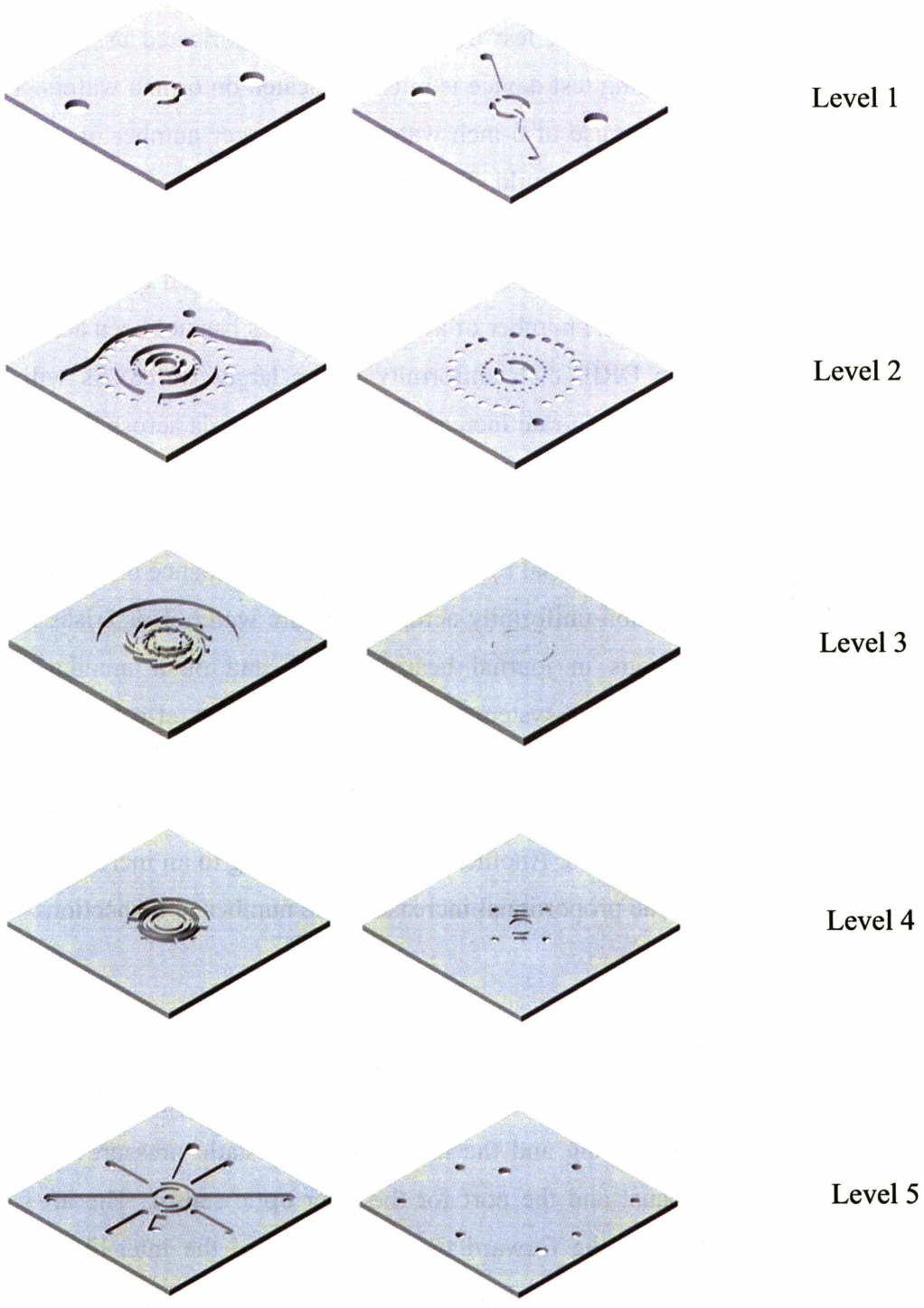

Figure 6-7: Exploded view of microbearing test device. Drawing is to scale. Each device measures 15 mm by 15 mm.

6.2 Key Microfabrication Challenges

Unlike the original microbearing test device which was fabricated using 4-inch wafers, the redesigned microbearing test device is microfabricated on 6-inch wafers. The main advantage accruing from the use of 6-inch wafers is the larger number of devices which can be accomodated on the same build. The original microbearing test device only allowed a maximum of 12 devices for each successful build, whereas the redesigned microbearing test device allows a total of 48 devices to be incorporated on each build. However, the potential increase in the number of available devices has not been achieved because of the deterioration in DRIE etch uniformity in the larger wafer. As will be discussed in Chapter 7, the global etch rate increases radially outwards across the wafer. Etch variations across a 6-inch wafer are thus expected to be significantly worse than those previously experienced on a 4-inch wafer. Although the exact depths of many features are not anticipated to play a crucial role on the overall performance of the device, it is still useful to limit the etch non-uniformity across the entire wafer. This arises from the fact that deliberate variations in journal bearing width and outer annular seal clearance have been incorporated to systematically investigate the effects of these variations on bearing performance and stability. A true, systematic investigation can be undertaken only if all other unintended variations, apart from the intentional variations introduced, are kept to a bare minimum. Another tradeoff pertaining to an increase in the number of available devices is the proportional increase in the number of inspections and etch-depth measurements.

6.2.1 Level 1

Level 1, which was fabricated on a 550 μm thick wafer, consists of the supply channels to the forward thrust bearing and the inter-blade row static pressure tap, the main turbine, the forward exhaust and the port for the fiber optic sensor. The aft side comprising of supply channels to the forward thrust bearing and the inter-blade row pressure tap was etched first, with the aim of achieving 300 μm deep channels. However, when DRIE was carried out on the wafer using STS2, an etch variation of approximately 80 μm existed at homologous points between the center and edge devices when the channels of the edge devices have achieved their target depths. Photoresist OCG825 was applied using Q-tips to cover up devices whose features have already reached their

desired depths. The wafer was subsequently etched for durations of 5-minute intervals, which yielded a nominal etch depth of 10 μm. The wafer was then reinspected and those devices which had achieved or exceeded the desired depth were covered using photoresist. The whole process was repeated until the features on all the devices reached or exceeded the desired depth. The above procedure involved successive arduous cycles of etching, measurement of etch depth, application and baking of photoresist.

6.2.2 Level 2

Level 2 consists of the forward thrust bearing plenum and orifices, the main turbine supply plena, the inter-blade row pressure tap, the forward exhaust and the window for the fiber optic sensor. Level 2 was also fabricated on a 550 μm thick wafer. One of the main challenges arose from the simultaneous etching of the turbine plenum and the forward thrust bearing plenum. The turbine supply plenum has a much larger area than the thrust bearing plenum, and the plasma etch rate in the vicinity of the turbine supply plenum was higher than that in the neighborhood of the thrust bearing plenum. Since the thrust bearing orifices are nominally 100 μm in length, the thrust bearing plenum has to be etched down by 450 μm. However, simultaneous DRIE of the turbine plenum can result in etch depths significantly greater than 450 μm. This would leave behind a flimsy membrane with a thickness of several tens of microns below the plenum, which might potentially give rise to structural integrity issues. Even worse, a marginally higher etch rate in this region might cause the turbine plenum to be etched through completely, as previously experienced on the micro-turbocharger. Note that it was not possible to use a halo etch for the turbine plenum, since this plenum was not formed from a through etch. This problem was alleviated by using the following approach. The wafer protected with 0.5 μm thick thermal oxide was patterned using the optical mask containing features for the forward thrust bearing clearance. The thickness of the thermal oxide protecting the forward thrust bearing plenum was reduced from 0.5 μm to 0.2 μm using timed BOE (Step 7 in Figure 6-2). The idea was to deliberately introduce a discernable difference in the thickness of the thermal oxide protecting the thrust bearing plenum and the turbine plenum and hence create a delay in the time taken for the oxide to etch through. When the forward side of the wafer was subjected to DRIE, the thinner oxide protecting the forward thrust bearing etched through first, and the dry etching of

the Silicon for the thrust bearing plenum thus occurred earlier. On the other hand, the oxide protecting the turbine supply plenum takes a longer time to etch through, and DRIE of the Silicon to from the turbine supply plenum begins later. In this manner, when the forward thrust bearing plenum was etched down to a depth of 450 μm, the depth of the turbine plenum was approximately 300 μm. This strategy thus averts the formation of an excessively deep turbine supply plenum.

Once again, etch rate non-uniformities across the wafer introduced differences in depth of up to 80 μm between the center and edge devices. This was again circumvented by repetitive cycles of DRIE for 3 minutes, etch depth measurements, application and baking of photoresist over devices whose depth of etch has exceeded the design value.

6.2.3 Level 4

Level 4 consists of the journal bearing supply plena, the balance plenum, the aft thrust bearing plenum and orifices, the inner and outer annular seals and the aft exhaust. One of the main challenges associated with the fabrication of Level 4 arises from the fact that features with different depths have to be etched on the same side of the wafer. These include the aft thrust bearing clearance, the inner and outer seal clearances, the journal bearing plena, the balance plenum, the aft-exhaust and the grooves of the labyrinth seals.

First, the aft thrust bearing clearance of nominally 2.5 μm has to be shallow etched (Step 1 in Figure 6-4). The aft thrust bearing orifices of nominally 100 μm depth have to be etched simultaneously with the journal bearing plena, the balance plenum and the aft-side exhaust. As compared to the thrust bearing orifices, which have a nominal diameter of 10 μm, these plena and channels are much larger features, and the etch rates associated with these are in turn significantly higher.

Finally, the inner and outer seal clearances have to be etched. However, this is not a trivial step, since deliberate variations in outer seal clearance have to be incorporated in order to systematically investigate its effect on bearing performance and stability. The two different variations are outer seal clearances of 10 μm and 12 μm, with corresponding inner seal clearances of 20 μm and 22 μm, respectively. The sequence for the etching of features with significantly different depths has to be planned with extra care. Etching the seal clearances prior to the journal bearing plena is challenging due to photoresist coverage issues. As a rule-of-thumb, a 10 μm thick photoresist layer is

capable of covering steps and trenches with depths of less than 4 μm. Since the seal clearances are significantly larger than 4 μm, topography coverage using photoresist prior to the deep etching of the journal bearing plena would be inadequate. The solution is thus to adopt a nested mask approach, where a different masking material is used for each etch, with all the materials patterned prior to any DRIE. The masking materials used are Silicon dioxide of different thicknesses and photoresist.

Subsequent to the thrust bearing clearance shallow etch, thermal oxide of 0.5 μm thickness is grown on the wafer (Step 2 in Figure 6-4). The thermal oxide is then patterned using the photolithographic mask containing the features for the inner seal. The exposed oxide defining the inner seal is then subjected to wet etching using buffered oxide etch (BOE) to remove the entire 0.5 μm thickness of oxide (Step 3 in Figure 6-4). The original photoresist coat is removed and a fresh layer of photoresist is dispensed and patterned with another photolithographic mask which contains the features for the outer seals. The photoresist is developed and the exposed thermal oxide defining the outer seals is then subjected to wet etching using BOE for 3 minutes, so as to leave behind an oxide thickness of approximately 0.3 μm (Step 4 in Figure 6-4). This step is necessary, in view of the different depths for the inner and outer seals. The photoresist layer is subsequently removed and a fresh layer of photoresist is deposited and patterned with the photolithographic mask containing the features for the journal bearing plena, the balance plenum and the thrust bearing orifices (Step 5 in Figure 6-4). These features are then etched into the Silicon substrate until a depth of approximately 250 μm is achieved for the journal bearing plena (Step 6 in Figure 6-4). The photoresist is stripped, leaving behind silicon dioxide films of two different thicknesses as the masking material (Step 7 in Figure 6-4). A double nested mask comprising of oxide with two different thicknesses thus remains, with the 0.3 μm thick oxide film masking the outer seals, and the 0.5 μm thick oxide film protecting the rest of the wafer where no bulk Silicon etching is required. The top surface of the Silicon corresponding to the inner seal is now exposed and ready for DRIE.

Dry etching is performed until the inner seal reaches a depth of 10 μm (Step 8 in Figure 6-4). The thermal oxide protecting the outer seal is then etched away using BOE for 4 minutes (Step 9 in Figure 6-4). The objective for this step is to completely remove all the oxide protecting the outer seal, whilst retaining an oxide thickness of

approximately 0.25 μm for protecting the rest of the wafer. The wafer is next subjected to DRIE until the clearance of the outer seals reaches a depth of 10 μm (Step 10 in Figure 6-4). During this process, the inner seal is simultaneously dry etched to a depth of approximately 20 μm. After this, the devices having outer seal clearance specifications of 10 μm are covered with photoresist OCG825 using a Q-tip. The remaining devices on the wafer with 12 μm outer seal clearance specifications are then subjected to further DRIE until the desired clearance is achieved.

The fabrication of Level 4 involved several unique challenges. First, in view of the lengthy process flow and the numerous fabrication steps involved to achieve the vastly different etch depths and desired variations, extreme care had to be exercised in the handling of the wafer. Since the wafer had to be subjected to many cycles of thermal oxidation, photoresist spin-coating, wet chemical cleaning, spin drying, ashing, wet and dry etching, the chances of wafer breakage was significantly enhanced. The likelihood of wafer breakage was further accentuated by increased handling of the wafer using tweezers and a rise in the required number of inspections and measurements of etch depth and oxide thickness. The steps in the process flow had to be strictly adhered to, as any careless mistake or negligence would render the wafer unusable and result in unnecessary delays and waste of resources. Control of oxide thicknesses and the time taken for wet oxide etching using BOE had to be controlled precisely in order for the multiple nested mask sequence to be successfully implemented. Under normal circumstances, the thermal oxide thickness could be ascertained in a straight-forward manner using Nanospec, a non-contact spectro-reflectometer. However, Nanospec was unfortunately non-operational during the entire period when Level 4 was microfabricated. The oxide thickness had to be determined indirectly using DekTak (a surface profilometer) instead. Since DekTak required a stylus to be placed in contact with, and dragged along the surface of the wafer, it was thus inferior compared to Nanospec's non-contact measurement technique. Furthermore, Nanospec was dedicated to thin film measurements, whereas DekTak was more suitable for surface roughness measurements. Despite the inconveniences arising from the use of DekTak, thorough measurements and meticulously timed wet etching using BOE enabled the thermal oxide thicknesses to be controlled to the desired level of accuracy.

6.2.4 Level 5

Level 5 consists of the feed channels for the journal bearing, the balance plenum, the aft thrust bearing and the aft exhaust. The fabrication of Level 5 followed essentially the same sequence as that for Level 1, except the fabrication was performed on a 450 μm thick wafer, and the forward side comprising of channels leading towards the journal bearing plena, the balance plenum and the aft exhaust was etched first. Once again, the main challenge was the non-uniformity in etch depths at homologous points between the center and edge devices when the DRIE was being carried out using STS2. Photoresist OCG825 had to be applied using Q-tips to cover up devices whose features had already reached their desired depths to prevent overetching. Successive cycles of short-interval DRIE, inspection and measurement of etch depths, application and baking of photoresist had to be performed until all the features reached their desired depths.

6.3 Fabrication of "D^3" Rotors – *D*ouble Layer, *D*onor-Receiver and *D*rop-in Rotors

A new rotor fabrication scheme has been proposed to fulfill two key objectives. The first is to reduce the radial imbalance of the rotors which would otherwise be unacceptable due to excessive DRIE etch variations. The second objective is to enable devices with variations in journal bearing width to be fabricated in the same build.

In the design of the original microbearing test device, the rotor was entirely fabricated from one single wafer. The turbine blades and the journal bearing were essentially etched on the same wafer. As will be presented in Section 7.1, the global etch variation across the wafer arising from the DRIE process gives rise to a net rotor radial imbalance. Rotors belonging to devices at the center of the wafer had typically lower etch variations and hence lower levels of imbalance than their counterparts near the edge of the wafer. This problem is aggravated on the redesigned microbearing test device which has a total of 48 devices, as compared to 12 devices on the original microbearing test device. Many of the devices on the redesigned microbearing test device are positioned at larger radial locations on the wafer and are hence expected to suffer from larger etch variations and hence imbalances. If the original technology for microfabricating the rotors is adopted, the excessively large radial imbalance on most of the devices will preclude transcritical operation and render them unusable for high speed testing. In order

to overcome the issue of excessive radial imbalance, Li [43] proposed a double layer rotor scheme in which the turbine blades and journal bearing are etched on separate wafers. The height of the turbine blades and the journal bearing length is specified by the thickness of their respective wafers, rather than the intrinsic DRIE process.

The double layer rotor process flow is shown schematically on Figure 6-3. Thermal oxide of 0.2 μm was first grown on the blade wafer L3B and journal bearing wafer L3J, both being 330 μm thick. This was followed by a deposition of 0.2 μm of silicon nitride. An etch stop pattern was formed on the forward side of L3J via a shallow etch into the Silicon and a 1 μm thermal oxidation was subsequently performed. The nitride on the bonding surfaces of L3B and L3J was removed by dry processing and the 0.2 μm thermal oxide underneath was removed using 0.5% HF (BOE was not used, since BOE introduces surface roughness, which precludes the perfect bonding of two wafers). Meanwhile, the thermal oxide constituting the etch stops was thinned down to 0.2-0.3 μm, prior to fusion bonding of L3B and L3J. The journal bearing was then being etched from the aft side of L3J with a slight negative taper to avoid the formation of spikes. This was followed by the etching of the blades from the forward side of L3B. Instead of using a large loading pattern, the blades were etched using a halo mask. Etching continued until the Silicon pieces above the etch stops fell off, leaving behind the turbine blades and the forward thrust bearing pad. Excessive etch variations across the surface of the wafer was thus avoided due to the presence of the etch stops. The rotors were freed from the wafer stack, cleaned individually and dropped into the six-layer structure during the final bonding assembly. As mentioned previously in Section 5.1.1.3, the drop-in rotor approach has significant advantages over the original snap-off tab approach. Most importantly, the drop-in rotor approach has been previously demonstrated to significantly increase the overall yield in the number of operational devices.

Apart from reducing the rotor imbalance, the drop-in rotor approach further provides an opportunity for journal bearings of different widths to be achieved on the same build. Previous experiences using an optical mask with different journal bearing clearances reveal the immense difficulties associated with the precision control of journal bearing profiles for journals with different clearances. Using the drop-in rotor approach, journal bearings with different outer diameters, but with the same journal bearing clearance, can be drawn on the same optical mask. Journal bearings with varying

clearances are subsequently achieved by exchanging rotors with different journal bearing outer diameters, as depicted schematically on Figure 6-8. Since the journal bearing width is identical for all the devices during the DRIE process, this novel donor-receiver technique only necessitates the etching recipe to be fine-tuned for one, rather than multiple journal bearing widths.

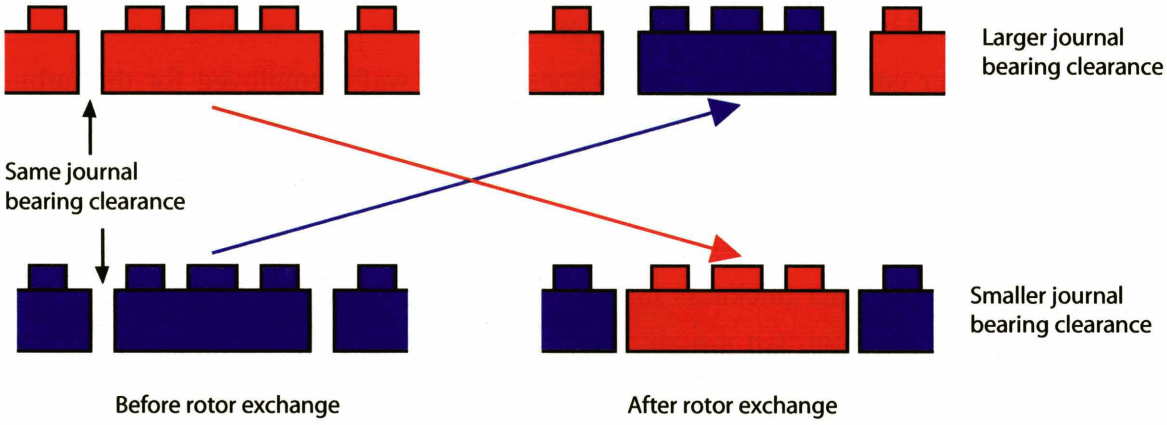

Figure 6-8: Swapping of neighboring rotors prior to the fusion bonding process. Journal bearings with the same width but different radii are etched. The exchanging of rotors result in devices having different journal bearing widths.

In summary, the novel rotor fabrication scheme serves to fulfill two key objectives. The first is to reduce the radial imbalance of the rotors which would otherwise be unacceptable because of excessive DRIE etch variations. The second goal is to enable devices with variations in journal bearing width to be fabricated in the same build. Since the rotors adopt a *d*ouble-layer, *d*onor-receiver and *d*rop in approach, they are thus called "D^3" rotors.

Several other issues have to be considered before the successful implementation of the double-layer rotor scheme. First, the donor-receiver approach where rotors at different locations along the wafer are exchanged is feasible only if the rotors have sufficiently small variations in total thickness. This is crucial because the total thrust bearing clearance is only on the order of 4.5 μm. Excessively large deviations in the rotor thickness adversely cause the total thrust bearing clearance to deviate significantly from its nominal design value. In this respect, it is necessary to ensure that the wafer total-thickness variation (TTV), which quantifies the maximum variation in wafer thickness across the entire wafer, is sufficiently small. The TTV value of the Okmetic wafers used in the double-layer rotor scheme is approximately 0.4 μm across the 150 mm diameter

wafer. However, it should be noted that the variation in wafer thickness between two points in close proximity is significantly smaller than the value quoted above. Care has been exercised during the design of the mask for the journal bearing so that the eventual rotor exchanging process only involves the swapping of rotors which are in close proximity to one another. This further assures that the total thrust bearing clearance is negligibly affected by the rotor exchanging process.

One other consideration is the thickness of the wafer employed for the turbine blades. This has been selected to be 330 μm, which is identical to the wafer thickness utilized for the journal bearing. Although it is not mandatory for the turbine blade height to be identical to the journal bearing length, there is a tradeoff between the maximum and minimum allowable wafer thickness for the turbine blades. The use of excessively thick wafers, resulting in overly tall turbine blades, increases the rotor tip deflection and the blade root stresses. On the other hand, wafer handling issues impose a lower bound on the allowable wafer thickness. The fragility of an excessively thin wafer renders it challenging to handle with tweezers and increases the likelihood of wafer fracture when it is subjected to commonly available microfabrication processes. According to Li [43], the wafer thickness should be kept above 250 μm from the point of view of wafer handling. Since 330 um thick wafers were readily available, the wafer thickness for the turbine blades was thus selected to be 330 μm. The additional 80 μm margin above the threshold thickness of 250 μm would further enhance the handling qualities of the wafer.

6.4 Summary and Conclusions

In this chapter, the process flow for the fabrication of the six-wafer stack redesigned microbearing test device was presented. The main challenges encountered during the course of fabricating each layer were described, and the pertinent steps taken to overcome these challenges were discussed. The novel fabrication techniques and procedures for "D^3" rotors (double layer, donor-receiver and drop-in rotors) were described in detail. "D^3" rotors serve as the important enabling technology for fabricating rotors with sufficiently low levels of radial imbalance, and for fabricating devices with different journal bearing widths on the same build.

CHAPTER 7

Experimental Investigation of Hydrostatic Gas Journal Bearings for Micro-Turbomachinery

This chapter focuses on experimental work pertaining to micro-hydrostatic gas journal bearings. In the first part of this chapter, measurement and analytical techniques for statically quantifying the radial imbalance of rotors arising from DRIE non-uniformities are presented. Experimental techniques using a high-resolution fiber optic sensor and data reduction schemes developed for determining imbalance-driven whirl amplitudes and response curves are described in detail. Salient rotordynamic quantities of micro-hydrostatic journal bearings, such as stiffness, natural frequency, damping ratio and rotor imbalance are quantified experimentally, and compared to analytical model predictions. Alternative and simplified experimental procedures for quantifying journal bearing natural frequencies are also presented. The chapter closes with experimental strategies for crossing journal bearing natural frequencies and procedures for accelerating to high speeds.

7.1 Quantification of rotor imbalance arising from DRIE etch variation

One of the most important geometric parameters affecting the rotordynamics of a rotor-journal bearing system is the radial imbalance of the rotor, which is defined as the distance between its geometric and mass centers. An excessively large radial imbalance decreases the distance to contact during transcritical operation and increases the likelihood of rotor collision with the static sidewalls of the journal bearing. Furthermore, journal bearing stability is also strongly influenced by rotor imbalance. During supercritical journal bearing operation, the rotor spins about its mass center and its whirl amplitude thus corresponds to the rotor imbalance. Large rotor imbalances also lead to stronger nonlinear supercritical subharmonic responses which result in larger whirling amplitudes and increase the possibility of a rotor crash and thus preclude high speed operation.

One of the major contributors to rotor imbalance arises from Deep Reactive Ion

Etching (DRIE) etch non-uniformity. The etch variation during the DRIE process results in a difference in blade heights and thus rotor imbalance. Since rotor imbalance plays such a significant role in affecting the rotordynamics, it is thus of utmost importance to statically quantify it during the microfabrication process. The data obtained is useful for several reasons. First, the available data can be correlated to actual experimental results to elucidate the effects of imbalance on bearing performance and stability. Furthermore, having a means to quantify the rotor imbalance permits fabrication specifications and tolerances to be imposed. The maximum allowable imbalance can be established using analytical models and rotors which exceed the imbalance limits are deemed to be "out-of-spec".

Each build of the original microbearing test device consists of 12 devices fabricated on a 4 inch wafer, as depicted in Figure 7-1. Devices 4, 5, 8 and 9 are identified as center devices, whereas the remaining devices are termed as edge devices. The etch depth is quantified by the maximum depth in the region enclosed by the two adjacent rotor blades and stator blades, such as the area a_1 surrounded by rotor blades #1 and #2 and the closest stator blade as illustrated in Figure 7-2.

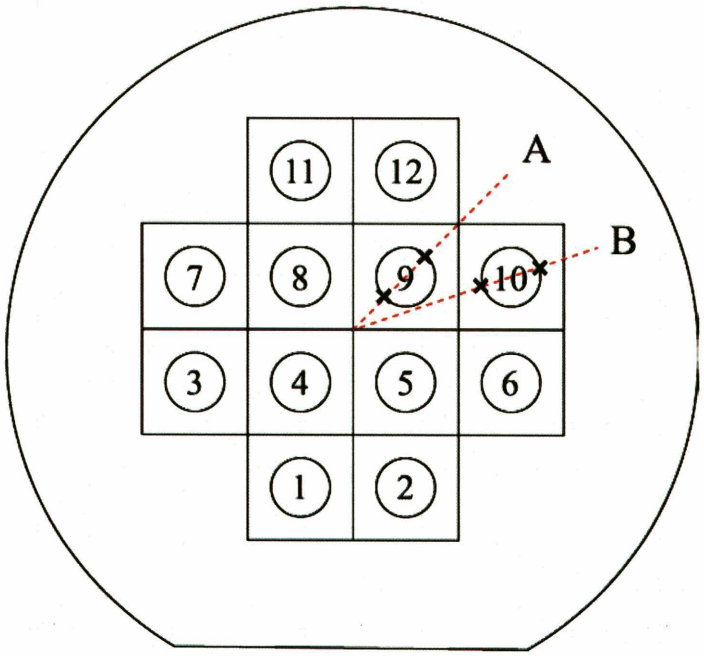

Figure 7-1: Location of the 12 devices on a 4-inch Silicon wafer.

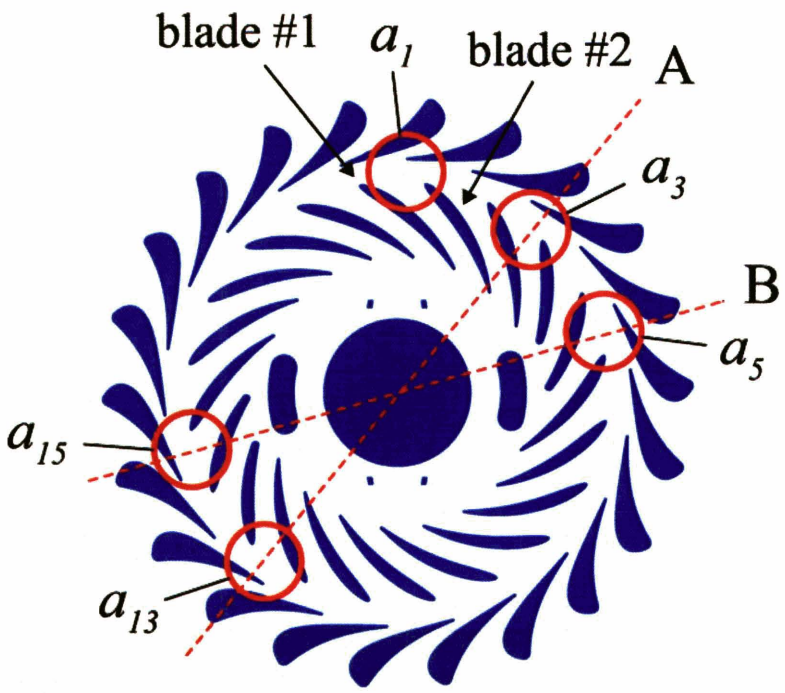

Figure 7-2: Measurement locations for each device.

The exact details of etch variation arising from DRIE are complicated. However, one simple way to model the etch non-uniformities arising from the intricate process is to decompose the etch variation into two dominant components: a *local* etch variation and a *global* etch variation. *Locally*, the etch variation depends on the concentration or proximity of the patterned geometry as illustrated in Figure 7-3. Figure 7-3 was obtained by post-processing etch-depth measurements using a non-contact optical profiler WYKO. As can be seen from the contour map, shallower etch depths are obtained in regions which are closer to contiguous features. The turbomachinery of the original microbearing test device consists of 22 stator blades and 20 rotor blades. Since the number of stator and rotor blades are both even, the layout of the features is thus symmetric diametrically. That is, the local geometric environment for the DRIE in area a_5 of Figure 7-2 is identical to that of area a_{15} at a location 180° away. The same can be said in comparing area a_3 with area a_{13}. This implies that the local etch variation is identical for diametrically opposite points on the rotor and hence, does not contribute to the rotor imbalance.

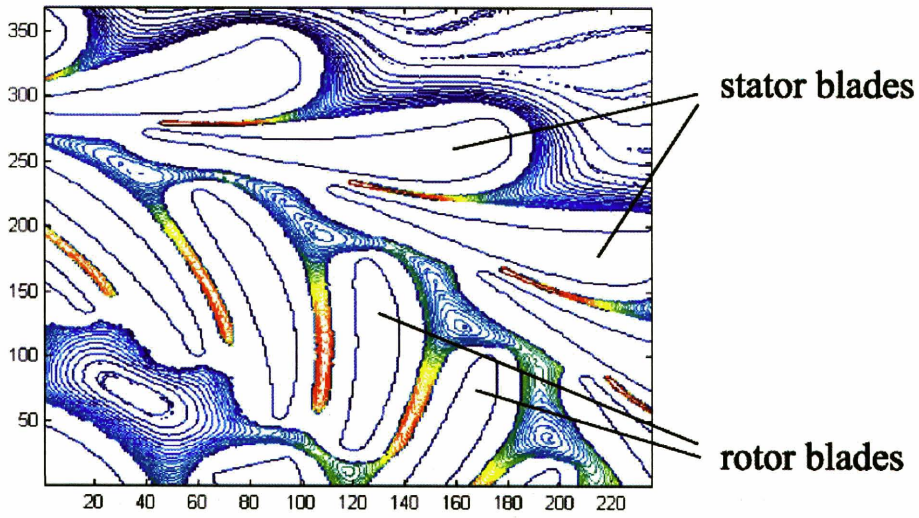

Figure 7-3: Measured contours showing DRIE etch variation in a micro-rotor.

Globally, DRIE typically causes the devices at the center of the wafer to have etch depths which are approximately 10% shallower than the devices at the edge of the wafer. This is a consequence of a non-uniform etch rate across the wafer. As shown in Figure 7-4, a *global* etch non-uniformity translates at the device level into a difference in blade height from one side of the rotor to the other. This results in a misalignment between the geometric center and the center of mass, i.e. an imbalance. The global etch variation is evaluated from the difference in etch depths corresponding to the two regions which are nearest and furthest from the center of the wafer. For example, referring to Figure 7-2, the difference in etch depths are measured in regions a_3 and a_{13} for device #9 and in regions a_5 and a_{15} for device #10. The etch rates in the regions closest and furthest from the center of the wafer are measured for the 4 center devices and 4 edge devices (die #1, 6, 7, 12 in Figure 7-1). In Figure 7-4, the left two and the right two data points represent the global etch non-uniformity across the center devices and the edge devices, respectively. The etch rate can be seen to increase monotonically with the distance from the center of the wafer.

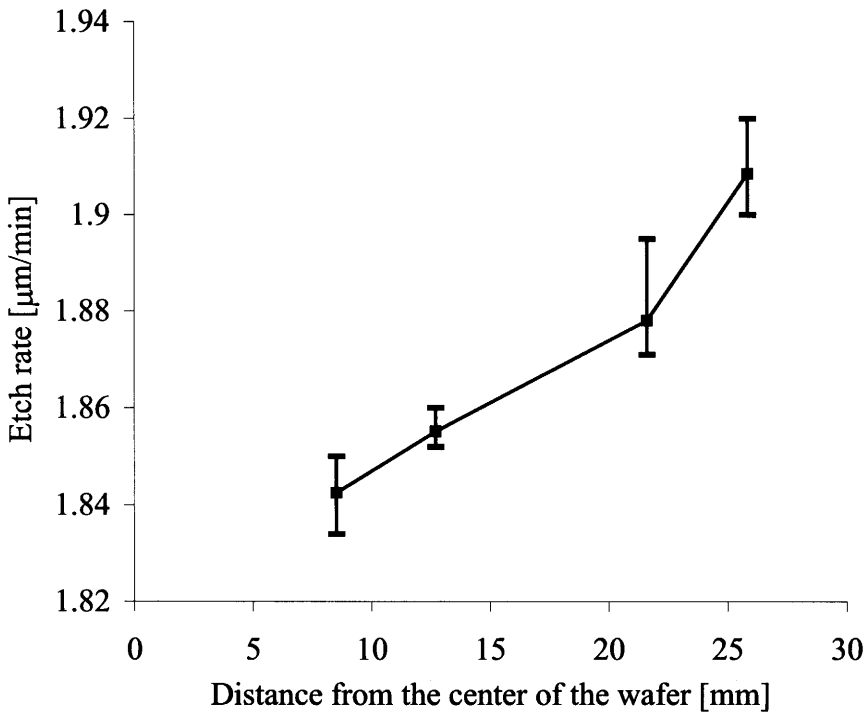

Figure 7-4: Etch rate variation across the wafer.

Figure 7-5 illustrates the etch depth along the circumference of rotors of a center device and an edge device. The etch depths were measured using WYKO. Plotted along the abscissa is the angular position on the rotor defined in a clockwise manner, with the data point at 0 degrees depicting the maximum etch depth in region a_1. By modeling the etch depth variation as a combination of local and global effects, a Fourier transform can be performed to segregate the local variations from the global contributions, as depicted in Figure 7-6. The first harmonic corresponds to the global etch variation, whereas the second harmonic results from the local etch variation due to the symmetric feature arising from the even number of rotor and stator blades. The edge device and the center device measured herein involved global etch variations of 5.1 μm and 1.4 μm, respectively.

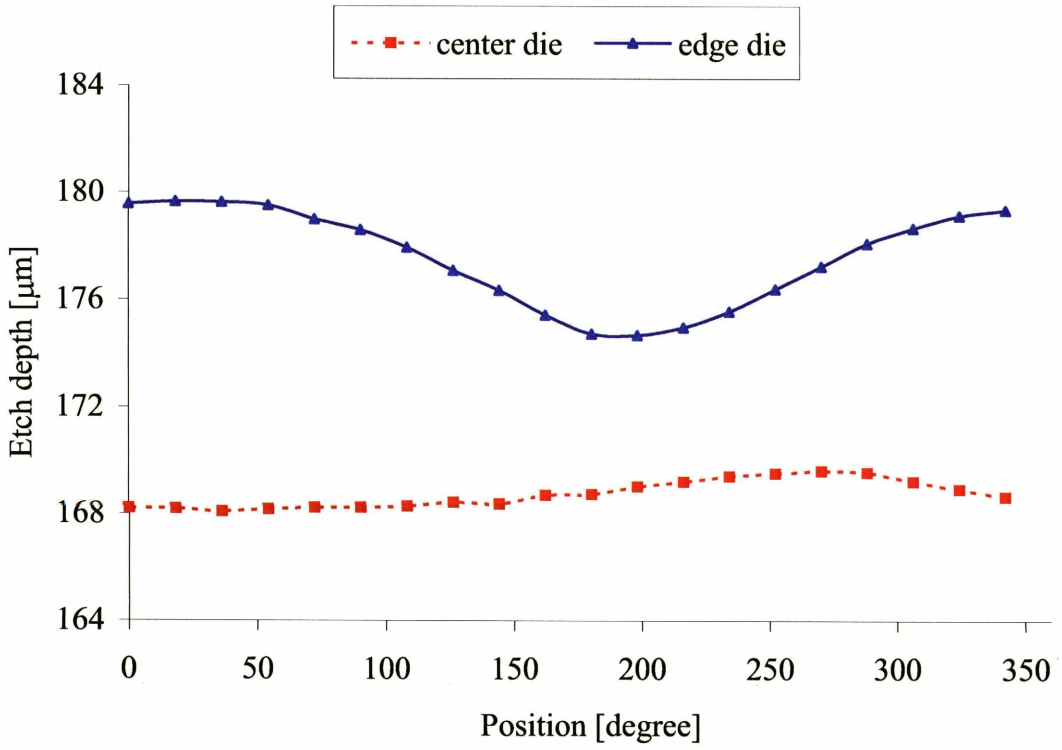

Figure 7-5: The etch depth along the periphery of the rotor.

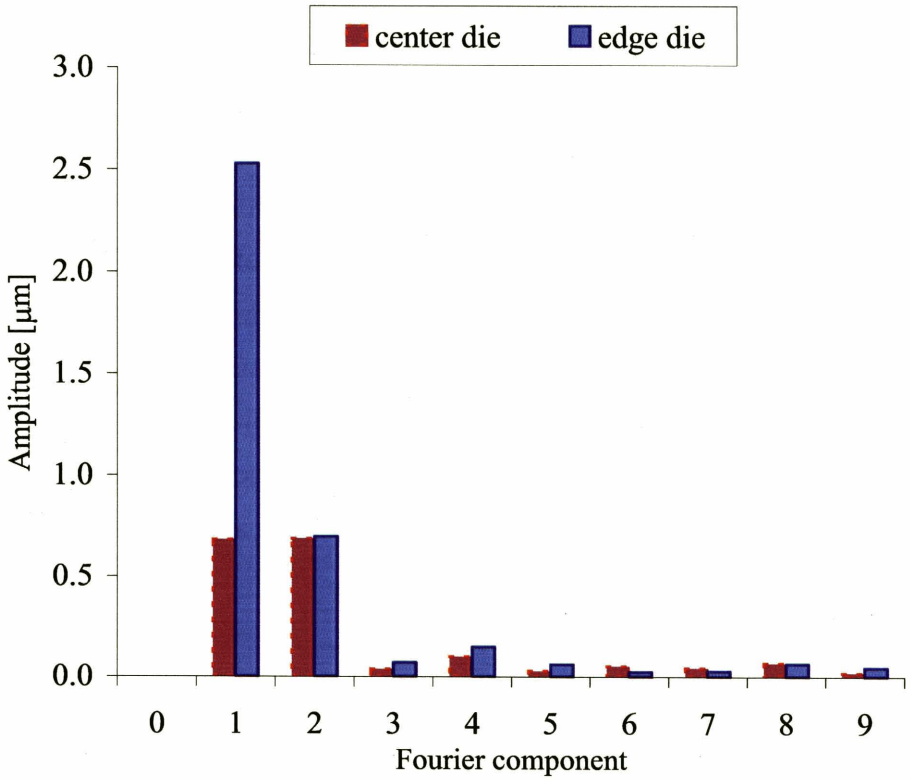

Figure 7-6: The Fourier spectrum of the etch variation along the periphery of the rotor.

The imbalance originating from the etch variation was estimated using AutoCAD by assuming a linear relationship between the global etch non-uniformity and the distance from the center of the wafer as shown in Figure 7-7. Figure 7-8 indicates that the imbalance increases almost linearly with the global etch uniformity. For example, a global etch variation of 3.0% (expressed as a percentage of the mean etch depth) results in a rotor imbalance of 2.7 μm for the microrotor with a diameter of 4.2 mm and a blade height of 150 μm. It should further be noted that the static imbalance determined using this technique compares favorably to the results inferred from dynamic measurements (which yields an imbalance value of 3 μm), details of which will be furnished later in this chapter.

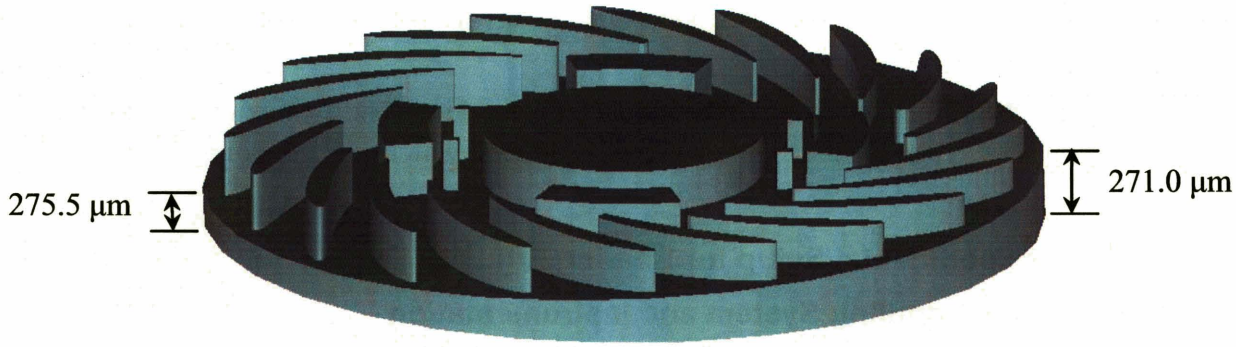

Figure 7-7: Schematics of the micro-rotor with greatly exaggerated global etch variation.

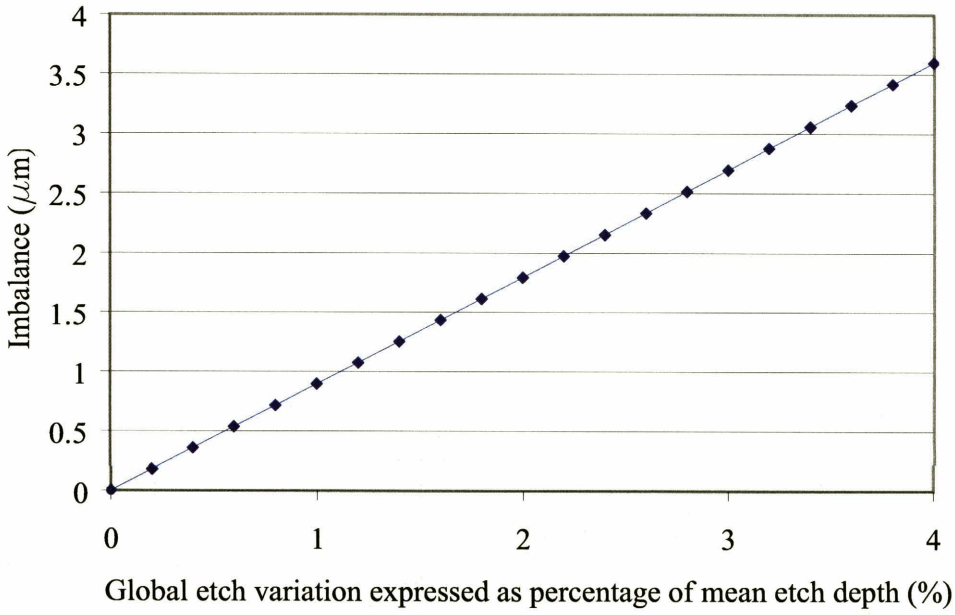

Figure 7-8: Imbalance due to the global etch variation. The estimation was based on an average blade height of 150 μm and total wafer thickness of 450 μm.

7.2 Experimental Setup for Bearing Rig

7.2.1 Gas Handling System and Instrumentation

The gas handling system shown schematically in Figure 7-9 provides controlled pressures or mass flows via pressure regulators or mass flow controllers to the individual ports of the packaging that houses the microbearing test device. Eight independent pressure supplies are required:

- Forward thrust bearing supply
- Aft thrust bearing supply
- Main turbine inlet supply
- Journal bearing supply (4 individual and independent supplies)
- Axial balance plenum supply

There are 2 exhaust ports on the packaging:

- Forward exhaust (for main turbine and forward thrust bearing)
- Aft exhaust (for aft thrust bearing and axial balance plenum)

In addition, there is a pressure tap for measuring the turbine inter-blade row pressure between the turbine NGV's and the rotor blades.

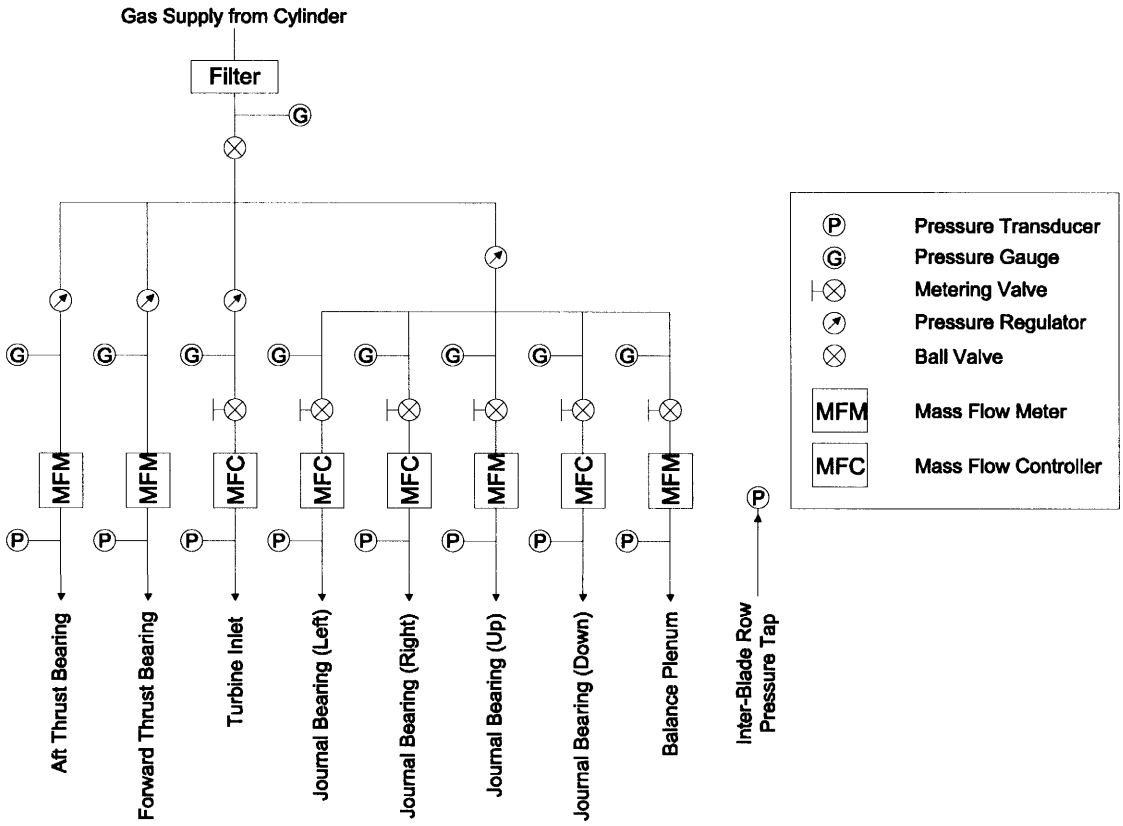

Figure 7-9: Schematic showing the gas-handling system.

The thrust bearings are supplied with their working fluid via Norgren pressure regulators to maintain a fixed supply pressure. Working fluids which have been used include Nitrogen, Argon and Helium. The pressure and mass flow to both the forward and aft thrust bearings are monitored and acquired at all times. The gas supplies to the journal bearing require finer control, since the hydrostatic differential pressure DP and hence the mass flow through the journal bearing do not remain constant throughout the experiment due to flow leakage through the annular seals. A sufficiently low DP and thus a large damping ratio is required to achieve transcritical operation. However, the value of DP has to be increased to attain a sufficiently high stability boundary in order to achieve the desired high DN numbers required for high power densities. The mass flow to each journal bearing supply plenum is regulated via a MKS mass flow controller having a range of 2000 sccm and a full scale accuracy of 1%. The total mass flow through the journal bearing is on the order of 1000 sccm corresponding to a DP of 5 psi using Nitrogen. The flow controller is regulated by supplying a set point control voltage signal

to it. A Honeywell pressure transducer placed downstream of the mass flow controller monitors the supply pressure to the journal bearing plenum. A similar pressure transducer measures the turbine inter-blade row pressure, which serves as an approximation for the static pressure at the exit of the journal bearing.

The working gas (Nitrogen, Argon or Helium) to the turbine is supplied via an MKS mass flow controller with a range of 20,000 sccm. The mass flow rate through the turbine using Nitrogen is anticipated to be approximately 13,000 sccm at the design speed. The rotational speed of the rotor is primarily controlled by regulating the mass flow through the turbine. The rotor axial position is controlled by supplying fluid to the axial balance plenum. The pressure supply and mass flow through the axial balance plenum are also monitored at all times.

The turbine rotational speed is measured using a Philtec D6 high frequency response fiber-optic displacement sensor which views the "speed bumps" designed for that function and located in the turbine rotor exhaust annulus. The output voltage from the sensor is a function of the proximity of the sensor from the reflecting surface it is directed at, and is also modulated by the reflectivity of the surface. This voltage is fed into a HP87410A DC-10MHz spectrum analyzer, which displays Fourier transforms of the voltage signal in real time. The rotational speed can be ascertained by identifying the frequency corresponding to the peak amplitude of the power spectral density (and dividing by the appropriate number of speed bumps on the rotor). The position of the sensor is controlled by a Newport 461 XYZ Ultralign Stainless Steel Linear Stage.

7.2.2 Data Acquisition System

All the pressures and mass flows are acquired at a sampling frequency of 1000 Hz per channel using a National Instruments PCI-6071E A/D board, whose output is connected to a 300 MHz desktop PC. The data from each channel are averaged over 200 scans before being written to a spreadsheet for the purpose of documentation. The data acquisition program is written in LabVIEW and it provides a real-time display of all the pressures and flow rates acquired. Communications between the PC and the spectrum analyzer is via a GPIB interface. This allows the settings on the spectrum analyzer to be adjusted by the PC and the rotor spinning speed evaluated by the spectrum analyzer to be acquired by the PC. During rotordynamic experiments to deduce the imbalance-driven

whirl response curve, it is necessary to acquire high frequency data from the fiber optic sensor. This is achieved using a National Instruments PCI-6110E A/D board, whose output is connected to another PC. The output from the fiber optic sensor can be acquired up to a maximum acquisition rate of 3 MHz. Another data acquisition program written in LabVIEW is used to set the sampling rate (typically 2 MHz), the number of data samples (typically 2 x 10^6) to write to file and the number of channels of data to acquire. The sampling frequency is selected to ensure that a sufficiently large number of data samples are acquired for each complete rotor revolution. The number of data samples to be written for each data file is chosen to allow for a minimum of 50 rotor revolutions.

7.3 Rotordynamics of Micro-Hydrostatic Gas Journal Bearings

7.3.1 Experimental Setup and Data Reduction Schemes

In this section, the first experimentally measured imbalance-driven whirl response curves for the microbearing test device are reported in detail. Data obtained using the signal from the fiber-optic sensor (whose primary purpose is sensing the rotor speed) are also employed in conjunction with accompanying data-reduction techniques to gain a deeper understanding of the rotordynamics of the journal bearing. The imbalance-driven whirl response curves of the rotor are obtained under different conditions of hydrostatic differential pressure DP. The stiffness and natural frequency of the journal bearing, its damping ratio and the imbalance of the rotor are subsequently deduced. Before proceeding any further, it should first be highlighted that one of the greatest challenges facing the testing and operation of micro-gas bearings is instrumentation and data analysis. Unlike conventional, macro-scale gas bearing systems, where displacement or proximity sensors can be conveniently positioned along several locations along the periphery of the rotor to deduce whirling orbits and journal bearing critical frequencies, similar experimental techniques cannot be readily applied to the micro-gas journal bearings for the MIT microdevice. New experimental methodologies and data reduction algorithms have to be developed in the pursuit for valuable journal bearing rotordynamic information. The experimental setup and procedure will be described as follows.

The salient steps for the experiment are shown schematically in Figure 7-10. The flow rates and pressures to the journal bearing are regulated to achieve an almost constant hydrostatic differential pressure DP across the journal bearing (the bearing pressure

difference DP essentially sets the stiffness and thus natural frequency of the journal gas bearing). The rotational speed is regulated by controlling the mass flow through the turbine. A Philtec fiber optic sensor, whose primary purpose is to determine the rotational speed of the rotor, is inserted through an opening on top of the device, tracking the passage of the speed bumps on the surface of the rotor (See Figure 7-10). The output voltages from the fiber-optic sensor are acquired over a range of rotational speeds at a very high sampling frequency of 2 MHz. The data is subsequently analyzed by means of waveform data reduction algorithms developed by Paduano [48] and the author.

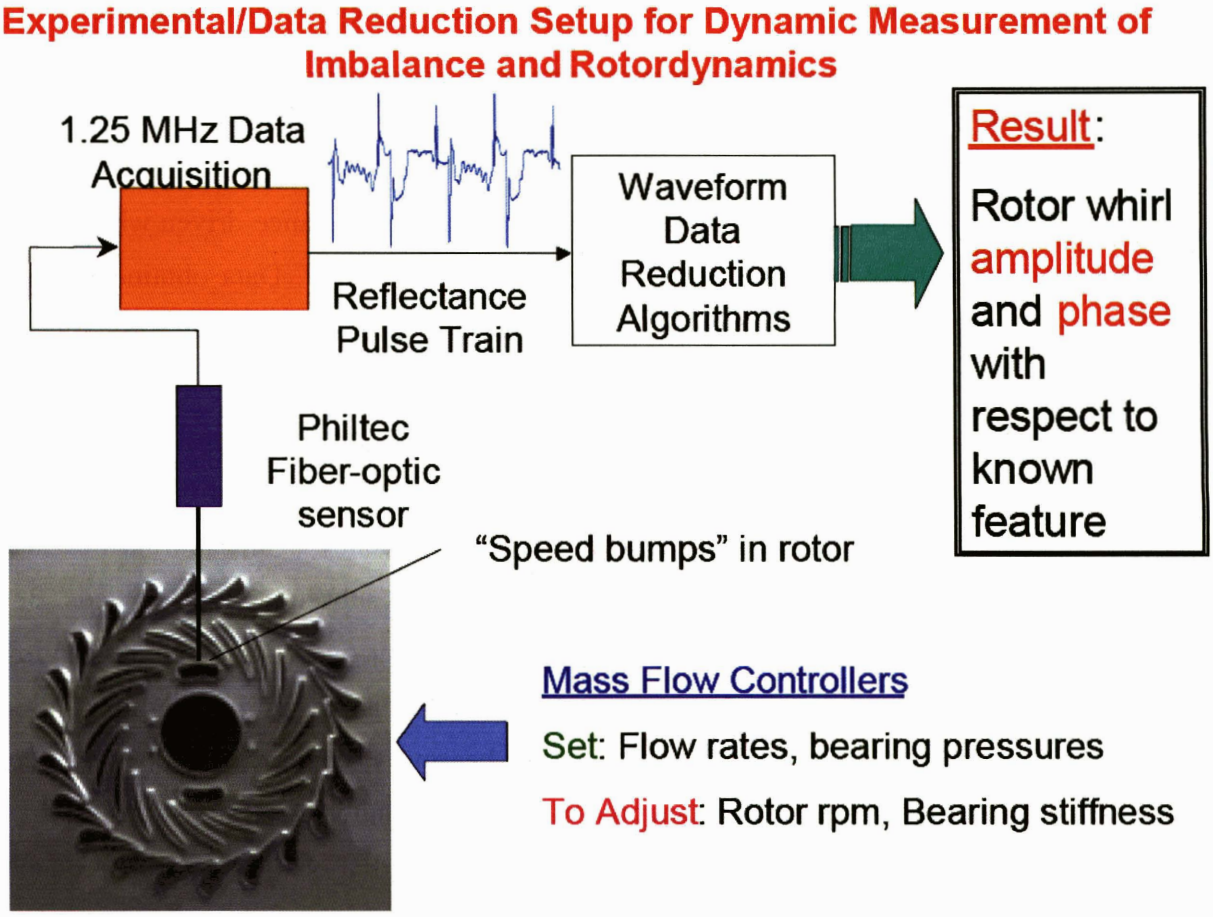

Figure 7-10: Experimental setup for journal bearing rotordynamic measurements.

In order to obtain the whirl response curve for a particular DP, fiber optic data are acquired over a range of rotational speeds. The data acquired at the lowest speed serves as the baseline for which data obtained at higher rotational speeds are compared against. As shown in Figure 7-11, the imbalance of the rotor (i.e. the distance between the geometric center of the rotor and its mass center) induces a whirling motion

superimposed on the rotational motion of the rotor. The whirling or precession frequency of imbalance-induced precession is assumed to be synchronous with the rotational frequency of the rotor. The precession velocity due to the imbalance-induced whirl yields an increase or decrease in the absolute velocity of the speed bumps, depending on the relative orientation between the rotation velocity and the precession velocity (see Figure 7-11). The effect of rotor whirl on the measured waveform is presented in Figure 7-12. In the absence of any whirl, successive sampled data correspond to features on the rotor which are evenly spaced circumferentially, i.e. the angular displacement of the rotor is constant between any two consecutive samples. However, in the presence of a whirl, the whirling velocity results in features of the speed bumps being cyclically compressed or dilated in time. The resulting optical waveform is essentially a pulse width modulation of the reference waveform obtained in the absence of any rotor whirl. Since the whirl amplitude of the rotor is negligible at very low speeds, it is reasonable to assume that the rotor has almost zero whirl at the lowest speed. An acquisition rate of 1.25 MHz might be insufficient to resolve the rotor induced whirl at higher rotational speeds. However, asynchronous sampling allows subsample resolution to be achieved through ensemble averaging of the shifted waveforms, as shown in Figure 7-13. By comparing the optical data at a higher speed to the reference (or baseline) waveform, a least squares technique is employed to deduce the optimum waveform dilation necessary to transform the whirl waveform to the reference waveform. Since the whirl and rotational frequencies are assumed to be synchronous, a simple sinusoidal waveform at the rotational frequency is employed as the pulse-width modulating function. The amplitude and the phase of this modulating function correspond to the size of the precession orbit and to the position or orientation of the orbit with respect to a particular feature on the rotor. The whirl-induced response curve is obtained by repeating this procedure for a range of rotational speeds at a fixed journal differential pressure DP.

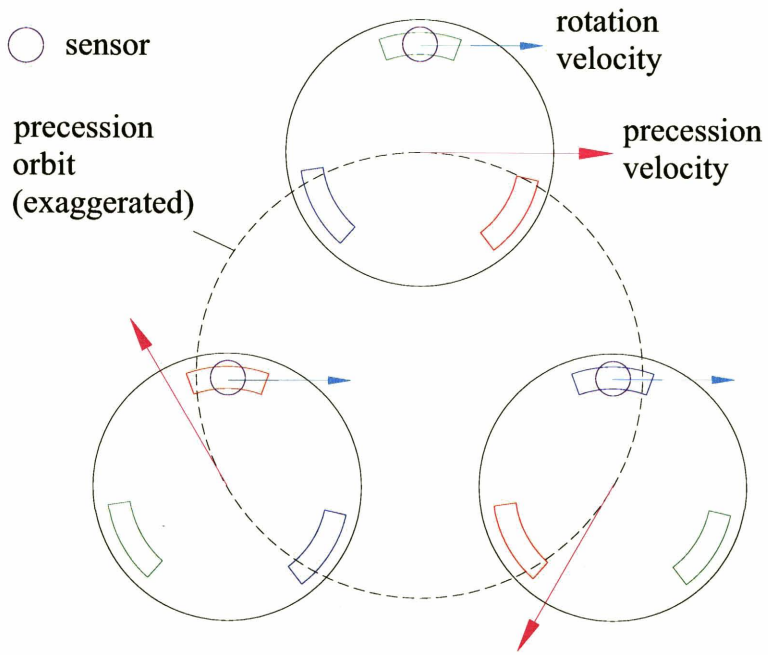

Figure 7-11: Effect of whirling motion on the absolute velocity of a speed bump.

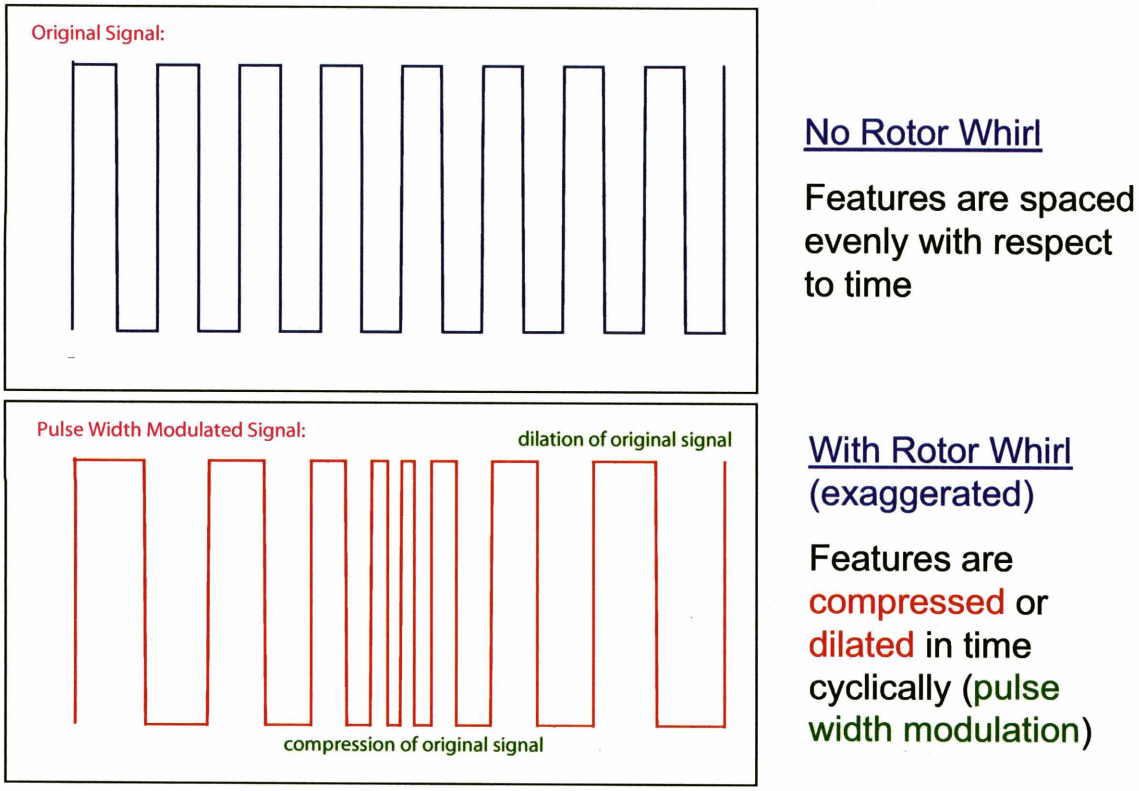

Figure 7-12: Effect of rotor whirl on measured waveform.

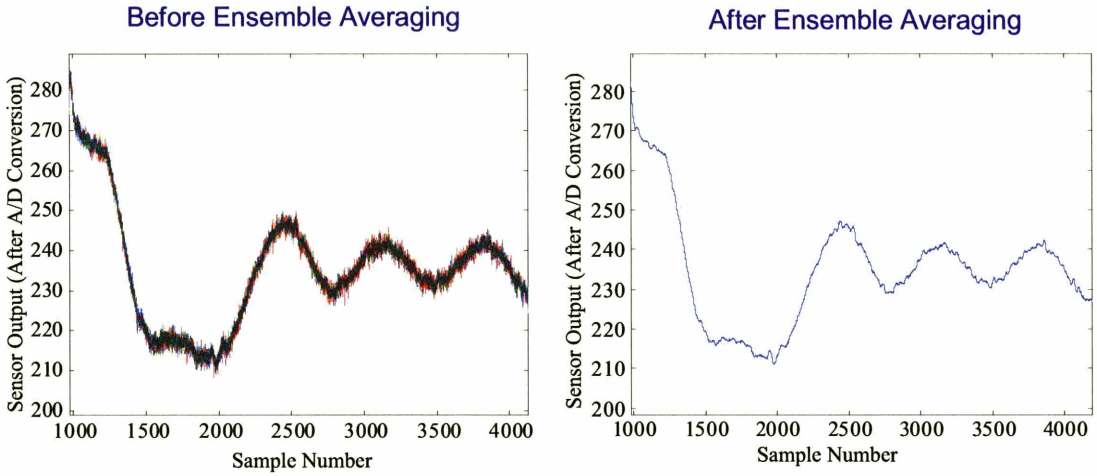

Figure 7-13: Asynchronous sampling permits sub-sample resolution to be obtained through ensemble averaging of shifted waveforms.

7.3.2 Measurements of Natural Frequency and Imbalance

Figure 7-14 depicts the response curve (amplitude and phase) of a microbearing test device rotor obtained from fiber optic measurements at a DP of 2.0 psi. The whirl amplitude peaks at 7.7 μm, corresponding to a natural frequency of 35,000 rpm. Since the journal bearing clearance is 12 μm, the absolute distance-to-contact is 4.3 μm. The transition from subcritical operation (rotation around the geometric center of rotor) to supercritical operation (rotor-inversion or self-centered rotation around the mass center of the rotor) is also visible in the phase shift of approximately 180°. near the natural frequency. One can also deduce the amplitude and location of the imbalance from the response curves. It should be noted that the magnitude of the amplitude response curve when the rotor operates supercritically or self centers corresponds to the magnitude of the imbalance. Hence, from Figure 7-14, it can be deduced that the mass center of the rotor is displaced by approximately 1.6 μm from the geometric center of the rotor, yielding an imbalance of about 1.6 μm. This compares favorably to the value of 2.0 μm obtained from etch variation estimates. Furthermore, the phase of the phase response curve when the rotor operates supercritically yields information pertaining to the location of the imbalance with respect to a particular feature on the rotor. This information is of critical importance, as it paves the way towards the goal of dynamically balancing the rotors by employing techniques such as laser ablation of the rotor disk. By selectively removing mass from the rotor and repeating the above procedure to measure its resulting

imbalance-driven whirl response curve, a rotor can be balanced using an iterative procedure.

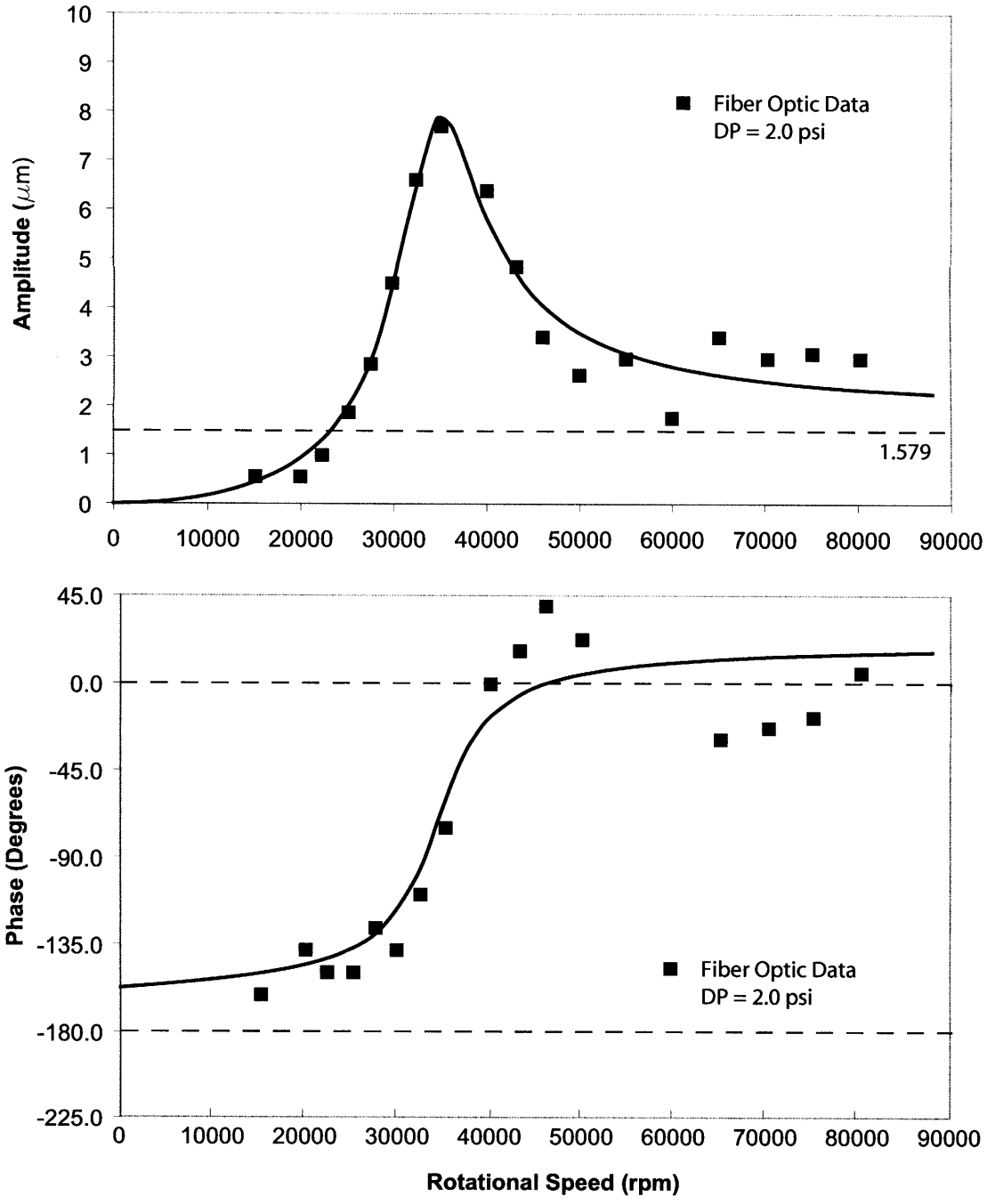

Figure 7-14 Experimentally measured response curve for a journal bearing differential pressure DP = 2.0 psi.

It is of importance to reduce the imbalance of the rotor, as the maximum peak

response near the natural frequency increases with the level of imbalance, resulting in higher likelihood of rotor collision with the surrounding wall. Transition from a subcritical to supercritical state of operation becomes increasingly difficult for higher levels of imbalance, and this precludes high speed performance. Higher imbalance also promotes instability, reduces the range of stable operation, and thus limits the maximum operational speed. In addition, the peak amplitude of supercritical subharmonic pseudo-critical peaks is proportional to the imbalance.

7.3.3 Effects of Journal Bearing Hydrostatic Differential Pressure on Natural Frequency and Damping Ratio

To further elucidate the effects of DP, response curves for the same device are shown on Figure 7-15 for three different values of DP. It can be seen that the natural frequency of the journal bearing increases monotonically with DP, indicating that a higher hydrostatic pressure across the bearing results in a stiffer bearing. This trend of increasing stiffness with increasing DP, as well as the magnitudes of the natural frequency compare well to the modeling results of Liu [3] and the scaling laws derived in Spakovszky & Liu [5]. According to the scaling laws, the natural frequency Ω_N and DP should scale according to

$$\Omega_N \propto (DP)^{0.5}. \tag{7.1}$$

Another crucial feature which can be observed from the plots is the rise in magnitude of the peak amplitude with increasing values of DP. This is equivalent to a reduction in the distance to contact with the surrounding stationary wall. When the peak amplitude reaches values equivalent to the journal clearance, a rotor crash or collision occurs. Although a higher DP results in stiffer bearings, the damping ratio $\zeta = c/(2m\omega_N)$ exhibits a decreasing trend with increasing DP. The damping ratios have been estimated to be 0.260, 0.130 and 0.112 corresponding to DP values of 1.0, 2.0 and 2.4 psi, respectively. This trend of decreasing damping ratio with increasing hydrostatic pressure across the journal bearing is also consistent with Liu's modeling results and the scaling laws of Spakovszky & Liu [5]. According to the scaling laws,

$$\zeta \propto (DP)^{-0.5}. \tag{7.2}$$

In fact, at higher values of DP, the damping ratio becomes excessively low that it is not

possible to map out the complete response curves like those shown on Figure 7-15, due to excessively large peak amplitudes experienced near the natural frequency, which render the transition from a subcritical to supercritical state of operation difficult. These findings yield far-reaching implications on the operational protocols employed for operating the bearings to high speeds. Low values of DP and thus higher damping ratios are necessary to cross the natural frequency without collision and contact with the journal bearing wall. This was also observed on tests performed on a micro-turbocharger, where very low values of DP were required to successfully cross the natural frequency and to "invert" the rotor [16] (that is, survive acceleration through the transcritical regime and operate at supercritical speeds with the rotor's mass center at 180° position from its location at very low subcritical speeds). Finally, from Figure 7-15, it can also be observed that the levels of imbalance obtained corresponding to the different values of DP are consistent at approximately 1.6 μm. It should also be mentioned that the above value deduced for the imbalance compares well to the static value deduced from etch-variation or blade height measurements along the periphery of the rotor prior to wafer bonding.

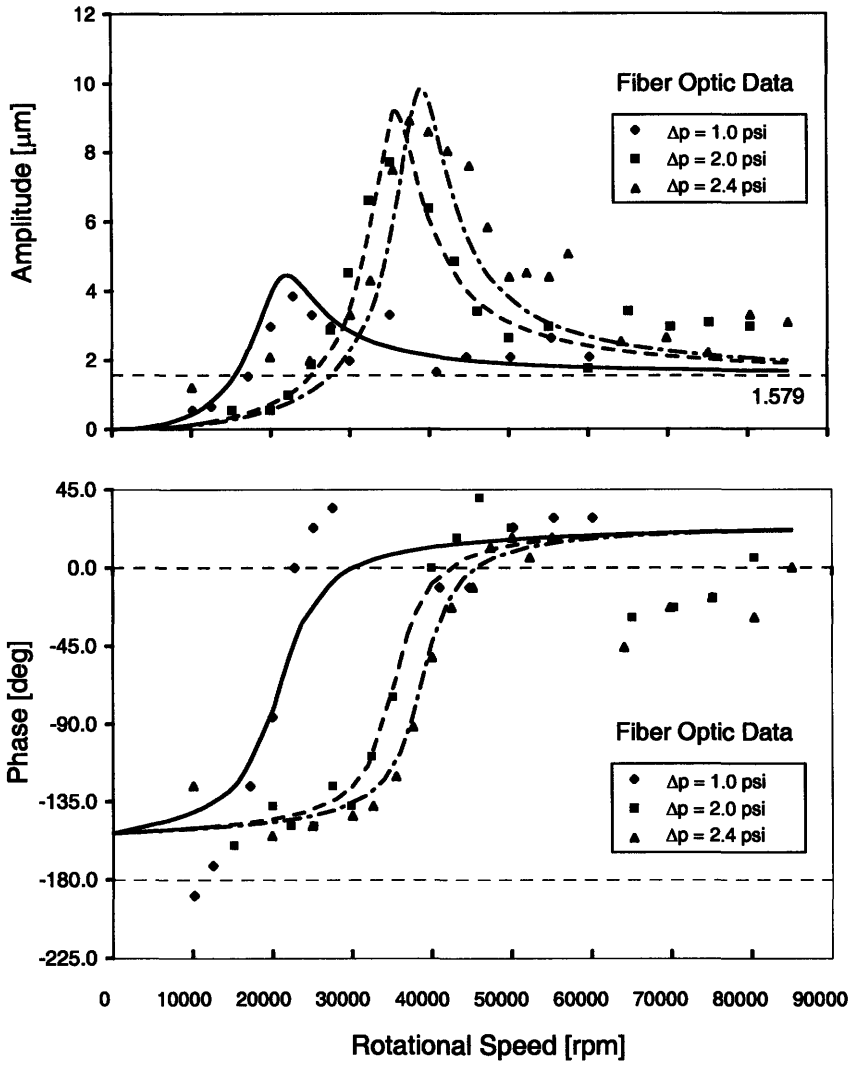

Figure 7-15: Amplitude and phase response curves of rotor for various pressure differences across the journal.

The above technique of employing the optical data to investigate the rotordynamics of the journal bearing has subsequently been successfully applied to the micro-turbocharger, the micro-turbopump and the micro-turbine-generator.

7.3.4 An Alternative Experimental Procedure to Measure Natural Frequencies

In addition to employing optical data to deduce information regarding the rotordynamics of the bearing, a separate procedure has also been successfully employed to deduce the natural frequency of the device under varying operating conditions. This

technique does not require data post-processing and provides a fast procedure to quantify the natural frequencies and to qualitatively capture the whirl-induced bearing response.

A flow controller which maintains the volumetric flow rate at ±1 % of the set-point is used to supply the working gas to the journal bearing. The flow rate through the journal bearing is held constant and the resulting hydrostatic pressure drop DP across the journal bearing is monitored during the acceleration from subcritical to supercritical speed. The rotor is accelerated through the critical frequency by increasing the turbine flow. A typical plot of the behavior of DP is shown in Figure 7-16. At rotational speeds below 20,000 rpm, the bearing differential pressure DP stays approximately constant, but at approximately 24,000 rpm, the value of DP drops precipitously, resembling the response curve shown previously. It is suggested that this distinct drop in the pressure difference across the journal is due to the rotor operating at larger eccentricities upon crossing the natural frequency. According to the modeling results of Liu [3], the flow resistance associated with a rotor operating at large eccentricities is significantly smaller than when it is centered. Since the flow controller keeps the flow rate through the journal bearing constant, this reduction in flow resistance thus translates into a reduction in DP across the journal. These measurements render a fast and accurate means to deduce the natural frequency and infer the onset of rotor operation at large eccentricities.

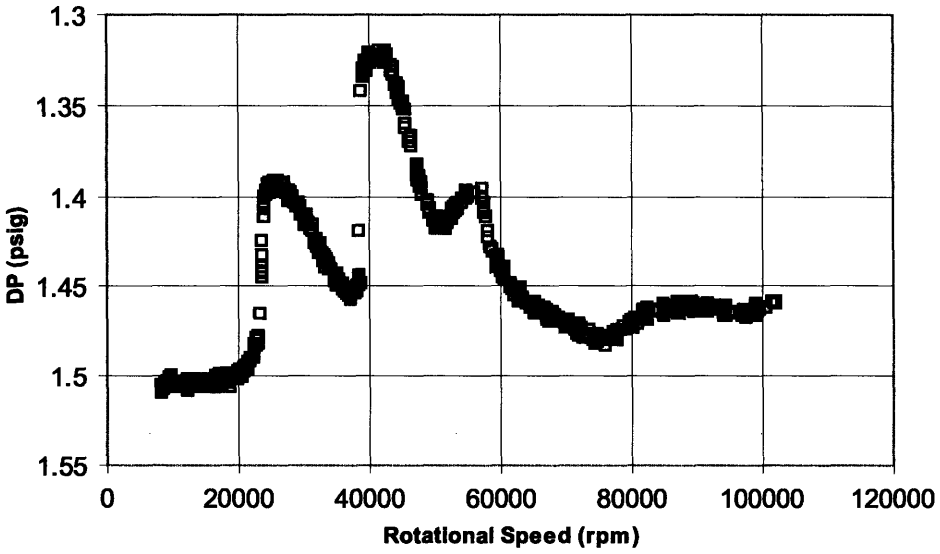

Figure 7-16: Behavior of bearing pressure difference at constant bearing flow rate during acceleration to high speed.

Upon increasing the rotational speed past the first natural frequency, subsequent reductions in DP were also observed at approximately integral multiples of the first natural frequency. Two hypotheses have been put forth to explain this phenomenon. The redesigned microbearing test device consists of four separately fed journal bearing plena. When the journal bearing is operated anisotropically, hydrostatic flow is only supplied to the two diametrically opposite plena which subtend an angle of 110° each, whereas the remaining two plena are blocked off. The second abrupt drop in the value of DP is thus conjectured to be due to the effects of journal bearing anisotropy, which gives rise to different stiffness values in orthogonal directions. Another explanation for these observed secondary drops in the values of DP is due to the presence of subharmonics when the rotor is operating at integral multiples of the natural frequency. These subharmonics have also been previously observed in the macro-bearing test device of Orr [9].

7.3.5 Model Predictions and Comparison to Experimental Data

The natural or critical frequencies deduced experimentally for a typical device are plotted on Figure 7-17 and compared to the modeling results of Liu [3]. The measurements using fiber optic data are plotted as full circles and the natural frequencies deduced from the pressure signals DP are plotted as squares and diamonds. The solid and dashed lines represent the natural frequencies in orthogonal directions obtained from the linear modeling approach. The favorable agreement between the experimental and modeling results attest to the accuracy of the models and the experimental techniques employed. This technique of tracking the abrupt drops in DP to deduce natural or critical frequencies has also been successfully implemented on the micro-turbocharger. Figure 7-17 also shows the prediction of the whirl instability limit together with measurements obtained in the microbearing test device. The experimental data points (pluses) correspond to crash points and suggest points of whirl instability.

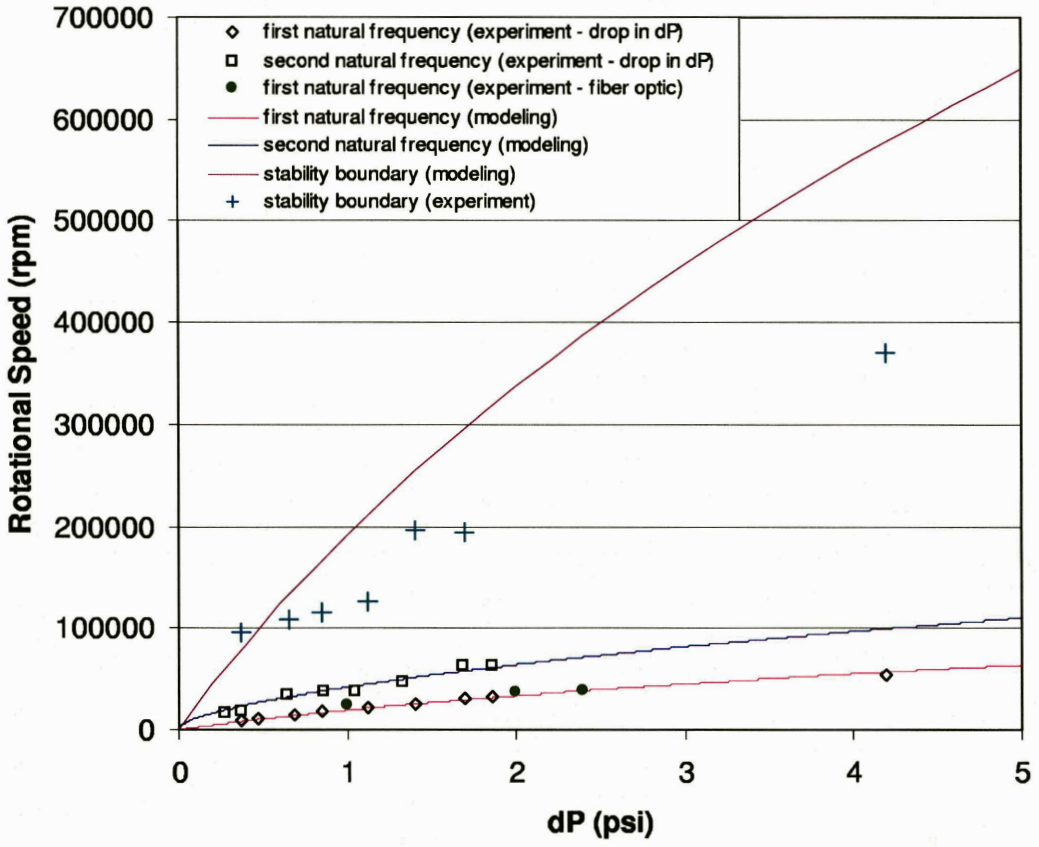

Figure 7-17: Comparison of experimentally measured natural frequencies and whirl instability limit with modeling results.

7.3.6 Strategies for Crossing Natural Frequencies

From the above discussion, it is clear that one of the challenges most often encountered is the ability to transit smoothly from a subcritical state of operation to a supercritical state. The peak whirling amplitude near the natural frequency increases with the level of rotor imbalance. Devices such as the micro-turbocharger with imbalance levels exceeding 5 μm may encounter difficulties crossing the natural frequency. Two different strategies to cross the natural frequency have been investigated. Figure 7-18 depicts the two strategies for acceleration from subcritical to supercritical speeds.

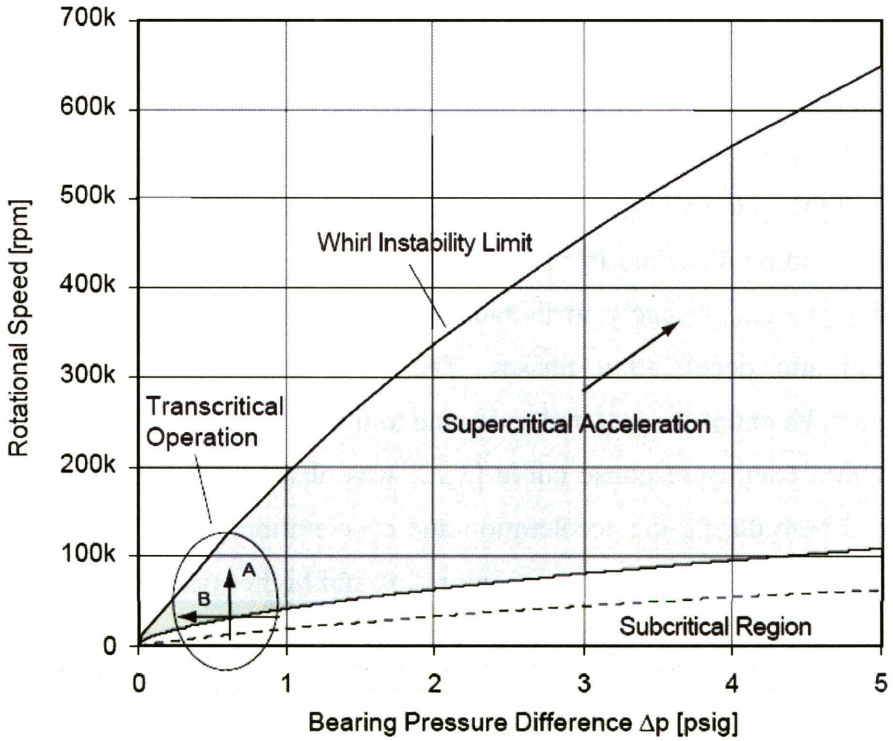

Figure 7-18: Two strategies for crossing the natural frequency: Acceleration by instantaneously increasing the air supply through the main turbine (A); Decreasing the pressure drop across the journal bearing (B).

The first strategy involves an instantaneous acceleration of the rotor past its natural frequency at constant bearing pressure difference DP (strategy A). This is carried out by a sudden increase in the main flow through the turbine and, as suggested by the model predictions and experimental data, the bearing pressure difference DP needs to be set to low values to yield a higher damping ratio (greater than 0.1) and an increased distance to contact (larger than 1 μm). The second strategy is to accelerate from subcritical to supercritical speed by decreasing the pressure difference across the journal DP at constant rotor speed as shown in Figure 7-18 by strategy B.

Both strategies have been successfully implemented and allowed the controlled operation of the microbearing test device from subcritical to supercritical speeds. Strategy A has been carried out on a microbearing test device which had difficulties going supercritical at a critical frequency of approximately 65 000 rpm for a DP of 2 psi. The spectral plots and the time history of the rotational speed deduced from the optical sensor are shown in Figure 7-19. Multiple crashes were seen to occur when the rotor attempted to cross the critical frequency due to the low values of damping ratio at a DP of 2 psi and

the high radial imbalance of the rotor. However, when the air supply to the main turbine was suddenly increased, the rotor was accelerated extremely rapidly to a supercritical state of operation and it operated stably thereafter. This shows the feasibility of a virtually instantaneous acceleration. It would further be of interest to observe the behavior of the rotor when it traverses from a supercritical to a subcritical state of operation. It can be observed from Figure 7-19 that no crashes were observed during the deceleration process, probably attributable to the existence of hysteresis effects during the acceleration and deceleration phases. The hysteresis effect is consistent with the modeling results and is conjectured to be due to the nonlinear stiffening effect that results in a rightward leaning response curve [3]. It was observed, however, that crashes were experienced both during the acceleration and deceleration phases when higher values of DP were used, due to the lower damping ratios and higher peak amplitudes encountered at higher values of DP. The observation that deceleration is "safer" than acceleration for low values of DP suggests an alternative means of crossing the critical frequency.

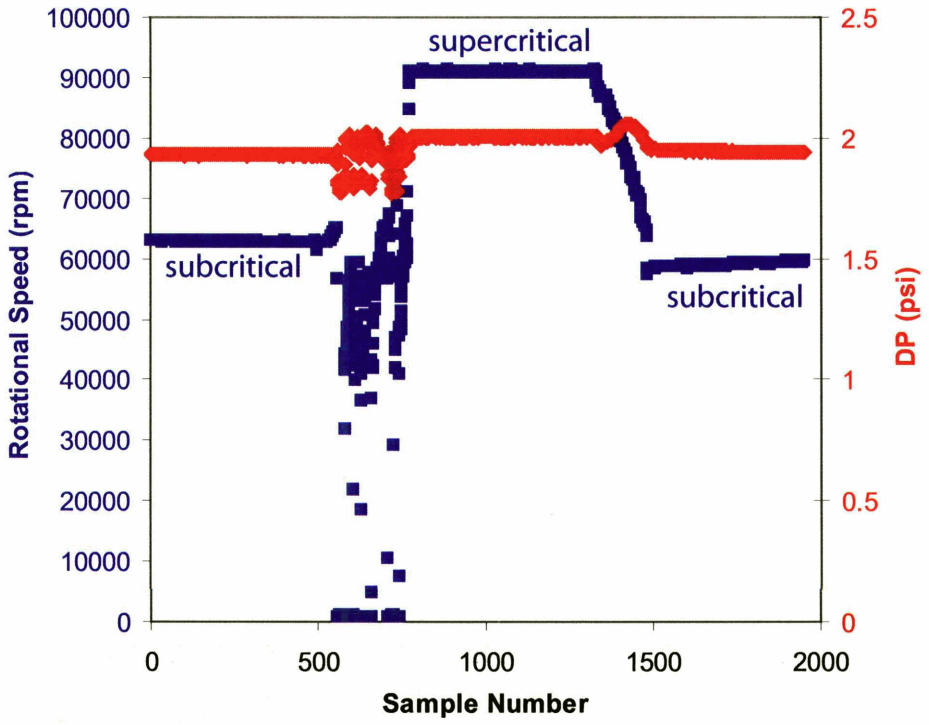

Figure 7-19: Time history showing the rotor crossing the natural frequency at a DP of approximately 2 psi.

Strategy B has been demonstrated on a rotor which was operating below the critical frequency at a DP of 2.9 psi. The corresponding time history of the rotational speed and the pressure difference across the journal are shown in Figure 7-20. When the hydrostatic pressure drop across the journal was decreased from 2.9 psi to 1.5 psi, the rotor went supercritical (since the rotational speed of the rotor was substantially higher than the critical frequency corresponding to a DP of 1.5 psi). The fact that the rotor had indeed gone supercritical could be further observed from the fact that it was capable of accelerating up to speeds in excess of 100,000 rpm, which was substantially higher than the natural frequency corresponding to a DP of 1.5 psi.

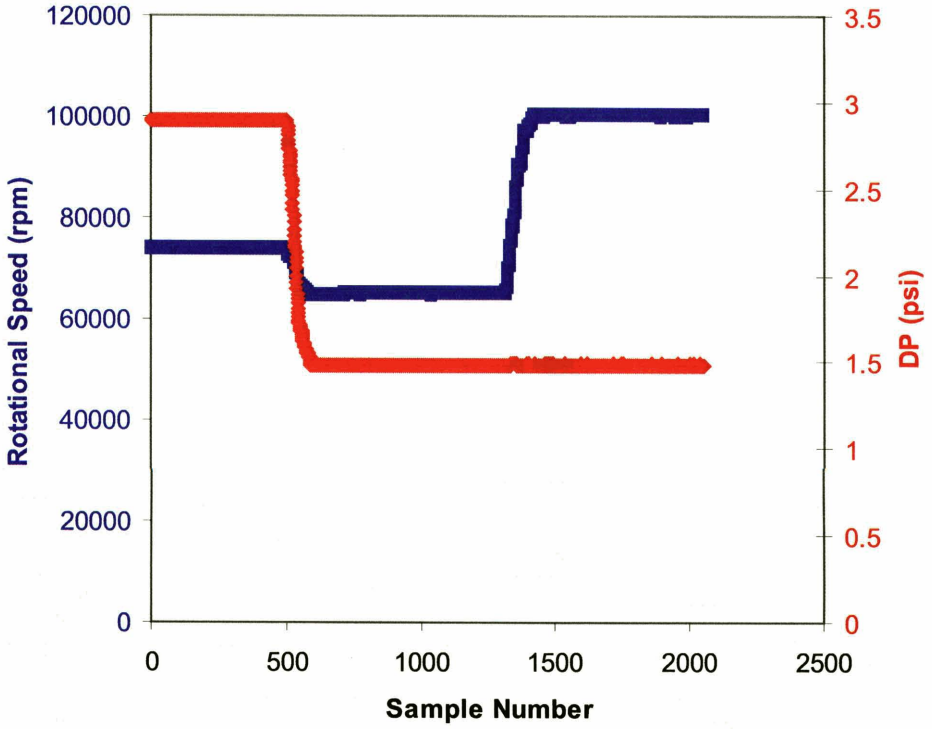

Figure 7-20: Crossing the natural frequency by decreasing the pressure difference across the journal bearing.

7.3.7 Accelerations to High Speed

From the above experimental data and the modeling results, an operating protocol can be established to guide the stable operation of the microbearing test device. The approach for controlled acceleration to high-speed is to cross the natural frequencies at low bearing pressure differences DP or low speeds and then to stay within the corridor bounded by the whirl instability limit and the highest natural frequency as illustrated in Figure 7-18 by the shaded area. This type of operating protocol has been successfully implemented in other MIT micro-devices [16].

One of the major complexities encountered in operating the microbearing test device arises from the use of separate pressure sources and control valves to supply the working gas independently to the main turbine and the hydrostatic journal. It would be useful to evaluate the feasibility of regulating the flow through the main turbine and the journal by means of one single control knob instead of two, and this has far-reaching consequences on the eventual automation of the other micro-devices.

Variations in the flow rates through the main turbine and the journal bearing were studied and it was observed that the pressure drop across the main turbine was significantly lower than the hydrostatic pressure drop across the journal. This was largely due to the fact that the main turbine of the microbearing test device was not designed to extract appreciable useful mechanical work from the fluid passing through. The main turbine was hence very lightly loaded and the pressure difference across the turbine blades was consequently small. It thus seems feasible to operate the main turbine and the hydrostatic journal bearing from the same pressure source, with a suitable flow restrictor connected between the hydrostatic source and the journal bearing for the purpose of tapping off a fraction of the hydrostatic supply air to run through the main turbine. Such a setup is shown schematically in Figure 7-21. Another advantage of employing the restrictor is that if a suitable valve setting is selected, it may be possible to achieve a fully supercritical acceleration schedule, thus avoiding the undesirable peak response during transcritical operation. A fully supercritical acceleration schedule is one that maintains supercritical operation starting from nearly zero rotor speeds, as shown schematically in Figure 7-22. A metering valve with suitable pressure-flow-rate characteristics was used as the restrictor and the setup was implemented on a microbearing test device.

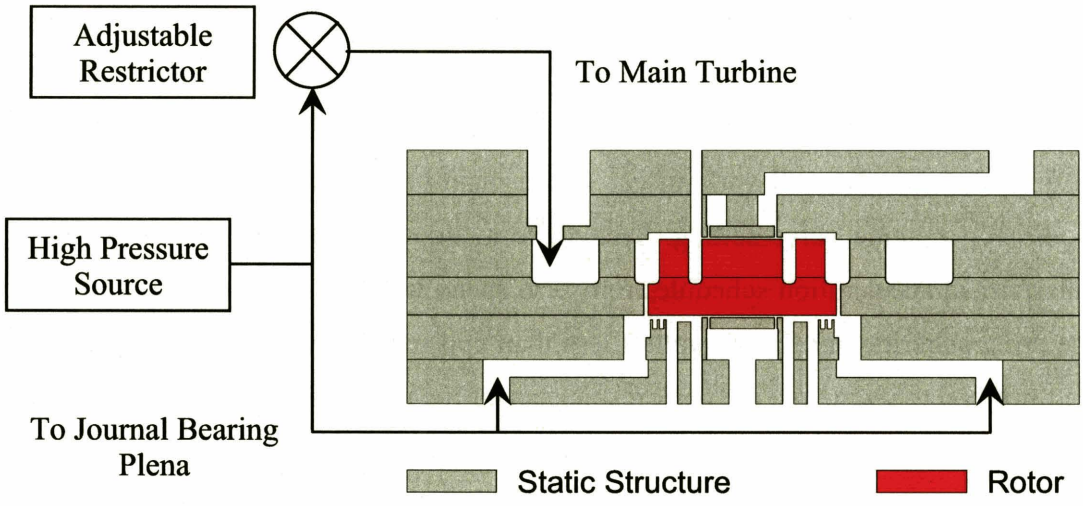

Figure 7-21: Use of restrictor or metering valve for transcritical operation.

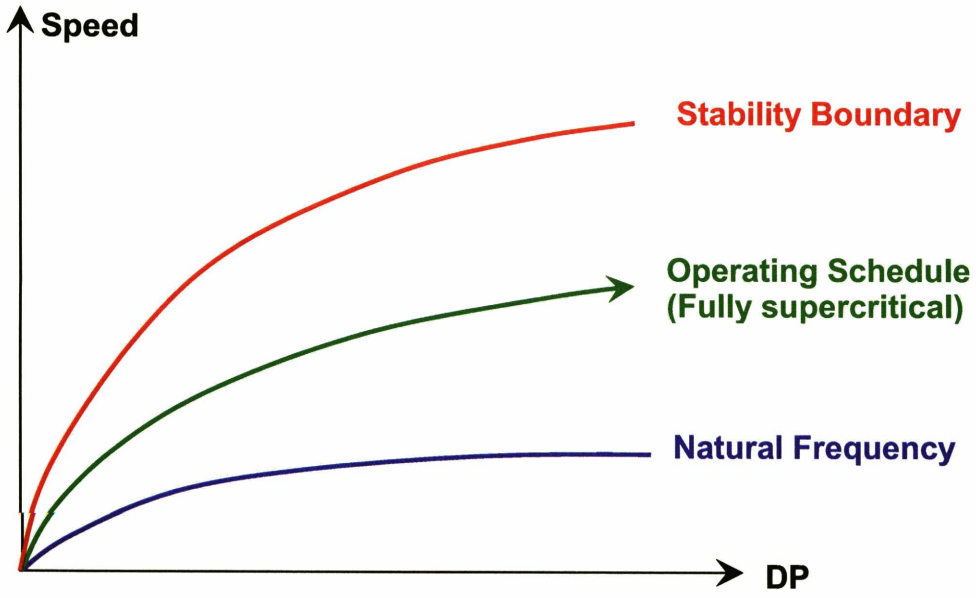

Figure 7-22: A fully supercritical acceleration schedule.

The results of the rotational speed for a range of hydrostatic pressure difference across the journal bearing obtained for a typical run are plotted in Figure 7-23. It was found that it was indeed possible to operate the device by regulating the pressure from a single source instead of two different sources, which greatly simplified the operating protocol and the hardware required. However, several shortcomings were also evident. First, due to the characteristics of the metering valve (restrictor) which maintained a fixed pressure-flow-rate relationship for a particular valve opening, it was difficult to supply a sufficiently high flow of working gas to the main turbine to achieve higher operational speeds for a single valve setting. Second, from Figure 7-23, it can be seen that a fully supercritical acceleration schedule from zero speed was not achieved since the rotor was operating subcritically for DP values less than approximately 0.6 psi, which implies that the rotor had to overcome the peak response near the natural frequency.

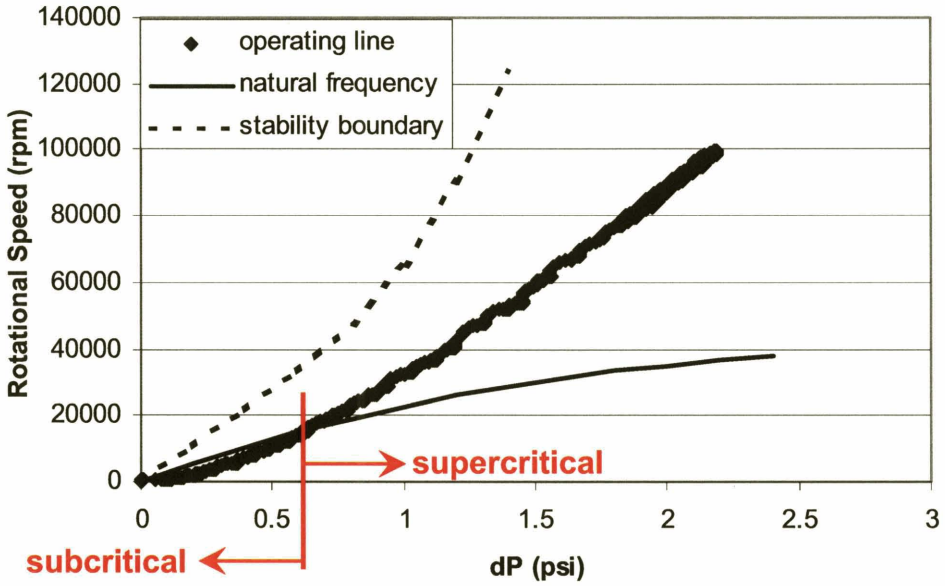

Figure 7-23: Plot of rotational speed against journal pressure difference DP for tests employing a metering valve.

7.4 Summary and Conclusions

Measurement and analytical techniques for statically quantifying the radial imbalance of rotors arising from DRIE non-uniformities were demonstrated. During the microfabrication process, these techniques are useful for ascertaining whether the rotor imbalance satisfies design specifications established using analytical models for transcritical and stable high-speed operation. Experiments were conducted in the MIT microbearing test device using a high-resolution fiber optic sensor for determining rotor speed. A data reduction scheme was implemented to infer the imbalance-driven whirl response curves of the rotor for different journal bearing operating conditions. The stiffness, the natural frequency and the damping ratio of the journal bearing and the imbalance of the rotor were deduced from the data. Additional experiments employed a flow control valve supplying the journal bearing with air. The natural frequency of the rotor bearing system was then deduced from bearing pressure measurements during rotor acceleration transients. The experimental data were compared against the model predictions of Liu [3], showing favorable agreement. Strategies for traversing the journal bearing natural frequency were proposed and demonstrated.

CHAPTER 8

Experimental Testing of High Speed and High Whirl-Ratio Gas Bearings for MEMS Devices

This chapter presents the experimental testing results for the redesigned microbearing test device. Static flow tests are first performed to assess whether the critical geometric dimensions have been fabricated to meet the design specifications. Experiments are subsequently performed to elucidate the effect of journal bearing hydrostatic differential pressure on both isotropic and anisotropic journal bearing operation. Appropriate operating protocols for achieving repeatable high speed bearing operation are explored. The redesign efforts are assessed and the experimental results are compared to analytical model predictions. Controlled high speed first-of-a-kind operation up to 70% of the design speed has been successfully demonstrated. This corresponds to a rotor rotation rate of 1.7 million rpm and a rotor tip speed of 370 m/s (equivalent to a DN number of about 7 million mm-rpm). In addition, high whirl-ratios in excess of 20 are demonstrated for the first time.

8.1 Static Flow Tests

Static flow tests are imperative for several reasons. First, static flow tests are crucial for assessing whether the device has been fabricated according to the specifications laid down during the design phase. In addition, static flow tests also serve to reveal any problems, flaws or defects arising from the microfabrication process. For example, excessive flow leakages through the thrust bearings often indicate a bonding failure or severe undercutting around critical features in the proximity of the thrust bearings. Static flow tests are also useful for verifying and calibrating analytical models. Since these models invariably rely on, and are constrained by the validity of simplifying assumptions, there arises the necessity of assessing the applicability and validity of the models by comparing model predictions with experimental measurements, both in terms of trends and magnitudes. It is also important to validate the models, since they are often utilized to establish operational protocols for the actual operation of the micro-devices.

8.1.1 Journal Bearing

First, static flow tests were performed for determining the journal bearing clearance of the individual devices. A cross-sectional view of the microbearing test device is shown in Figure 8-1, which also includes details regarding the configuration of the flow connections to the device on the aft side to elucidate how the static flow tests were performed. It should be noted that unlike in the original microbearing test devices, where the rotors were localized by means of "break off tabs" subsequent to the microfabrication process, the rotors in the redesigned microbearing test device were already free, as discussed in Chapter 6. Since the hydraulic resistance across the journal bearing depends strongly on the rotor eccentricity, it was necessary to determine the rotor eccentricity for the purpose of journal bearing characterization. However, this was difficult to achieve when the rotor was stationary, in view of the absence of any instrumentation to determine the rotor eccentricity when the rotor was stationary. Hence, the flow tests had to be performed with the rotor spinning at low subcritical speeds, since such conditions ensure that the rotor is spinning about its geometric center.

A flow was supplied to each of the 4 journal bearing plena, maintaining them at the same static pressure. The same mass flow Q_{ATB} was applied to both the forward and aft thrust bearings to maintain the rotor in an axially centered location. The flow to the balance plenum Q_{BP} was blocked off and the aft exhaust was connected to a mass-flow meter. A portion of the mass flow supplied to the journal bearing plena would leak through the annular labyrinth seals instead of flowing through the journal bearing. The mass-flow meter connected to the aft exhaust ($Q_{exhaust}$) measures this leakage flow, in addition to the flow through the aft thrust bearing. The actual mass flow through the journal bearing can then be deduced by subtracting the mass flow through the aft exhaust from the sum of the mass flow supplied to the journal bearing plena Q_{JB} and the aft thrust bearing Q_{ATB}. The journal differential pressure can be obtained from the difference between the inter-blade row static pressure and the average journal plena static pressure. Although no mass flow is directly supplied to the turbine, the mass flow through the journal bearing is forced to flow through the rotor blades, thus exerting a torque on the rotor and causing it to spin.

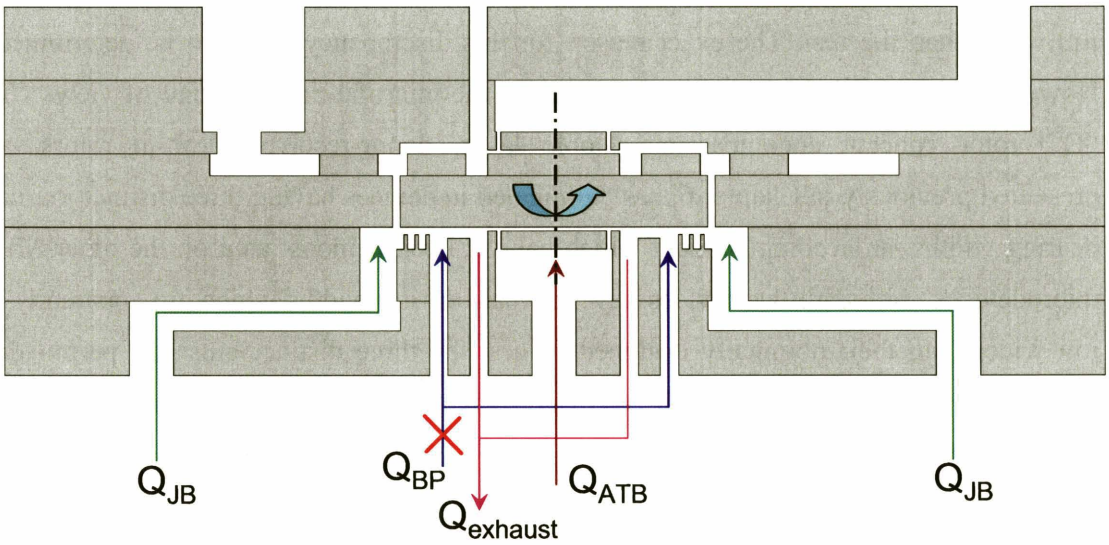

Figure 8-1: Cross-sectional view of redesigned microbearing test device showing the relevant flow paths for performing static flow tests on the journal bearing.

The mass flow through the journal bearing Q_{JB} is plotted against the journal differential pressure DP in Figures 8-2, 8-3 and 8-4 for devices with target journal bearing widths (that is, clearance) of nominally 14 μm, 16 μm and 18 μm, respectively. Results obtained from the analytical model are also plotted in the three figures for a comparison to the experimental results. The analytical model is essentially an incompressible fluid resistance model which accounts for the inlet losses arising from the Lomakin seal effect [10] and the Poiseuille losses for the fully developed viscous flow through the journal bearing. It is evident that the experimental results fall essentially into three different bins, manifesting that the devices yield three distinct journal bearing widths. However, the analytical models indicate that the journal bearing width corresponding to each bin of devices is approximately 2 μm above the nominal design value. With the exception of Devices 1-4 and 2-3 in Figure 8-2, Figures 8-2, 8-3 and 8-4 show that the variation in journal bearing width within each of the bins is less than 1 μm, consistent with the tolerance limitations imposed by the journal bearing DRIE. Since the precision control of journal bearing width and profile constitutes one of the most significant microfabrication challenges encountered in the history of the MIT microengine project, the variation in journal bearing width of less than 1 μm for devices belonging to the same bin symbolizes a great microfabrication success. Figure 8-2 which shows the experimental results for the nominally 14 μm wide journal bearing devices,

shows two outliers (Devices 1-4 and 2-3) with journal bearing widths approximately 2 μm wider than the rest. The exact reason for this discrepancy is yet to be determined. However, the above results are a triumph from the microfabrication point of view. The "D^3" rotor concept encompassing double layer, donor-receiver, drop-in rotors, as presented previously in Chapter 6, has culminated in devices having three distinct journal bearing widths, an accomplishment which has yet been demonstrated on the other MIT microdevices. Although the devices have journal bearing widths which are apparently 2 μm wider than their nominally designed values, the three distinct bins still permit the effect of journal bearing width on rotordynamic stability to be systematically investigated.

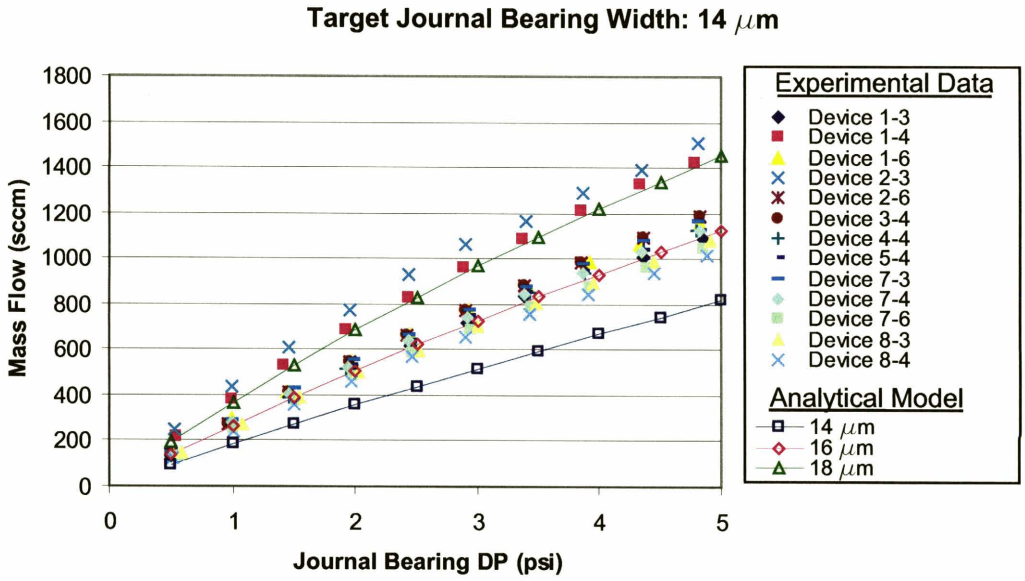

Figure 8-2: Journal bearing flow characteristics of devices with nominally 14 μm journal bearing clearance.

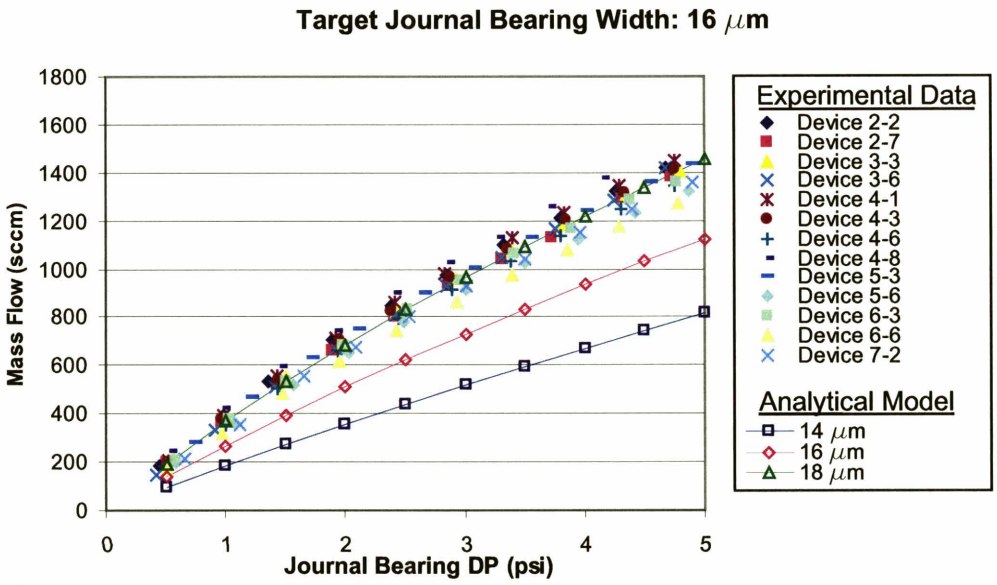

Figure 8-3: Journal bearing flow characteristics of devices with nominally 16 μm journal bearing clearance.

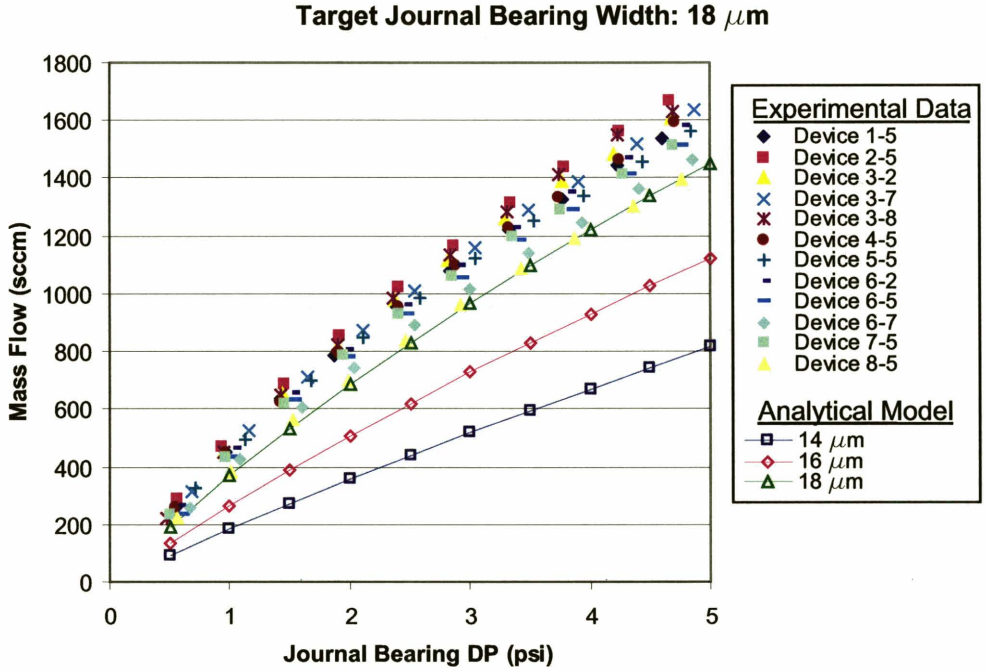

Figure 8-4: Journal bearing flow characteristics of devices with nominally 18 μm journal bearing clearance.

8.1.2 Outer Annular Seals

Static flow tests were also performed to determine the clearance of the outer annular labyrinth seal separating the journal bearing plena from the balance plenum (refer to Appendix A). Knowledge that the seal clearance has been fabricated according to the design specification is important for two main reasons: First, according to a 4 degree-of-freedom rotordynamic model [3], the seal clearance has a direct impact on the rotordynamic stability of the rotor-seal-journal bearing system. Second, the seal clearance has to accommodate for the axial tip deflection of the rotor disk at high speeds. Two different experimental schemes have been employed to characterize the outer seals, and the setup for each scheme is shown in Figures 8-5 and 8-6.

Figure 8-5 shows the setup for the first scheme, where a mass flow Q_{JB} is supplied to the 4 journal bearing plena, maintaining them at approximately the same static pressure. The mass flows through the aft thrust bearing Q_{ATB} and the aft exhaust $Q_{exhaust}$ are blocked off. A mass-flow meter measures the mass flow emerging from the balance plenum Q_{BP}, which equals the mass flow passing through the outer seal. The pressure difference across the outer seal is determined from the difference between the balance plenum static pressure and the mean static pressure of the 4 journal bearing plena.

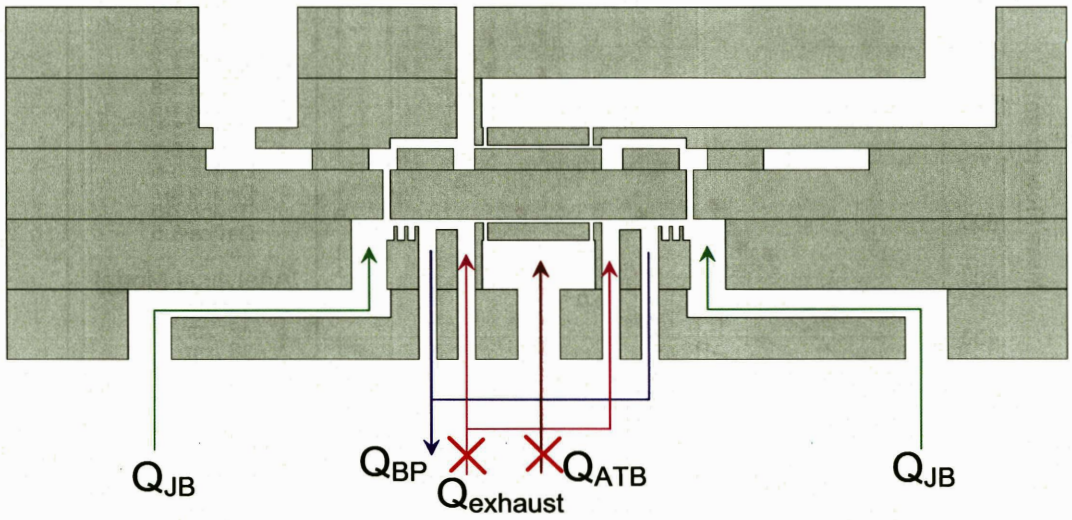

Figure 8-5: Cross-sectional view of redesigned microbearing test device showing the relevant flow paths for performing static flow tests on the outer annular seals (Method 1).

The second scheme, shown in Figure 8-6, is very similar to the first one, except that the mass flow through the balance plenum Q_{BP}, instead of the aft exhaust, is blocked off. A mass-flow meter measures the mass flow through the aft exhaust $Q_{exhaust}$, which again corresponds to the mass flow through the outer labyrinth seal. The pressure difference across the outer seal is again deduced from the difference between the balance plenum static pressure and the mean static pressure of the 4 journal bearing plena.

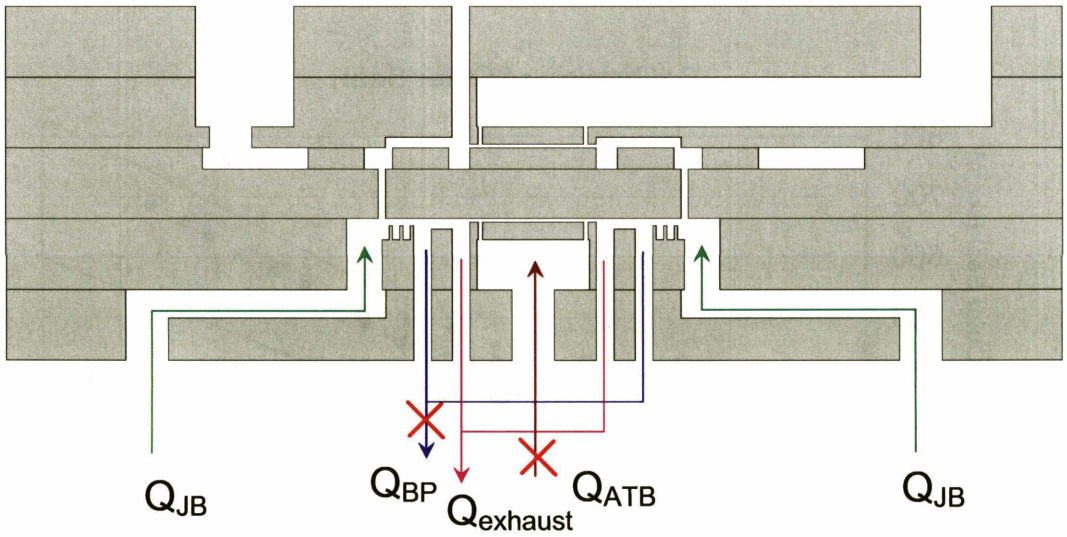

Figure 8-6: Cross-sectional view of redesigned microbearing test device showing the relevant flow paths for performing static flow tests on the outer annular seals (Method 2).

The second scheme is deemed to be more accurate than the first one. This is due to the presence of a mass flow Q_{BP} through the balance plenum in the first scheme, which results in turning losses as the flow occurs through the balance plenum. The pressure transducer downstream of the balance plenum may not accurately depict the static pressure along the innermost rim of the annular labyrinth seal, since the turning losses have not been accounted for. However, in the second scheme, the balance plenum pressure transducer should accurately measure the static pressure along the outlet of the annular outer seal, since there is no mass flow through the balance plenum and hence no turning losses are incurred.

The above schemes were implemented on a device with a nominal outer seal clearance of 12 μm. Figure 8-7 shows results for the mass flow rate through the outer seal plotted as a function of the pressure difference across the seal for both schemes. Also plotted on the same figure are the analytical results for outer seal clearances of 10 μm and

12 μm. The analytical results were obtained using an influence-coefficient based approach to model the viscous, compressible flow through annular seals, as elaborated in Section 3.7. Apparently, both experimental schemes yield consistent results, which indicate an outer seal clearance of approximately 11.5 μm. This discrepancy of 0.5 μm from the nominal value of 12 μm is within the ±0.5 μm tolerance arising from the shallow DRIE process. Once again, the microfabrication process has yielded encouraging results.

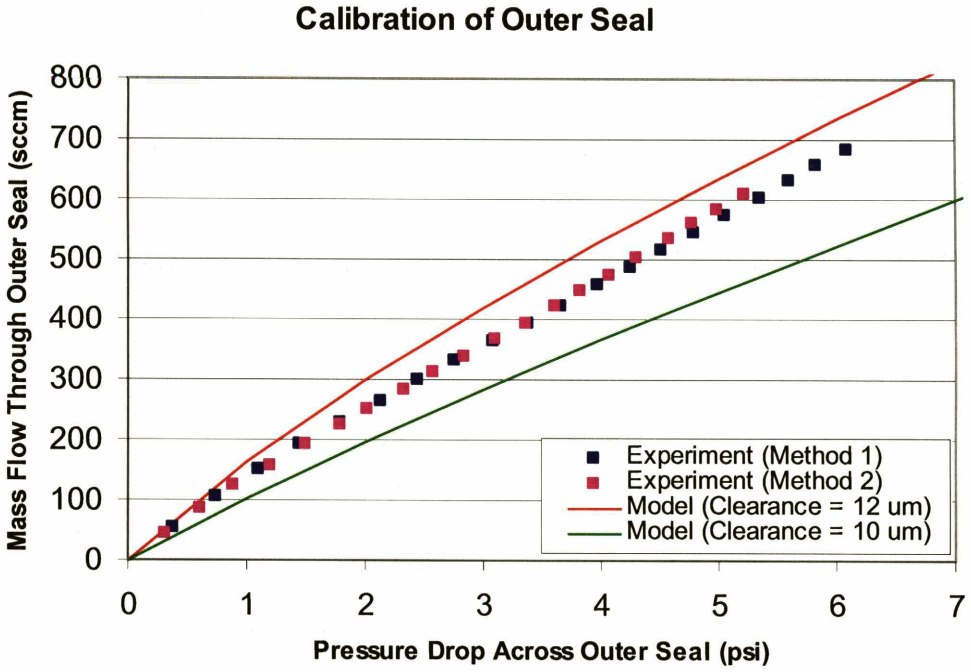

Figure 8-7: Flow characteristics across outer annular seals.

8.1.3 Thrust Bearings

Static flow tests were also performed to ensure that the thrust bearings were fabricated according to the design specifications. Apart from playing the essential role of providing for adequate axial stiffness, the thrust bearing mass flows also serve as a useful indicator for monitoring the axial location of the rotor. Figures 8-8 and 8-9 show experimental results obtained from static flow tests performed on the forward and aft thrust bearings, respectively, of a typical device. Three sets of experimental results, plotted in terms of the mass flow rate versus the thrust bearing supply pressure, are

shown in each figure. Referring to Figure 8-8, one set of results corresponds to the scenario where a flow is supplied solely to the forward thrust bearing and the rotor is resting against the aft thrust bearing. Another set of results corresponds to the scenario where the same pressures are supplied to the forward and aft thrust bearings. The last set of experimental results corresponds to the situation where both thrust bearings are operated with the same mass flow rates through them. Figure 8-9 is plotted in a similar manner to Figure 8-8, except that the results pertain to the aft thrust bearing instead. Comparing each set of experimental results in Figures 8-8 and 8-9, it is apparent that both thrust bearings have seemingly different characteristics, as manifested by the marginally different mass flows through both thrust bearings corresponding to the same supply pressure. However, this discrepancy can be easily attributed to the diameter of the thrust bearing orifices. Figure 8-10 shows analytical model predictions of the mass flow through the thrust bearing plotted as a function of the thrust bearing orifice diameter when a supply pressure of 60 psi is applied to one of the thrust bearings, with no flow applied to the other thrust bearing (i.e. the rotor is either fully upwards or downwards and is held against the other thrust bearing). Analytical models for predicting the performance of hydrostatic thrust bearings have previously been elaborated in Chapter 2. It can be seen from Figure 8-10 that the thrust bearing mass flow is a very strong function of the orifice diameter. In particular, increasing the orifice diameter from 9 μm to 11 μm increases the mass flow by 63% from 38 sccm to 62 sccm. Comparing the analytical results of Figure 8-10 with those of Figures 8-8 and 8-9, it can be deduced that the orifices of the forward thrust bearing have an average diameter of 9.4 μm, whereas those of the aft thrust bearing have a mean diameter of 10.4 μm. Since a design value of 10 μm has been prescribed for the thrust bearing orifice diameter, and a fabrication uncertainty of ±1 μm is anticipated to arise from the DRIE process, the values of the orifice diameter deduced from the analytical model for both thrust bearings are thus within the design specifications. Furthermore, there were no signs of excessive flow leakages which frequently gave rise to undesirable consequences in the previous microbearing test device builds. This indicates a reasonably good bond between the relevant layers housing the forward and aft thrust bearings, and the lack of any unwanted "short-circuiting" between flow passages of high and low pressures. This also alludes to the fact that the redesign efforts to improve the structural integrity and to increase the available bonding area

surrounding critical features of the thrust bearing have been generally successful.

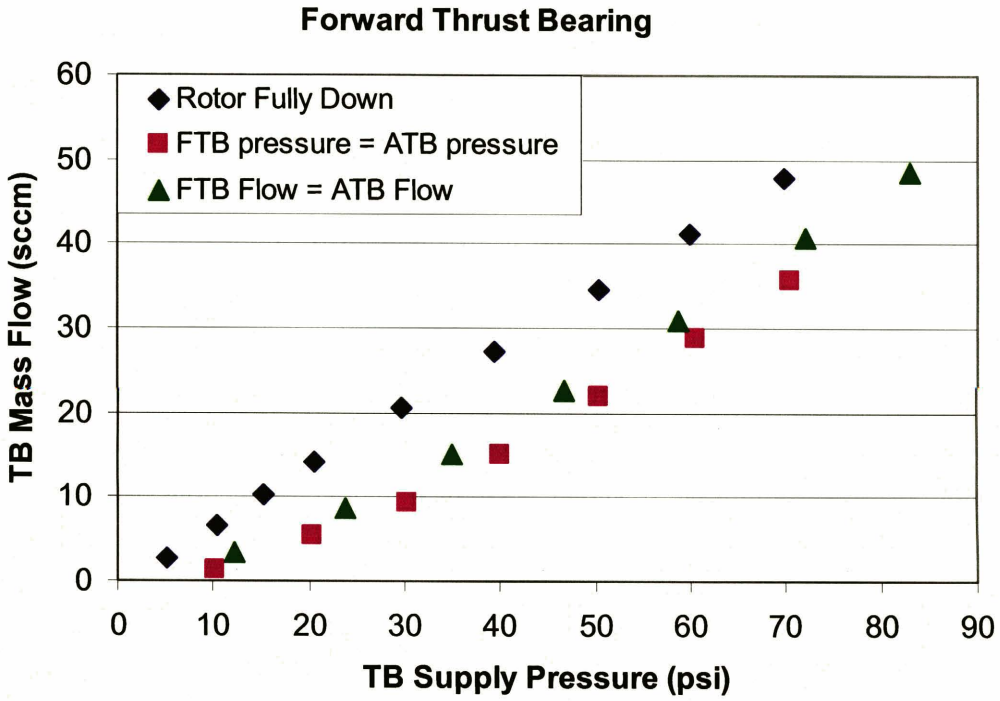

Figure 8-8: Flow characteristics of forward thrust bearing.

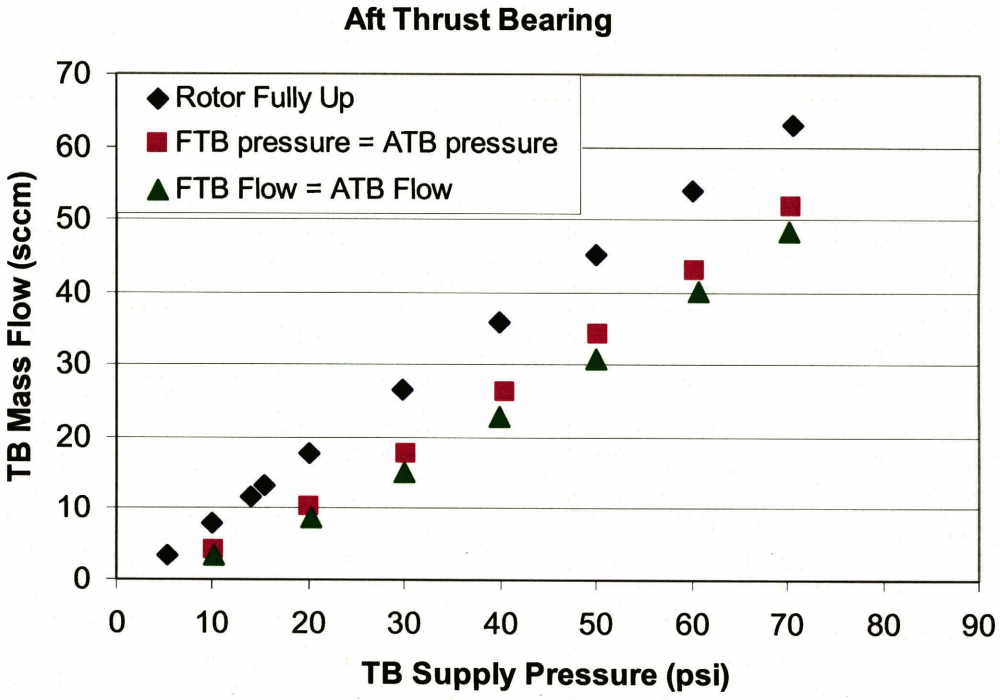

Figure 8-9: Flow characteristics of aft thrust bearing.

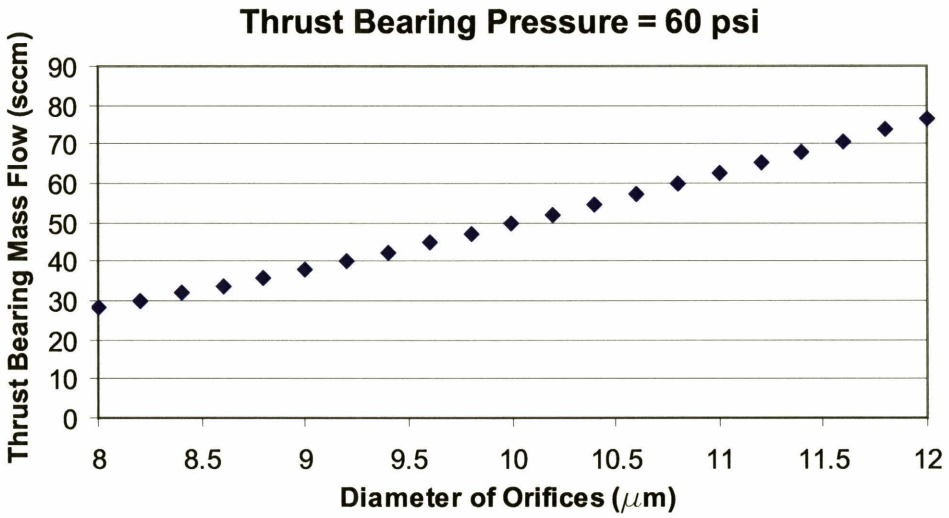

Figure 8-10: Variation of mass flow rate through either thrust bearing plotted as a function of orifice diameter.

To further illustrate that the thrust bearings were indeed functioning normally, experiments were performed to obtain the S-curves on both thrust bearings. As explained previously in Chapter 2, S-curves were obtained by keeping the supply pressure to one of the thrust bearings fixed, and monitoring the flow rate through that thrust bearing while altering the supply pressure to the other thrust bearing. S-curves serve as a useful and convenient test to qualitatively assess the ability of the thrust bearings to provide an axial stiffness. S-curves test results for the forward and aft thrust bearings are shown in Figures 8-11 and 8-12, respectively. Two sets of experimental results have been plotted in each figure, corresponding to supply pressures of 60 psi and 30 psi applied to the thrust bearing under investigation. Analytical predictions for the S-curves have also been included on both figures for the purpose of comparison. The reasonably close agreement between the model predictions and the experimental results offer further confidence that the thrust bearings are indeed behaving as designed and that the models are capable of capturing the salient behavior of the thrust bearings.

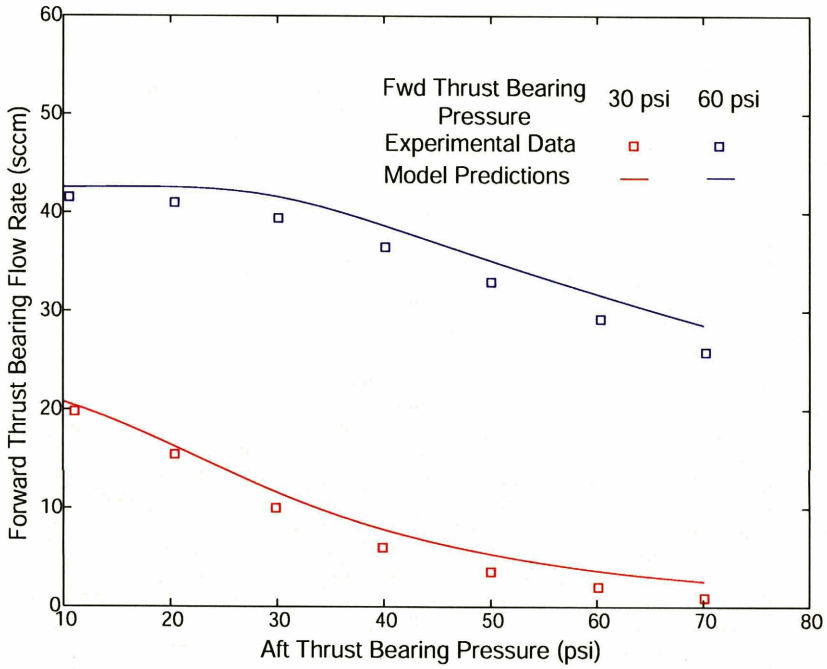

Figure 8-11: S-curves obtained by fixing the forward thrust bearing supply pressure at 60 psi and 30 psi.

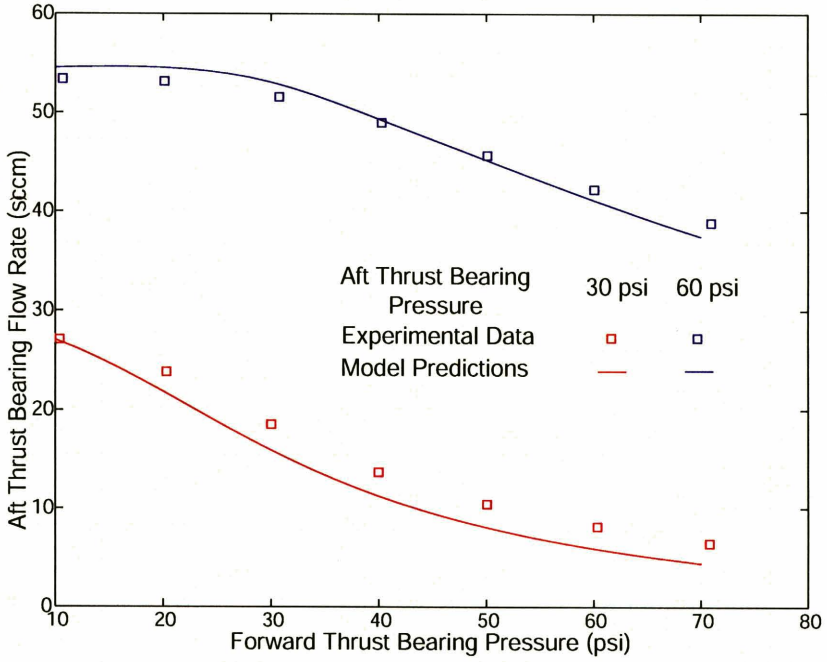

Figure 8-12: S-curves obtained by fixing the aft thrust bearing supply pressure at 60 psi and 30 psi.

8.2 Demonstration of Isotropic and Anisotropic Journal Bearing Operation

The redesigned microbearing test device provides an avenue for both isotropic and anisotropic journal bearing operation to be implemented on the same device. This is made possible by the introduction of four separate journal bearing plena, as discussed in Section 5.2.1.1. Maximum anisotropy can be achieved by supplying a flow to the two diametrically opposite plena of 110° circumferential extent, whilst simultaneously blocking off the flow to the other two plena. On the other hand, an almost isotropic operation can be achieved by supplying all four plena with the same supply pressure. One simple experiment to demonstrate the essential difference between isotropic and anisotropic journal bearing operation is to track the natural frequency as the rotor is accelerated under conditions of almost constant journal differential pressure DP. An isotropic journal bearing system has a single characteristic radial stiffness and hence one radial natural frequency, whereas an anisotropic system has two distinct orthogonal stiffness values, thus yielding two distinct radial natural frequencies. As previously presented in Section 6.2.5, one quick way to determine the journal bearing natural frequency is to utilize mass-flow controllers to feed the journal bearing with a constant mass flow and monitor the drops or excursions in DP as the rotor is accelerated. These drops in DP are a result of the reduced journal bearing hydraulic resistance arising from the rotor whirling at large eccentricities when it is traversing the journal bearing natural frequency.

Figures 8-13 and 8-14 present the variation of DP with rotational speed for a typical device with the journal bearing operating in anisotropic and isotropic modes, respectively. Both experiments were performed with a nominal or starting DP of approximately 0.86 psi. Figure 8-13 shows the presence of two distinct dips in DP as the rotor is accelerated. These two drops in DP signify the rotor traversing through two distinct natural frequencies, consistent with the anisotropy in journal bearing stiffness which is anticipated when only two of the four journal bearing plena are supplied with a mass flow. The first drop in DP occurs at a rotational speed which is approximately half that of the second dip, implying that the journal bearing stiffness is four times stiffer in the x-direction than in the orthogonal y-direction. The second dip in DP exhibits a larger drop in magnitude, which is again expected, due to the lower damping ratio associated

with the higher natural frequency.

On the other hand, the results corresponding to isotropic journal bearing operation shown in Figure 8-14 shows one major drop in DP, which signifies the rotor traversing only one natural frequency. This further implies equal magnitudes of journal bearing stiffness in both the x- and y-directions, which is characteristic of isotropic journal bearing operation. The comparatively larger drop in DP for isotropic journal bearing operation may possibly be attributed to the synchronous circular orbits of large amplitudes associated with the imbalance driven whirling motion of the rotor. In contrast, for anisotropic journal bearing operation, the whirling motion of the rotor takes on the form of an elliptical orbit when the rotor crosses the natural frequency. The average eccentricity associated with an elliptical orbit is anticipated to be smaller than that due to a purely circular orbit. A larger reduction in overall hydraulic resistance is thus expected to result from isotropic transcritical operation, which in turn gives rise to stronger dips in DP. Furthermore, for the same value of DP, the isotropic natural frequency is approximately equal in magnitude to the anisotropic natural frequency corresponding to the stiffness in the x-direction.

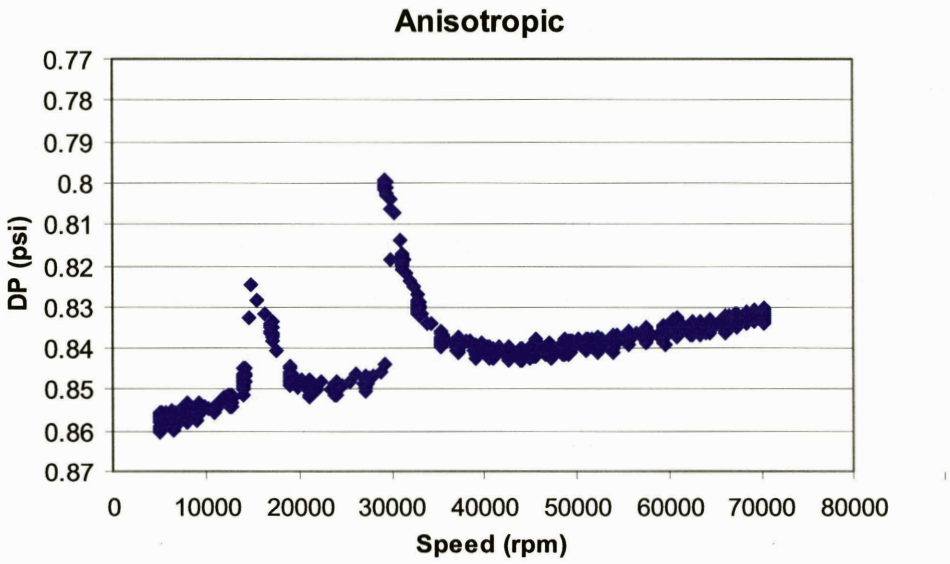

Figure 8-13: For anisotropic journal bearing operation, two distinct dips in DP are observed during rotor acceleration.

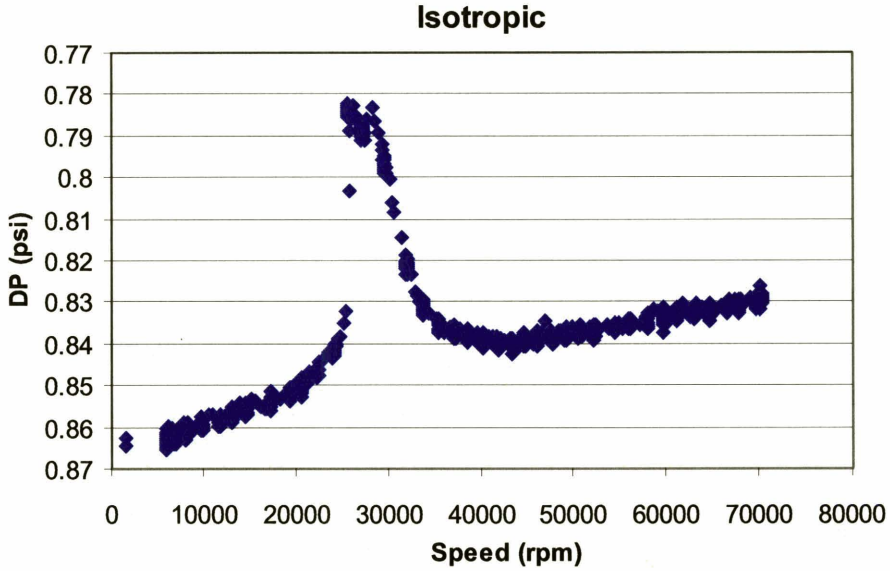

Figure 8-14: For isotropic journal bearing operation, only one distinct dip in DP is observed during transcritical operation.

The above experiments are indeed reassuring, and they explicitly elucidate the successful realization of one of the objectives of the four-plena journal bearing design. As demonstrated in the above experiments, the four plena design permits varying levels of anisotropy to be implemented on the same device. This paves the way for investigating journal bearing performance and stability for both isotropic and anisotropic journal bearing configurations.

8.3 Operation at Low Journal Bearing Differential Pressures

For low levels of journal bearing differential pressures DP up to 2 psi, experiments indicate similar level of performance achieved by both isotropic and anisotropic modes of journal bearing operation, as will be described in the following.

Experiments were performed to shed light on the difference in performance arising from isotropic and anisotropic journal bearing operation for low values of DP up to 2 psi. The experimental results are plotted in Figure 8-15. It is helpful to provide some explanation on the different symbols used in the figure. Symbols of different colors are employed to denote journal bearing clearances of different width. Journal bearing clearances of nominally 14 μm, 16 μm and 18 μm are represented using blue, green and

red symbols respectively. Additionally, solid symbols are used to represent crash points, whereas open symbols denote non-crash points, or the maximum speed attained when the rotor is operated in either the isotropic or anisotropic mode without encountering a rotor crash. Solid squares and solid diamonds denote crash points obtained under conditions of anisotropic and isotropic journal bearing operation, respectively. Open triangles represent non-crash points with upright and inverted triangles denoting journal bearing operating under isotropic and anisotropic modes, respectively. All the above symbols pertain to results obtained using Nitrogen. Experiments have also been performed using Helium, and solid circles, and rightward pointing triangles have been employed to denote anisotropic, crash points and isotropic, non-crash points, respectively.

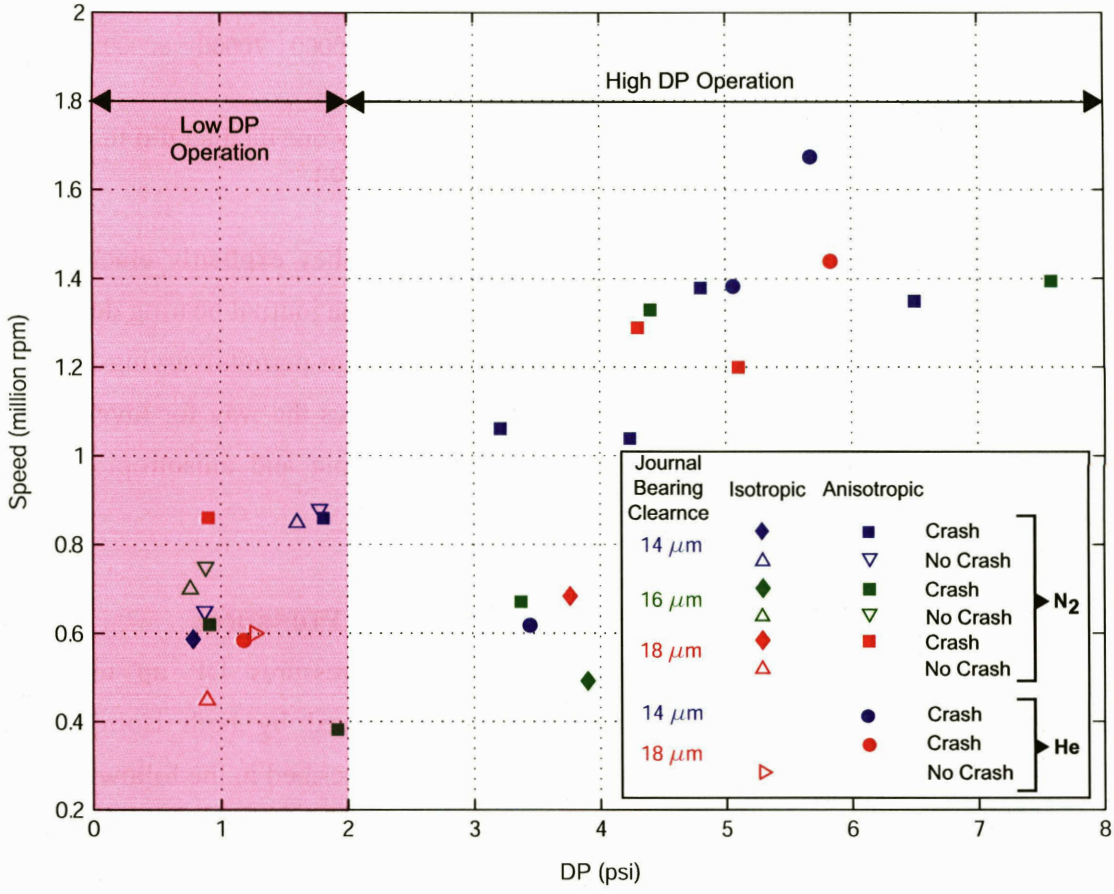

Figure 8-15: Summary plot of maximum speeds achieved for different devices plotted as a function of journal differential pressure DP.

One general conclusion that can be drawn from the test data is the similar level of performance achieved by both isotropic and anisotropic modes of journal bearing

operation at low levels of DP. In fact, it is also interesting to note that most of the devices which suffered from fatal crashes were operating in the anisotropic mode. There is hence no concrete evidence which indicates that for low values of journal bearing hydrostatic differential pressures DP, anisotropic journal bearings yield higher stability boundary boundaries than their isotropic counterparts.

At this point, it is imperative to compare the experimental observations with analytical model predictions to assess the ability of the models to predict the experimental trends and observations. Shown in Figure 8-16 are analytical-CFD predictions of the stability boundary for isotropic journal bearing operation corresponding to journal bearing widths of nominally 14 μm, 16 μm and 18 μm, respectively. Recall from Chapter 4 that these results have been obtained using an analytical rotordynamic model for the stability boundary. As for the rotordynamic coefficients, the hydrostatic direct-coupled stiffness and damping terms are obtained using analytical fluid dynamic models, whereas the cross-coupled hydrodynamic stiffness due to viscous pumping and viscous drag have been obtained using CFD. This approach is necessary to account for the presence of a non-fully-developed circumferential flow due to the excessively low L/D ratio of the journal bearing microfabricated using DRIE.

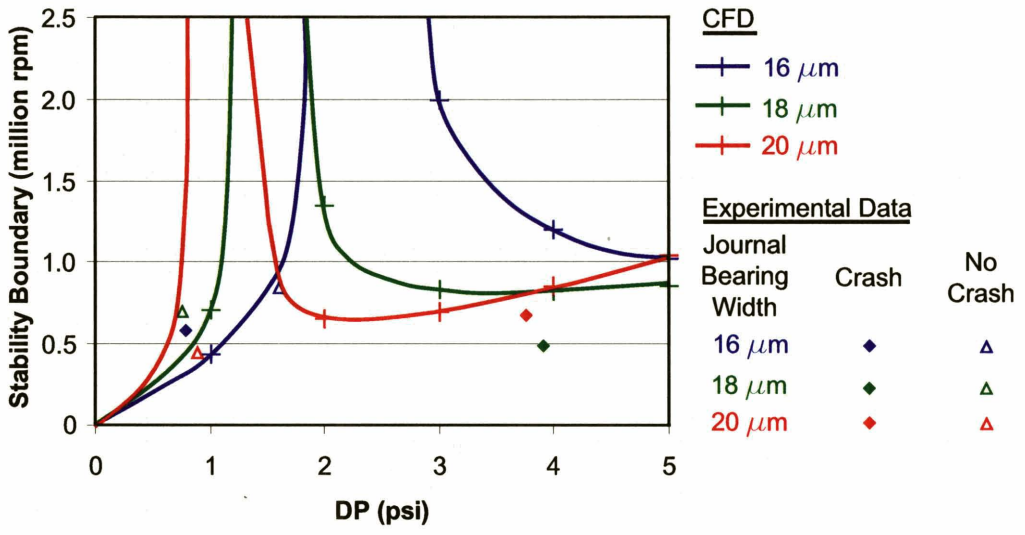

Figure 8-16: Comparison of experimental results and analytical predictions of isotropic journal bearing stability boundary for journal bearing widths of 16 μm, 18 μm and 20 μm.

Also plotted in Figure 8-16 are the available experimental data for purposes of

comparison to the analytical-CFD results. For the range of journal bearing widths under investigation, singular behavior in journal bearing whirl stability is predicted to occur at relatively low values of DP ranging between 1 and 2.5 psi. Hence, at low values of DP, it is likely that isotropic journal bearings exhibit similar or even superior levels of performance as compared to their anisotropic counterparts, in terms of the whirl instability limit. This is largely in agreement with the experimental results, and provides confidence for the validity of the analytical results. There is also relatively good agreement between the experimental and analytical results. Several other points should also be noted. First, majority of the experiments at low DP were performed by toggling between isotropic and anisotropic modes of journal bearing operation. The rotor was first accelerated up to 200,000 rpm in the anisotropic mode, decelerated to subcritical speeds, before it was accelerated to the same speed isotropically and decelerated again. It was subsequently accelerated anisotropically up to 250,000 rpm, decelerated and accelerated isotropically to the same speed and decelerated. This whole process was repeated in increasing steps of 50,000 rpm, toggling between isotropic and anisotropic modes of journal bearing operation until a fatal crash eventually occurred. Most of the experimental data points pertaining to isotropic journal bearing operation are maximum speeds achieved without a rotor crash. Hence, even higher speeds may be achievable if the rotor had not suffered from a fatal crash while operating anisotropically. Moreover, according to the analytical models, the stability boundary is very sensitive to both the journal bearing width and journal differential pressure DP. Some discrepancy between the experimental data and modeling predictions is anticipated, in view of the fact that the devices have been categorized into three distinct bins, whereas the DRIE process would inherently introduce uncertainties in the actual journal bearing widths which deviate from the bin values.

At this point, it is also invaluable to assess the performance of the devices operating under conditions of low DP. One common metric frequently employed for quantifying journal bearing stability is the whirl-ratio, which is defined as the speed at which instability arises over the journal bearing natural frequency. The whirl-ratio corresponding to the results shown in Figure 8-15 is plotted in Figure 8-17. One feature which is worthy of highlighting is the high magnitudes of whirl-ratio achieved. The maximum whirl-ratios achieved by the four devices operated using Nitrogen ranged

between 27.5 and 36.5. Such high magnitudes of whirl-ratio have never been previously demonstrated on previous builds of the microbearing test device, nor on any of the other MIT micro-devices. For the purpose of comparison, the highest whirl-ratio previously achieved on the original microbearing test device incorporating the original design was 14, which corresponded to a rotational speed of 1.4 Mrpm at a DP of 5 psi. In terms of absolute speeds at the same levels of DP, the devices from the present build are capable of running up to speeds which are typically several times higher than those ever achieved by devices from previous builds. Referring to Figure 7-17, for DP values ranging between 1 and 2 psi, the typical speeds achieved by devices from previous builds ranged between 100,000 and 200,000 rpm.

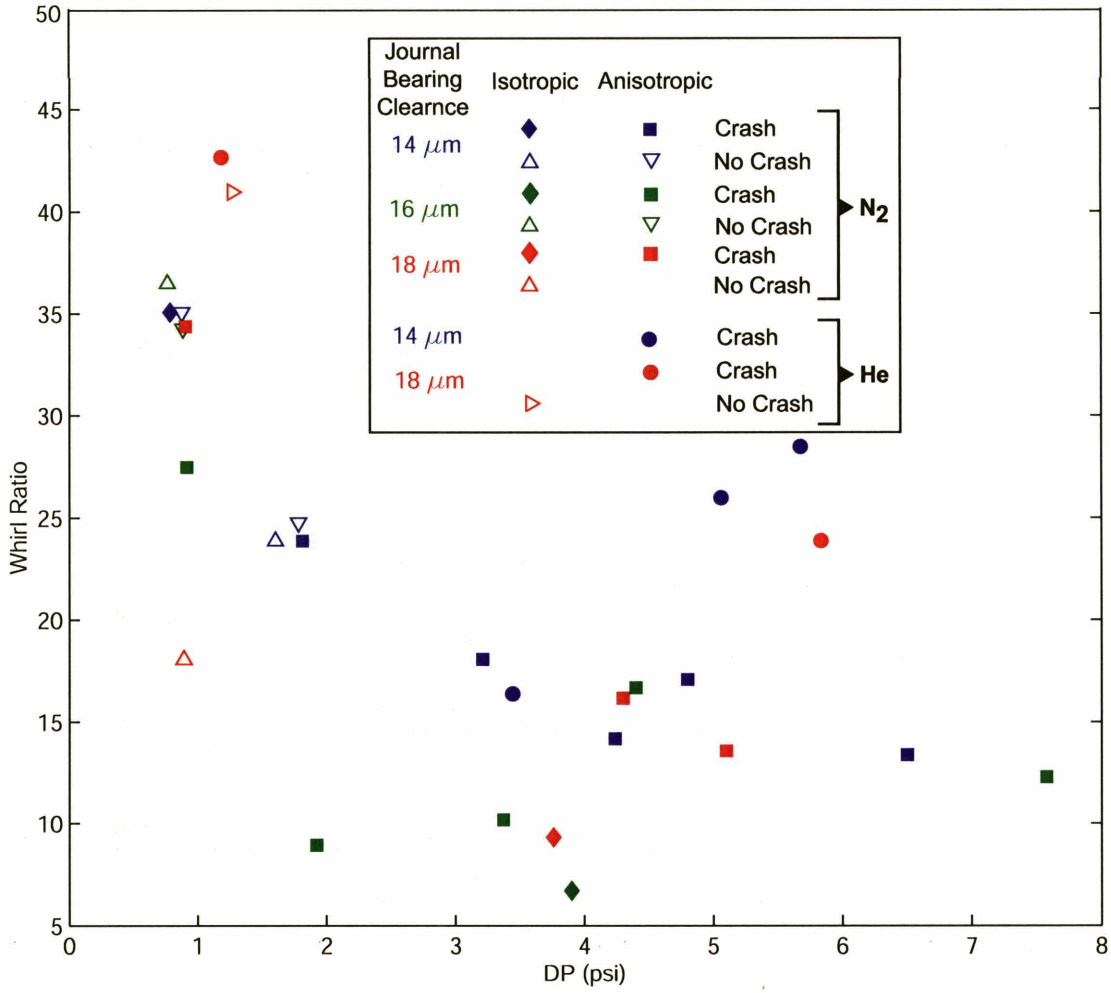

Figure 8-17: Summary plot of whirl-ratio for different devices plotted as a function of journal differential pressure DP.

It is further of interest to evaluate the redesign efforts on the aft side of the rotor.

It should be pointed out that the experiments at low values of DP were all performed by the mere turning of a single knob which regulates the flow through the turbine. Prior to each high speed run, the supply pressures to both thrust bearings were regulated to maintain approximately the same mass flow rates through both bearings. This ensures that the rotor was axially centered, as previously explained. The thrust bearing supply pressures were subsequently held constant throughout the entire course of the high speed runs. The mass flows to the journal bearing were held constant by means of mass-flow controllers. During the acceleration process, there were negligible variations in the thrust bearing mass flows, which can be attributed to one or both of the following reasons. First, the redesign of the annular seals on the aft side of the rotor has significantly enhanced their thrust balancing ability. The seals and plena on the aft side are capable of providing an upward force which counteracts the monotonically increasing downward force due to the turbine as the rotor speeds up. Second, the thrust bearings are sufficiently stiff to counteract the effects of axial force variations. Since there were negligible variations in the rotor axial position during the entire course of the acceleration, there was no need to supply a mass flow to the balance plenum to axially center the rotor. This implies that only the mass flow to the turbine had to be regulated to accelerate the rotor, and it was possible for the entire operation to be performed by adjustments made to a single knob. Such a single knob operation is undoubtedly vital for the ultimate automation of the operating protocols being employed for accelerating the rotor to design speeds.

8.4 Operation at High Journal Differential Pressures

8.4.1 Experimental Testing Using Nitrogen

Unlike at low values of DP, isotropic and anisotropic modes of journal bearing operation showed distinctly different behaviors at high values of DP. In general, anisotropic journal bearing operation exhibits superior performance over its isotropic counterpart for values of DP exceeding 3 psi. Referring to Figure 8-18, for values of DP greater than 3 psi, even though only two devices have been subjected to isotropic testing marked using diamond shaped symbols, the crash speeds of these two devices are generally much lower than their anisotropic counterparts.

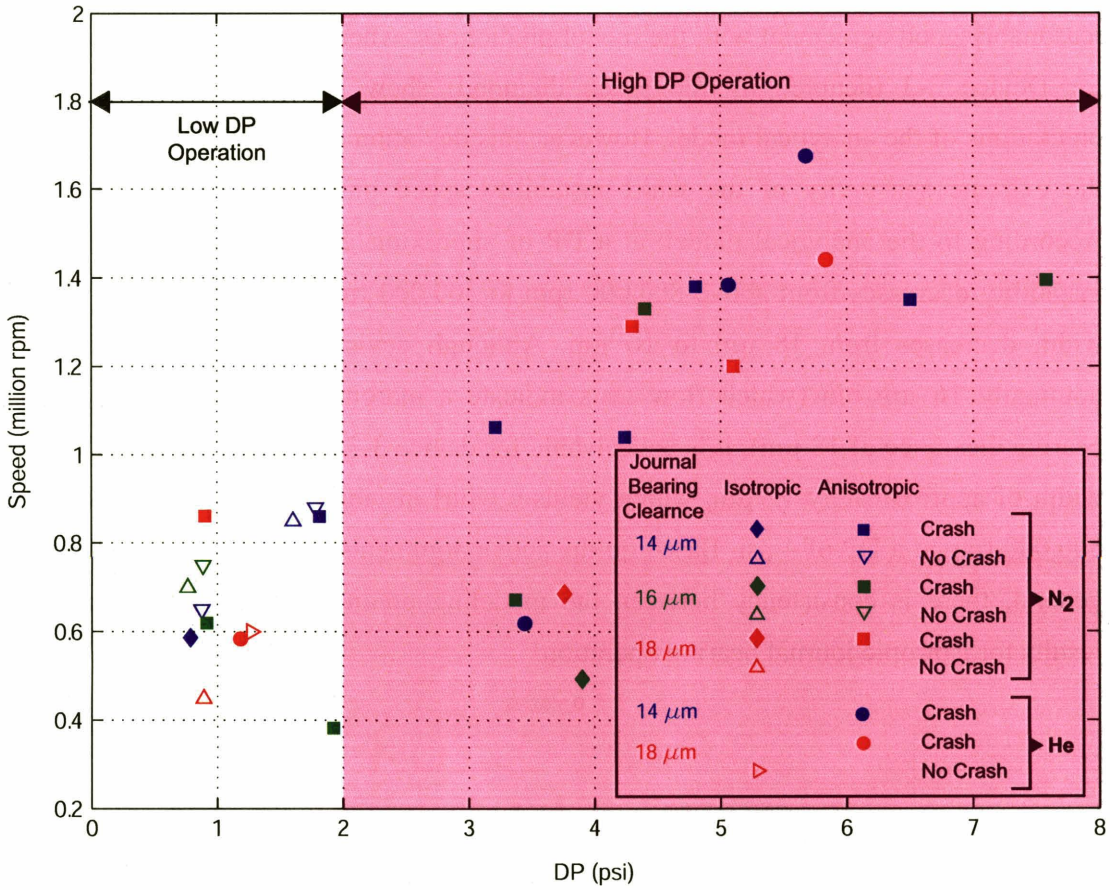

Figure 8-18: Summary plot of maximum speeds achieved for different devices plotted as a function of journal differential pressure DP.

The operating schedules of these two devices (Device 3-3 and Device 3-2) are shown in Figures 8-19 and 8-20. Both devices showed anomalous behaviors prior to crashing fatally. Device 3-3 exhibited a distinct dip in rotational speed as the value of DP was increased. This could signify a deceleration of the rotor arising from the larger viscous drag due to the rotor whirling at large radial eccentricities in the presence of a whirl instability. Device 3-2 showed significantly more drastic unstable, erratic behavior prior to its fatal crash, with the values of DP and the rotational speed displaying huge uncontrollable fluctuations.

The experimental results are plotted alongside the analytical model predictions for isotropic journal bearing operation in Figure 8-16. Recall from Chapter 4 that the analytical model uses CFD to evaluate the magnitudes of the hydrodynamic stiffness coefficients due to the presence of a non fully-developed journal bearing circumferential

flow. As can be seen from Figure 8-16, Device 3-2 (denoted by the red diamond) shows reasonably good agreement with the model predictions, whereas the experimental results for Device 3-3 (denoted by the green diamond) show greater deviation from the predictions of the analytical model. However, this deviation can possibly be attributed to the extreme sensitivity of the whirl instability speed on journal bearing clearance. According to the analytical model, at a DP of approximately 4 psi, the onset of whirl instability decreases from above 800,000 rpm to 300,000 rpm when the journal bearing width decreases from 18 μm to 16 μm. Although device 3-3 was placed into the nominally 16 μm bin (which flow tests indicate a marginally larger average journal bearing clearance of 18 μm), it is conceivable for device 3-3 to possess a journal bearing width of approximately 17 μm, which yields a whirl instability speed of approximately 500,000 rpm at a DP of 4 psi. Based on the above arguments, it can be concluded that in general, there is consistency between the modeling predictions and the experimental results for isotropic journal bearing operation.

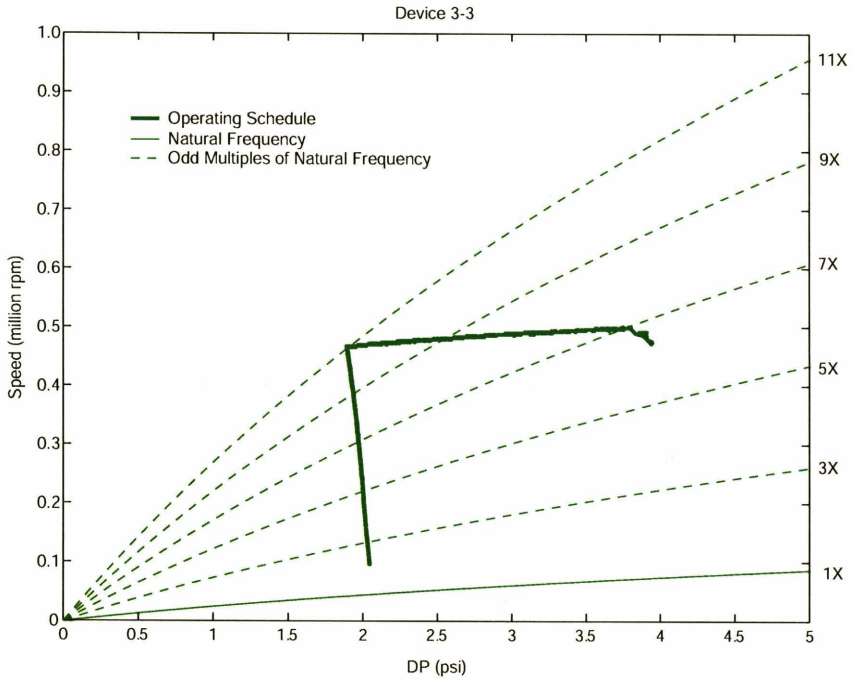

Figure 8-19: Operating schedule for Device 3-3 isotropic operation.

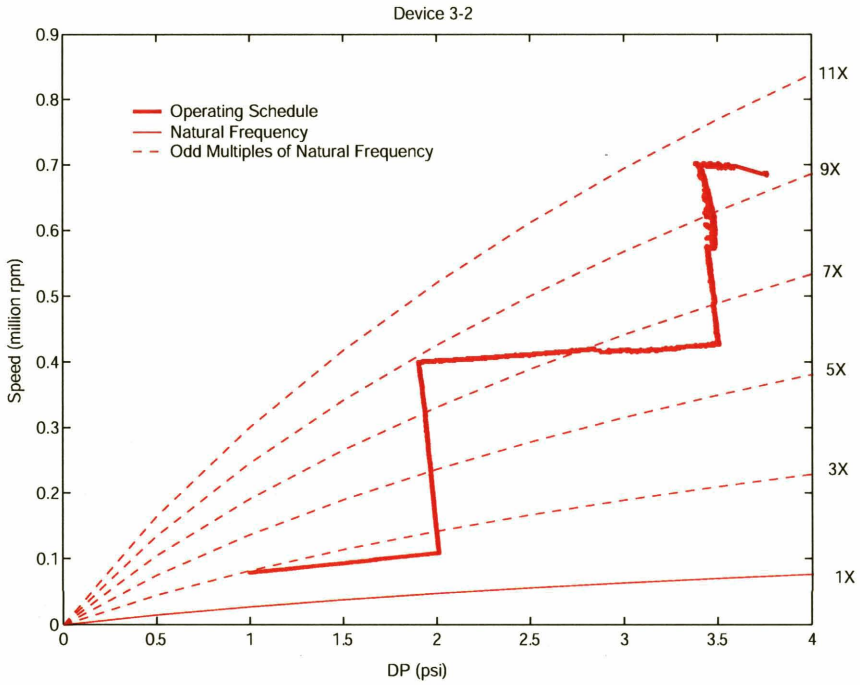

Figure 8-20: Operating schedule for Device 3-2, isotropic operation.

The crash speeds for devices operated anisotropically at DP values exceeding 3 psi are shown in Figure 8-18. It is evident that almost all but one of the devices are capable of achieving speeds in excess of 1 million rpm, thus attesting to the improvements in bearing design, the high reliability of the novel fabrication processes, and the repeatability and successful implementation of the testing procedures and operating protocols.

The operating schedule or protocol adopted for a typical device is presented in Figure 8-21. Once again, for majority of the tested devices, the rotor axial position varied very slightly throughout the entire course of rotor acceleration. There was hence no necessity to supply a mass flow to the balance plenum for the purpose of thrust balancing. Since thrust balancing was almost automatically achieved, this alleviates the operator from the arduous task of having to continuously monitor and regulate the rotor axial position. It was thus possible to devote more attention to the careful regulation of the journal bearing and turbine mass flows. One other sign of improved bearing performance is reflected by the very low levels of sideloading encountered for most of the tests, even at speeds in excess of 1 Mrpm. During anisotropic journal bearing operation, hydrostatic flow is independently supplied to the two diametrically opposite journal bearing plena

subtending a circumferential extent of 110° each. When the supply pressures to both plena were matched or identical, the difference in mass flow to both plena was at most 1% of the total mass flow to the journal bearing. During the testing of microbearing test devices incorporating the original design, inadvertent sideloading was often encountered during the rotor acceleration process, where the mass flows to the two diametrically opposite journal bearing plena frequently diverged even though equal supply pressures were applied to both of them. It was not unusual for the mass flow supplied to both plena to differ by 15% of the total mass flow supplied to the journal bearing.

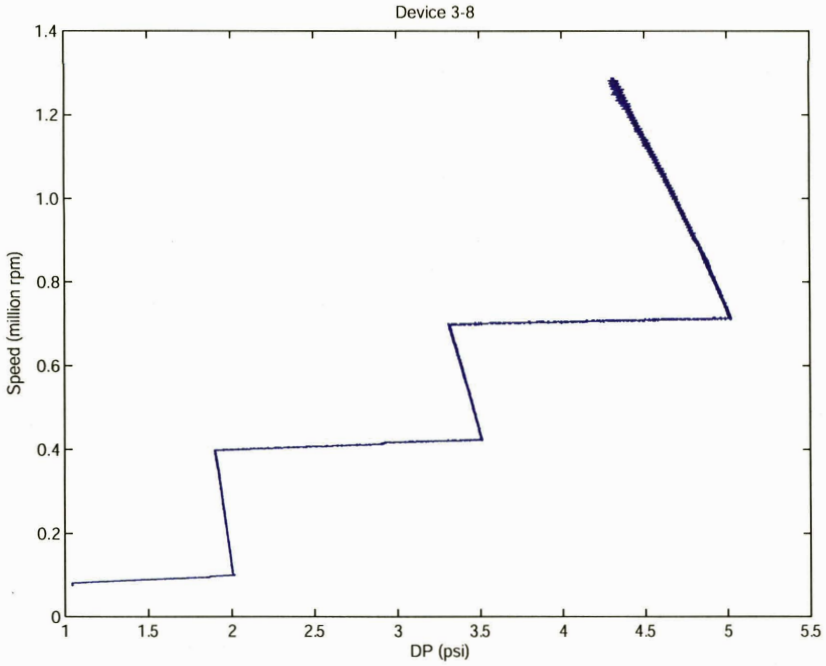

Figure 8-21: Operating schedule for Device 3-8, a typical device which was capable of achieving speeds in excess of 1 million rpm when operated anisotropically at high values of DP.

Referring to Figure 8-18, it appears that the crash speed shows a weakly increasing trend with increasing values of DP ranging between 3 psi and 5 psi. However, for values of DP larger than 5 psi, the crash speed is apparently relatively independent of the magnitude of DP. Plausible explanations for this trend are given in Section 8.5. Furthermore, for approximately the same values of DP, there does not seem to be a strong nor systematic dependence of the crash speed on the journal bearing clearance.

Referring once again to the operating protocol for a typical device shown in Figure 8-21, a disconcerting observation can be made at speeds in excess of

approximately 1 Mrpm up till the eventual fatal crash speed. The broadening of the line depicting the operating schedule at high speeds signifies the existence of increasing magnitudes of fluctuations in DP. This is also accompanied by the broadening of the synchronous frequency tracking the rotational speed on the spectrum analyzer, which indicates increasing levels of fluctuation in the rotor speed. The reason for this anomalous behavior is explained later in Section 8.4.3.

8.4.2 Effects of Different Gases

The following conjecture was proposed to explain the inability of the devices to achieve operating speeds in excess of 1.4 Mrpm. The journal bearing supply plenum, in conjunction with the journal bearing clearance constitute a Helmholtz resonator, with a resonance frequency of

$$\omega_H = a\sqrt{\frac{A}{VL}}, \tag{8.1}$$

where L and A are the length and cross sectional area of the duct, respectively, V is the volume of the plenum and a is the speed of sound (see [39], for example). The total volume V of the journal bearing supply plena is 2.67 mm^3, the length of the journal bearing L is 330 μm, and the cross sectional area A of the journal bearing clearance is 0.21 mm^2. Assuming the speed of sound in Nitrogen to be 330 m/s, the Helmholtz resonance frequency works out to be 25.7 kHz, or 1.54 Mrpm. This frequency is of the same order of magnitude as the crash speeds obtained for high values of DP, and might hence hinder attempts to achieve higher operating speeds. From Equation (8.1), one direct way to alter the Helmholtz frequency is to change the speed of sound. In order to ensure that the resonance frequency is much higher than the rotational speed, a gas whose speed of sound is significantly higher than that of Nitrogen has to be used. One possible candidate is Helium, whose speed of sound is approximately 1008 m/s, which is approximately 3 times higher than that of Nitrogen. This immediately implies that the Helmholtz frequency increases by 3 times to 78.5 kHz, which is significantly higher that the design speed of 2.4 Mrpm.

One further advantage which arises from the use of Helium rather than Nitrogen is the increase in journal bearing damping ratio ζ for the same value of DP. The journal bearing physical damping c, which depends on the fluid dynamic viscosity μ and the

bearing geometry, is given by

$$c = \pi\mu R\left(\frac{L}{C}\right)^3, \tag{8.2}$$

where R, L and C are the rotor radius, the journal bearing length and clearance, respectively. Since Nitrogen and Helium have approximately the same dynamic viscosity μ, the physical damping is thus almost equivalent for both Nitrogen and Helium. However, Helium is approximately 7.3 times less dense than Nitrogen, and this directly influences the journal bearing inlet loss and hence the stiffness and natural frequency. Assuming the flow to be incompressible, the natural frequency Ω_N for a 14 μm wide and 330 μm long journal bearing is plotted as a function of the hydrostatic differential pressure DP for four different gases in Figure 8-22. The four gases under investigation are Nitrogen, Helium, Argon and Xenon, and their gas properties are plotted in Figure 8-23. It is evident that corresponding to the same value of DP, the use of Helium results in the lowest journal bearing natural frequency. Figure 8-24 shows the damping ratio $\zeta = c/(2m\Omega_N)$ plotted against DP for all four gases. It should be noted that Xenon has the highest dynamic viscosity μ among all four gases, and hence yields the largest physical damping c. However, Xenon has the highest density ρ among all four gases, and yields the highest natural frequency for the same value of DP. In terms of damping ratio, for the same value of DP, Helium shows the best performance among all four gases, owing to its significantly lower natural frequency. In summary, apart from increasing the Helmholtz frequency, the use of Helium instead of Nitrogen has the added advantage of increasing the damping ratio at a fixed DP.

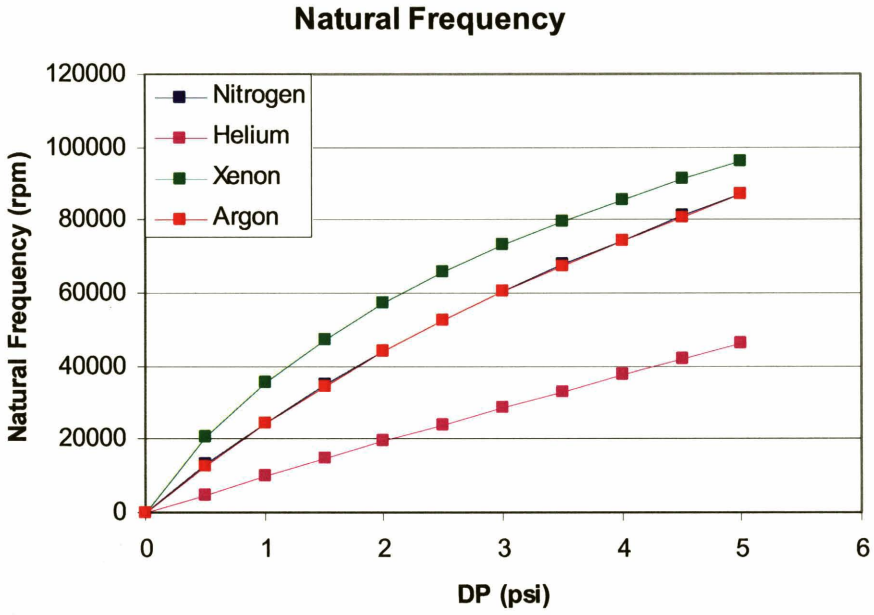

Figure 8-22: Variation of journal bearing natural frequency with hydrostatic differential pressure DP for four different inert gases.

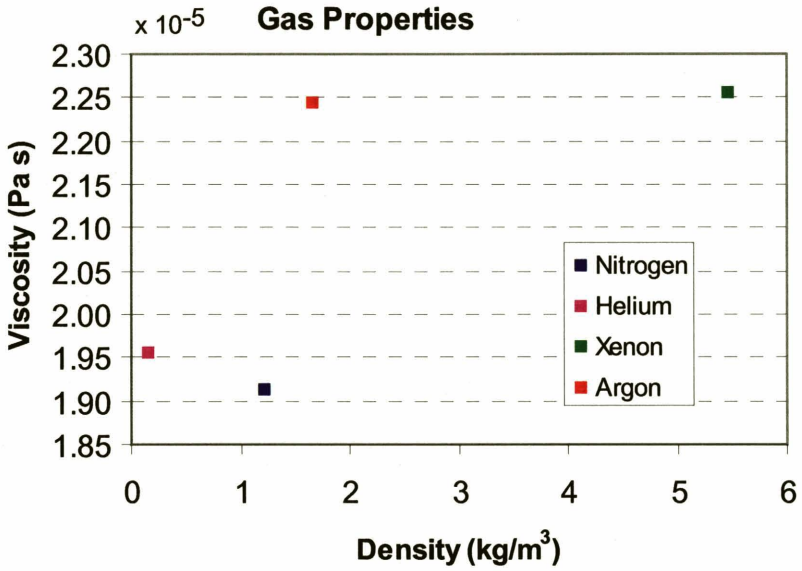

Figure 8-23: Physical properties of four different inert gases.

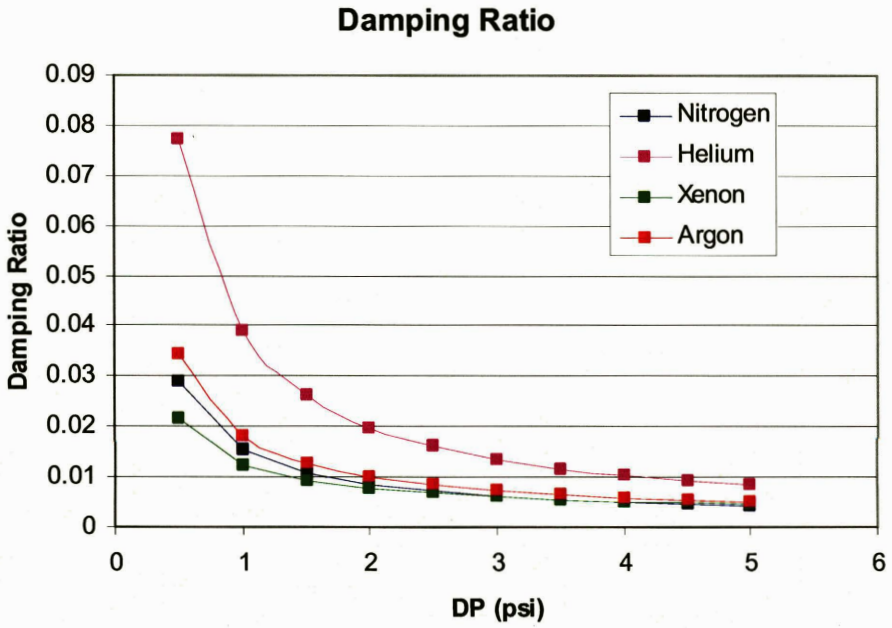

Figure 8-24: Variation of journal bearing damping ratio with hydrostatic differential pressure DP for four different inert gases.

8.4.3 Mass-flow controllers Versus Mass-flow meters

Attempts were subsequently made to operate a device using Helium. The rotor was accelerated using the schedule shown in Figure 8-25. This schedule was similar to the operating protocols which had been adopted for all the previous devices which were capable of achieving speeds in excess of 1 million rpm using Nitrogen.

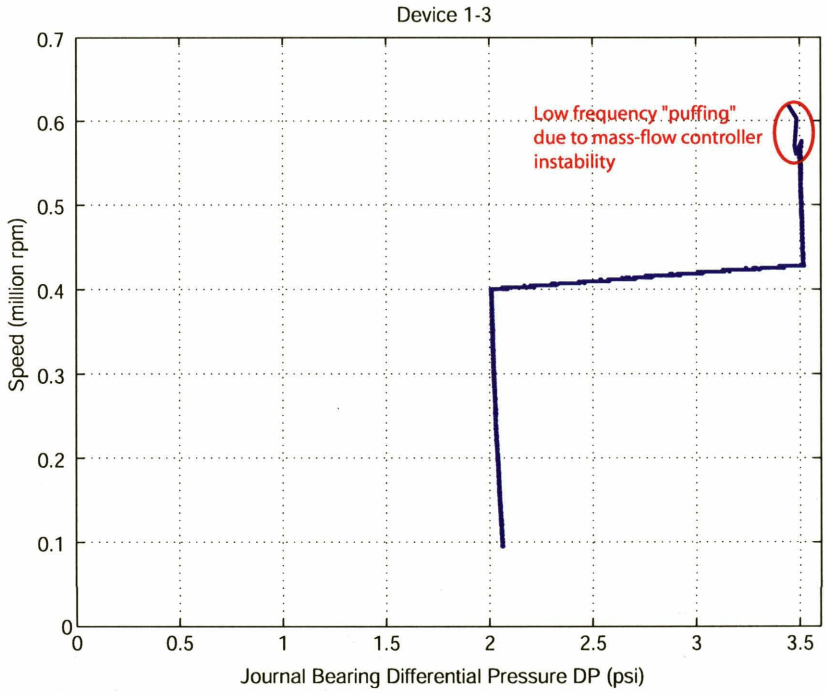

Figure 8-25: Operating schedule for Device 1-3 using Helium, where a low frequency "puffing" oscillation occurred due to mass-flow controller instability.

Several challenges were encountered during the initial runs. First, substantial difficulties were encountered in traversing the journal bearing natural frequency. At low values of DP below 1.5 psi, the rotor failed to spin smoothly, whether in the presence or absence of a turbine flow. As the journal bearing DP was increased beyond 1.5 psi, the rotor started to spin smoothly. However, at such high values of DP, there was substantial difficulty inverting the rotor (that is, traversing the transcritical regime). When the same device was operated using Nitrogen, it was capable of spinning smoothly even at very low values of journal bearing DP. The difference in behavior must therefore arise from the use of different gases, which advocates the hypothesis of a negative journal bearing stiffness at low values of DP with the use of Helium. It was possible to attribute the failure of the rotor to spin smoothly at low values of DP using Helium to the presence of a negative journal bearing stiffness. This arose due to the slight negative taper of the journal bearing profile, which was deemed to be useful for eliminating the presence of spikes along the sidewalls of the journal bearing, as previously mentioned in Section 5.1.1.2. Although the use of Helium results in higher values of damping ratio ζ for the same value of DP, the presence of a negatively tapered journal bearing profile results in a

negative radial stiffness at low values of DP less than 1.5 psi when Helium is used. At low values of DP, the detrimental effects of a negative stiffness arising from a negatively tapered journal bearing profile overwhelms the beneficial effects of a higher damping ratio when Helium is employed. Steps were subsequently taken to avoid crossing the natural frequency using Helium. This was achieved by inverting the rotor using Nitrogen at low values of DP. The magnitude of DP was subsequently increased, while maintaining the rotor in a supercritical state of operation. The gas supply to the device was then being switched from Nitrogen to Helium. Due to the long pipings and tubings connecting the gas supply to the device, a substantial amount of time elapsed before the supply lines to the device were completely filled with Helium. The mass flows to the turbine and the journal bearing plena were continuously regulated and monitored to maintain the rotor in a supercritical state of operation. In this manner, the rotor was alleviated from the burden of transcritical operation using Helium.

With the rotor spinning supercritically, it was subsequently accelerated using the schedule as depicted in Figure 8-25. However, a major peculiarity never previously observed cropped up when the rotor was spinning at 570,000 rpm. A low frequency "puffing" oscillation was audible, accompanied by large fluctuations in rotor speed. The rotor subsequently suffered from a fatal crash and the low frequency "puffing" oscillation persisted after the crash. After much troubleshooting and replumbing of the gas handling system, the cause of the low frequency "puffing" oscillation was identified. It was traced to an instability arising from the 20,000 sccm range MKS mass-flow controller utilized to regulate the mass flow to the turbine. The "puffing" oscillations were absent and inaudible at low mass flow rates, and appeared precipitously when the mass flow rate was increased beyond a certain limit. These "puffing" oscillations were accompanied by large fluctuations in mass flow rates, which could be read off the controller's display panel. This phenomenon was repeatable, whether or not the packaging housing the device was connected to the mass-flow controller. Furthermore, several other spare 20,000 sccm MKS mass-flow controllers showed similar behavior. However, when the mass-flow controller was reconfigured and used as a mass-flow meter, the anomalous behavior no longer surfaced. It was observed that the mass-flow meter was capable of accommodating sufficiently large magnitudes of mass flows (beyond that required by the turbine at the design speed) without exhibiting any low frequency "puffing" oscillations. The mass-

flow meter's display panel no longer gave indications of large fluctuations in mass flow. The low frequency oscillations were conjectured to be due to an instability arising from the built-in feedback control circuitry of the mass-flow controller. However, when the controller was used solely as a meter, the feedback control circuitry was bypassed (i.e. open loop control was employed) and the instability was suppressed. When the mass-flow controller was employed, a set point voltage signal proportional to the desired mass flow was applied to the controller from a potentiometer. On the other hand, the use of a mass-flow meter necessitated a Norgren pressure regulator for regulating the mass flow through the turbine.

8.4.4 High Speed Operation Using Helium

After ascertaining the absence of low frequency "puffing" oscillations over the entire range of mass flows of interest, high speed runs using Helium were performed on another operational device. Controlled high-speed operation was demonstrated up to 70% of design speed. This corresponds to a rotor rotation rate of 1.7 million rpm and a rotor tip speed of 370 m/s (equivalent to a DN number of about 7 million mm-rpm). The operating protocol employed on this device has been plotted in Figure 8-26.

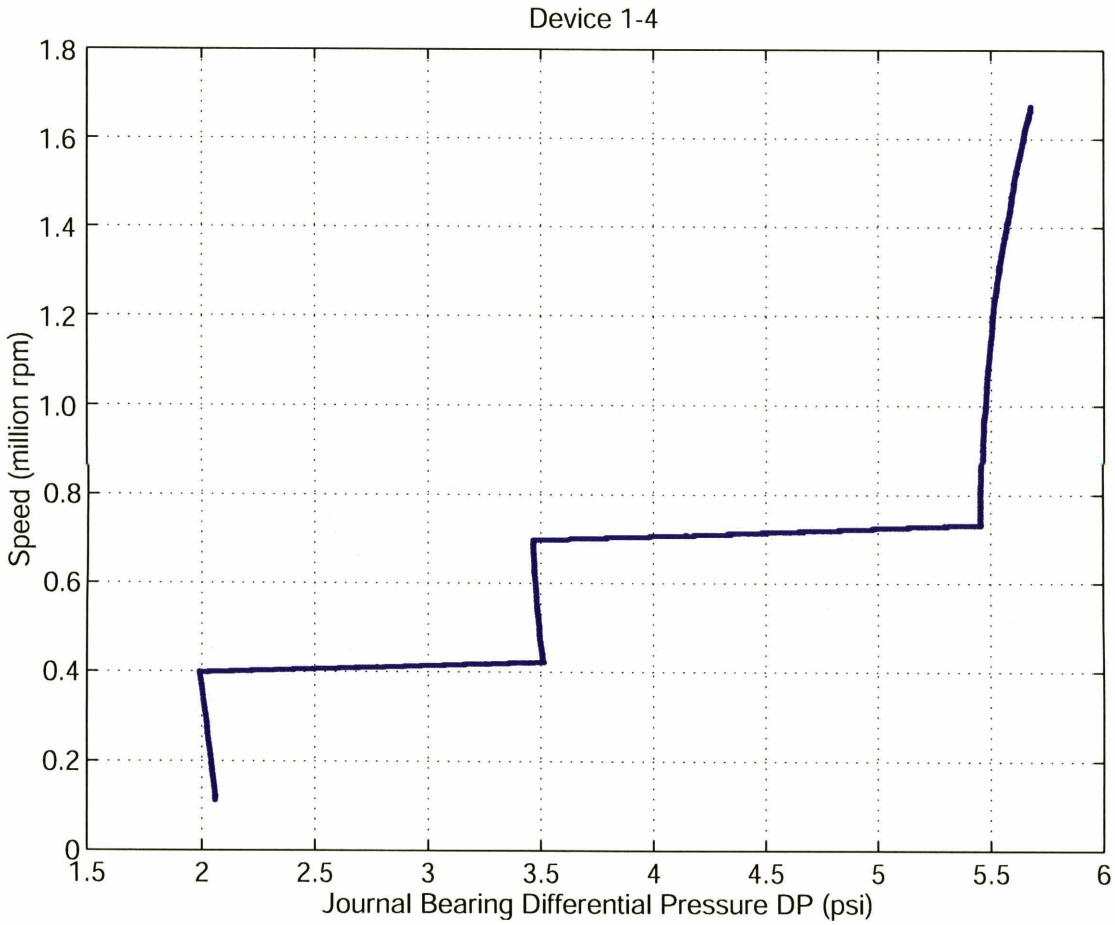

Figure 8-26: Operating schedule for Device 1-4 using Helium which achieved a record speed of 1.7 million rpm.

The above results correspond to the highest rotor tip speed and DN number ever achieved in the history of the MIT microengine project. Once again, such a record speed and achievement can be attributed to the successful redesign efforts. The new insight and lessons learnt in Section 5.1 which have been incorporated into the redesign have led to repeatable high speed bearing operation.

8.5 Operating Speed Limitations

Although operating speeds of up to 70% of the design speed has been successfully demonstrated, a remaining issue which needs to be addressed is the plausible causes which prevent even higher operating speeds from being achieved. Suggested reasons which limit the operating speed include structural failure of the rotor blades, non-linear effects which manifest themselves as supercritical subharmonic resonances, journal

bearing whirl instability and axial resonance due to the four speed bumps. Figure 8-27, which shows a summary of the test data, indicates the various regions or intervals over which the above suggested causes are deemed to limit the operating speed.

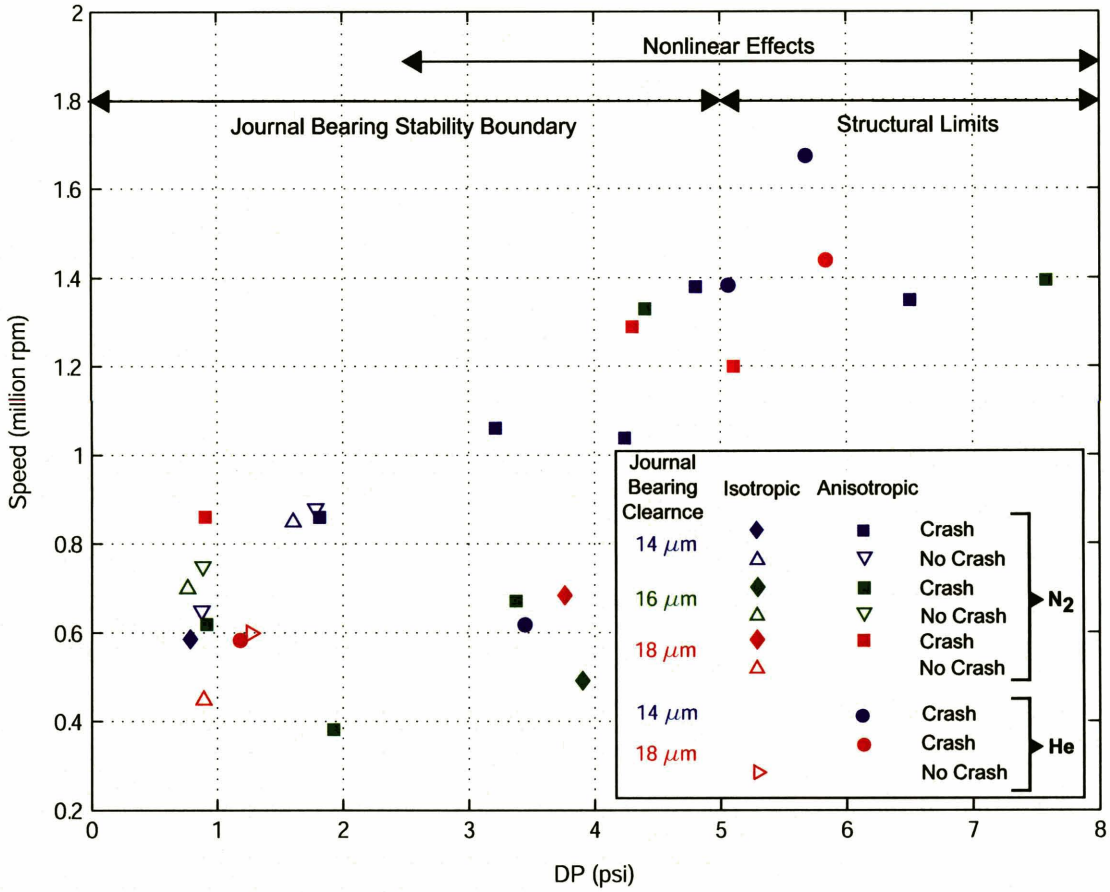

Figure 8-27: Summary plot of crash speeds versus journal bearing hydrostatic differential pressure DP. Various effects which might possibly limit high speed operation are indicated.

In the following subsections, the individual plausible causes limiting operation at speeds above 1.7 million rpm are discussed in detail.

8.5.1 Rotor Structural Issues

Referring to Figure 8-27, it appears that the crash speed increases monotonically with the journal differential pressure DP for anisotropic journal bearing operation, up till a DP of approximately 5 psi. For values of DP greater than 5 psi, with the exception of the device which achieved the record speed of 1.7 Mrpm, the crash speeds appear to be

relatively independent of the magnitude of DP, up till a DP of 8 psi. It is also interesting to note that the two devices that achieved the highest crash speeds were operated using Helium, which among all commonly available gases, offers the highest damping ratio for a given DP. The independence of crash speeds with DP for values of DP greater than 5 psi raises suspicion that issues which are not rotordynamic in origin might have been responsible for the failure of these devices. One possible culprit is the bonding quality between the rotor blades and the disk. Another possibility is the excessively high centrifugal stresses in the vicinity of the blade roots.

To further investigate these possibilities, fragments of fractured rotors which suffered from fatal high-speed crashes were examined in detail with the aid of scanning-electron microscopy (SEM). One technique involved grinding down Levels 1 and 2 (see Appendix A) using sandpaper mounted on a spinning wheel to expose the fractured rotor. Fragments of the fractured rotor were subsequently extracted and examined using SEM. Typical SEM photographs depicting the structure of the rotor fragments are shown in Figure 8-28. Although there were many instances of broken blades, there was no concrete evidence that the blades had delaminated along the bonding interface. Hence, it was plausible to conclude that the bonding quality between the blades and the rotor disk was sufficiently good, and it was not possible to attribute structural failure to the poor quality of the bonding. Figure 8-29 shows SEM photographs of a fractured rotor blade which was spotted at the turbine exhaust subsequent to a high-speed fatal crash. Once again, careful examination of the blade did not show any indication of delamination along the bonding interface.

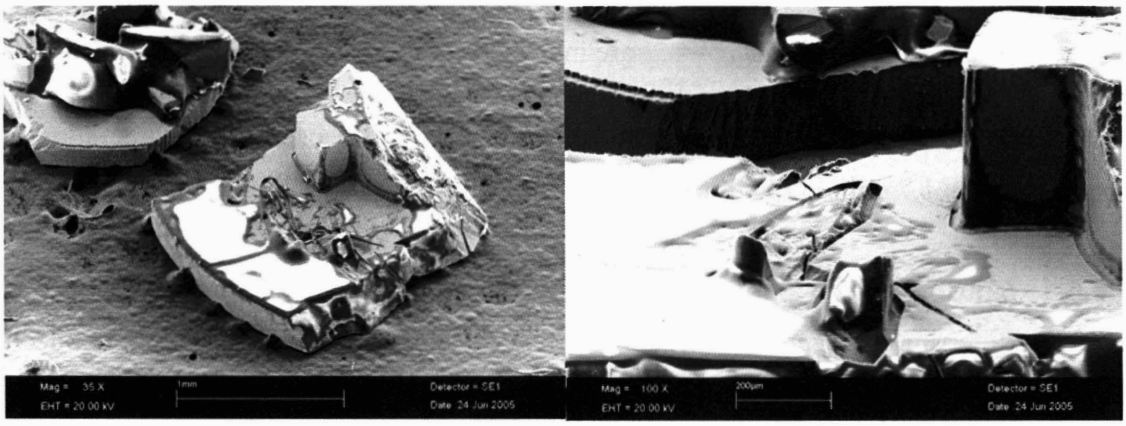

Figure 8-28: SEM pictures of fragments of fractured rotor.

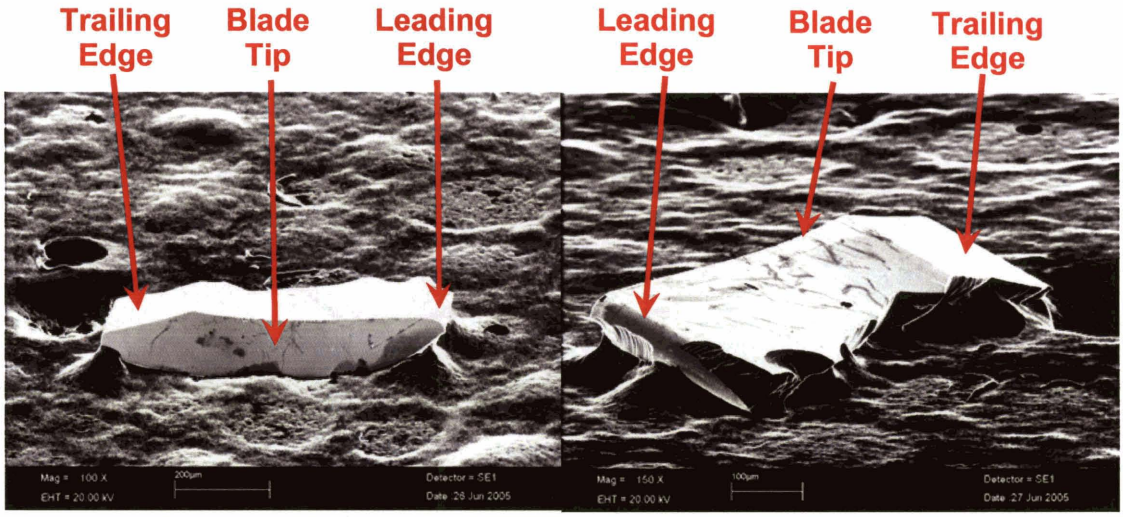

Figure 8-29: SEM pictures of fractured rotor blade.

However, the possibility of structural failure due to excessive centrifugal stresses still remains. To further assess this possibility, it is of vital importance to investigate the structural details in the vicinity of the blade roots. Figure 8-30 shows SEM photos depicting the detailed geometry in the neighborhood of a blade's root. These photos are of great significance, since they are the first pictures delineating the geometric details of the blade roots of a double-layer rotor. Details regarding the fabrication of the double-layer rotors are given in Section 6.3. Since the double-layer rotor technology will probably be incorporated on all future MIT spinning micro-devices, it is useful to gain a good understanding of the structural details surrounding the blade roots. The root of each blade is surrounded by a trench of approximately 20 μm width and 20 μm depth, consistent with the process flow for microfabricating the double-layer rotors. Of particular interest is the geometric dimension of the fillet at the base of each blade. From Figure 8-30, the fillet radius between the blade and the trench is on the order of 10 μm. This fillet radius is consistent with the value obtained by Chen [44], who quotes a value of 10 to 12 μm, which is deemed to be extremely repeatable.

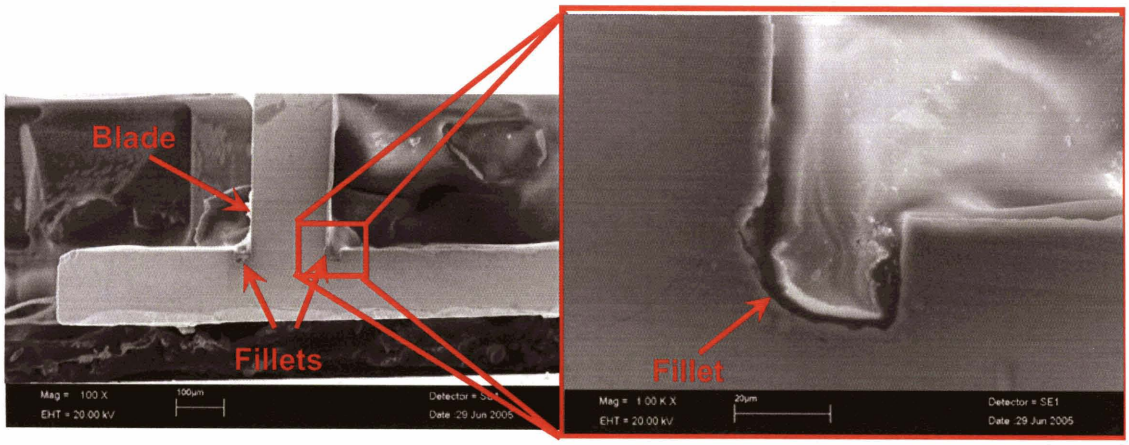

Figure 8-30: SEM pictures depicting details of fillet at root of turbine blade.

Having ascertained the details of the fillet, a Finite Element Analysis was performed to evaluate the principal stresses in the vicinity of the blade roots. Before this can be executed, it is necessary to model the structural details of the blade roots. This is depicted in Figure 8-31, where the base of each blade is assumed to be enclosed throughout by a trench of 20 µm width and 20 µm depth. The fillet radius between the blade and the trench has been assumed to be uniform at 10 µm, whereas the fillet radius along the outer corner of the trench has been assumed to be uniform at 2 µm. The Finite Element Analysis was performed by Berry [49] using MSC.NASTRAN. Due to limited computational resources, only a quarter of the rotor was modeled. A total of 300,000 nodes was employed and the model was created using 10 node, 2^{nd} order interpolation tetrahedral elements.

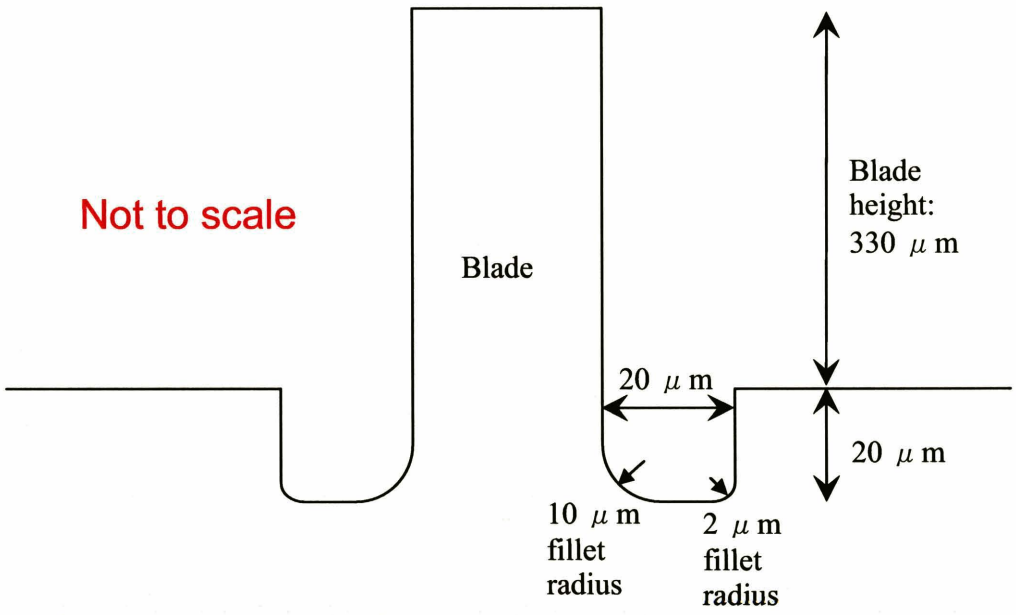

Figure 8-31: Geometric dimensions in the neighborhood of blade root used for Finite Element Analysis.

Figure 8-32 shows the finite element model and the boundary conditions used in the analysis. Figures 8-33 and 8-34 show contour plots for the maximum principal stresses for rotor spinning rates of 1.5 Mrpm and 2.4 Mrpm, respectively. The maximum principal stresses are found to occur in the fillet of the blade root, attaining values of 800 MPa and 2.1 GPa for rotational speeds of 1.5 Mrpm and 2.4 Mrpm, respectively. Chen [45] demonstrated that the fracture strength of Silicon is very sensitive to the details of the surface processing and etching techniques. Similar to all other brittle materials, the fracture strength of Silicon depends on the processing induced flaw population and has to be described using statistical distributions. Traditionally, the Weibull probability density function has been employed to model brittle material fracture strength. Chen reports that the Weibull reference strength (corresponding to 50% failure probability) of DRIE Silicon specimens in the presence of stress concentrations varies between 1.5 and 4 GPa. The lower and higher fracture strengths correspond to the absence and presence of an isotropic etch after the initial DRIE etch, respectively. However, there are substantial uncertainties associated with the above reference strengths and Weibull moduli. Given the margin of error, it is not possible to discount the likelihood that the maximum principal stress of 800 MPa encountered at a rotational speed of 1.5 Mrpm is sufficient to culminate in a structural failure along the blade root. Hence, it may be argued that the

apparent independence of the crash speed for a large number of devices tested at DP values greater than 5 psi can be attributed to the stress concentration associated with the excessively small fillet radii at the blade root.

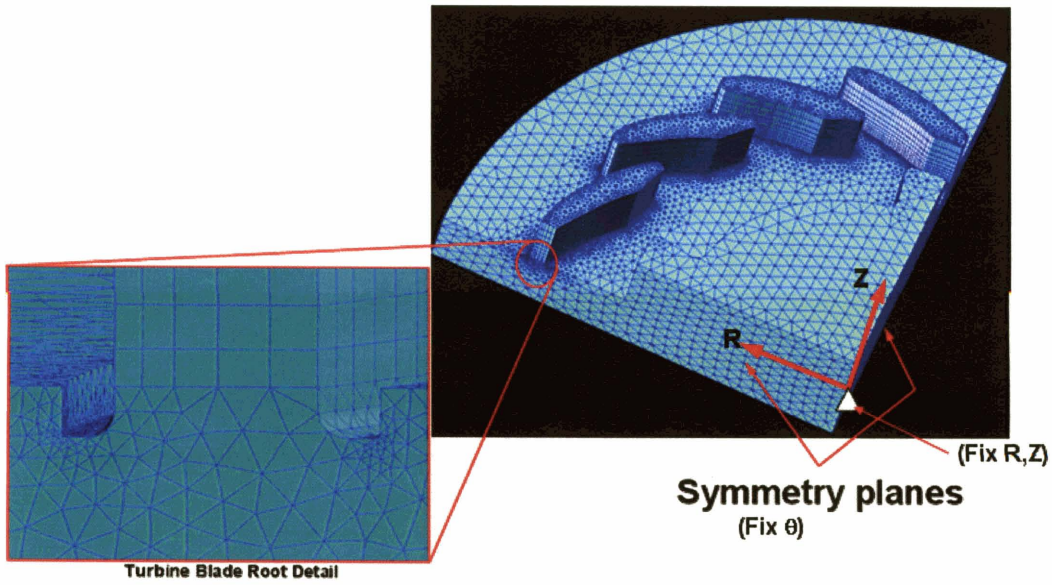

Figure 8-32: Computational grid used in the Finite Element Analysis. Courtesy of Berry [49].

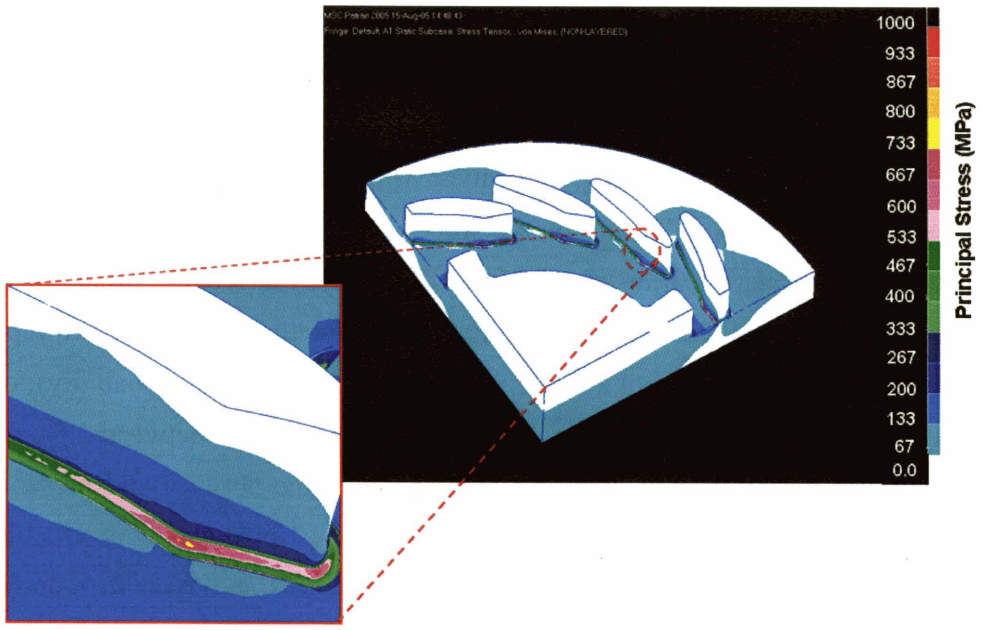

Figure 8-33: Maximum principal stress at a rotational speed of 1.5 Mrpm. Courtesy of Berry [49].

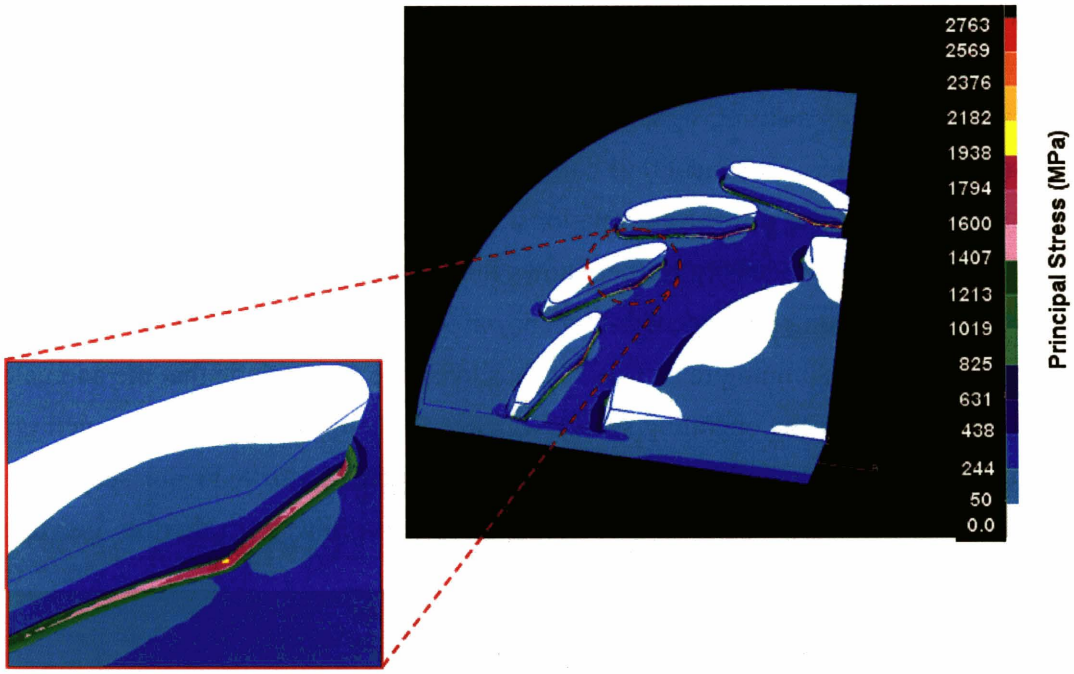

Figure 8-34: Maximum principal stress at a rotational speed of 2.4 Mrpm. Courtesy of Berry [49].

8.5.2 Non-linear Effects

One other possible cause which might potentially limit high speed bearing behavior is non-linear effects. Such non-linear effects manifest themselves as supercritical subharmonics, during which the distance-to-contact between the rotor and the journal bearing sidewall decreases, thus increasing the likelihood of a rotor crash. According to Ehrich [50], these non-linear effects occur at an odd-multiple of the non-linear large-amplitude natural frequency. Details of the non-linear orbits are very sensitive to rotor imbalance, sideloading, damping ratio and the non-linear functional relationship between the bearing stiffness on the rotor eccentricity.

The experiments showed that non-linear effects were at play in some high-speed runs. For example, Figure 8-35 depicts the operating protocol adopted for Device 2-7. Some anomaly in DP and speed were observed in the neighborhood labeled 'A'. Corresponding to a DP of 7.6 psi and a rotational speed of 704,000 rpm, the output voltage from a fiber optic sensor, which overlooks the speed bumps to measure the rotor speed, was acquired at 2 MHz for a duration of 10 seconds. The acquired data was subdivided into 20 contiguous subsets and a Fast Fourier Transform (FFT) was

performed on each subset. The ensemble averaged power spectral density is plotted on a log-linear scale in Figure 8-36. Since there are four speed bumps on the rotor, the fiber-optic sensor picks up a strong signal four times per rotor revolution. The peak possessing the maximum Fourier component thus corresponds to four times the rotor spinning speed. The peak corresponding to the rotor rotational rate of 704,000 rpm is labeled in Figure 8-36. The power spectral density further shows the presence of other peaks, most notably the presence of a strong fundamental frequency at 99,810 rpm, which corresponds to one-seventh of the rotor spinning rate. There is thus evidence to conclude that the anomalous behavior observed in the operating schedule is due to the occurrence of a seventh-order supercritical subharmonic. The "bulges" marked 'D' in Figure 8.36 are suspected to correspond to instabilities due to the main turbine mass-flow controller, as previously discussed in Section 8.4.3.

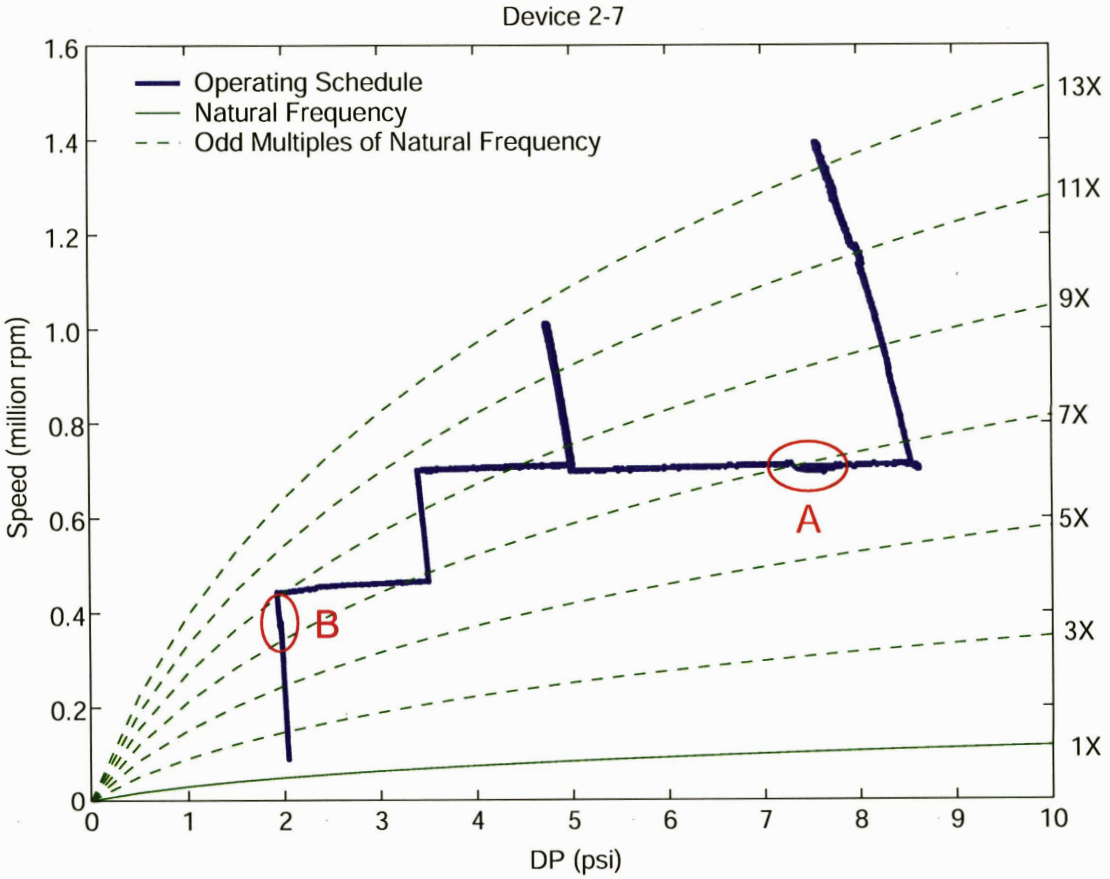

Figure 8-35: Operating Schedule for Device 2-7. Non-linear behavior was observed in regions marked 'A' and 'B'.

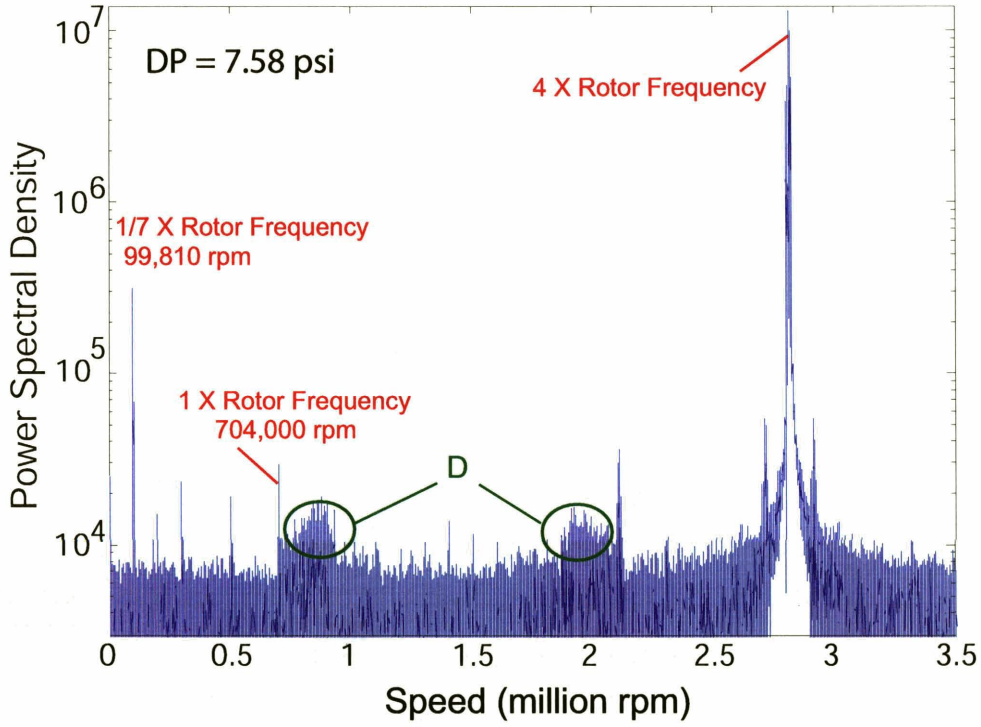

Figure 8-36: Power spectral density of fiber-optic data acquired in region 'A' of Figure 8-35.

Another experimental evidence of non-linear behavior is shown in Figure 8-35. Details of the operating schedule in the region labeled 'B' on the operating schedule are shown in Figure 8-37. There is a precipitous drop in DP from 1.96 psi to 1.94 psi when the rotor achieves a spinning speed of 400,000 rpm at a DP of 1.96 psi. This is accompanied by a slight reduction in spinning speed, consistent with the increase in viscous drag due to a reduction in the distance-to-contact between the rotor and the static structure when non-linear effects occur. When the rotor is decelerated, it follows an alternative route from the accelerating schedule. At a rotor speed of approximately 380,000 rpm, the value of DP rises abruptly from 1.94 psi to 1.96 psi once again, exhibiting hysteretic behavior. This hysteresis was indeed repeatable, and the rotor was found to display the same speed-DP dependence for multiple acceleration-deceleration cycles, with the rotor following different paths for acceleration and deceleration, as indicated in Figure 8-37. This non-linear behavior was found to occur when the rotor spinning rate was approximately 9 times the journal bearing natural frequency in the x-

direction.

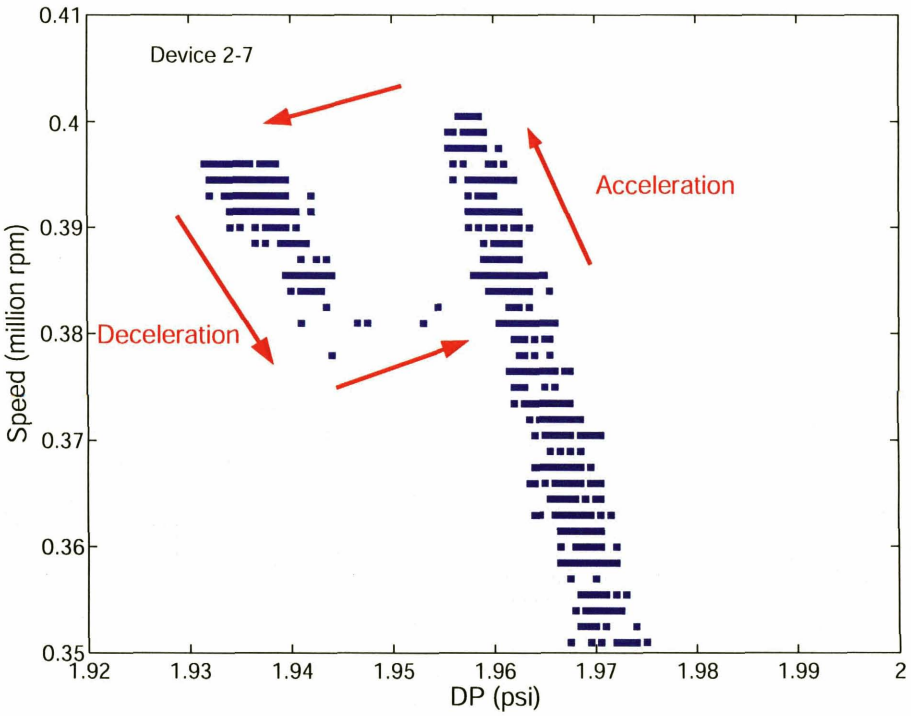

Figure 8-37: Nonlinear hysteretic effect observed during rotor acceleration and deceleration in region marked 'B' in Figure 8-35.

At significantly lower rotational speeds and lower values of DP, non-linear effects were also observed in the testing of several devices. However, these experimental occurrences of non-linear phenomena had benign effects and did not lead to fatal rotor crashes. Figure 8-38 shows the operating schedule employed for Device 7-2. The region labeled 'C' is magnified and plotted in Figure 8-39. The first two lower dips in DP correspond to the rotor traversing the journal bearing anisotropic natural frequencies in the x- and y-directions. However, in addition to the two lower dips in DP, there exists a third drop in DP at approximately 60,000 rpm, which is suspected to be due to the presence of non-linear effects.

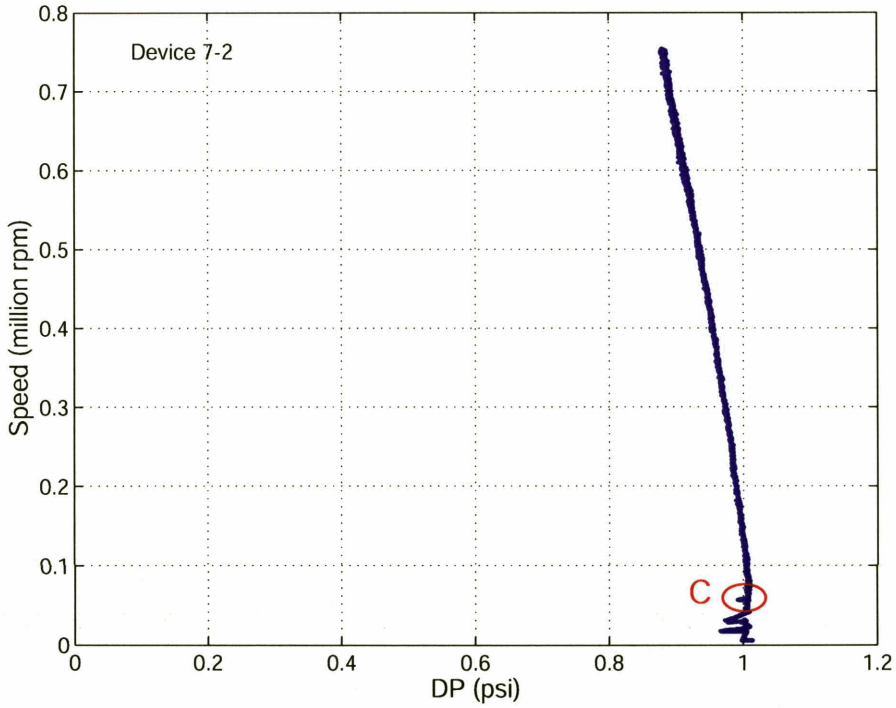

Figure 8-38: Operating schedule for Device 7-2. Nonlinear behavior observed in region marked 'C'.

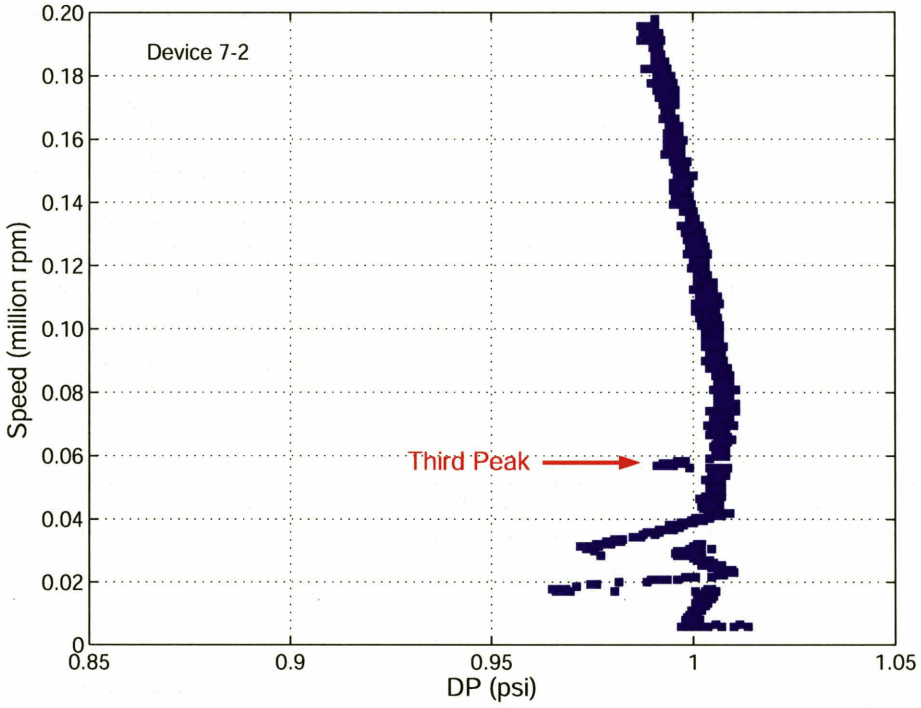

Figure 8-39: Third dip in DP observed at approximately 3 times the natural frequency in the y-direction.

Ehrich [50] performed numerical simulations on a trilinear isotropic journal bearing system. The rotor-bearing system was modeled using a Jeffcott rotor [38,51], a single point mass with two degrees-of-freedom mounted on a massless flexible shaft. The governing equations of motion are given by

$$m_R \frac{d^2(X + a\cos\Omega t)}{dt^2} + c\frac{dX}{dt} + F_x = 0 \tag{8.3}$$

and

$$m_R \frac{d^2(Y + a\sin\Omega t)}{dt^2} + c\frac{dY}{dt} + F_y = 0, \tag{8.4}$$

where F_x and F_y are the non-linear spring reaction forces, a is the rotor radial imbalance, m_R is the rotor mass and c is the physical damping. The non-linear system of equations was then solved numerically. The simulations showed the occurrence of supercritical subharmonic resonances at odd multiples of the large amplitude non-linear natural frequency. The normalized peak amplitude (normalized using the rotor imbalance) of the subharmonic resonance was approximately equal to the order of the subharmonic resonance. The non-linear response was shown to be a strong function of the damping ratio ζ, as shown in Figure 8-40. The number of orders of subharmonic resonances observed depended on ζ. Decreasing the value of ζ increased the number of orders of subharmonic resonances observed. This led Ehrich [49] to conclude that there was a region which was free from non-linear subharmonic resonances. Ehrich [49] examined the experimental data and suggested that it was possible to classify the crash data into two different categories, as shown in Figure 8-41. The lower solid line demarcates crash points for devices which have suffered from fatal crashes due to non-linear subharmonic resonances, whereas the upper line attempts to collapse the crash points corresponding to devices which are suspected to have failed due to whirl instability. Except for one single outlying point (and ignoring the data obtained using Helium), the above interpretation suggests that there is a possible acceleration corridor sandwiched between the two solid lines where non-linear subharmonic resonances "disappear" and whirl instability does not occur. A device was subsequently operated to investigate the validity of this hypothesis. The acceleration schedule adopted on this device is plotted in Figure 8-41, where it is evident that a staircase-like accelerating protocol was employed to meticulously ensure

operation within the proposed acceleration corridor. However, the device suffered from a fatal crash at a rotational rate of 1.05 Mrpm. Hence, there is no concrete evidence that verifies the possible existence of the proposed safety corridor. However, it should be noted that there are many differences between the actual rotor-bearing system being experimentally tested and the model system simulated by Ehrich. The numerical simulations were carried out on an isotropic stiffening system with a sharp discontinuity in stiffness. Similar subharmonic resonances were not observed when numerical simulations were performed on a softening system. Figure 8-42 shows modeling predictions of the journal bearing natural frequency for different radial eccentricities corresponding to a journal bearing clearance of 18 μm without taper. The different curves correspond to different values of bearing differential pressure DP. The analytical models predict that the rotor and bearing form a softening system. However, in reality, the journal bearing was etched with a slight negative taper to prevent the formation of spikes, as discussed in Section 5.1.1.2. This further enhances the softening effect of the rotor-bearing system [3].

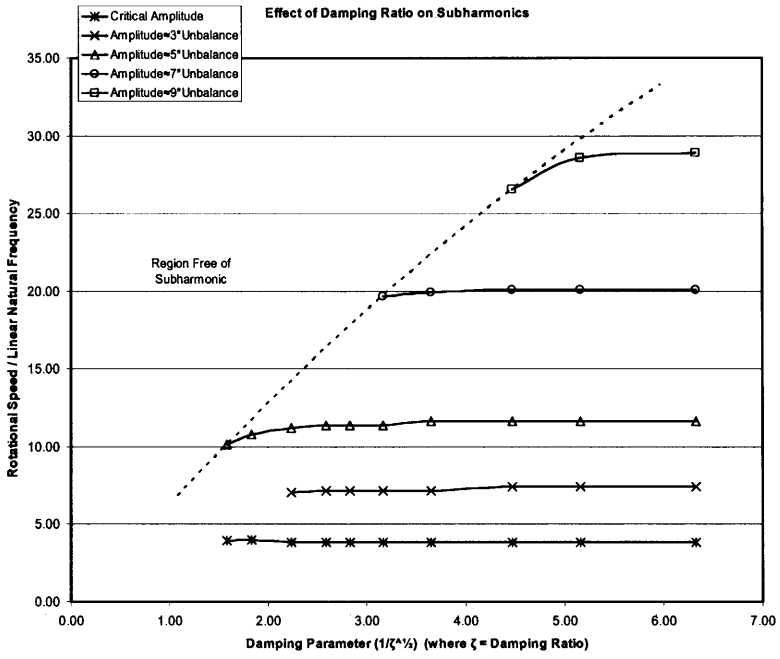

Figure 8-40: Effects of damping ratio ζ on the number of supercritical subharmonics observed. Courtesy of Ehrich [49].

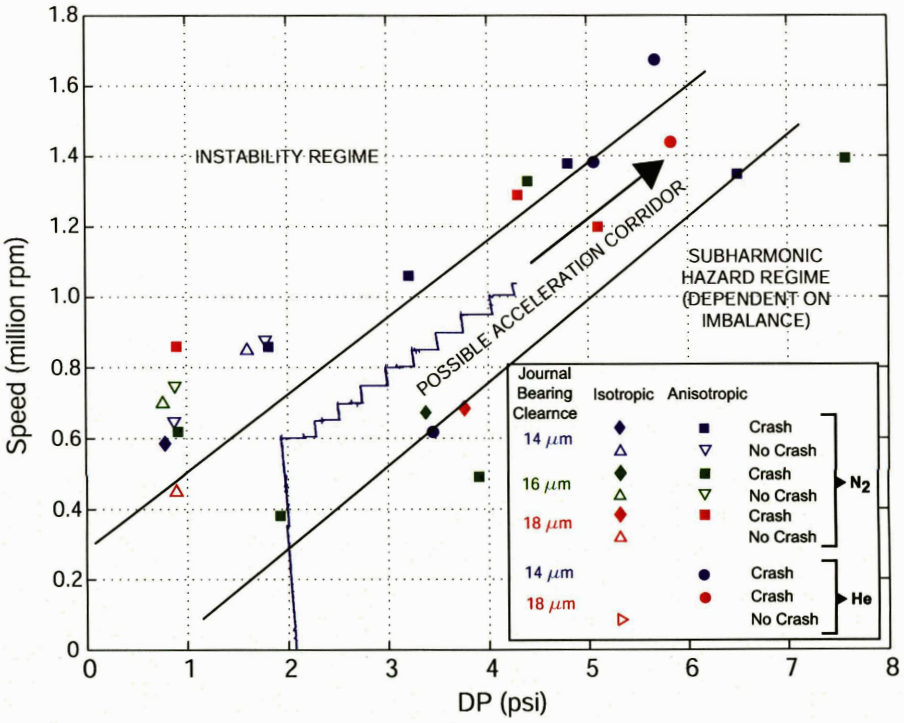

Figure 8-41: Proposed acceleration along corridor separating conjectured stability boundary and region where subharmonics are suspected to be present. Courtesy of Ehrich [49]. Operating schedule for a device within the acceleration corridor is also shown.

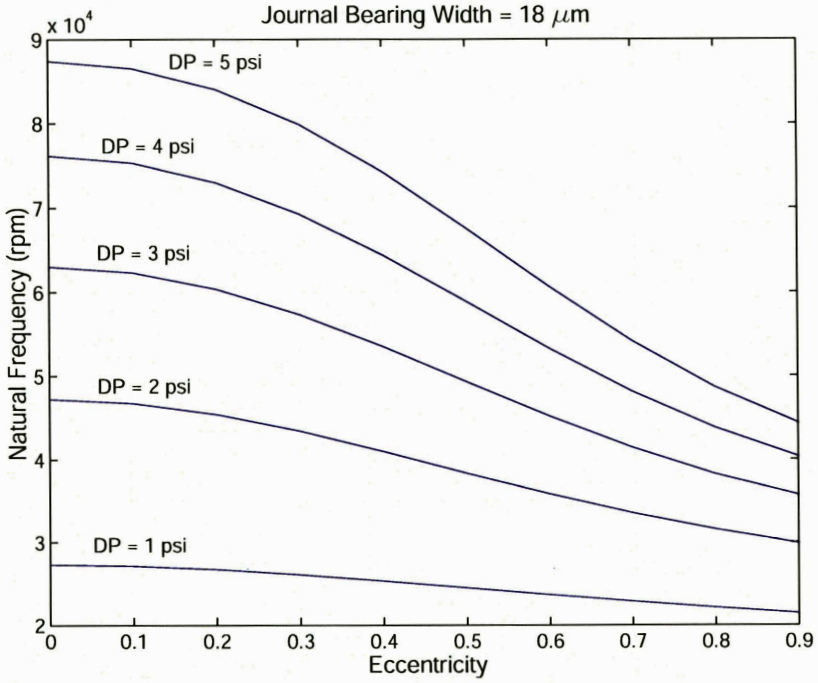

Figure 8-42: Journal bearing with zero taper has stiffness which decreases as a function of radial eccentricity.

Liu [3] has employed the method of multiple scales to perform preliminary studies on the non-linear dynamics of the journal bearing system. However, in view of the complexity of the mathematical analysis, it was only possible to analytically obtain low order secondary resonances. The multiple-scale analysis only yields information pertaining to the rotational speeds at which low order supercritical subharmonics set in, as well as the general shape of the non-linear rotor orbits, but does not give any information on the amplitude of the orbits, nor the distance-to-contact. Furthermore, only non-linearities in the hydrostatic force were considered, and non-linearities in the hydrodynamic and damping forces were not taken into account. The dynamic stability (or lack thereof) of the highly complicated non-linear orbits also need to be analyzed.

In view of the lack of numerical results or analytical models to accurately predict the existence (or lack thereof) of high order subharmonic resonances, especially for softening systems, it is impossible to discount the possibility that the some of the fatal crashes previously experienced were due to resonances arising from non-linear effects.

8.5.3 Axial Resonance due to Speed Bumps

Another proposed cause for high-speed failures stems from observations that the crash mode for two of the devices (which constituted less than 10% of the total number of devices tested to high speeds) was significantly different from the rest of the devices. The forward thrust bearing of these two devices was found to have given way subsequent to high speed fatal crashes at 580,000 rpm and 620,000 rpm.

Two hypotheses are proposed for the forward thrust bearing failure. The first hypothesis is failure due to structural integrity issues. However, this is rather unlikely due to the fact that substantial effort has been expended in the redesign to rectify all possible shortcomings of the original forward thrust bearing structural design. The structural components surrounding the forward thrust bearing have been redesigned and reinforced to increase the available bonding area and sidewall thicknesses[1]. Furthermore, most of the other devices have been subjected to equivalent or even higher forward thrust bearing pressures and hence structural loading, but have shown no signs of forward thrust bearing

[1] The minimum physical separation between critical features has been increased from 40 μm in the original microbearing test device to 200 μm in the redesigned microbearing test device.

failure. The thrust bearings on majority of the devices have also been subjected to longer periods of structural loading, since the time taken to achieve speeds in excess of 1 Mrpm was substantially longer than that taken by the two devices in question.

The other hypothesis is motivated by the observation that the only two devices which exhibited forward thrust bearing failures crashed at speeds which were remarkably close to one another, thus alluding to the possibility of an axial resonance. One potential issue which might contribute to an axial resonance is the presence of 4 identical, evenly spaced speed bumps. The passage of each speed bump underneath the structures supporting the forward thrust bearing causes the rotor to be subjected to a 4 per-rev axial excitation. The frequency of this axial excitation is of the same order as the axial natural frequency of the thrust bearings. It can thus be argued that the forward thrust bearing failure might have been caused by axial excitations from the speed bumps. However, the fact that more than 90% of the devices did not fail in a similar manner might imply that the axial resonance is rather benign in nature and can be possibly circumvented by rapidly and carefully accelerating the rotor past the critical zone ranging between approximately 550,000 rpm and 650,000 rpm.

8.6 Summary and Conclusions

This chapter documents the main findings of the experimental testing performed on the redesigned microbearing test devices. Static flow tests revealed that the devices meet the salient design specifications. In particular, the devices can be separated into three bins with distinctively different journal bearing widths, thus paving the way for the effects of journal bearing clearance on bearing performance and stability to be investigated. Low speed spinning tests demonstrated the ability of the four-plena journal bearing design to achieve both isotropic and anisotropic journal bearing operation. At low values of journal bearing DP less than 2 psi, similar levels of bearing performance were achieved using both isotropic and anisotropic journal bearing operation. This was in broad agreement to analytical model predictions, which predict singular whirl stability behavior at low values of DP for isotropic journal bearing operation. High whirl-ratios between 20 and 40 were also demonstrated at low values of DP. At high values of DP, anisotropic journal bearing operation was found to be superior to isotropic operation, which was again consistent with the model predictions. Almost all devices tested

anisotropically at high values of DP were capable of achieving speeds in excess of 1 million rpm. This attests to the improvements in bearing design, high reliability of the novel microfabrication processes, and the repeatability and successful implementation of the operating protocols. Controlled high speed operation up to 70% of the design speed has been demonstrated on a device using Helium. This corresponds to a rotation rate of 1.7 million rpm, a rotor tip speed of 370 m/s and a DN number of 7 million mm-rpm. Finally, several issues which potentially limit high speed operation were identified and assessed. These issues include excessively high blade root stresses due to small fillet radii, non-linear supercritical subharmonic resonances and axial resonance due to the speed bumps.

CHAPTER 9

Summary and Contributions of Thesis

This chapter summarizes the research performed in this dissertation and the main contributions. Recommendations for future research are also outlined.

9.1 Summary and Conclusions

This thesis presents the analysis, design, microfabrication, testing and operation of micro-hydrostatic gas thrust and journal bearings for application to MEMS-based turbomachines.

Chapter 2: Modeling and Experimental Investigation of Micro-Hydrostatic Gas Thrust Bearings for Micro-Turbomachines

In Chapter 2, extensive analytical models for assessing the performance and stability of hydrostatic thrust bearings for application to micro-turbomachines have been developed. A hydraulic resistance model which accounted for the effects of both compressibility and viscous effects has been introduced. The model is capable of predicting variations in axial stiffness, natural frequency and mass flow rates as functions of the thrust bearing supply pressure. Dynamic instability of hydrostatic thrust bearing systems manifested as axial oscillations of the rotor has also been assessed using an analytical model. A simple yet useful criterion has been established, where the occurrence of choked flow through the orifices of both thrust bearings give rise to dynamic instability.

Operating protocols have been subsequently developed using the analytical model for the MIT micro-devices such as the micro-electrostatic turbine-generator and the micro-turbopump. The strong coupling effects of the accompanying components within these micro-devices introduce undesirable negative stiffness, subjecting the bearings to static instability. The validity and usefulness of these operating protocols were verified during experimental testing of these micro-devices. In the micro-electrostatic turbine-

generator, implementation of the operating protocols enabled stable operation up to 93% (850,000 rpm) of the design speed to be achieved. No observable electrostatic pull-in effects were observed for voltages of up to 120 V applied between the electrodes. Experiments performed at low pump outlet pressures in the micro-turbopump demonstrated the validity of the operating protocols in successfully preventing the leakage of liquid from the pump outlet into the thrust bearing pads.

In addition to static stability, the analytical model was utilized to investigate the thrust bearing dynamic stability of a micro-turbocharger. A-priori predictions were made pertaining to the thrust bearing supply pressures necessary for dynamic instability to occur. The predicted axial dynamic instability was subsequently verified and demonstrated in experiments performed on a micro-turbocharger. The frequency of unstable axial oscillations was found to show good agreement with the model predictions, thus verifying the ability of the analytical model to capture the key mechanisms responsible for dynamic instability. The combined experimental and modeling efforts further demonstrate that a simple criterion for the onset of dynamic instability is the occurrence of flow choking through the orifices of both the forward and aft thrust bearings.

Chapter 3: Analysis of Tilting effects and Geometric Non-uniformities in Micro-Hydrostatic and Hydrodynamic Gas Thrust Bearings

A Green's function approach has been employed in Chapter 3 to extend and generalize the simple hydraulic resistance analytical model introduced in Chapter 2 for hydrostatic thrust bearings. The hydrodynamic thrust bearing forces induced by the pumping action of the rotor rotation are evaluated by solving the Reynolds equation. The extended model serves as an effective tool for addressing two key issues: (i) the thrust bearing tilting stiffness, and (ii) the effects of geometric non-uniformities due to micro-fabrication uncertainties. Other attributes and capabilities of the enhanced model include the prediction of the steady-state performance of thrust bearings with unconventional arrangement of orifices, the investigation of coupling effects with the turbomachinery components in annular thrust bearings, and the quantification of the rotor tilting angle

using experimentally measured thrust bearing mass flow rates. The torques and rotor tilting angles arising from geometric non-uniformities in orifice lengths and diameters can also be assessed effectively using the Green's function formulation. Effects arising from a wide range of micro-fabrication defects and anomalies such as the presence of unetched or missing orifices are readily assessed. Additionally, an influence-coefficient approach for modeling compressible, viscous internal flows through orifices of varying cross-sectional areas has been employed to analyze the effects of orifice taper.

A two degree-of-freedom rotordynamic model has been applied to analyze the roll and pitch dynamics of a rotor-thrust-bearing system in the presence of dynamic or moment imbalance. The model is capable of evaluating the static rotor tilting angles and dynamic stability of a rotor-thrust-bearing system for different operating speeds and thrust bearing conditions.

The generalized Green's function formulation for modeling the thrust bearings finds further application in evaluating the impact of micro-fabrication tolerances and manufacturing uncertainties on thrust bearing performance. The maximum allowable geometric non-uniformity in terms of thrust bearing clearance and orifice diameter and taper can be specified to ensure a sufficiently high level of thrust bearing performance. The maximum allowable dynamic imbalance for stable high speed operation can also be quantified.

An analytical model for evaluating the viscous, compressible flow through annular seals using the influence-coefficient based approach has been developed. The model was applied during experiments performed on the MIT micro-turbopump to ascertain the rotor axial position with high precision. The feasibility of employing a Lomakin effect seal thrust bearing in lieu of a hydrostatic thrust bearing has been investigated. Lomakin effect seal thrust bearings are found to be unsuitable substitutes for the hydrostatic thrust bearings currently employed in providing sufficient axial support and stiffness. Lomakin effect seal thrust bearings consume more mass flow and have axial stiffness values several orders of magnitude lower than their hydrostatic counterparts. They are also liable to suffer from static instability at high pressure ratios when compressibility effects become dominant.

Chapter 4: Modeling of Micro-Hydrostatic Journal Bearing for Micro-Turbomachines

Chapter 4 addresses the effects of a non fully-developed circumferential flow in the ultra short (low L/D) micro-hydrostatic journal bearing configuration adopted for the MIT micro-devices. Two major implications arise from the non fully-developed nature of the circumferential flow. First, the non fully-developed circumferential flow affects the magnitudes of the hydrodynamic forces and stiffness acting on the rotor. It is thus necessary to assess the effects of a non fully-developed circumferential flow on journal bearing whirl stability, which depends strongly on the cross-coupled hydrodynamic stiffness. Furthermore, since the non fully-developed circumferential flow alters the wall shear stress and viscous drag acting on the rotor, effects on torque and journal bearing viscous dissipation have to be reassessed.

The impulsive startup of a plane Couette flow has been employed to shed light on the salient fluid dynamic mechanisms responsible for the evolution of the non fully-developed circumferential flow. A dimensionless parameter $\beta_{FD} = \nu L/\left(\overline{U}C^2\right)$, which characterizes the ratio of the flow-through time of the axial hydrostatic flow to the viscous diffusion time, has been identified to be a crucial parameter which dictates the evolution of the circumferential flow field. In particular, there is good agreement between CFD calculations and the model-predicted circumferential flow field. CFD has been used to evaluate the hydrodynamic forces acting on the rotor due to viscous pumping and viscous drag. The hydrodynamic stiffness coefficients thus obtained are subsequently applied to a rotordynamic model for assessing journal bearing whirl stability. In particular, the dimensionless parameter β_{FD} is found to be capable of collapsing all the available CFD data for the whirl-ratio. Singular whirl-ratio behavior occurs when the flow through time of the axial hydrostatic flow is approximately half of the characteristic viscous diffusion time. This criterion for the singular whirl-ratio behavior depends on the hydrostatic axial differential pressure DP and the fluid properties. This is in contrast to model predictions assuming a fully-developed circumferential flow, where the criterion for singular whirl behavior depends solely on bearing geometry. The analytical models

developed for evaluating the evolution of the circumferential flow can be further applied to obtain more realistic estimates for the actual journal bearing torque requirements and viscous power dissipation.

Chapter 5: Analysis and Redesign of High Speed and High Whirl-Ratio Gas Bearings for MEMS Devices

In the first part of Chapter 5, major lessons acquired from the microfabrication and testing of previous builds of microbearing test devices are discussed and analyzed. The lessons learnt are classified into three categories, namely microfabrication issues, rotordynamic issues and structural issues. In terms of microfabrication, issues which potentially have adverse effects on high speed bearing operation include the formation of a "fence" at the exit of the journal bearing and the existence of spikes in the journal bearing. Microfabrication solutions are subsequently developed to eradicate these undesirable features. On the other hand, a new "drop-in rotor" approach has been found to significantly increase the yield in the number of operational devices as compared to the former "snap-off tabs" approach. In terms of rotordynamics, sources of negative radial and tilting stiffness arising from coupling effects have been identified. Numerous structural integrity flaws and issues pertaining to the forward thrust bearing and rotor blades have been uncovered. Majority of these flaws originate from the excessively close proximity between features subjected to large pressure differences, as well as the low radius of curvature of features which give rise to "dimples" at the root of the blades' trailing edge and the thrust bearing plenum.

These lessons learnt and new insight gained are subsequently applied to the analysis and redesign of a microbearing test device. The key elements and components addressed in the redesign include annular seals, multiple journal bearing plena, turbomachinery, thrust bearings, structural integrity considerations and device variations.

Chapter 6: Microfabrication of High Speed and High Whirl-Ratio Gas Bearings for MEMS Devices

Microfabrication of the redesigned microbearing test device was carried out in the MIT Microsystems Technology Laboratories (MTL). The salient steps in the process flow employed for the microfabrication of the six-wafer stack redesigned bearing test devices have been presented in Chapter 6. The main challenges encountered during the course of fabricating each layer were described, and the pertinent steps taken to overcome these challenges were discussed. The novel fabrication techniques and procedures for "D^3" rotors (*d*ouble layer, *d*onor-receiver and *d*rop-in rotors) have been described in detail. "D^3" rotors serve as the important enabling technology for fabricating rotors with sufficiently low levels of radial imbalance, and for fabricating devices with different journal bearing widths on the same build. The redesigned microbearing test device was successfully completed after ten weeks of intensive microfabrication efforts.

Chapter 7: Experimental Investigation of Hydrostatic Gas Journal Bearings for Micro-Turbomachinery

Experimental techniques and procedures developed for quantifying the rotordynamic behavior of micro-hydrostatic gas journal bearings are presented in Chapter 7. Measurement and analytical techniques for the static quantification of the radial imbalance of rotors arising from DRIE non-uniformities have been demonstrated. These techniques are invaluable during the microfabrication process. They allow the rotor imbalance to be quantified in order to ascertain whether the imbalance satisfies a-priori design specifications established using analytical models for transcritical and stable high-speed operation.

Experiments using a high-resolution fiber optic sensor have been conducted in the MIT micro-bearing test device. A data reduction scheme has been implemented to infer the imbalance-driven whirl response curves of the rotor for different journal bearing hydrostatic differential pressures. The reduced data facilitates the successful evaluation of key journal bearing rotordynamic information such as the stiffness, the natural frequency and the damping ratio of the journal bearing and the imbalance of the rotor. Another more straightforward approach for experimentally deducing the journal bearing natural frequency has been developed by employing a flow control valve to provide the

necessary journal bearing mass flow. The natural frequency of the rotor bearing system is then deduced by monitoring sudden dips or excursions in bearing hydrostatic differential pressure measurements during transcritical operation. Experimental data for the natural frequencies have been compared against the analytical model predictions by Liu [3], showing favorable agreement. Several strategies for traversing the journal bearing natural frequency have been proposed and demonstrated.

Chapter 8: Experimental Testing of High Speed and High Whirl-Ratio Gas Bearings for MEMS Devices

Experiments performed on the redesigned microbearing test devices are presented in Chapter 8. The devices meet the salient design specifications, as revealed from extensive static flow tests. In particular, the devices can be separated into three bins with distinctively different journal bearing widths, thus paving the way for the effects of journal bearing clearance on bearing performance and stability to be systematically investigated. The ability of the four-plena journal bearing design to achieve both isotropic and anisotropic modes of journal bearing operation has also been successfully demonstrated.

At low values of journal bearing differential pressures DP less than 2 psi, similar levels of bearing performance have been achieved using both isotropic and anisotropic journal bearing operation. This is in broad agreement to analytical model predictions, which predict singular whirl stability behavior at low values of DP for isotropic journal bearing operation. High whirl ratios ranging between 20 and 40 have also been demonstrated at low values of DP. Consistent with the model predictions, anisotropic journal bearing operation exhibits superior performance as compared to isotropic operation at high values of DP greater than 2 psi. Almost all devices tested anisotropically at high values of DP were capable of achieving speeds in excess of 1 million rpm. This attests to the improvements in bearings and seals design, the high reliability of the novel microfabrication processes, and the repeatability and successful implementation of the operating protocols.

A first-of-a-kind controlled high speed operation up to 70% of the design speed has been demonstrated on a device using Helium. This corresponds to a rotation rate of 1.7 million rpm, a rotor tip speed of 370 m/s and a DN number of 7 million mm-rpm. Finally, several issues which potentially limit high speed operation have been identified and assessed. These issues include excessively high blade root stress concentrations due to small fillet radii, non-linear supercritical subharmonic resonance effects and axial resonance due to the speed bumps.

9.2 Thesis Contributions

Analytical Modeling

- Development of extensive analytical models for micro-hydrostatic gas thrust bearings to predict key steady-state thrust bearing performance indicators for design purposes.
- Establishment and experimental demonstration of operating protocols for ensuring thrust bearing static stability on several MIT micro-devices.
- Analysis and experimental verification of dynamic stability in micro-hydrostatic gas thrust bearings. Identification of a simple and useful dynamic stability criterion: flow choking in both thrust bearings results in dynamic instability.
- Development of a generalized analytical model for analyzing tilting effects and geometric non-uniformities in micro-hydrostatic gas thrust bearings using a Green's function approach.
- Establishment of analytical models for predicting the performance of annular seals.
- Analysis of non fully-developed circumferential flow effects on journal bearing whirl stability and viscous power dissipation in ultra short (low L/D) micro-hydrostatic journal bearing configurations. Identification of a dimensionless parameter governing the whirl-ratio of isotropic hydrostatic journal bearings.

Determination of a simple criterion for singular behavior of stability boundary or whirl-ratio.

Design and Microfabrication

- Identification of issues related to microfabrication, rotordynamics and structural integrity from extensive experimental testing. Conception and design of novel microbearing test device based on new insight and improved understanding.
- Microfabrication of redesigned microbearing test devices incorporating a novel double-layer, donor-receiver, drop-in rotor scheme.

Experimental Testing

- Development of experimental techniques and procedures for determining the imbalance-driven whirl response curves of micro-hydrostatic gas journal bearings. Implementation of data reduction schemes for evaluating key journal bearing rotordynamic information such as the stiffness, natural frequency and damping ratio, as well as the imbalance of the rotor.
- Experimental demonstration and systematic investigation of isotropic and anisotropic micro-hydrostatic journal bearing operation. Experimental demonstration of high whirl-ratios ranging between 20 and 40 (one order of magnitude higher than those in macro-scale journal bearings) at low values of journal bearing hydrostatic differential pressures.
- Experimental demonstration of repeatable high speed performance (in excess of 1 million rpm) for devices tested anisotropically at high values of journal bearing hydrostatic differential pressures. First-of-a-kind experimental demonstration of a micro-machine operating at a rotor circumferential tip speed of 370 m/s, corresponding to a rotation rate of 1.7 million rpm, a DN number of 7 million mm-rpm and controlled operation up to 70% of the design speed.
- Demonstration of technical feasibility of high-speed gas bearings required for achieving high power densities in MEMS-based micro-turbomachinery.

9.3 Recommendations for Future Work

Several conjectures that potentially limit high speed operation were identified in Section 8.5. The excessively small fillet radii have been shown using FEM to introduce significant stress concentrations in the blade roots near their trailing edges. The development of microfabrication techniques to increase the fillet radii should be pursued. Efforts should also be directed towards the use of thinner wafers for microfabricating rotors with smaller blade heights. Recall that the original blade height of 150 μm could not be incorporated for the double-layer rotor scheme, in view of the fragility of the wafers and the associated difficulties pertaining to wafer handling. Several other research groups are working with wafers of 100 μm thickness, so it might be worthwhile to study the wafer handling schemes adopted by them. A 50% reduction in blade height has the benefits of reducing the stress levels and rotor tip deflection by approximately four times.

Furthermore, there are at present no satisfactory analytical models for analyzing the non-linear supercritical subharmonic resonances in micro-hydrostatic gas bearings. However, non-linear effects have previously been observed during the testing of several devices. The effects of non-linearities on journal bearing whirl stability are hitherto unknown. Ehrich [46] has performed simulations which indicate that the amplitude of the subharmonic resonances increases for higher order subharmonics. Chaotic behavior might even arise as a result of non-linear bearing stiffness and damping. The dynamic stability of these large amplitude non-linear orbits is also an open question, and more sophisticated modeling approaches and numerical simulations would have to be performed to address this teething issue.

APPENDIX A

Cross Sectional Details of Redesigned Microbearing Test Device

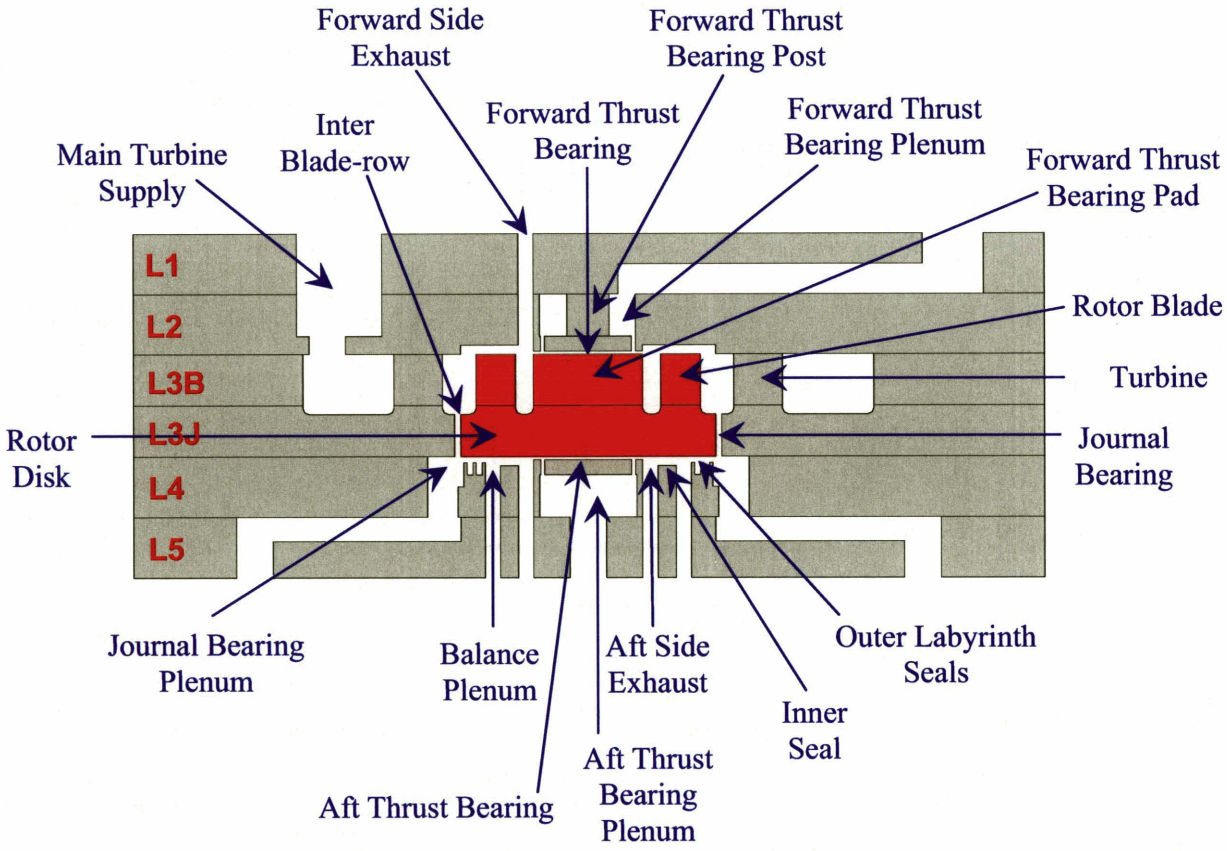

Figure A-1: Cross sectional view of redesigned microbearing test device showing details of individual components.

APPENDIX B

Detailed Components of Individual Layers of Redesigned Microbearing Test Device

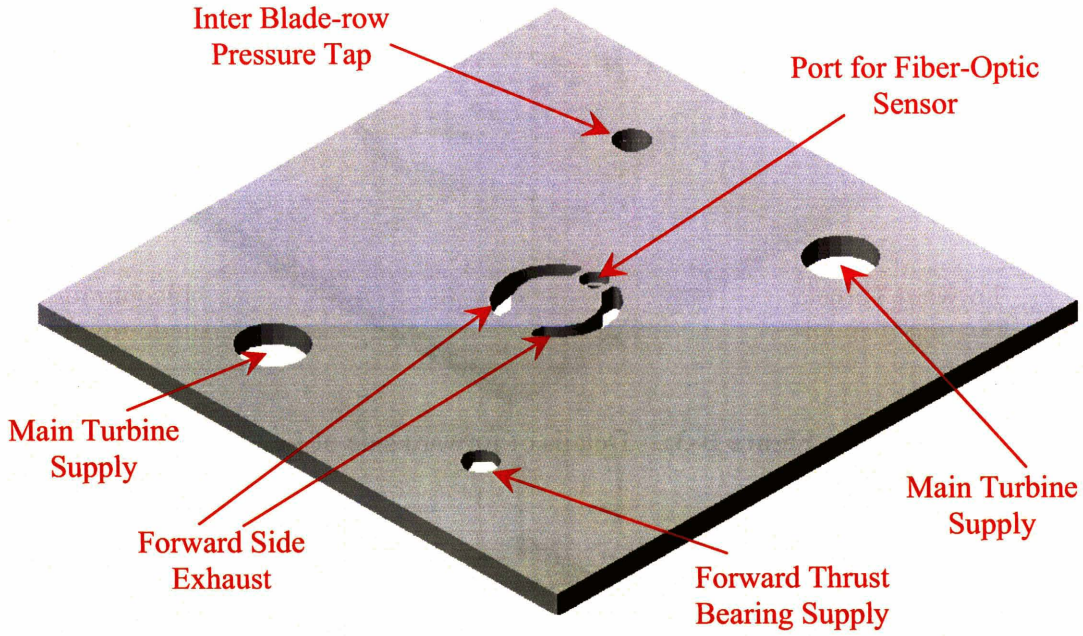

Figure B-1: Details of forward side of Level 1.

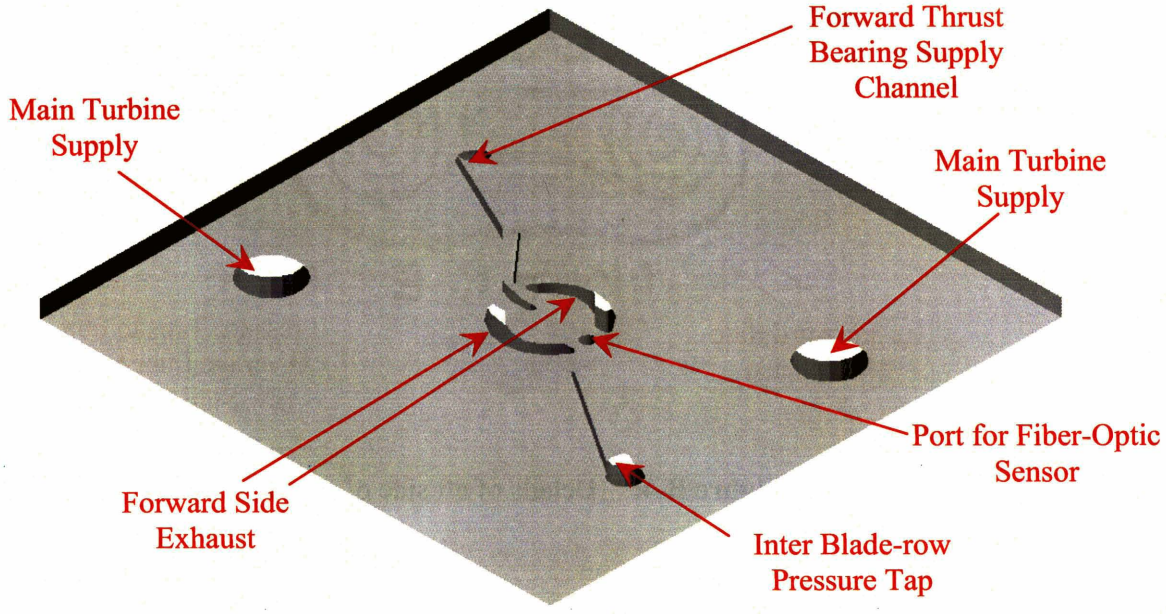

Figure B-2: Details of aft side of Level 1.

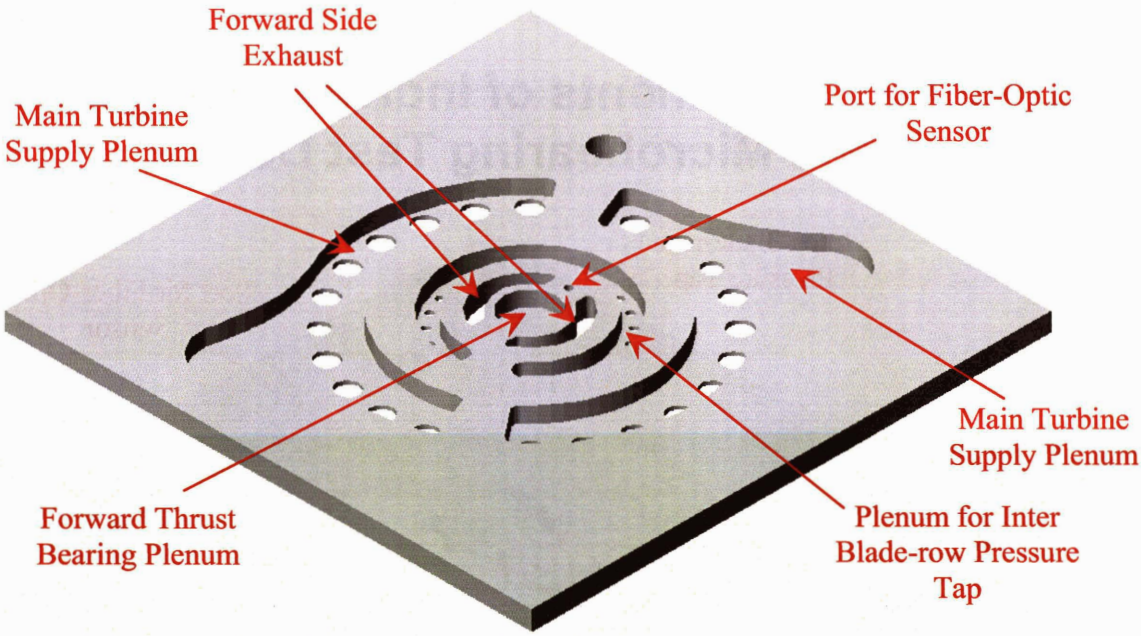

Figure B-3: Details of forward side of Level 2.

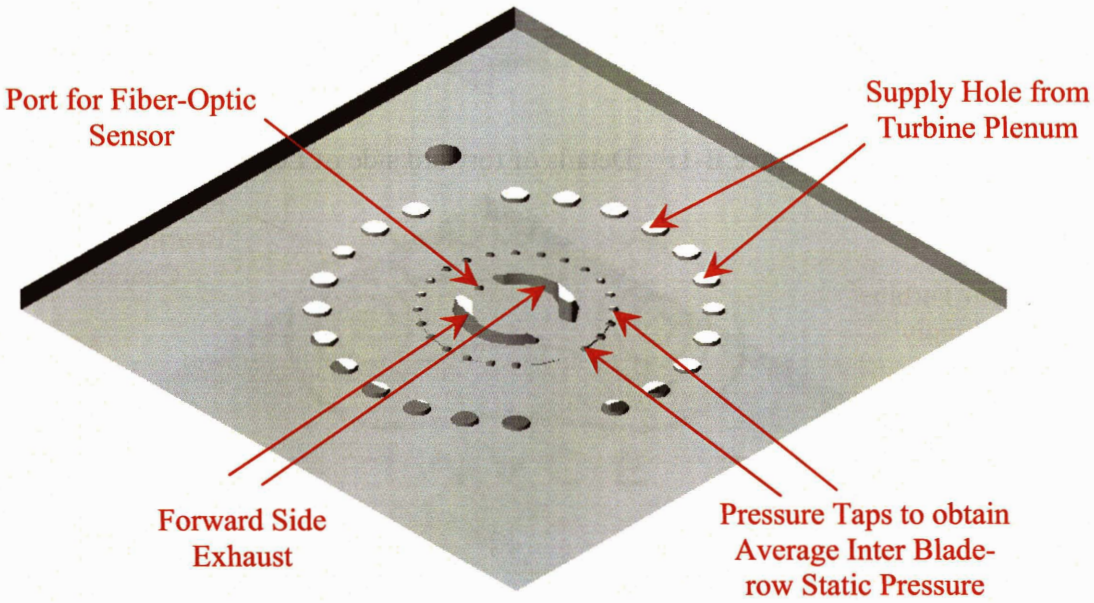

Figure B-4: Details of aft side of Level 2.

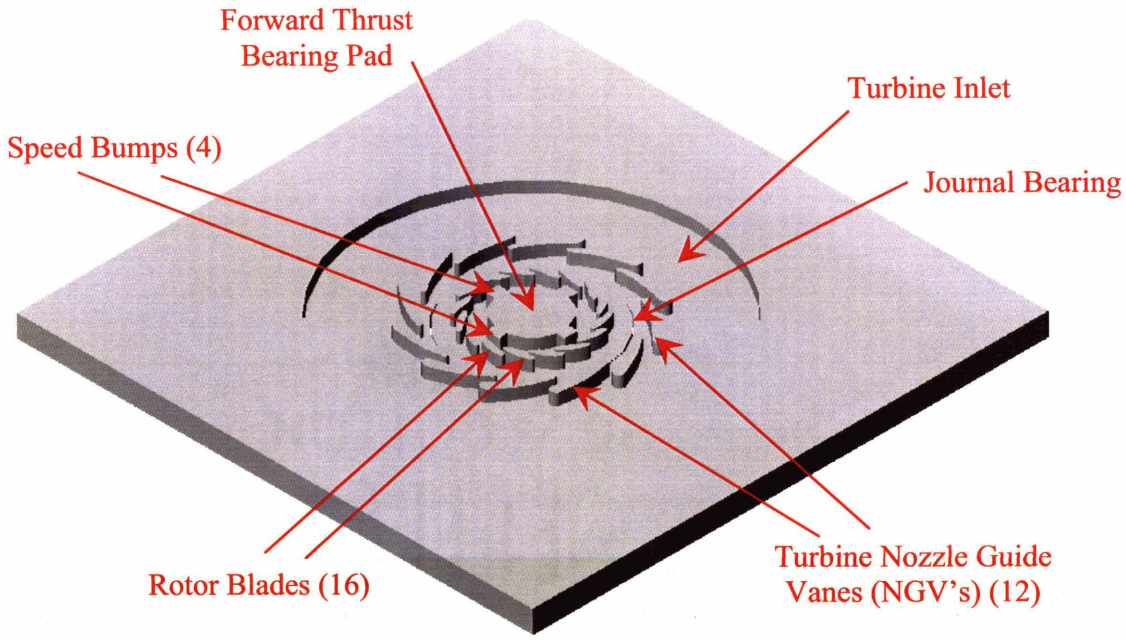

Figure B-5: Details of forward side of Level 3.

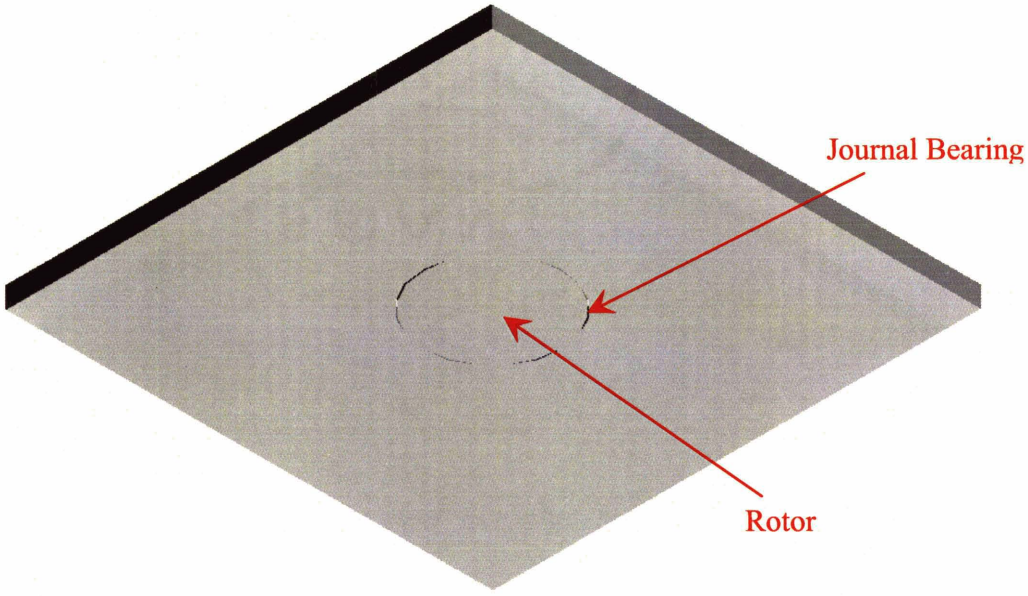

Figure B-6: Details of aft side of Level 3.

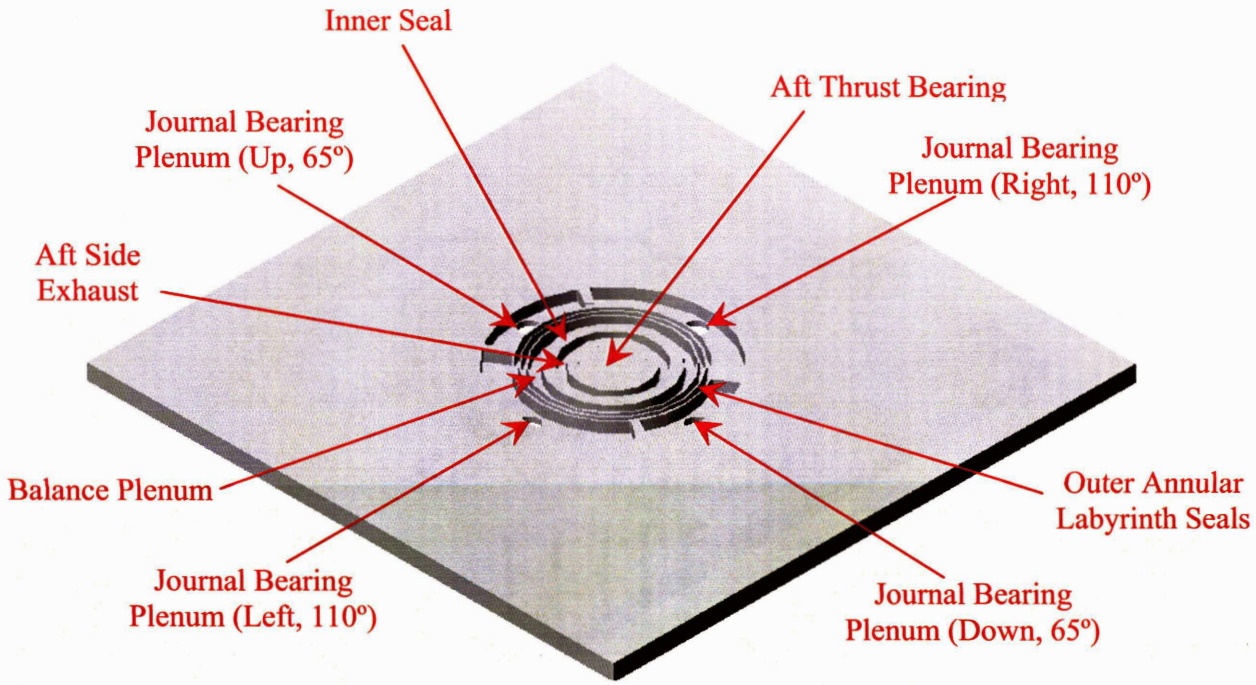

Figure B-7: Details of forward side of Level 4.

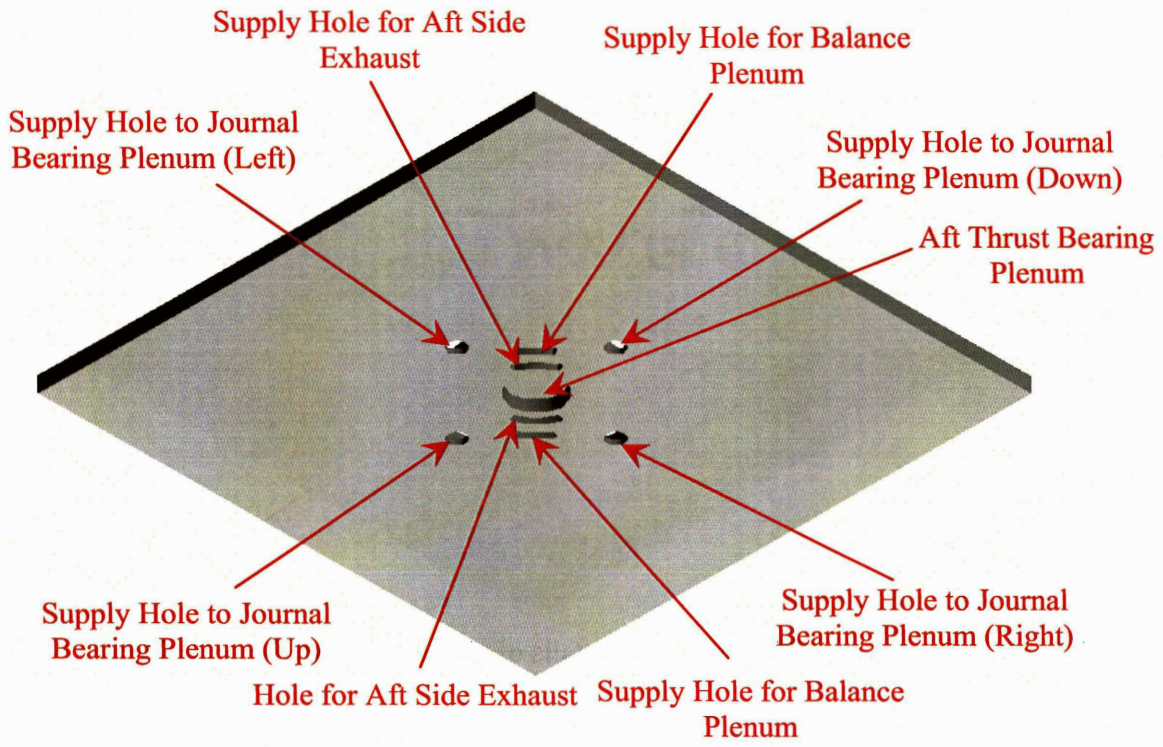

Figure B-8: Details of aft side of Level 4.

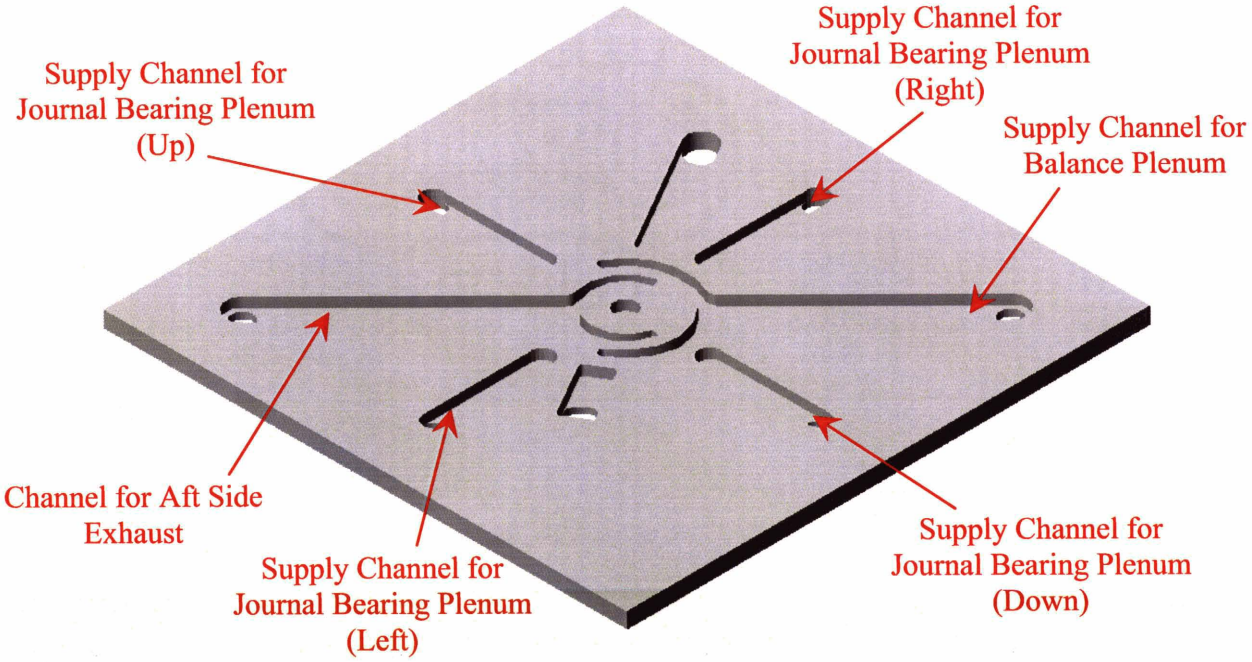

Figure B-9: Details of forward side of Level 5.

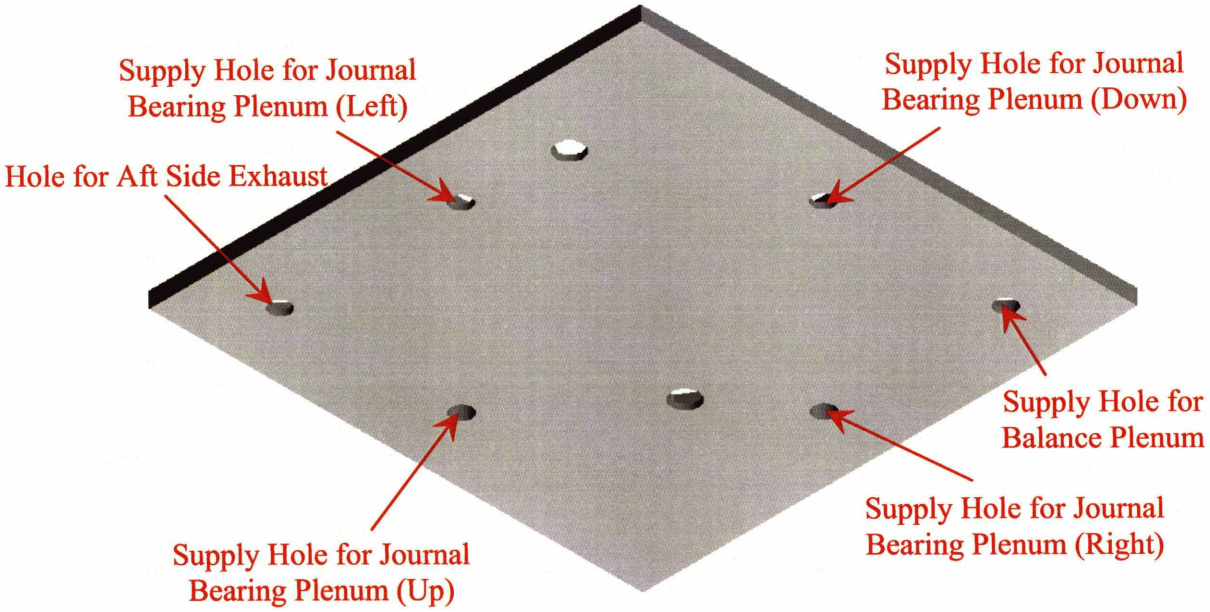

Figure B-10: Details of aft side of Level 5.

REFERENCES

[1] Epstein A. H. and Senturia S. D., 1997, "Macro Power from Micro Machinery", *Science*, 276, p. 1211.

[2] Epstein A. H., 2004. "Micro-Engines – Scholar Lecture". *ASME J. of Turbomachiney*, Vol. 5, 204-211.

[3] Liu L. X., 2005. *Theory for Hydrostatic Gas Journal Bearings for Micro-Electro-Mechanical Systems.* PhD thesis, Department of Mechanical Engineering, MIT.

[4] Liu L. X., Teo C. J., Epstein A. H. and Spakovszky Z. S., 2005. "Hydrostatic Gas Journal Bearings for Micro-Turbomachinery." *Journal of Vibration and Acoustics*, Vol. 127, 157-164.

[5] Spakovszky Z. S. and Liu L. X., 2005. "Scaling Laws for Ultra-Short Hydrostatic Gas Journal Bearings." *Journal of Vibration and Acoustics*, Vol. 127, 254-261.

[6] Ehrich F. F. and Jacobson S. A., 2002. "Development of High-Speed Gas Bearings for High-Power Density Microdevices." *Journal of Engineering for Gas Turbines and Power*, Vol. 125, 141-148.

[7] Lin C. C., 1999. *Development of a Microfabricated Turbine-Driven Air Bearing Rig.* PhD thesis, Department of Mechanical Engineering, MIT.

[8] Piekos E. S., 2000. *Numerical Simulation of Gas-Lubricated Journal Bearings for Microfabricated Machines.* PhD thesis, Department of Aeronautics and Astronautics, MIT.

[9] Orr D. J., 2000. *Macro-Scale Investigation of High Speed Gas Bearings for MEMS Devices.* PhD thesis, Department of Aeronautics and Astronautics, MIT.

[10] Lomakin A., 1958. "Calculation of Critical Number of Revolutions and the Conditions Necessary for Dynamic Stability of Rotors in High-Pressure Hydraulic Machines when Taking into Account Forces Originating in Sealings." In *Journal for Power and Mechanical Engineering* (in Russian), 14, No. 4, 1-5.

[11] Savoulides N., 2000. *Low Order Models for Hybrid Gas Bearings.* MS thesis, Department of Aeronautics and Astronautics, MIT.

[12] Frechette L. G., 2000. *Development of a Silicon Microfabricated Motor-Driven Compression System*, PhD thesis, Department of Aeronautics and Astronautics, MIT.

[13] Frechette L. G., Jacobson S. A., Breuer K. S., Ehrich F. F., Ghodssi R., Khanna R., Wong C. W., Zhang X., Schmidt M. A., Epstein A. H., 2000. "Demonstration of a Microfabricated High Speed Turbine Supported on Gas Bearings." Presented at Solid-State Sensor and Actuator Workshop, Hilton Head Island, SC, June 2000.

[14] Wong C. W., 2001. Design, Fabrication, Experimentation and Analysis of High-Speed Microscale Gas Bearings. MS thesis, Department of Mechanical Engineering, MIT.

[15] Liu L. X. and Spakovszky Z. S., 2006. "Effects of Bearing Stiffness Anisotropy on Hydrostatic Micro Gas Journal Bearing Dynamic Behavior." *Journal of Engineering for Gas Turbines and Power*, Vol. 128.

[16] Savoulides N., 2004. *Development of a MEMS Turbocharger and Gas Turbine Engine.* PhD thesis, Department of Aeronautics and Astronautics, MIT.

[17] Diez S., 2003. *Preliminary Performance Characteristics of a Microfabricated Turbopump*. M. Sc. Thesis, Department of Aeronautics and Astronautics, MIT.

[18] Steyn J. L., 2005 *A Microfabricated ElectroQuasiStatic Induction Turbine-Generator*. PhD thesis, Department of Aeronautics and Astronautics, MIT.

[19] Constantinescu V. N. and Galetuse S., 1987. "On the dynamic stability of the spiral-groove gas-lubricated thrust bearing." *Journal of Tribology*, Vol. 109, pages 183-188.

[20] Constantinescu V. N. and Galetuse S., 1990. "Stability criterion for spiral grooved thrust gas bearings." *Journal of Tribology*, Vol. 112, pages 734-737.

[21] Idelchik I. E., 1994. Handbook of Hydraulic Resistance. 3rd ed., CRC Press.

[22] Gong Y., 2006. Private Communications, MIT Gas Turbine Laboratory.

[23] Shapiro A. H., 1953. *The Dynamics and Thermodynamics of Compressible Fluid Flow, Vol. I.* New York: Ronald Press.

[24] Eshghy S., 1975. "Optimum Design of Multiple-Hole Inherently Compensated Air Bearings." *Journal of Lubrication Technology*, Vol. 97, 221-227.

[25] Vohr J. H., 1966. "An experimental study of flow phenomenon in the feeding region of an externally pressurized gas bearing." *ASME Lubrication Symposium.*

[26] Licht L., Fuller D. D. and Sternlicht B., 1958. "Self excited vibrations of an air-lubricated thrust bearing." *Trans. ASME*, Vol. 80, No. 2, Feb 1958, pages 411-414.

[27] Roudebush W. H., 1957. "An analysis of the effect of several parameters on the stability of an air-lubricated hydrostatic thrust bearing." *NACA Technical Note* 4095.

[28] Allen D. S., Stokes P. J. and Whitley S., 1961. "The Performance of Externally Pressurized Bearings Using Simple Orifice Restrictors." *ASLE Transactions*, Vol. 4, 181-196.

[29] Stowell T. B., 1971. "Pneumatic Hammer in a Gas Lubricated Externally Pressurized Annular Thrust Bearing." *Trans. ASME*, Vol. 93, 498-503.

[30] Chen N. N. S. and Ho K. W., 1981. "Performance Study of a Hydrostatic Air Thrust Bearing." *Wear*, Vol. 70, 207-217.

[31] Senturia S., 2001. *Microsystem Design*. Kluwer Academic Publishers.

[32] Jacobson S. A., 2006. Private Communications, MIT Gas Turbine Laboratory.

[33] Al-Bender F. and Brussel H. V., 1992. "Tilt characteristics of circular centrally fed aerostatic bearings." *Tribology International*, Vol. 25, 189-197.

[34] Yabe H. and Watanabe N., 1988. "A Study on the Running Accuracy of an Externally Pressurized Gas Thrust Bearing (Load Capacity Fluctuation Due to Machining Errors of the Bearing)." *JSME International Journal*, Series III, Vol. 31, 114-120.

[35] Yabe H. and Yamamoto M., 1989. "A Study on the Running Accuracy of an Externally Pressurized Gas Thrust Bearing (Bearing Stiffness and Damping Coefficient)." *JSME International Journal*, Series III, Vol. 32, 618-624.

[36] Nakamura T. and Yoshimoto S., 1996. "Static tilt characteristics of aerostatic rectangular double-pad thrust bearings with compound restrictors." *Tribology International*, 29, 145-152.

[37] Nakamura T. and Yoshimoto S., 1997. "Static tilt characteristics of aerostatic rectangular double-pad thrust bearings with double row admissions." *Tribology International*, 30, 605-611.

[38] Childs D., 1993. *Turbomachinery Rotordynamics – Phenomena, Modeling and Analysis.* John Wiley and Sons.

[39] Greitzer E. M., Tan C. S. and Graf M. B., 2004. *Internal Flow: Concepts and Applications*. Cambridge University Press.

[40] Kwan Y. P. and Post J. B., 2000. "A tolerancing procedure for inherently compensated, rectangular aerostatic thrust bearings." *Tribology International*, 33, 581-585.

[41] Sirakov B., 2004. *Characterization and Design of Non-Adiabatic Micro-Compressor Impeller and Preliminary Design of Self-Sustained Micro Engine System.* PhD thesis, Department of Aeronautics and Astronautics, MIT.

[42] Batchelor G. K., 1967. *An Introduction to Fluid Dynamics*. Cambridge University Press.

[43] Li H. Q., 2006. Private Communications, MIT Gas Turbine Laboratory.

[44] Drela, M. and Youngren H., 1995. *A User's Guide to MISES 2.1*. Technical report, Massachusetts Institute of Technology.

[45] Chen K. S., 1999. *Materials Characterization and Structural Design of Ceramic Micro Turbomachinery.* PhD thesis, Department of Aeronautics and Astronautics, MIT.

[46] Young W. C. and Budynas R. G., 2002. *Roark's Handbook of Stress and Strain,* 7th Edition. McGraw-Hill Book Company.

[47] Blevins R. D., 1984. *Formulas for Natural Frequency and Mode Shape.* Krieger Publishing Company, Malabar, Florida.

[48] Paduano J. D., 2006. Private Communications, MIT Gas Turbine Laboratory.

[49] Berry S., 2006. Private Communications, MIT Lincoln Laboratory.

[50] Ehrich F. F., 2006. Private Communications, MIT Gas Turbine Laboratory.

[51] Ehrich F. F. 1995. "Nonlinear Phenomena in Dynamic Response of Rotors in Anisotropic Mounting Systems." *Journal of Mechanical Design*, Vol. 117, 154-161.